2011

EVALUATION OF THE PHYSICOCHEMICAL PROPERTIES AND STABILITY OF SOLID LIPID NANOPARTICLES DESIGNED FOR THE DELIVERY OF DEXAMETHASONE TO TUMORS

Melissa Howard
University of Kentucky, meldi614@aol.com

Recommended Citation

Howard, Melissa, "EVALUATION OF THE PHYSICOCHEMICAL PROPERTIES AND STABILITY OF SOLID LIPID NANOPARTICLES DESIGNED FOR THE DELIVERY OF DEXAMETHASONE TO TUMORS" (2011). *University of Kentucky Doctoral Dissertations*. 806.
https://uknowledge.uky.edu/gradschool_diss/806

ABSTRACT OF DISSERTATION

Melissa Howard

The Graduate School

University of Kentucky

2011

EVALUATION OF THE PHYSICOCHEMICAL PROPERTIES AND STABILITY OF SOLID LIPID NANOPARTICLES DESIGNED FOR THE DELIVERY OF DEXAMETHASONE TO TUMORS

ABSTRACT OF DISSERTATION

A dissertation submitted in partial fulfillment of the
requirements for the degree of Doctor of Philosophy in the
College of Pharmacy at the University of Kentucky

By
Melissa Howard

Lexington, Kentucky

Co-Director: Dr. Michael Jay, Fred N. Eshelman Distinguished Professor of Molecular
Pharmaceutics, University of North Carolina at Chapel Hill
and Co-Director: Dr. Paul Bummer, Associate Professor of Pharmaceutical Sciences,
University of Kentucky

Lexington, Kentucky

2011

ABSTRACT OF DISSERTATION

EVALUATION OF THE PHYSICOCHEMICAL PROPERTIES AND STABILITY OF SOLID LIPID NANOPARTICLES DESIGNED FOR THE DELIVERY OF DEXAMETHASONE TO TUMORS

Pre-clinical and clinical trials suggest that pre-treatment with dexamethasone (Dex) may facilitate enhanced uptake of subsequently administered chemotherapeutic agents. To reduce the side effects associated with systemic administration of Dex, solid lipid nanoparticles (SLNs) containing dexamethasone palmitate (Dex-P) were prepared as a means of achieving tumor-targeted drug delivery. These studies were aimed at evaluating the physicochemical properties and both the physiological and storage stability of the SLNs.

SLNs were prepared using nanotemplate engineering technology. Stearyl alcohol (SA) was used as the lipid phase with Brij® 78 and Polysorbate 60 as surfactants and PEG6000 monostearate as a long-chain PEGylating agent. Both formulations exhibited a small particle size, ellipsoidal shape, and low polydispersity. ^{1}H-NMR spectroscopy confirmed that SLNs have the expected solid core and PEGylated surface. Analysis of the bulk materials indicated that a number of complex interactions are present among the SLN components, including a eutectic between SA and Brij® 78.

Dex-P could be incorporated in SLNs at 10-30% w/w SA with encapsulation efficiencies >85%. A preferential interaction with the SA-Brij® 78 eutectic was identified, indicating a possible interfacial localization. For comparison, SLNs were also prepared with ascorbyl palmitate (AP) and curcumin. Higher drug loads were achieved with both palmitate-containing prodrugs than curcumin, though all appeared to align differently within the SLNs.

SLNs undergo a concentration-dependent particle size growth when incubated at physiological temperature. However, they appear to remain intact with over 85% of the added Dex-P retained at 24 h in conditions mimicking human plasma. In the presence of carboxylesterase, SLNs became turbid and showed a reduction in particle size as compared to controls. This instability was shown to be a result of the hydrolysis of PEG6000 monostearate and Polysorbate 60.

To enhance storage stability, a lyophilization protocol designed to minimize changes in the physicochemical properties of SLNs was developed. During a 3 month period, lyophilized SLNs stored at 4°C demonstrated the greatest stability, showing a consistent particle size and an encapsulation efficiency >80%. Overall, these results indicate that Dex-P loaded SLNs possess the physicochemical properties and stability desirable for development as a tumor-targeted drug delivery system.

Keywords: solid lipid nanoparticles, crystallinity, drug loading, PEGylation, stability

Melissa Howard
Student's Signature

July 19, 2011
Date

EVALUATION OF THE PHYSICOCHEMICAL PROPERTIES AND STABILITY OF SOLID LIPID NANOPARTICLES DESIGNED FOR THE DELIVERY OF DEXAMETHASONE TO TUMORS

By

Melissa Howard

Dr. Michael Jay
Co-Director of Dissertation

Dr. Paul Bummer
Co-Director of Dissertation

Dr. Jim Pauly
Director of Graduate Studies

July 19, 2011
Date

RULES FOR THE USE OF DISSERTATIONS

Name	Date

DISSERTATION

Melissa Howard

The Graduate School

University of Kentucky

2011

EVALUATION OF THE PHYSICOCHEMICAL PROPERTIES AND STABILITY OF SOLID LIPID NANOPARTICLES DESIGNED FOR THE DELIVERY OF DEXAMETHASONE TO TUMORS

DISSERTATION

A dissertation submitted in partial fulfillment of the
requirements for the degree of Doctor of Philosophy in the
College of Pharmacy at the University of Kentucky

By
Melissa Howard

Lexington, Kentucky

Co-Director: Dr. Michael Jay, Fred N. Eshelman Distinguished Professor of Molecular Pharmaceutics, University of North Carolina at Chapel Hill
and Co-Director: Dr. Paul Bummer, Associate Professor of Pharmaceutical Sciences, University of Kentucky

Lexington, Kentucky

2011

ACKNOWLEDGEMENTS

I would like to express my gratitude to the countless people who have helped and supported me through the course of my graduate work. This dissertation would not have been possible without you.

First and foremost, I would like to thank my committee. You have all played an integral role in my success. To my advisor, Dr. Michael Jay, it has been a privilege to work with you. I have seen your dedication to your students evidenced in so many ways, and I will always admire you for that. You taught me what it means to be a mentor, and I hope that someday my students will appreciate me as much as I appreciate you. To Dr. Tom Dziubla, I will forever be grateful to the IGERT program for "forcing" me to work with you. You have challenged my thinking and inspired me to become a better scientist. Not only that, your support has simply been invaluable. To Dr. Paul Bummer, thank you for accepting me into your lab and serving as my co-advisor in a rather non-traditional situation. Your willingness to help has not gone unnoticed. To Dr. Leggas and Dr. Rinehart, this project would never have come to fruition without you. Our collaborations have expanded my knowledge and taught me how to think about my work from a different perspective. I would also like to give a special thanks to Dr. Stefan Stamm for agreeing to serve as my outside examiner.

Beyond my committee, there are so many other people at the University of Kentucky that have contributed to me reaching this point. I would like to thank the administration of the Department of Pharmaceutical Sciences, especially Dr. Patrick McNamara, for having enough faith in me to support my continued work under Dr. Jay. I would also like to thank all the members of the IGERT program for supporting me and challenging me in my work. I am grateful to have been a part of such a program; the opportunities provided were truly exceptional. To Catina Rossoll and Erin Pyrek, these programs would not be the same without you. I thank you not only for your dedication to the administrative tasks you perform but also for your willingness to lend an ear or a hand to students whenever necessary. To Dr. Younsoo Bae, thank you for sharing your knowledge with me and allowing me to be an honorary member of your lab; it was a pleasure. To Dr. Bradley Anderson, you inspire me with your passion for science, and I appreciate your encouragement.

I would also like to thank all the students and postdocs I have had the opportunity to work with; please know that you have all contributed to my growth, both as a scientist and as a person. I would like to give a special thanks to the members of Dr. Bummer's lab (Salin Gupta Patel, Lin Song, and Abebe Mengesha) for sharing your space and treating me as one of your own. It would have been a lonely few years without you. To Dr. Xiuling Lu, I am so fortunate to have met you when I joined Dr. Jay's lab; your enthusiasm for this work was contagious.

On a personal note, I would like to thank my family and friends for their love and support. To my Mom, I would not be who I am today without you. You taught me that I could achieve anything in life and supported me in every step I have taken. I would never have made it to this point if it were not for you. Finally, to my husband, Joshua, I am so grateful that you have been by my side the last four years. Your love and encouragement have kept me going in the face of frustration. Thank you for understanding me and my need to dream big dreams. I love you.

TABLE OF CONTENTS

LIST OF TABLES

LIST OF FIGURES

Chapter 1

Introduction and Statement of Problem

In spite of the development of an arsenal of highly potent chemotherapeutic agents, clinical success in treating cancer remains a challenge. Tumors are characterized by a number of properties (e.g., high interstitial fluid pressure (IFP), irregular vasculature, efflux pumps) that may act as barriers to drug delivery [1, 2]. As a result, many drugs fail to perform *in vivo* as well as would be predicted from *in vitro* studies due to a failure to reach the target site in adequate quantities. Correspondingly, a high amount of the administered drug is left to act on healthy tissues, often to the point of generating dose-limiting side effects.

Pre-treatment with Dexamethasone (Dex) is one possible technique for improving the *in vivo* success of chemotherapeutic agents. Dex is a synthetic gluococorticoid well known for its anti-inflammatory properties [3, 4]. However, recent pre-clinical and clinical trials have indicated that it may also have use as a chemotherapeutic adjuvant. Pre-administration of Dex was shown to reduce the toxicity and, in some cases, increase the efficacy of chemotherapeutic agents. For instance, Dex pre-treatment was shown to significantly increase the efficacy of carboplatin (DNA alkylating agent), gemcitabine (antimetabolite), or a combination of both drugs by 2-4 fold in six xenograft models tested (2 colon, 2 breast, 1 lung, and 1 glioma cancers) [5]. Dex pre-treatment also reduced the significant decrease in granulocyte counts seen with carboplatin treatment in CD-1 mice [6]. In clinical trials, Dex pre-treatment has resulted in a reduction in hematopoietic toxicity and an improvement in absolute granulocyte count and platelet count recovery times [7, 8].

The complete mechanism behind Dex's beneficial effects remains elusive but is likely a result of its inhibition of the nuclear factor kappa B (NF-κB) signaling pathway [9, 10]. Disruption of this signaling pathway is thought to be associated with a change in the tumor cytokine profile [11] that results in decreased IFP [12, 13] and a normalization of the tumor vasculature [11, 14]. In turn, it is suspected that these effects allow for the enhanced uptake of chemotherapeutic agents into tumors [5, 11], improving their efficacy and limiting their toxic side effects [6]. However, there may be some limitations to this therapy. First, the results do appear to be schedule, dose, and possibly chemotherapeutic agent-dependent with some literature indicating that Dex may result in a decrease in the efficacy of chemotherapeutic agents [15-18]. Additionally, there are a number of side effects associated with systemic administration of Dex that may be undesirable for patients undergoing chemotherapy, most notably immunosuppression through T-cell depletion and inhibition [3, 19].

In order to maximize the potential of Dex to serve as a chemotherapeutic adjuvant while minimizing its toxicities, a localized delivery system would be preferable. Nanoparticles are one potential means of achieving this goal. Though a number of advantages, including enhanced solubilization [20], controlled/bioresponsive release capacity [21-24], evasion of multidrug resistance (MDR) mechanisms [25, 26], and limited drug degradation [27] have been claimed for these systems over their solution counterparts, the most notable is their targeting ability. Due to the enhanced permeability and retention (EPR) effect of tumors [28, 29], nanoparticles of the appropriate size are able to passively target tumors [30, 31]. This can enhance drug uptake into the tumor while limiting its presence throughout the rest of the body.

While a number of nanoparticle drug delivery systems are available, solid lipid nanoparticles (SLNs) have received considerable attention due to their low toxicity [32-34] and amenability to large-scale production methods [33, 34]. Early work from this laboratory resulted in two SLN formulations encapsulating dexamethasone palmitate (Dex-P), an ester prodrug of Dex [35]. This prodrug was chosen because the palmitate moiety was expected to associate with the hydrophobic core of the SLNs and enhance the drug loading. Additionally, Dex-P has previously been used in humans with a good safety profile [36]. Interestingly, drug release from the nanoparticles appeared to be dependent on the carboxylesterase (CE) activity of the surrounding environment [37].

This dissertation will focus on gaining a thorough understanding of the physicochemical properties of the Dex-P loaded SLN formulations as well as evaluating them for both physiological and storage stability. Initially, SLNs will be assessed for their size, shape, core-shell structure, and crystallinity. The extent and mechanism of drug loading will be evaluated, and comparisons will be made with other drugs of similar structure and lipophilicity. Secondly, the stability of SLNs will be evaluated under physiological conditions, both in the absence and presence of CE enzymes. Finally, a lyophilization protocol designed to minimize changes in the physicochemical properties of the SLNs will be developed, and the long-term storage stability of lyophilized SLNs and SLN suspensions will be compared. These studies may provide valuable information regarding the structure and stability of not only the drug delivery system under consideration, but also nanoparticles in general.

Chapter 2

Plan of Research

Pre-clinical and clinical trials suggest that delivery of Dex to tumors can lower the IFP [13], thereby reducing this physiological barrier to the uptake of administered chemotherapeutic agents. However, Dex exhibits toxicities such as immunosuppression that can adversely affect patients undergoing chemotherapy. Targeting the delivery of Dex specifically to tumors would minimize the undesirable side effects associated with systemic administration of the drug. Nanotemplate engineered SLNs containing Dex-P were prepared as a means of achieving tumor-targeted drug delivery. The overall hypothesis of this dissertation is that the interactions among the components of SLNs decrease the crystallinity of nanoparticle lipids resulting in enhanced drug loading and limited stability of the nanoparticles under both physiological and storage conditions. The following specific aims will be pursued in order to test this hypothesis:

Specific Aim 1: To fully characterize the physicochemical properties of nanotemplate engineered SLNs, including particle size, shape, structure, and changes in the extent or type of crystallinity from the starting materials due to interactions among the nanoparticle components.

Specific Aim 2: To assess the degree of loading of Dex-P into nanotemplate engineered SLNs as compared to other compounds of similar structure or lipophilicity.

Specific Aim 3: To evaluate the stability of nanotemplate engineered SLNs in conditions mimicking those of human plasma as a function of time.

Specific Aim 4: To determine if the PEGylating agents incorporated into SLNs are affected by the CE activity of the surrounding environment.

Specific Aim 5: To determine if the storage stability of drug loaded SLNs is enhanced when using lyophilization protocols that minimize changes in the physicochemical properties of the nanoparticles.

To achieve these Specific Aims, the research plan described in sections 2.1 through 2.5 was carried out.

2.1. Preparation and Characterization of Blank SLNs

The objective of this section was to compare the physicochemical properties of two SLN formulations previously developed for Dex-P loading. SLNs were prepared using nanotemplate engineering technology (NET). Stearyl alcohol (SA) was used as the lipid phase with Brij® 78 and Polysorbate 60 (PS60) as surfactants in both formulations; the second formulation differed by the inclusion of a long-chain PEGylating agent, PEG6000 monostearate (PEG6000MS). Nanoparticle size and shape were assessed using a combination of dynamic light scattering (DLS) and transmission electron microscopy (TEM) techniques. SLN structure was determined through a comparison of the ^{1}H-NMR spectra of solubilized and intact SLNs accompanied by relaxation time measurements. Powder X-ray diffraction (PXRD) and differential scanning calorimetry (DSC) were used to analyze the crystallinity of the SLNs.

2.2. Preparation and Characterization of Drug Loaded SLNs

The use of Dex-P has been shown to enhance drug loading in the SLNs. The goals of this section were 1) to prepare and characterize SLNs loaded with Dex-P and 2) to make comparisons with other drugs of similar structure or lipophilicity. In addition to the properties described above (size, shape, structure, and crystallinity), SLNs will be assessed for the extent of drug loading and encapsulation efficiency. Ultrafiltration will be used for separation of free and encapsulated drug; quantification will be performed using an HPLC-UV assay. Curcumin and ascorbyl palmitate (AP) will be used for the comparison studies. Both drugs are lipophilic, but curcumin lacks the palmitate moiety that may align with the SLN lipids.

2.3. Stability of Drug Loaded SLNs in Human Plasma-mimicking Conditions

Release of Dex from the SLNs appeared to be dependent on the presence of CE activity. The aims of this section were 1) to confirm the stability of SLNs and 2) to confirm the retention of Dex-P with the SLNs under conditions mimicking those found in human plasma (specifically the absence of CE activity). Initial studies were focused on monitoring the size and shape of SLNs incubated at 37°C. To further elucidate the mechanism of particle size growth, the effect of SLN concentration on particle size growth was evaluated, and SLNs returned to 4°C following incubation at 37°C were tested for size recovery. SLNs were then exposed to human serum albumin (HSA) as a representative protein and monitored for size and turbidity changes. Size exclusion chromatography (SEC) was used as a secondary technique to confirm the intact state of the SLNs in the presence of HSA. To determine the retention of Dex-P with the SLNs in the presence of human plasma, a multi-step filtration process was employed, consisting of an initial filtration through a 0.2 μm membrane followed by ultrafiltration. By accounting for the known protein binding, the amount of drug retained with the SLNs was calculated.

2.4. Stability of PEGylating Agents in the Presence of CE Activity

The objective of this section was to determine if the accelerated drug release observed in the presence of CE enzymes may be partially attributable to hydrolysis of the ester-containing materials, PS60 and PEG6000MS, leading to increased accessibility of the prodrug to enzymes. Hydrolysis of PEG6000MS was monitored using SEC, and hydrolysis of PS60 was monitored using a pH-stat assay. Comparisons were made between the materials in SLNs and in micelles, and controls were run using bis(4-nitrophenyl) phosphate (BNPP) as a CE inhibitor. In parallel, the effects of hydrolysis on the stability of SLNs were evaluated through monitoring changes in turbidity, particle size, and particle shape.

2.5. Storage Stability of Drug Loaded SLNs

The goals of this section were 1) to optimize a protocol for lyophilizing SLNs and 2) to compare the long-term stability of aqueous and lyophilized SLNs. In optimizing the lyophilization protocol, the following aspects were considered: lyoprotectant (LP) type and concentration, SLN concentration, freezing temperature, rate of freezing, and drying time. SLNs were assessed for changes in the particle size, shape, monodispersity, and drug loading. For the long-term stability study, lyophilized SLNs and SLN suspensions were stored at 4°C and 25°C/60% RH. Samples were removed at days 0, 1, 3, 7, 14, and months 1, 2, and 3 for measurement of the particle size and drug loading.

Chapter 3

Background and Significance

3.1. CANCER AND CHEMOTHERAPY

Cancer can be defined as the uncontrolled growth and spreading of abnormal cells [38]. As of 2010, it remained one of the leading causes of death in the United States of America, second only to cardiovascular disease [39]. Although the final numbers are not in, it is estimated that nearly 600,000 Americans died from cancer in 2010 and another 1.5 million people were diagnosed with new cases [39]. Due to the staggering numbers associated with this disease, a variety of treatment options are currently being utilized, and a number of others are under development [38, 40, 41].

Surgical resection is typically employed with early-stage disease [38, 41]. Unfortunately, it cannot be utilized in all cases, such as when the cancer is undetectable, has metastasized, or is not confined to a solid tumor (e.g., leukemia). Further, it may be difficult to completely remove the affected cells, and surgery may trigger a faster metastatic process for any remaining cells [38]. For this reason, chemotherapy, radiation therapy, hormone therapy, immunotherapy, or a combination of these may be employed, either in lieu of or following surgery [38]. Of these, chemotherapy is the most mainstream.

3.2. BARRIERS TO CHEMOTHERAPY

Chemotherapy refers to the use of drugs directed at killing or controlling the growth of cancer cells. Despite extensive research on the development of highly potent chemotherapeutic agents, clinical success in treating cancer remains limited. Although many of these drugs demonstrate *in vitro* potency, they are often less successful than anticipated *in vivo* because of drug delivery limitations. Following injection, a drug must be distributed throughout the vascular space, transported across the vascular wall, transported through the interstitial space, and finally transported across the cell membrane [42]. Unfortunately, many obstacles exist on this path that may prevent drug from reaching the site of action in sufficient quantity. As a result, drug distributes into healthy tissues, potentially inducing dose-limiting toxicities [38].

The irregular vasculature of tumors is the first barrier to tumor drug delivery (Figure 3.1) [1]. Tumor vasculature consists of blood vessels co-opted from the host vasculature as well as vessels that result from the angiogenic response of host vessels to cancer cells [1, 43]. As a result, tumor vasculature may display different fractal dimensions and minimum path lengths from normal blood vessels. Some regions of a tumor may be well-vascularized, while others may be necrotic regions based on a lack of blood flow. This may prohibit drug from reaching all regions of the tumor. Unfortunately, this issue is further complicated by the fact that the characteristics of the vasculature may be dependent on the tumor type, growth rate, location, and disease stage.

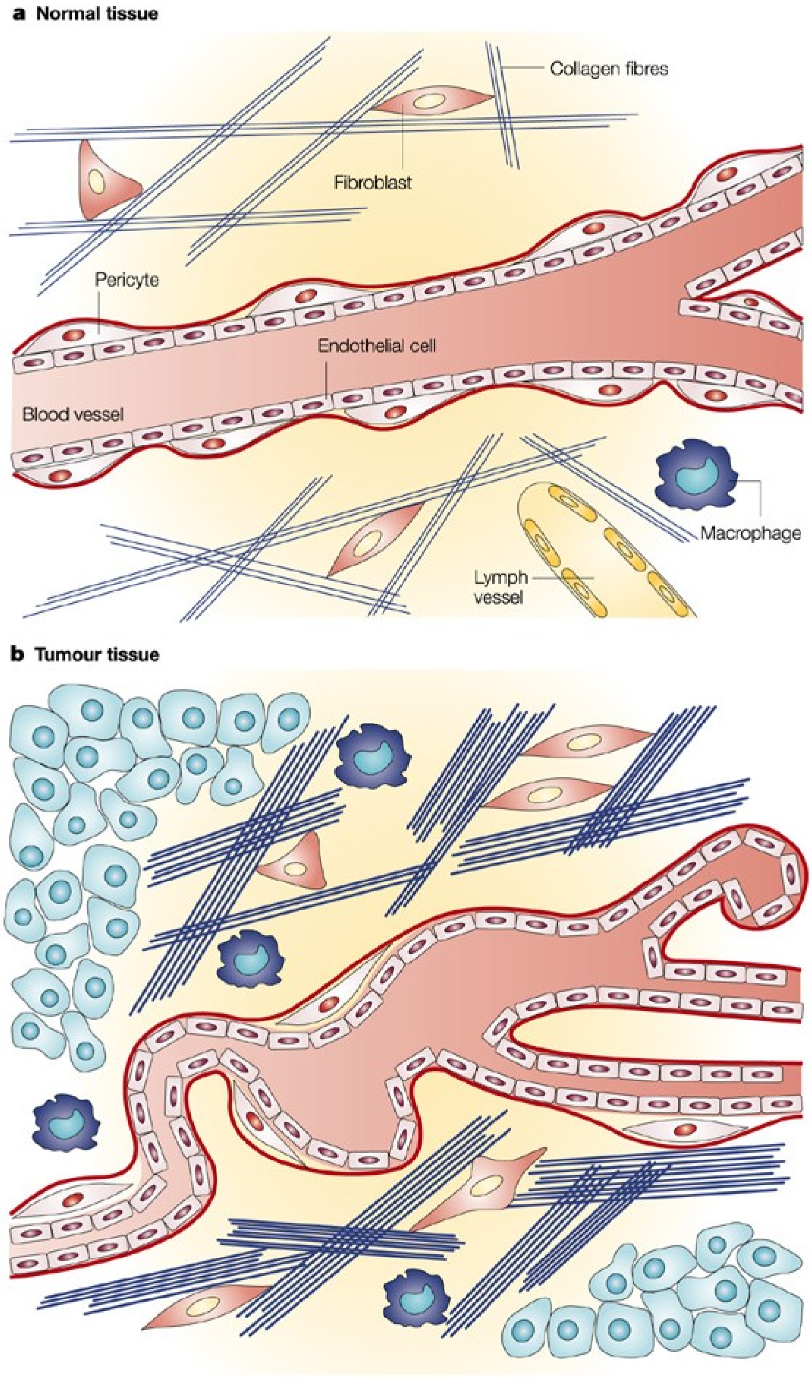

Nature Reviews | Cancer

Figure 3.1. Differences in the stroma of normal tissue (a) and tumo(u)r tissue (b). Adapted from [44]. Reprinted by permission from Macmillan Publishers Ltd: Nature Reviews Cancer, 4(10), 806-813 (2004), copyright © 2004.

High IFP is a second barrier that may be encountered during the extravasation step [1, 44]. The IFP of tumors is controlled by a combination of the hydrostatic pressure (pressure exerted by a fluid due to the force of gravity) and colloid osmotic pressure (pressure built up by the tendency of water to diffuse through a semipermeable membrane into a compartment with higher concentration of high molecular weight molecules, such as proteins that are unable to pass through the membrane) (Figure 3.2). While normal blood vessels display a net outward pressure of 1-3 mm Hg, tumor blood vessels may exhibit a net inward pressure of up to 18 mm Hg. This may limit the transport of molecules out of the vasculature into the interstitial space.

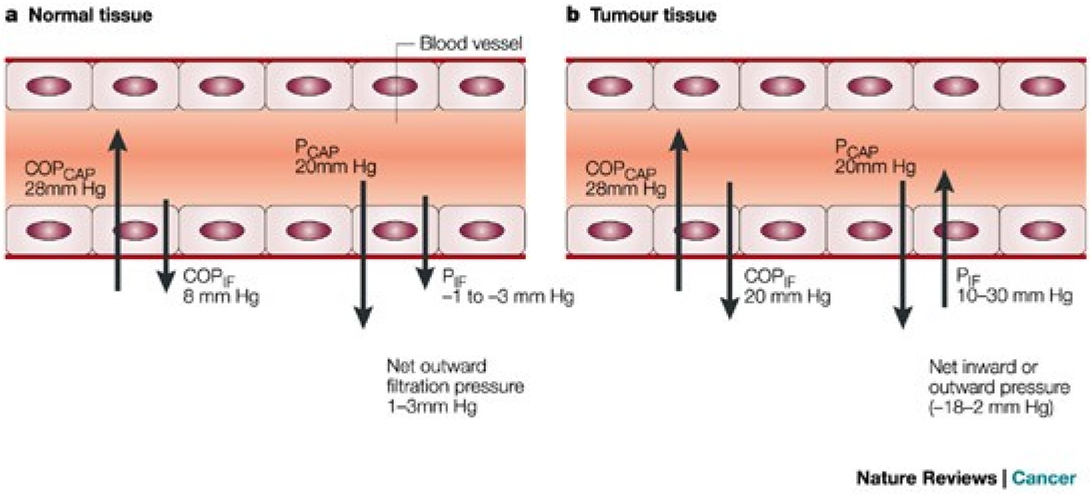

Figure 3.2. Schematic showing the hydrostatic and colloid osmotic pressures in capillaries (P_{CAP} and COP_{CAP}, respectively) and the surrounding interstitium (P_{IF} and COP_{IF}, respectively) in normal tissues (a) and tumo(u)r tissues (b). It should be noted that values are approximate. Adapted from [44]. Reprinted by permission from Macmillan Publishers Ltd: Nature Reviews Cancer, 4(10), 806-813 (2004), copyright © 2004.

It is thought that there may be several contributors to this high IFP (Figure 3.1) [44]. First, as mentioned above, tumor vasculature is highly irregular with numerous convolutions and defects. It is also characterized by enhanced “leakiness” as a result of larger inter-endothelial pores than are present in healthy blood vessels. This may lead to larger numbers of proteins exiting the vasculature. Secondly, tumor lymphatic vessels may be underdeveloped or defective, preventing adequate drainage of fluid and proteins from the tumor tissue. Finally, the interstitial matrix may be contracted based on the work of tumor fibroblasts. While higher concentrations of proteins in the tumor interstitium may result in higher colloid osmotic pressures, increased fluid may lead to elevated hydrostatic pressures. Depending on their balance, the net pressure may oppose flow of molecules into the interstitial space.

If molecules successfully extravasate from the blood vessels into the tumor interstitium, they must then traverse the interstitial space in order to reach tumor cells. Unfortunately, numerous impediments may again exist. First, tumors are characterized by a large interstitial space [42], and drug transport by diffusion may be slow [1]. This can be exacerbated by non-specific binding of the drug to various proteins. Secondly, the IFP is higher in the center of the tumors than it is in the periphery, forcing materials to overcome this outward convection to diffuse into the tumor center [1]. Thirdly, the tumor stroma itself may be prohibitive of drug transport (Figure 3.1). Tumors are characterized by elevated collagen concentrations, resulting in a dense network that may impede drug movement [42]. Macrophages and other inflammatory cells are also known to infiltrate tumors, releasing cytokines and growth factors that may act on cells of the blood vessels and stroma fibroblasts to further increase interstitial fluid pressure [45].

Finally, drugs may face obstacles in achieving high intracellular drug concentrations. In order to protect themselves, many cancer cells overexpress transporters that serve to pump drugs out; these are also known as efflux pumps [2, 46]. The most well-known efflux pump is *P*-glycoprotein (*P*-gp/MDR1), an ATP-dependent transporter encoded for by the ABCB1 gene. Others that have received attention include the multidrug resistance associated proteins (MRP1, MRP2, and probably MRP3, MRP4, and MRP5) and the ABCG2 protein. Thus, although the drugs may pass readily through the cellular membrane, they are rapidly effluxed from the cell and are unable to achieve therapeutic efficacy. This is termed MDR and can be apparent from an initial treatment (intrinsic MDR) or can be developed following treatment (acquired MDR).

3.3. DEXAMETHASONE (Dex)

In order to reduce or eliminate these barriers to chemotherapy, additional drugs may be administered either prior to or concurrently with the chemotherapeutic agents. These drugs may or may not have therapeutic properties of their own but are primarily used as adjuvants in order to improve the efficacy and/or decrease the toxicity of the chemotherapeutic agents. One example of such a drug is Dex (Figure 3.3). Dex is a synthetic glucocorticoid most well known for its anti-inflammatory and immunosuppressive properties [3, 4]. It has shown effectiveness against certain types of cancers, such as leukemia [47, 48], and it has been extensively used in conjunction with chemotherapeutic agents as an anti-emetic [49, 50].

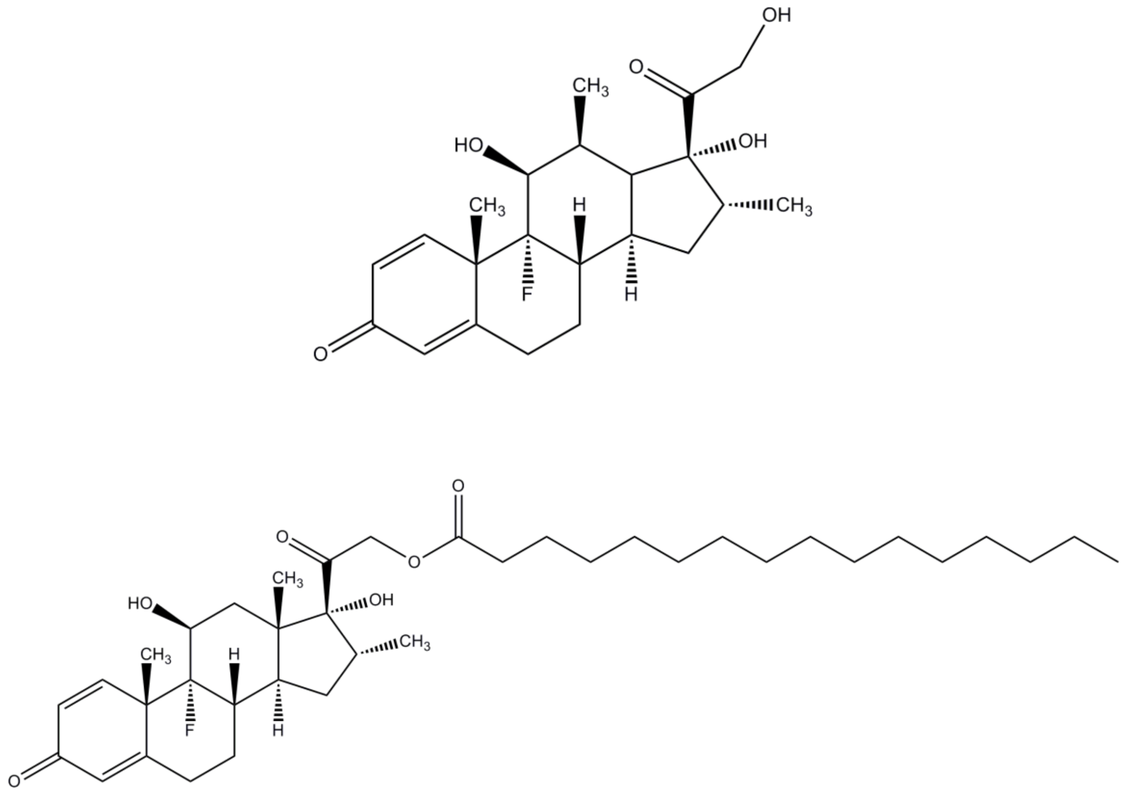

Figure 3.3. Structures of Dexamethasone (Dex, top) and Dexamethasone palmitate (Dex-P, bottom)

However, recent pre-clinical and clinical trials have focused on its use as a chemotherapeutic adjuvant. Studies have shown that Dex pre-treatment can reduce the toxicity and, in some cases, increase the efficacy of chemotherapeutic agents. For instance, both prednisolone and Dex effectively protected progenitor cells in four strains of mice against 5-fluorouracil, a cell-cycle-specific antimetabolic chemotherapeutic agent [51]. Bone marrow progenitors and blood cell numbers were shown to return to normal from 3-5 days and from 1-2 days earlier, respectively, than without glucocorticoid treatment. The same level of efficacy could be achieved with Dex at an approximately 16.5-fold lower dose than with prednisolone. A synergistic growth inhibition was also observed in six B-cell non-Hodgkin lymphoma cell lines when tumor cells were pre-treated with Dex prior to treatment with rituximab, a chimeric human immunoglobulin G1 (IgG1) anti-CD20 monoclonal antibody known to induce cytotoxicity in malignant B cells [52]. Wang et al demonstrated that pre-administration of Dex was able to significantly increase the efficacy of carboplatin, a DNA alkylating agent; gemcitabine, an antimetabolite; or a combination of both drugs by 2-4 fold in six xenograft models tested (2 colon, 2 breast, 1 lung, and 1 glioma cancers) [5]. Correspondingly, Dex pre-treatment was effective in reducing the decrease in granulocyte counts shown to occur with carboplatin treatment in CD-1 mice [6]. The same group also examined the effects of Dex on adriamycin (an anthracycline antibiotic capable of intercalating DNA, also known as doxorubicin) therapy with similar results. Pre-administration of Dex resulted in almost complete inhibition of tumor growth in a syngeneic model of breast cancer [11]. In clinical trials, Dex pre-treatment has resulted in a reduction in hematopoietic toxicity and an improvement in absolute granulocyte count and platelet count recovery times [7, 8].

The complete mechanism (Figure 3.4) behind Dex's beneficial effects remains elusive, but it is assumed to be rooted in Dex's inhibition of the NF-κB signaling pathway [9, 10]. Dex administration induces production of the inhibitory protein IκBα, which can bind to activated NF-κB and prevent its entrance into the nucleus [9, 10]. As the NF-κB signaling pathway is known for its role in the production of a number of pro-inflammatory cytokines [53, 54], its inhibition would be expected to have major repercussions. This is in alignment with the significant change in the tumor cytokine expression profile that has been reported upon administration of Dex [11]. For example, Dex treatment was shown to upregulate tumor necrosis factor-α (TNF-α), a cytokine known to enhance tumor development and metastasis at low concentrations but to induce necrosis and apoptosis of tumor cells at high concentrations. Administration of Dex also resulted in the downregulation of vascular endothelial growth factor (VEGF), a marker for angiogenesis, and interleukin 1β (IL-1β), a pro-inflammatory cytokine. It is thought that this change in cytokine expression plays a role in the reported ability of Dex to decrease the interstitial fluid pressure of tumors [12, 13] and normalize the vasculature [11, 14]. With these barriers to drug delivery reduced, subsequently administered chemotherapeutic agents may be taken up into tumors to a greater extent [5, 11], improving their efficacy. Also, as more drug is delivered to tumors, less is delivered to healthy tissues, and side effects may be reduced or eliminated [6].

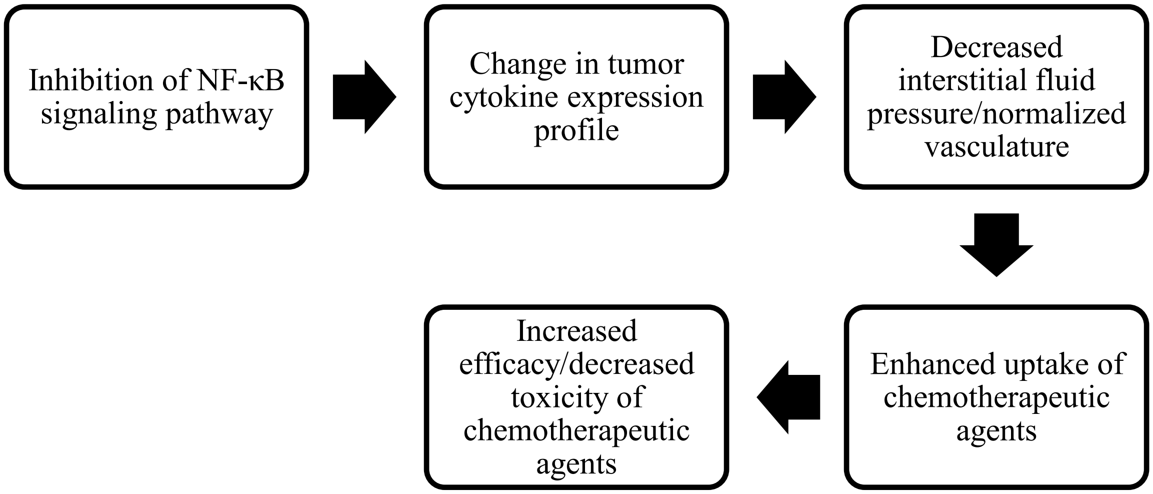

Figure 3.4. Proposed mechanism of action for Dex's chemotherapeutic adjuvant properties

Yet, despite the potential for this therapy, there may be some limitations. Some studies have shown antagonistic results with pre- or co-administration of Dex actually resulting in a decrease in the therapeutic efficacy of chemotherapeutic agents. For example, Herr at al demonstrated that co-administration of Dex negated some of the effects of cisplatin. This was traced to a down-regulation of some pro-apoptotic elements of the death receptor and mitochondrial apoptosis pathways resulting in decreased activity of various caspases [55]. Meyer et al also found a reduction in the therapeutic efficacy of cisplatin with pre-administration of Dex [18]. Through an upregulation of the survival factor Akt and an attenuation of the activation of the mitochondrial apoptotic pathway, Dex reduced the high dose cisplatin induced apoptosis by 10-25% in human osteosarcoma cells. Studies by Sui et al showed that pre-treatment with Dex reduced the therapeutic efficacy of paclitaxel against human breast and ovarian xenografts tumors by 20-25% [17]. These results, however, are in contrast with clinical observations [8].

A second potential limitation of this therapy is that Dex is capable of inducing a number of side effects when administered systemically [56]. The most notable of these is immunosuppression through T-cell depletion and inhibition [3, 19]. For patients undergoing chemotherapy with already weakened immune systems, this can be a limiting factor. In order to maximize the therapeutic potential of Dex while minimizing its side effects, a localized delivery system is desirable.

3.4. NANOPARTICLES

3.4.1. Definition and Advantages

Nanoparticles are increasingly being used as drug delivery systems. In strictest terms, the word nanoparticle refers to a structure in the 1-100 nm size range in at least one dimension [57]. However, more commonly the term is applied to any particle within the nanometer size range. Possibly of more importance is the fact that materials at this scale frequently display different properties than those of the bulk material.

A number of nanoparticle drug delivery systems have been developed, including solid lipid nanoparticles (SLNs, dispersions of solid lipids), liposomes (self-assembled lipid bilayers), micelles (self-assembled amphiphilic molecules) and dendrimers (repeatedly branched spherical polymers) (Figure 3.5). These systems display a number of advantages over conventional drug delivery systems. First, nanoparticles are capable of achieving enhanced solubility [20]. This is critical in an age of increasingly hydrophobic drugs, where new methods are continually required for solubility enhancement. Depending on the type and composition, nanoparticles may also be able to provide this enhancement with considerably decreased toxicity as compared to earlier methods (e.g., Cremophor) [58]. Secondly, nanoparticles have the capacity for controlled and/or bioresponsive drug release. Systems can be designed so that drug is released slowly over an extended period of time, generally by a diffusion process [59, 60]. Alternatively, systems can be developed that achieve a rapid release of drug upon the addition of a biological stimulus, such as a change in pH, redox potential, temperature or the presence of a relevant enzyme [21-24]. Thirdly, nanoparticles have been reported to evade MDR mechanisms. This can be a result of their cellular internalization pathway [61, 62] or P-gp inhibition [26]. Fourthly, nanoparticles have been shown to protect loaded molecules from enzymatic degradation [27]. This advantage is particularly relevant for proteins and other enzymatically-labile compounds that would quickly become inactivated in the absence of a protective drug carrier.

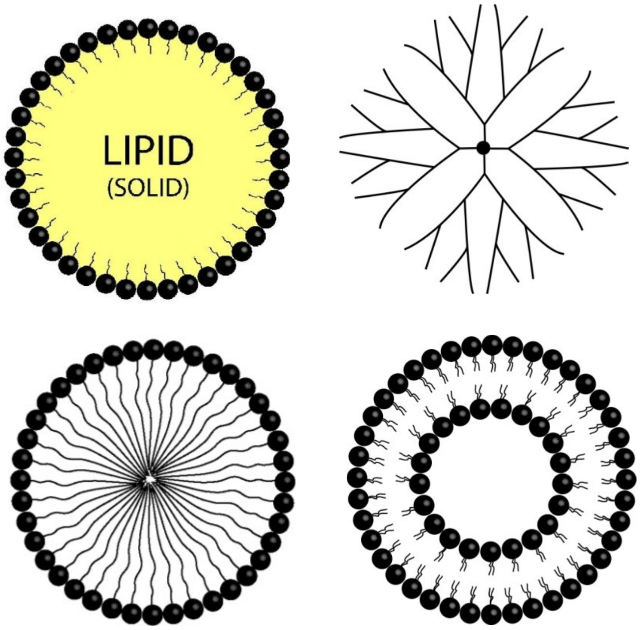

Figure 3.5. Representative nanoparticle drug delivery systems: solid lipid nanoparticles (top left), dendrimers (top right), micelles (bottom left), and liposomes (bottom right). Adapted from [63]*

However, of the most relevance in terms of drug delivery for chemotherapeutic purposes is the ability of nanoparticles to target drug to tumors. As described above for Dex as well as for many chemotherapeutic agents, there is a desire to localize drug delivery to tumors as much as possible in an attempt to maximize the efficacy of the drug while minimizing its toxic side effects. Nanoparticles have two potential means of achieving this.

The first and most widely-applied targeting approach is passive targeting, which is based on the well-known EPR effect [29, 64]. The permeability portion of the EPR effect results from the fact that tumor vasculature is irregular and “leaky”, or characterized by larger inter-endothelial junctions than are present in healthy tissue, as mentioned above (Figure 3.6). Therefore, by incorporating a drug into a nanoparticle of an appropriate size, the drug should be targeted to the tumor simply based on the size effect. Studies have shown that tumors have a characteristic pore size of 200 nm to 1.2 μm [29]. However, the average size varies based on the type of tumor and its location within the body. Therefore, the generally recommended size limit for nanoparticles designed for tumor-targeted drug delivery is <200 nm. Coupled with the leaky vasculature, the poorly developed lymphatic system of tumors may lead to enhanced retention of materials within the tumor tissue. Notably, based on similar conditions found at sites of inflammation, nanoparticles may also be used to provide targeted drug delivery for diseases such as arthritis [65-67].

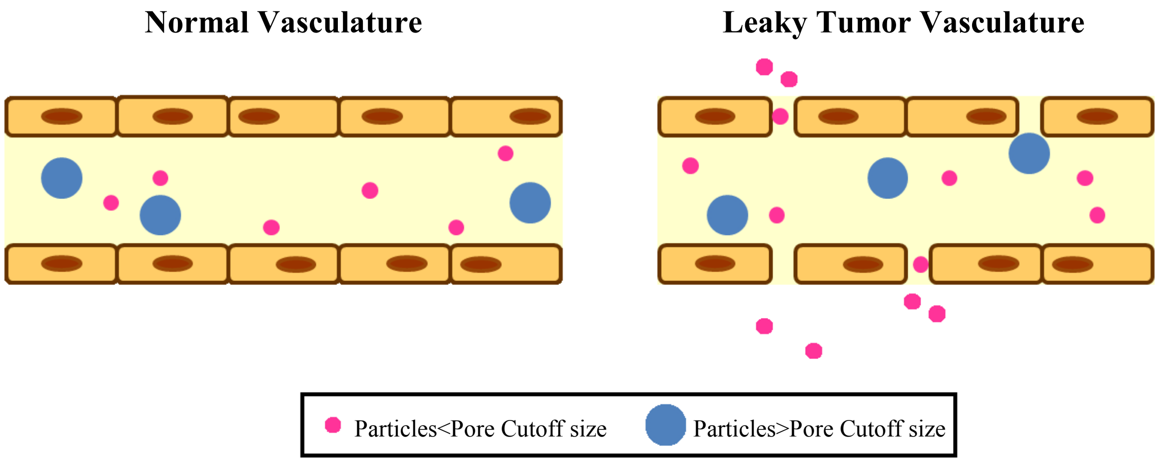

Figure 3.6. Schematic depicting nanoparticle extravasation into tumor tissue via the enhanced permeability and retention (EPR) effect

Active targeting is the second targeting approach that can be employed [57]. Using this technique, ligands that can interact with cell surface receptors are attached to the nanoparticle surface. Receptors upregulated on either tumor cells or on tumor-associated endothelial cells can be chosen for targeting. Because tumor cell receptors are inaccessible from the blood, extravasation into the tumor tissues remains primarily a product of the EPR effect. However, following extravasation, higher intracellular drug concentrations can be obtained through receptor-mediated endocytosis of the nanoparticles [68]. Because endothelial cell receptors are accessible from the vasculature and transport mechanisms are available that ferry materials across the endothelial cell barrier, vascular targeting may potentially be used to increase extravasation into the tumor tissue [69]. Vascular targeting may also be used for therapies targeted at endothelial cells (e.g., anti-angiogenic drugs).

3.4.2. Nanoparticle PEGylation*

3.4.2.1. Theory

In order for nanoparticles to serve as successful tumor-targeted drug delivery systems, they must first remain in circulation long enough to reach the tumor site. Before this can happen, many colloidal carriers are cleared from the circulation as a result of opsonization of the particles and subsequent uptake by cells of the reticuloendothelial system (RES) [70-72]. Though some studies have shown an opsonin-independent uptake of liposomes by macrophages in mice [73-76], the macrophage uptake of nanocarriers in most species appears to be dependent on interaction with proteins adsorbed on the nanoparticle surface [77-80]. Opsonin proteins, such as the complement protein C3b, immunoglobulins G and M, fibronectin, C-reactive protein, β2-glycoprotein, and apolipoproteins [71, 76, 81, 82] may recognize nanoparticles based on their size, charge, rigidity, or hydrophobicity, instigating removal of the foreign particles by the RES. Complement proteins, immunoglobulins, and fibronectin were found to be the major opsonin proteins, but which protein serves as the dominant opsonin appears to depend on the specific characteristics of the nanocarrier with most showing high levels of adsorption of at least several different proteins [81, 82]. Thus, in order for nanoparticles to become viable alternatives to traditional delivery systems, they must be made less susceptible to recognition by these opsonins.

The neutrality, hydrophilicity, molecular flexibility, and non-immunogenicity of poly(ethylene glycol) (PEG) made it a natural initial choice for surface modification of nanoparticles, and today, PEGylation (the coating of a surface with PEG via adsorption, grafting, or entrapment methods) is considered the means of choice for decreasing protein adsorption and imparting ‘stealthiness’ (the ability of avoid RES uptake) to nanocarriers. Several theories have been proposed to explain why PEG increases the stealthiness of nanocarriers (Figure 3.7). Simple explanations include the reduction in surface charge [71] and/or hydrophobicity [83, 84] and, hence, a decrease in the attractive forces between the nanoparticle and opsonin proteins. However, numerous other hydrophilic molecules have been used as coatings and failed to produce similar results [85]. Nagaoka et al discuss the possibility that the high mobility of the longer PEG chains simply prevents proteins from interacting with a surface for a time sufficiently long enough to bind [86]. Coupled with the hydrophilicity and mobility of PEG is its wettability [87]. Highly flexible PEG chains are able to squeeze water molecules out of the polymer layer, creating a large water cloud impermeable to proteins [88, 89]. Others have posited that PEG creates a minimum interfacial free energy and decreases the necessity of protein binding in order to reduce the interfacial energy. However, based on protein adsorption studies performed by Jansen et al, this theory appears to hold only in limited situations [90]. In fact, in several other cases, it has been shown that minimizing interfacial free energy results in additional protein binding [90, 91]. The most widely accepted explanation, put forth by Jeon et al, relies on a description of the interactions between proteins and PEGylated surfaces [70, 92]. PEG chains are hydrophilic and flexible, leading to an extended conformation when free in solution. When proteins encroach on the nanoparticle surface, the PEG chains are compressed. This change to a higher energy conformation in turn creates a repulsive force that can inhibit protein binding.

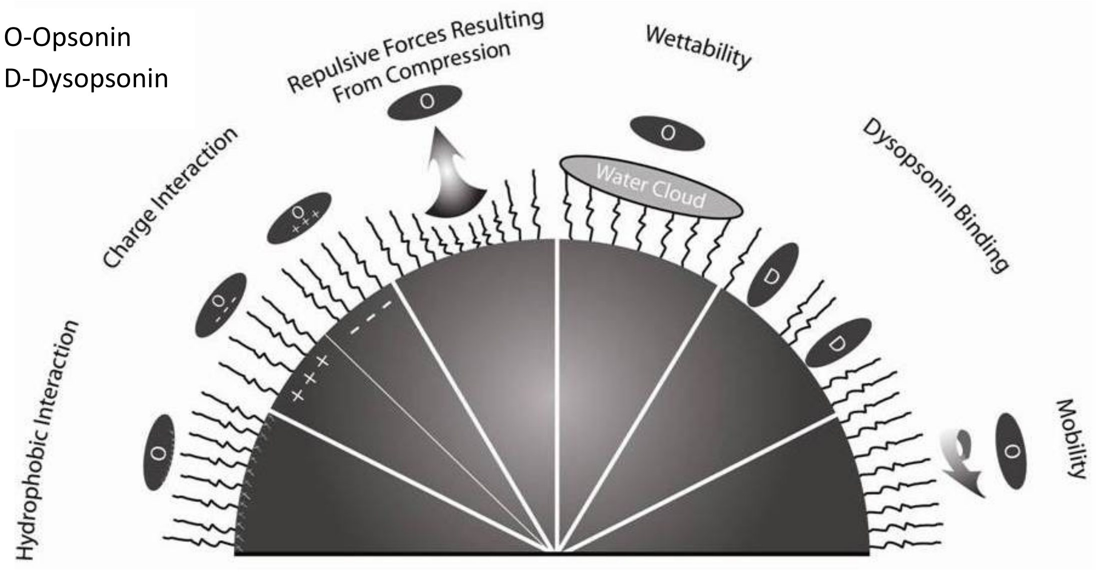

Figure 3.7. Mechanisms by which PEG prevents opsonin adsorption when grafted in an optimal configuration. Adapted from [63]*

As an alternative theory, some investigators have proposed that long-circulating characteristics are not a matter of avoiding protein adsorption, but of attracting the appropriate proteins. While it is thought that PEG causes a nonspecific decrease in protein adsorption [81], some have proposed that it instead alters the profile of adsorbed proteins. Moghimi and Patel have performed several studies that support the idea of the existence of liver- and spleen-specific opsonins [93-96], which may cause an altered distribution profile. Additionally, there appear to be some proteins that behave as dysopsonins, suppressing phagocytic uptake [72, 97] (Figure 3.7). Early studies identified two serum components, one with a molecular weight < 30,000 Da and one with a molecular weight > 100,000 Da, that remained bound to poloxamine 908 (four PEG polymers attached to four poly(propylene glycol) (PPG) polymers all connected by an ethylene diamine moiety, MW ~ 25,000 Da) coated polystyrene particles and decreased uptake by liver cells beyond that seen with poloxamine 908 alone [98, 99]. More recent studies by Dunn et al and Mosqueira et al also support the concept of dysopsonic activity but fail to show such promising results with their covalently PEGylated nanostructures [100, 101]. Dunn et al utilized similar polystyrene particles and saw decreased uptake by liver non-parenchymal cells for both polystyrene particles and poloxamine 908 coated polystyrene particles. Additionally, those particles with a low surface coating of covalently attached 2,000 Da PEG (PEG2000) showed a significant decrease in uptake after incubation with serum. However, as the PEG2000 surface concentration was increased from a PS:PEG2000 ratio of 1:0.025 (~15% C-O surface coverage) to a ratio of 1:1.053 (~41% C-O surface coverage), the significant reduction in liver uptake was no longer observed, possibly because the PEG coating was too dense to allow dysopsonin binding.

3.4.2.2. Optimization of Surface Coverage

Despite the apparent value of PEGylation, guidelines remain elusive for achieving optimum surface coverage. If one accepts the Jeon theory, adequate surface coverage of the particle with PEG must be achieved in order to block adsorption of proteins. The ideal coverage has been described as intermediate between the “mushroom” and “brush” configurations [70, 102]. The “mushroom” configuration is characterized by very low surface coverage, leading to large areas available for protein binding. The “brush” configuration is characterized by a very high surface coverage, which could theoretically lead to a restriction of PEG flexibility and a potential decrease in its steric repulsion properties. However, most experimental data indicate that a predominantly brush configuration provides the most effective opsonin repulsion [103, 104]. This might be attributable to an inability to attain a sufficiently high density such that PEG flexibility is restricted.

Coverage of the surface can be controlled through chain molecular weight, surface chain density, and chain conformation. Although each individual system requires optimization, several trends in surface coverage have emerged: (i) the surface density is more important than the molecular weight of the PEG chain [92, 100, 105], (ii) there is a threshold molecular weight for PEG chains to be effective because of a loss of flexibility and hydration with shorter PEG chains [70, 106, 107], (iii) linear PEG chains of molecular weight greater than 5,000 Da rarely provide improved results and may show an increase in protein adsorption because of an inability to obtain high surface density [82, 108, 109], and (iv) branched PEG chains are less effective at preventing adsorption than linear PEG chains [106, 110]. Generally, linear PEG chains of molecular weight 1,500-5,000 Da have been shown to provide efficient stealthiness [82, 106, 111]. The exact length necessary likely depends on the curvature of the surface and other attractive forces. As an overarching rule, it has been recommended that a minimum effective hydrodynamic layer thickness of approximately 5-10% of the particle's diameter should be sought for sufficient coverage [102, 112].

This list is by no means exhaustive, and there have been several exceptions noted. For example, Mosqueira et al found that when PEG chains of 20,000 Da and 5,000 Da were both grafted at a distance of 4.5 nm between PEG chains, PEG20000 was better able to prevent cell uptake of nanocapsules. A grafting distance of only 2.2 nm was required for

PEG5000 to achieve the same results as PEG20000 at a distance of 7.8 nm, and PEG20000 continued to decrease cell uptake at higher grafting densities. They proposed that the PEG chains could have different conformations at the surface resulting in different efficiencies in preventing interaction between the nanocapsule and a cell, or that since there is a low surface coverage, the chain length became the limiting factor [101]. Gref et al also found improved circulation times as well as reduced liver uptake with PEG20000 over PEG with 0, 5, and 12 kDa chains [113].

3.4.2.3. Attachment Methods

One common method for attaching PEG to the surface of nanoparticles is surface adsorption. This can be done through the use of linear PEG polymers or through the use of poloxamers (nonionic block copolymers composed of a central hydrophobic chain of poly(propylene glycol) (PPG) flanked by two hydrophilic chains of PEG) and poloxamines where the hydrophobic PPG chains insert into the hydrophobic particle and the PEG chains orient themselves toward the aqueous environment [102]. Alternatively, 1,2-Distearoyl-*sn*-Glycero-3-Phosphoethanolamine-PEG (DSPE-PEG) is commonly used in the preparation of liposomes. These methods have been used since the early 1980s and are thoroughly reviewed elsewhere [102, 107]. Though many particles exhibited improved stealth capacities, some results were less than satisfactory.

The major hypothesis to explain these less than optimal results was the desorption of PEG or displacement by proteins when in the bloodstream [114, 115]. Thus, there was a move towards ensuring more stable linkages. Harper et al was one of the first groups to attach PEG via a covalent linkage. They showed an average reduction in macrophage uptake of approximately 40% by preparing polystyrene-poly(ethylene glycol) (PS-PEG) particles as opposed to adsorbing PEG onto the surface of PS particles. An even greater decrease was seen when poloxamer 238 was adsorbed onto the surface of the PS-PEG particles [116]. Bazile et al found improved results with polymeric nanoparticles made from poly(d,l-lactic acid)-poly(ethylene glycol) (PLA-PEG) diblock copolymers. The *in vivo* plasma half-life of the PLA-PEG nanoparticles was increased by a factor of 180 as compared to the poloxamer-stabilized PLA nanoparticles [117]. Later, *in vitro* assays revealed that, in the presence of serum, PLA nanocapsules coated with a poloxamer showed higher levels of protein adsorption [109] and cell uptake [101] than nanocapsules with covalently attached PEG.

Today, many polymeric micelles and nanoparticles are made from PEG-based diblock copolymers, which ensure a stable coating. Liposomes are also being further developed into polymersomes, composed entirely of PEG-based block copolymer amphiphiles. Those systems not composed of block copolymers rely on the inclusion of a certain percentage of pre-formed PEG-lipids or PEG-phospholipids in addition to their non-PEGylated counterpart. By using a compound already integral to the particle, a stable linkage may be obtained. What follows is a sampling of recent reports. Nanoparticles prepared with PEG-lipids were capable of delivering 70-80% of injected siRNA to tumors by four hours [118]. SLNs prepared with dipalmitoylphosphatidylethanolamine-PEG2000 or stearic acid-PEG2000 showed 30-40% less uptake by murine macrophages than non-stealth SLNs [119]. Doxorubicin-loaded SLNs containing stearic acid-PEG2000 exhibited reduced clearance as well as an improved biodistribution over non-stealth SLNs [120]. Lidocaine-loaded poly(lactic-co-glycolic acid)(80kD)-PEG(20kD) nanoparticles showed less than 30% uptake by the liver Küpffer cells at five hours compared to 66% uptake in five minutes for uncoated particles [113]. Doxorubicin-loaded poly(β-benzyl-L-aspartate)-PEG copolymer micelles showed a sustained drug release and increased antitumor activity over free drug [60]. Sustained release of salvicine over 28 days was obtained with poly(n-hexadecyl cyanoacrylate)-poly(ethylene glycol) (PHDCA-PEG) nanoparticles [121]. Phagocytosis of poly(hydroxyethylaspartamide methacrylated)-PEGylated nanoparticles was reduced based on the degree of PEGylation [122]. Poly(methoxy-polyethyleneglycol$_{5000}$ cyanoacrylate-co-n-hexadecyl cyanoacrylate) (PHDCA-PEG5000) niosomes were prepared that exhibited a half-life of 11.46 hours and that reduced tumor weight by 89.3% at half the dose given via a normal injection of solution [108]. Camptothecin-loaded nanocapsules prepared with PLA-PEG showed an increase of approximately 30% in the reduction of metastatic nodules over uncoated nanocapsules [123].

3.4.2.4. Current State of the Art

Currently, there are several PEGylated nanocarriers approved for therapeutic use or undergoing testing [124]. Of these, Doxil is probably the most well-known as it was the first liposomal drug formulation approved by the Food and Drug Administration (FDA). In this formulation, doxorubicin HCl is encapsulated (>90%) in a liposome composed of cholesterol, hydrogenated soy phosphatidylcholine (HSPC), and DSPE-mPEG. Doxil was originally approved for the treatment of AIDS associated with Kaposi’s sarcoma in 1995

[125] but is now also used for the treatment of metastatic breast and ovarian cancers and multiple myeloma. Compared to the non-liposomal drug, Doxil achieves up to 10-fold higher levels in tumors. It is also noted for its long-circulating characteristics and reduction in toxicity, especially cardiotoxicity. Beyond these PEGylated nanocarriers, there are a variety of PEGylated protein products on the market, including PEGylated arginine deaminase, PEGylated interferon, and PEGylated L-asparaginase. As evidenced by these products and the wide variety of other products in which PEG is used as an excipient, PEG has repeatedly been deemed safe by the FDA.

3.5. SOLID LIPID NANOPARTICLES

3.5.1. Definition and Advantages

Several reports exist of Dex being loaded into nanoparticle systems, including polymeric nanoparticles [59, 126, 127], polymer-drug conjugates [67], and liposomes [128, 129]. Unfortunately, these systems may be limited by a number of disadvantages, including toxicity, low drug encapsulation efficiency, unknown or unproven safety of some of the materials used in their preparation, and rigorous or high-cost production methods [130, 131]. For this reason, solid lipid nanoparticles (SLNs) were proposed as an alternative nanoparticle system.

SLNs are characterized by a solid lipid core with stabilizing surfactants and/or polymers on the particle surface [132]. They have gained increasing attention since their development in the early 1990s based on their reported ability to combine the advantages of several nanoparticle systems while negating some of their disadvantages [33, 34].

First, they can be prepared from inexpensive, readily available materials. A wide variety of both lipids (e.g., triglycerides, partial glycerides, waxes, PEGylated lipids, fatty acids/alcohols, steroids) and surfactants/polymers (e.g., polysorbates, brijs®, lecithin, bile acids) have been used in their preparation. Secondly, because the lipid matrix can be prepared from biocompatible lipids and the surfactants and/or polymers used can be chosen based on FDA approval status, these drug delivery systems typically exhibit very low toxicity. Coupled with the low toxicity of the materials used in SLN preparation is the fact that most SLN preparation methods do not rely on the use of organic solvents, eliminating that as a possible toxicity concern. Thirdly, and possibly of most importance, is the fact that SLNs can be prepared using simple, scalable production methods, a requirement for translation from academic labs to industrial labs.

3.5.2. Production Methods

The two most commonly used SLN production methods are the high pressure homogenization (HPH) and microemulsion techniques [34]. HPH was the earliest method used for SLN preparation. This technique arose from its use in the preparation of o/w emulsions for parenteral nutrition. Although a liquid lipid is replaced with a solid lipid for SLN preparation, a similar procedure can be employed if conducted at temperatures above the melting point of the lipid. This is referred to as hot homogenization. Basically, the drug is added to the lipid at 5-10°C above the lipid melting point, and then the melt is dispersed with stirring in an aqueous surfactant solution at the same temperature. The pre-emulsion is then homogenized, and the resulting hot o/w microemulsion is cooled to room temperature (or lower). SLNs are produced as the lipid solidifies.

The cold homogenization technique can be applied when 1) drugs exhibit temperature sensitivity, 2) hydrophilic compounds partition into the aqueous phase at elevated temperatures, and 3) lipid crystallization is complex leading to multiple polymorphic forms of the lipid and/or supercooled melts [33, 34]. The first step of this process is the same as that in the hot homogenization. Drug is added to the melted lipid. However, following this step, the melt is cooled, and the solid lipid is ground to lipid microparticles. The lipid microparticles are then dispersed in a cold surfactant solution. Homogenization is conducted at room temperature or below, producing SLNs.

SLNs can also be produced from o/w microemulsions using scalable methods [34, 131]. Microemulsions can be defined as stable biphasic mixtures of two immiscible liquids stabilized by a surfactant and usually a co-surfactant [131]. It may be necessary to add the co-surfactant in order to generate the low interfacial surface tensions (γ) between the dispersed and continuous phases required for the preparation of stable microemulsions. Because microemulsions are characterized by a large surface area, the interfacial surface tension must be low enough so that the positive interfacial energy (γA, where A is the interfacial area) can be balanced by the negative free energy of mixing (ΔG_m).

Microemulsions can be prepared using solid lipids by employing a preparation temperature above their melting point. The lipid will solidify upon cooling, generating SLNs. Initially, the cooling procedure was performed through dilution in cold water [133]. More recently, a process known as nanotemplate engineering technology (NET) was developed in which "direct cooling" is utilized [131, 134]. A schematic of the preparation procedure is shown in Figure 3.8. Basically, the process consists of three steps: 1) melting a pharmaceutically acceptable matrix comprised of lipid(s), surfactant(s), polymer(s), and drug at 55-70°C, 2) adding pre-heated water with stirring to form the o/w microemulsion, and 3) cooling to room temperature with stirring to generate the SLNs.

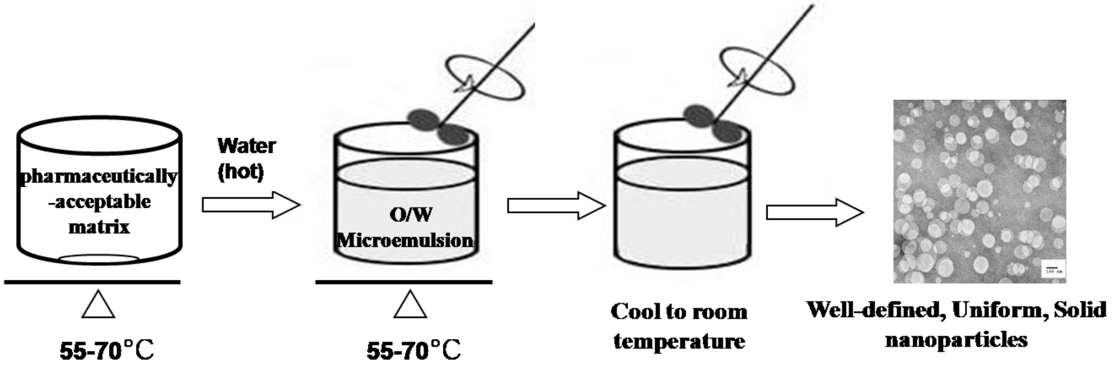

Figure 3.8. Nanotemplate engineering technology (NET)

In comparison to the dilution method, NET has the advantage of being a single vessel preparation method. By utilizing a direct cooling approach, it becomes unnecessary to optimize the rate and ratio of mixing, which have been reported to have a significant impact on the properties of the resulting SLNs [34]. Further, much higher concentrations may be obtainable using NET than using the dilution method as microemulsion:water dilution ratios of 1:10 v/v up to 1:100 v/v have been reported in the literature [131]. This represents a major improvement in microemulsion technology as low concentrations were previously considered a significant disadvantage of the microemulsion technique as compared to the HPH technique [34].

3.5.3. Limitations

As described above, SLNs have the potential to overcome many of the disadvantages associated with other nanoparticle drug delivery systems. However, they too may have limitations, most of which are associated with the lipid crystallinity of the particles. On one end of the spectrum, SLNs that exhibit high crystallinity may be limited by low drug loading [135]. There may simply be little room for the drug to be inserted among the tightly packed lipid molecules. On the other end of the spectrum, working with less crystalline lipids (or reducing the crystallinity of the lipid through the addition of other lipids and/or surfactants) may lead to stability issues. If the lipid crystallizes over time, it may lead to drug expulsion [136-138], particle size growth [138, 139], or gelation [140-143]. However, by characterizing the physicochemical properties of the SLNs, these issues may be anticipated and avoided through changes to the composition (e.g., lipids, surfactants) [144, 145], preparation procedure [33], or storage conditions [146].

3.6. PRELIMINARY WORK**

3.6.1. Formulation Optimization

In preliminary work from this laboratory designed to develop Dex loaded SLNs using NET, approximately 160 formulations containing various combinations of cetyl alcohol, stearyl alcohol, polysorbates (20, 40, 60 or 80), and Brij® 78 were prepared. Cremophor, lecithin, and various PEGylating agents were added to some formulations. An optimized formulation that yielded clear nanoparticle suspensions and a small particle size distribution was obtained. The formulation was comprised of SA (1.6 mg/mL), PS60 (0.4 mg/mL), and Brij® 78 (3.5 mg/mL) (structures are shown in figure 3.9). To potentially improve the stealthiness of the nanocarriers, the formulation was adjusted for the inclusion of a long-chain PEGylating agent, PEG6000MS. This is essentially a PEGylated analog of a stearyl (C16) function and is expected to be more compatible with the primary component of the lipid matrix, SA, than other commonly used PEGylating agents, such as DSPE-PEG. Because the PEGylating agent is able to function as a surfactant, the Brij® 78 concentration could be reduced to 2.8 mg/mL when PEG6000MS was included.

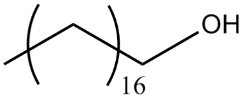

Stearyl alcohol (SA)

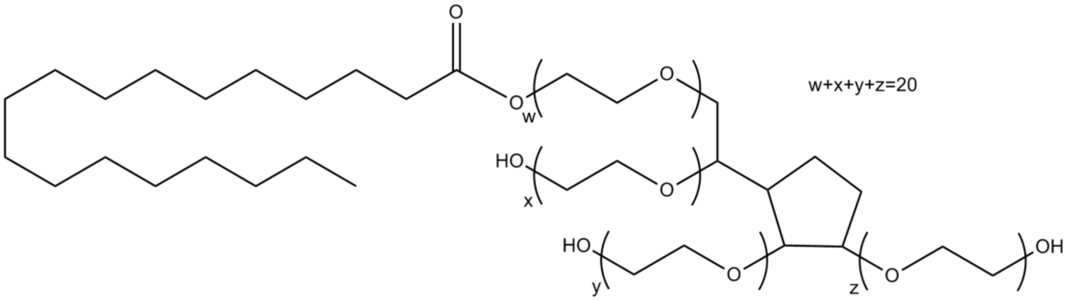

Polysorbate 60 (PS60)

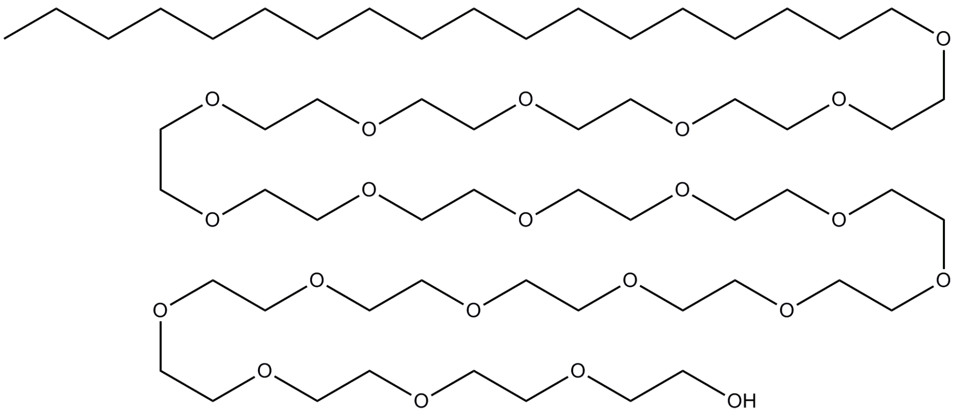

Brij® 78

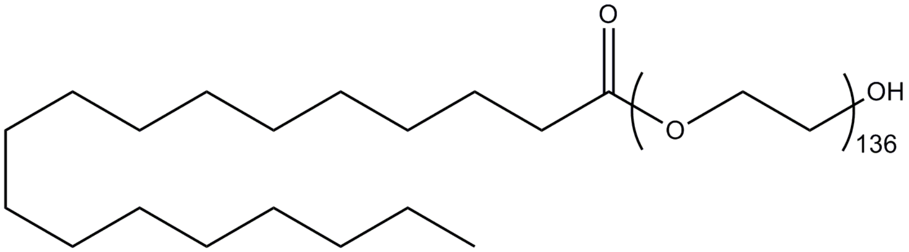

PEG6000 monostearate (PEG6000MS)

Figure 3.9. Structures of SLN components

3.6.2. Drug Loading

Dex could be loaded into SLNs (without PEG6000MS) at a drug load of 3.5% w/w SA (e.g., 0.056 mg/mL Dex in comparison to 1.6 mg/mL SA) while maintaining a small particle size (~70 nm). Following incubation in PBS at 37°C, a burst release of drug was observed, accounting for 45–55% of the original amount of Dex loaded into the SLNs. In considering the time required for SLNs to distribute throughout the circulation and extravasate into tumors, it was decided that these SLNs would not deliver Dex to tumors in sufficient quantities.

For this reason, Dex-P (Figure 3.3) was chosen as an alternative drug for loading. Dex-P is a lipophilic ester of Dex that has been used in marketed products, such as Limethason®, an intravenously administered lipid emulsion [36]. A liposome formulation containing Dex-P has also been described, and a conformational analysis showed that the palmitate chain was aligned with the acyl chains of the phospholipids while Dex was oriented towards the aqueous phase [129]. It was expected that Dex-P would align similarly when incorporated into SA-based SLNs. Early studies indicated that Dex-P could be loaded in SLNs with or without PEG6000MS at 10-30% w/w SA with high encapsulation efficiencies. This was confirmed at a later time; results are discussed in chapter 5.

3.6.3. Evaluation of Stealth Properties

The stealth properties of the nanoparticles were evaluated by determining the adsorption of a model opsonin, ^{125}I-IgG. 10% Dex-P loaded SLNs with and without 2.5 mg/mL PEG6000MS were compared. Latex particles (90 nm) were used as a positive control because they are hydrophobic and readily adsorb IgG. Nanoparticle-adsorbed IgG was separated from free IgG by SEC using a Sepharose CL-4B column. Representative elution profiles are shown in Figure 3.10. Expressed in quantitative terms as the mean ± standard deviation (SD) of 3 measurements, this equates to an adsorption of the following (all values in µg IgG/mg nanoparticle): latex, 185.0±9.5; non-PEGylated SLNs, 20.8±1.6; PEGylated SLNs, 6.7±0.7. Both SLNs with and without PEG6000MS exhibited considerably lower protein adsorption as compared to latex particles. In the absence of PEG6000MS, this could be attributed to the presence of the polyether portion of Brij® 78 and PS60. Although not as long as suggested based on most PEG research as described above, these surfactants apparently exhibit some protective capacity. However, the SLNs containing PEG6000MS exhibited a statistically lower amount of protein adsorption as compared to SLNs without PEG6000MS ($P<0.05$).

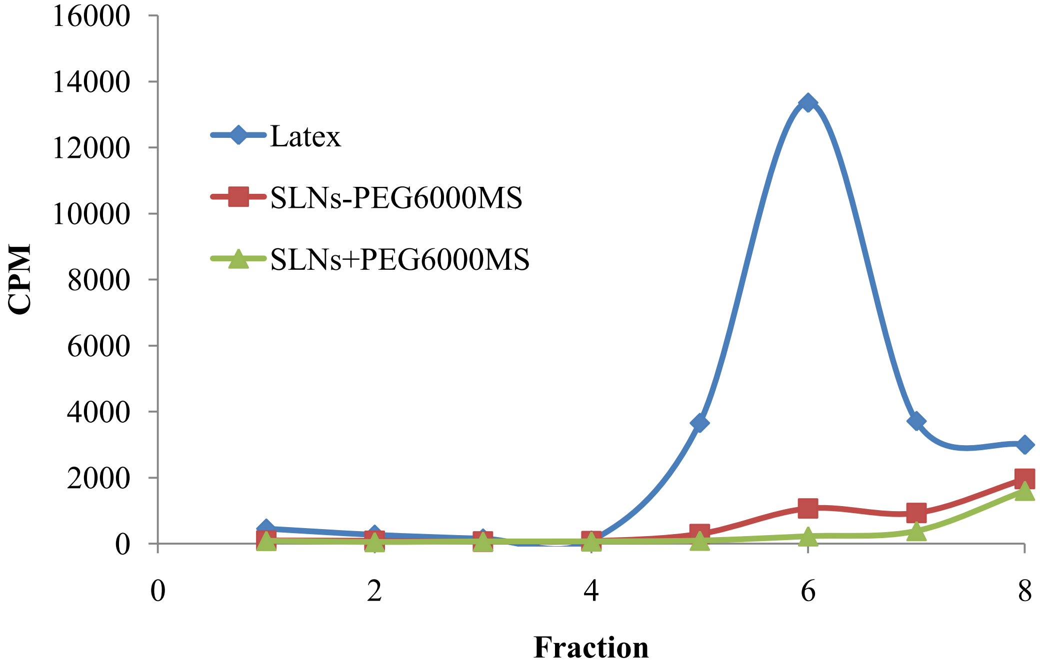

Figure 3.10. Adsorption of IgG (as measured by radioactive CPM) on SLNs. Nanoparticle-adsorbed protein was separated from free protein using a Sepharose CL-4B column; nanoparticles eluted in fractions 5-7. Adapted from [35]**

As a second test of the stealth properties, SLNs that had been radiolabeled with ^{14}C-SA were evaluated for uptake by murine macrophages. The initial study was conducted using SLN prepared with 2.5 mg/mL PEG6000MS as in the IgG adsorption studies. While there was a difference in the SLNs taken up by these cells after a 90 min incubation as compared to SLNs without PEG6000MS, the difference at earlier time points was minimal. Additional studies were performed to evaluate the effect of including higher concentrations of PEG6000MS in the SLN formulation. The results are shown in Figure

3.11. Two-way ANOVA revealed that the effect of different formulations depends on what time uptake was evaluated. There was a statistically significant interaction between formulation and time ($P<0.001$). Multiple comparisons versus control group (SLNs with 0 mg/mL PEG6000MS) were done using the Holm–Sidak method. The addition of PEG6000MS significantly decreased the macrophage uptake at the 30, 60, and 90 min time points as compared to the control group ($P<0.05$). At the 90 min time point, each of the two groups was significantly different ($P<0.05$). As more PEG6000MS was used in the preparation of SLNs, the macrophage uptake decreased. The uptake of SLNs with 0 mg/mL PEG6000MS was 36.6%/mg cell protein. As the amount of PEG6000MS in the formulation increased, the uptake of the ^{14}C-labeled nanoparticles was observed to decrease, reaching a low of 14.7%/mg cell protein for SLNs formulated with 4 mg/mL of PEG6000MS. These results indicated that as the concentration of PEG6000MS was increased, there was a corresponding increase in the stealth properties.

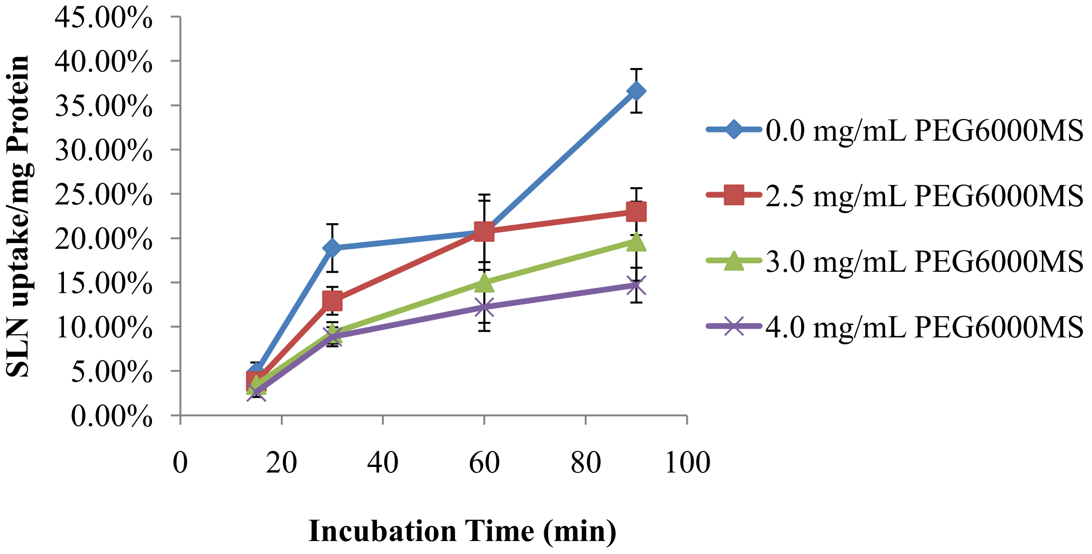

Figure 3.11. Uptake of ^{14}C-labeled Dex-P loaded SLNs with varying amounts of PEG6000MS by murine macrophages as a function of time. All data represents the mean ± SD of 5 measurements. Adapted from [35]**

Based on the above studies, two formulations were chosen for evaluation in this project (Table 3.1). Formulation 1 did not include PEG6000MS. Although the addition of the molecule appeared to increase the stealthiness of the nanoparticles, it was considered worthwhile to compare formulations with and without this molecule to determine if the increased complexity was warranted. PEG6000MS was included in formulation 2 at a concentration of 3 mg/mL. This was considered to provide the optimal combination of particle size, drug loading, and stealth capacity.

Table 3.1. SLN formulations

	Formulation 1	Formulation 2
Stearyl alcohol (SA)	1.6 mg/mL	1.6 mg/mL
Polysorbate 60 (PS60)	0.4 mg/mL	0.4 mg/mL
Brij® 78	3.5 mg/mL	2.8 mg/mL
PEG6000 monostearate (PEG6000MS)	0.0 mg/mL	3.0 mg/mL
Dexamethasone Palmitate (Dex-P)	0.16-0.48 mg/mL	0.16-0.48 mg/mL

*The text from the Nanoparticle PEGylation section as well as Figures 3.5 and 3.7 were previously published in [63]. Reproduced with minor modifications from American Scientific Publishers: Journal of Biomedical Nanotechnology, PEGylation of Nanocarrier Drug Delivery Systems: State of the Art, 4, 2008, 133-148, M.D. Howard, M. Jay, T.D. Dziubla, X. Lu. Copyright © American Scientific Publishers 2008.

Portions of the text from the preliminary work section, Figure 3.10 (originally presented in table format), and Figure 3.11 were previously published in [35].** Reproduced with kind permission from Springer Science+Business Media: The AAPS Journal, Nanoparticles containing Anti-inflammatory Agents as Chemotherapy Adjuvants: Optimization and In Vitro Characterization, 10(1), 2008, 133-140, X. Lu, M.D. Howard, M. Mazik, J. Eldridge, J. Rinehart, M. Jay, M. Leggas. Copyright © Springer Science+Business Media 2008.

Chapter 4

Physicochemical Characterization of Nanotemplate Engineered Solid Lipid Nanoparticles*

4.1. INTRODUCTION

Due to their simplicity of formulation and basic biocompatibility of the constituent materials, SLNs have become an exciting area for nanomedicine research. As with other systems, they have the potential for targeted drug delivery [147, 148], controlled or triggered drug release [149-151], enhanced drug solubility [152, 153], and improved drug stability [154, 155]. Yet, SLNs also possess low inherent toxicity due to the use of physiological lipids and non-organic solvents during preparation [33, 34, 130] and are amenable to large-scale production methods [33, 34]. Of course, SLNs possess some limitations, including low drug loading [135], drug expulsion [136-138], particle size growth [138, 139], and a tendency to form gels [140-143]. These issues are linked to the fundamental physicochemical properties that are predominately controlled by the material of composition (e.g., lipids, surfactants) and preparation procedure [33]. For example, SLNs prepared from highly crystalline triglycerides have lower drug loading capacity than SLNs prepared from complex glycerides [138]. Lipids with multiple polymorphic forms can lead to drug expulsion upon form transitions [138], which are kinetically modulated by surfactant choice [145, 156]. The choice of lipid(s) and surfactant(s) and their concentrations have been found to affect SLN aggregation and gelation [139, 157]. Even the choice of formulation parameters has been shown to affect drug loading, release profiles, and long-term physical stability [158, 159].

The SLNs under consideration in this study are prepared using NET. While *in vitro* and *in vivo* results have been promising [160, 161], there exists relatively little physicochemical characterization of nanotemplate engineered SLNs beyond particle size and zeta potential measurements [162, 163]. Indeed, the complex interplay of the multicomponent systems used in SLN preparations make *a priori* predictions of the overall stability and phase behavior of the SLN difficult, necessitating a more thorough understanding of the SLN physiochemical properties. As such, the objective of this study was to perform a thorough characterization of the two SLN formulations being considered for development as a Dex-P delivery system, providing comparisons and possible advantages/disadvantages of the two.

4.2. MATERIALS AND METHODS

4.2.1. Materials. PS60 and Brij® 78 were obtained from Uniqema (Chicago, IL). PEG6000MS was a gift from Stepan (Northfield, IL). SA was purchased from Spectrum Chemicals and Laboratory Products (Gardena, CA). Water was obtained from a Milli-Q Synthesis ultrapure water system (Millipore; Billerica, MA). Chloroform-*d* ($CDCl_3$) and deuterium oxide (D_2O) were products of Acros Organics; the deuteration of both NMR solvents was at least 99.8%.

4.2.2. SLN Preparation. SLNs were prepared using NET as previously described [131]. Briefly, the process consists of three steps: 1) melting an appropriate mixture of lipids, surfactants, and (optionally) long-chain PEGylating agents; 2) adding pre-heated water with stirring to generate an o/w microemulsion; and 3) cooling the microemulsion to form a suspension of SLNs. For this study, microemulsions were prepared at 70°C in order to facilitate the melting of all components. SLNs were cooled in a room temperature water bath. Formulation 1 composition was 1.6 mg/mL SA, 0.4 mg/mL PS60, and 3.5 mg/mL Brij® 78. Formulation 2 composition was 1.6 mg/mL SA, 0.4 mg/mL PS60, 2.8 mg/mL Brij® 78, and 3.0 mg/ml PEG6000MS. Batch size ranged from 2-10 mL. SLNs were filtered using a 0.2 μm polyethersulfone membrane prior to analysis. SLNs for DSC and PXRD analysis were freeze-dried using a Virtis Advantage benchtop freeze-dryer following freezing at -40°C. Freeze-dried SLNs were tested for water content using a Karl Fischer coulometric assay.

4.2.3. DLS and TEM. DLS particle size measurements were performed in triplicate at 25°C on a Delsa™ Nano Zeta Potential and Submicron Particle Size Analyzer (Beckman Coulter Inc., Brea, CA) following a 1:30 dilution with Milli-Q water. TEM images were obtained using a Philips Tecnai Biotwin 12 equipped with a Gatan ES 1000W CCD digital camera (FEI, Hillsboro, OR). A drop of sample (7 μl) was incubated for 1.5 min on a carbon coated TEM grid. The grid was then dried and stained (0.2 μm filtered 2% uranyl acetate) for an additional 1.5 min. For each formulation, three samples were analyzed with a minimum of five images taken per sample at different locations on the grid. Analysis of the images was performed using ImageJ [164]. The lengths of both the major and minor axes were obtained using the manual analytical tools. Assuming a prolate spheroid shape for the ellipsoid where the minor axis is the same in the x and y directions, the volume of an ellipsoid with these dimensions was calculated according to the following:

$$\mathrm{Volume} = \frac{4}{3}\pi r_{\mathrm{major}} r_{\mathrm{minor}}^{2}$$

where r is the radius of the relevant axis. Using this value as the volume of an equivalent sphere allowed for the calculation of an approximate particle diameter according to the following equation:

$$\mathrm{Diameter} = \left[\left(\frac{V}{\frac{4}{3}\pi}\right)^{\frac{1}{3}}\right]^{2}$$

In order to apply a quantitative measurement to the particle shape analysis, the aspect ratio for the particles was calculated by dividing the length of the major axis by that of the minor axis. These calculations were performed for 20 particles per image, giving a total of 100 measurements per sample. The average measurement for each sample was used in calculating the average and standard deviation for particles in each formulation.

As a measurement of the homogeneity of the size distribution (comparable to the PI values obtained by DLS), a pooled standard deviation (PSD) was also calculated using the following equation:

$$\sqrt{\mathrm{PSD}^2} = \sqrt{\frac{\sum_{i=1}^{k}((n_i - 1)s_i^2)}{\sum_{i=1}^{k}(n_i - 1)}}$$

where s_i represents the standard deviations obtained from each individual sample of 100 particles, n_i represents the sample size (i.e., 100 for all 3 samples), and k represents the number of samples (i.e., 3). This differs from the standard deviation calculated above which represents the variability in the average size obtained from the three samples.

4.2.4. NMR Spectroscopy. NMR experiments were performed on a Varian 500 MHz NMR (Varian Inc., Palo Alto, CA). ^{1}H-NMR spectra were obtained for the individual SLN components and SLNs dissolved in $CDCl_3$ and for intact SLNs in D_2O. Peaks were assigned to their associated structures based on available NMR tables. Benzenesulfonic acid sodium salt was added in a known concentration to the D_2O samples as an internal standard. Molecular relaxation times were calculated for the three main signals (0.9, 1.3, and 3.6 ppm) in the intact SLN spectra and in spectra obtained from the surfactant micelles in D_2O. Spin-lattice (T_1) relaxation times were analyzed using an inversion recovery experiment, and spin-spin (T_2) relaxation times were analyzed using a Carr Purcell Meiboom Gill (CPMG) sequence.

4.2.5. DSC. DSC analysis was performed on a TA Instruments DSC 2920 (TA Instruments, New Castle, DE) using a 1°C/min heating rate from 25°C-75°C in triplicate. The corresponding TA Instruments Universal Analysis software was used to identify peak maxima temperatures and peak enthalpies; in the case of mixtures, the enthalpy associated with a peak was corrected for the proportion of its associated material in the mixture. Where appropriate, samples were cooled to 0°C at a 5°C/min rate and subjected to a second heating cycle. SA, Brij® 78, and PEG6000MS were analyzed initially in their original state; PS60 exhibited no thermal events in this range. These components were then analyzed following exposure to the thermal treatments used in the preparation method described above but without forming an aqueous dispersion (referred to as "processed"). Basically, samples were melted at 70°C with stirring followed by cooling in a room temperature water bath. This same technique was used to evaluate mixtures of the SLN components (prepared in the same ratios found in SLNs). All combinations are denoted as Component X-Component Y. These are differentiated from SLNs, which are prepared using the NET method and freeze-dried prior to DSC analysis. Phase diagrams covering the full range of molar ratios were prepared for SA-Brij® 78, SA-PEG6000MS, and Brij® 78-PEG6000MS. Following preparation, all samples were stored at room temperature for 24 hours prior to analysis. Hermetically sealed aluminum pans were used with loadings of 5-6 mg for all single component and mixture samples and 1-2 mg for freeze-dried SLNs.

4.2.6. PXRD. A MultiFlex X-ray powder diffractometer (Rigaku, The Woodlands, TX) and Jade XRD pattern processing software (Materials Data Inc., Livermore, CA) were used to obtain the x-ray diffraction patterns of SA, Brij® 78, PEG6000MS, and freeze-dried SLNs. The scan parameters were set at a range of 5-60° 2θ, step size of 0.02° 2θ, and scan speed of 2° 2θ.

4.2.7. SLN Temperature-Dependent Stability Study. Particle size measurements were performed on SLNs as described above at temperatures ranging from 20-65°C for formulation 1 SLNs and from 25-70°C for formulation 2 SLNs, both in 5°C intervals. Samples were incubated in the DLS chamber, and measurements were automatically recorded every 30 min for 6 h. In determining particle size, the solution viscosity was adjusted as a function of temperature. As the change in particle size was observed to be linear for the duration of the experiments, growth rates were obtained through a linear least squares fit. Growth rate was then plotted as a function of temperature, and a double tangent approach was applied to determine a critical point.

4.2.8. Statistical Analysis. All data is presented as the mean ± SD of three independent measurements unless otherwise noted. Comparisons were made using a t-test (paired two sample for means). Results are considered statistically significant at a level of $p<0.05$.

4.3. RESULTS

4.3.1. DLS and TEM Analysis. Particle size measurements were taken by DLS. Both formulations produced nanoparticles of a small size (<100 nm) and low polydispersity (Table 4.1). No differences were observed for particles before and after filtration (Table 4.2) or among batches ranging from 2-10 mL (Table 4.3). SLNs were also analyzed by TEM (Figure 4.1). As the particles appeared to have a slightly ellipsoidal shape, particle size was calculated by determining the volume of the ellipsoid and back-calculating the particle size of a sphere with the equivalent volume. For purposes of analysis, it was assumed that the particles were prolate spheroids and not oblate spheroids. The data from these two techniques is in reasonable agreement. The size obtained for formulation 1 SLNs by TEM was larger than that obtained by DLS, whereas no significant difference ($P>0.05$) was found for the particle size of formulation 2 SLNs determined by the two techniques. The aspect ratio of the particles was also calculated as a quantifiable marker for particle shape differences. Formulation 1 appeared slightly more spherical than formulation 2.

Table 4.1. Particle size and shape data (n=3)

Formulation	DLS		TEM		
	Particle size (nm)	PI	Particle size (nm)	PSD (nm)	Aspect Ratio
1	53.2±1.4	0.119±0.041	69.8±5.3	15.2	1.24±0.02
2	89.4±1.9	0.111±0.023	92.9±3.7	16.4	1.30±0.02

Table 4.2. Effect of filtration (0.2 μm polyethersulfone membrane) on SLN properties (n=2)

Property	Formulation 1		Formulation 2	
	Unfiltered	Filtered	Unfiltered	Filtered
Particle size (nm)	56.4±1.4	56.7±0.6	91.4±0.8	90.7±0.7
PI	0.094±0.021	0.048±0.001	0.058±0.020	0.048±0.011
Intensity	11468±223	10575±723	11416±136	11995±761
Density (mg/mL)	1015.8±4.2	1017.9±2.7	1012.7±0.6	1013.9±2.5

Table 4.3. Effect of batch volume on SLN properties (n=3)

Batch Volume	Formulation 1		Formulation 2	
	Size (nm)	PI	Size (nm)	PI
2 ml	54.9±1.0	0.094±0.011	89.6±3.4	0.114±0.033
5 ml	55.1±2.3	0.097±0.016	90.1±2.3	0.085±0.049
10 ml	55.1±1.3	0.114±0.052	87.7±0.8	0.051±0.033

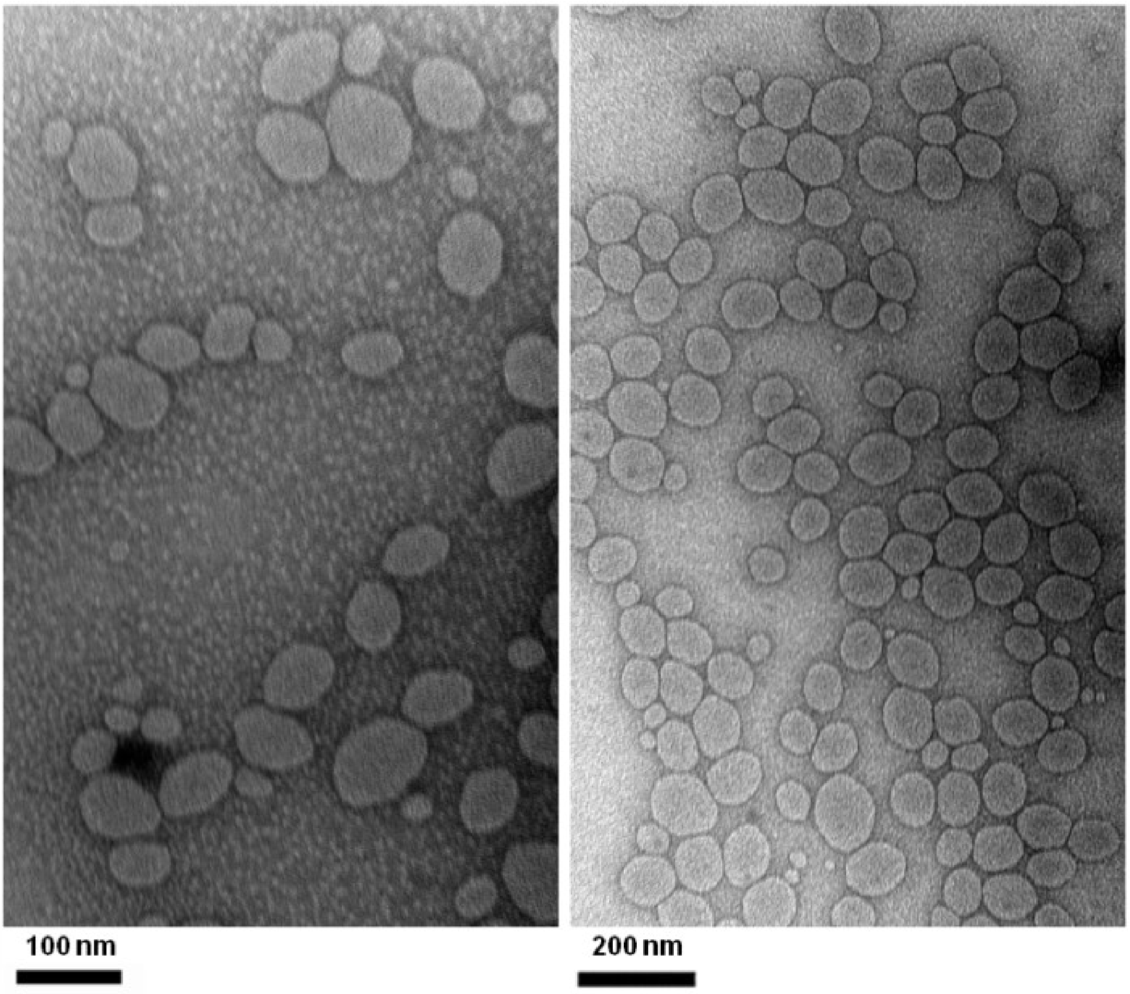

Figure 4.1. TEM images of formulation 1 (left) and 2 (right) SLNs. Images were taken at a magnification of 98000x (formulation 1) and 68000x (formulation 2).

4.3.2. NMR Analysis. SLN components were dissolved in $CDCl_3$, and ^{1}H-NMR spectra were obtained for each. The following ^{1}H-NMR signals were detected - 0.9 ppm (R-C**H**$_3$): SA, PS60, Brij® 78, PEG6000MS; 1.3 ppm (R-C**H**$_2$CH$_3$): SA, PS60, Brij® 78, PEG6000MS; 1.6 ppm (R-C**H**$_2$-CH$_2$-OR): SA, PS60, Brij® 78, PEG6000MS; 2.3 ppm (R-C**H**$_2$-COOR): PS60, PEG6000MS; 3.6 ppm (R-C**H**$_2$-OR): SA, PS60, Brij® 78, PEG6000MS; 4.2 ppm (CH$_2$-COO-C**H**$_2$CH$_2$OR): PS60. Of these signals, the most important to consider are the ether signal at 3.6 ppm generated from the PEG portions of PS60, Brij® 78, and in formulation 2, PEG6000MS, as well as the prominent aliphatic signal seen at 1.3 ppm in all four components.

^{1}H-NMR spectroscopy was further applied to SLNs to gain structural information on the nanoparticles. There is a significant reduction in the size and number of aliphatic peaks present in the intact SLNs in D_2O as compared to solubilized SLNs in $CDCl_3$ (Figure 4.2). This is likely attributable to the peak broadening that occurs due to solid phase intermolecular interactions, rendering the peaks associated with the solid lipid core undetectable. To quantify the reduction, benzenesulfonic acid sodium salt was added to the D_2O samples as a reference standard. There was essentially no loss in the PEG peak at 3.6 ppm moving from the solubilized to intact SLNs. Approximately 100% (97.8% in formulation 1 and 106.7% in formulation 2) of the added PEG (from Brij® 78, PS60, and PEG6000MS) remained in a detectable liquid state in the intact SLN sample, presumably on the surface of SLNs but also potentially in micellar form. This allowed us to use the 3.6 ppm peak as a reference to determine the reduction in size of the aliphatic peaks in the intact SLNs as compared to the solubilized SLNs. The signal at 1.3 ppm was reduced by 79.4% in formulation 1 and 90.5% in formulation 2.

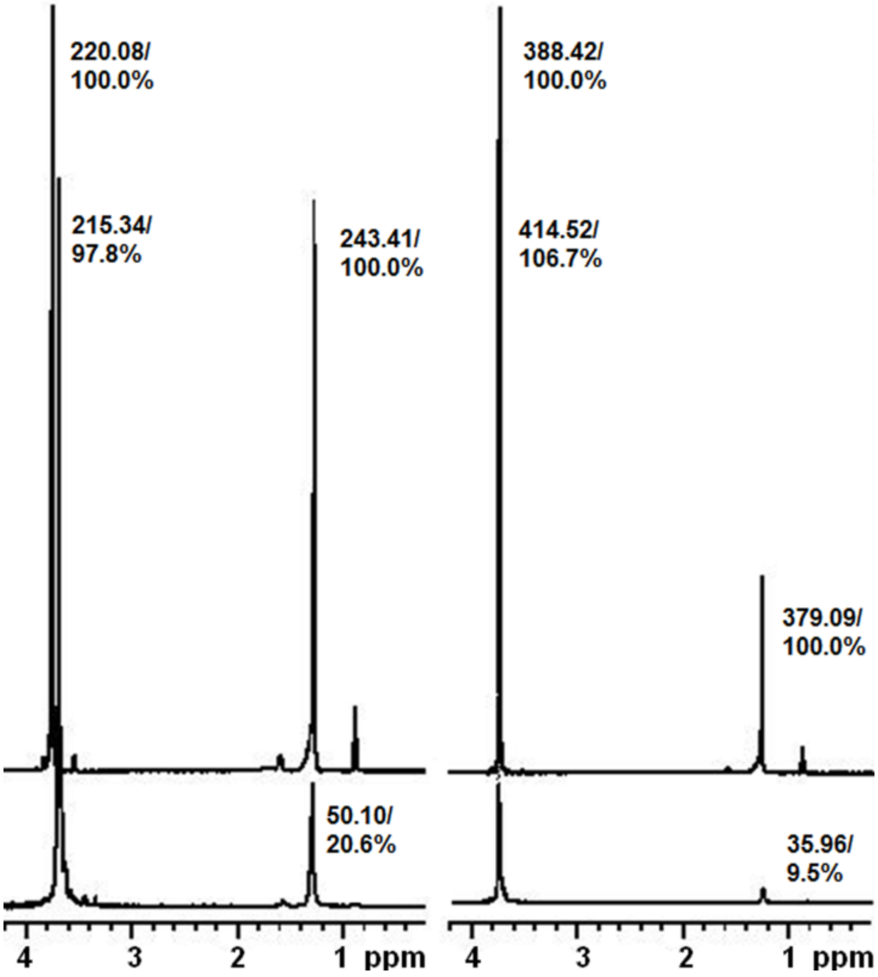

Figure 4.2. ^{1}**H-NMR spectra of formulation 1 (left) and formulation 2 (right) solubilized SLNs in $CDCl_3$ (top) and intact SLNs in D_2O (bottom). Integrations are given for the PEG peak (3.6 ppm) and the main aliphatic peak (1.3 ppm). Percentages are calculated using the $CDCl_3$ spectra as the control.**

Additional complementary information on the structure of SLNs was gained by determining the relaxation times for the remaining signals [165]. Similar spin-lattice (T_1) and spin-spin (T_2) relaxation times are indicative of a group with high molecular mobility, whereas a T_1 value significantly larger than the corresponding T_2 value is indicative of a group with limited molecular mobility. Table 4.4 shows the data obtained for the three major peaks seen in all D_2O samples. It can be seen that the T_1/T_2 ratios for the 3.6 ppm PEG peak are in the range of 1.1-1.3 for the SLNs, indicating a high degree of molecular mobility. This corresponds well with the expected localization of PEG on the surface of the particles. Alternatively, the T_1/T_2 ratios for the aliphatic peaks at 0.9 ppm and 1.3 ppm are significantly larger, indicating that the remaining lipid molecules (not in the solid state) have limited molecular mobility. These signals may be attributed to the aliphatic chains of the surfactants that adsorb to the surface and form a loose shell around the solid core, or to the presence of micelles. In order to investigate these possibilities, the individual micellar suspensions were also analyzed (Table 4.4). At the concentrations used in this study (the same as in SLNs), less than 10% of each component would be expected to exist free in solution based on previously determined CMC values (appendix C). Thus, the T_1/T_2 ratios for the micellar suspensions should primarily reflect the signals of the molecules in micelle form. The T_1/T_2 ratio for the SLN 1.3 ppm peaks is approximately 7.5-9.0 whereas that for the micelles is only in the range of 1.2-3.4, indicating that the aliphatic chains of micelles are not the primary contributors to the aliphatic peak signals in the SLN samples. Interestingly, the 0.9 ppm peaks showed similar T_1/T_2 ratios across both SLN and micelle samples. As this peak arises from the –CH_3 portion of the aliphatic chains, it is likely that this signal is reflective of a very small proportion of molecules in the loose shell orientation or in micelles.

Table 4.4. T_1 and T_2 relaxation times determined for SLNs and SLN components prepared using SLN preparation conditions

	ppm	T_1(s)	T_2 (s)	T_1/T_2
Formulation 1	0.9	0.9229	0.2876	3.2085
	1.3	0.6045	0.0796	7.5976
	3.6	0.6662	0.5749	1.1589
Formulation 2	0.9	0.8967	0.2745	3.2667
	1.3	0.6391	0.0720	8.8764
	3.6	0.7401	0.6046	1.2241
PS60	0.9	0.9343	0.4371	2.1375
	1.3	0.4454	0.3669	1.2140
	3.6	0.6990	0.6099	1.1460
Brij® 78	0.9	0.9822	0.3097	3.1711
	1.3	0.5865	0.1752	3.3484
	3.6	0.6888	0.5219	1.3199
PEG6000MS	0.9	0.8770	0.1969	4.4540
	1.3	0.5687	0.2291	2.4820
	3.6	0.6936	0.5782	1.1996

4.3.3. DSC and PXRD Analysis. DSC was used to evaluate a series of samples, including the SLN starting materials, mixtures of the SLN components, and the SLNs themselves, for melting point and enthalpy changes. Samples were stored at room temperature for 24 hours prior to analysis, but no differences were observed for samples run immediately following preparation versus those stored for up to one month at room temperature. Freeze-dried SLNs were shown to have low water content (1.17±0.91% H_2O for Formulation 1 and 0.69±0.22% H_2O for Formulation 2). The observed melting point reductions of the SLNs were primarily attributable to interactions among the SLN components with the SLN preparation procedure having a minimal effect, as evidenced by the data obtained with the "processed" materials (Table 4.5). Phase diagrams were constructed for three of the analyzed mixtures: SA-Brij® 78 and SA-PEG6000MS because of the large reductions in the SA melting point and Brij® 78-PEG6000MS because of the development of an intermediate peak (Figures 4.3-4.5).

Table 4.5. Melting points (T_{fus}) determined from DSC peak maxima temperatures (Data is represented as the mean ± SD of 3 independent measurements of the T_{fus} value)

Sample[1]	SA:PS60:Brij 78:PEG6000MS weight ratio	T_{fus} (°C)		
		Brij® 78[2]	SA	PEG6000MS
SA	-	-	58.16±0.46	-
Brij® 78	-	44.39±0.14	-	-
PEG6000MS	-	-	-	63.09±0.78
SA (processed)	-	-	57.98±0.32	-
Brij® 78 (processed)	-	42.93±0.27	-	-
PEG6000MS (processed)	-	-	-	61.20±0.70
SA-PS60	1.6 : 0.4 : 0.0 : 0.0	-	56.30±0.22	-
SA-Brij® 78	1.6 : 0.0 : 2.8 : 0.0	41.61±0.56	51.48±0.25	-
SA-PEG6000MS[3]	1.6 : 0.0 : 0.0 : 3.0	-	47.09±0.66	58.79±0.25
PS60-Brij® 78	0.0 : 0.4 : 2.8 : 0.0	42.55±0.39	-	-
Brij® 78-PEG6000MS[4]	0.0 : 0.0 : 2.8 : 3.0	41.50±0.29	-	59.15±0.20
SA-Brij® 78-PS60	1.6 : 0.4 : 3.5 : 0.0	40.42±0.22	50.13±0.35	-
SA-Brij® 78-PS60-PEG6000MS	1.6 : 0.4 : 2.8 : 3.0	38.70±0.09	51.20±0.11	58.01±0.14
Formulation 1 SLNs	1.6 : 0.4 : 3.5 : 0.0	40.24±0.33	48.50±0.23	-
Formulation 2 SLNs	1.6 : 0.4 : 2.8 : 3.0	36.40±0.18/ 39.87±0.59	49.86±0.35	57.73±0.11

---

[1] Combinations prepared by subjecting materials to the NET procedure but without the addition of water are represented as component X-component Y. SLNs were freeze-dried prior to analysis.

[2] Brij® 78 or SA-Brij® 78 eutectic

[3] An additional small peak was present at 50.40±0.26°C.

[4] An additional small peak was present at 50.38±0.21°C.

The SA-Brij® 78 phase diagram (Figure 4.3) revealed that at low SA concentrations (<15 mole %), a solid solution with SA dissolved in Brij® 78 was apparent. At the concentrations of interest (Formulation 1, 66.06 mole % SA; Formulation 2, 70.97 mole % SA), the sample was characterized by the presence of both an SA phase and a eutectic phase. The eutectic composition was observed at approximately 30-40 mole %. The solid-liquid equilibrium line was modeled with good agreement using the van't Hoff freezing point relationship [166] as follows:

$$\ln(x) = \frac{\Delta H_{fus}}{R}\left(\frac{1}{T_{fus}} - \frac{1}{T}\right)$$

where x is the mole fraction of the major component at the temperature T, R is the gas constant, ΔH_{fus} is the molar enthalpy of fusion of the pure component, and T_{fus} is the melting temperature of the pure component. Residuals [experimental value (y) – model value (m)] were calculated and used in the determination of the sum of squares due to error [$SSE = \sum_{i=1}^{n}(y - m)^2$], giving a low value of SSE = 10.26. Goodness of fit [$R^2 = 1 - \frac{SSE}{SST}$, where SST = y – y_{avg}] was calculated to be 0.9997.

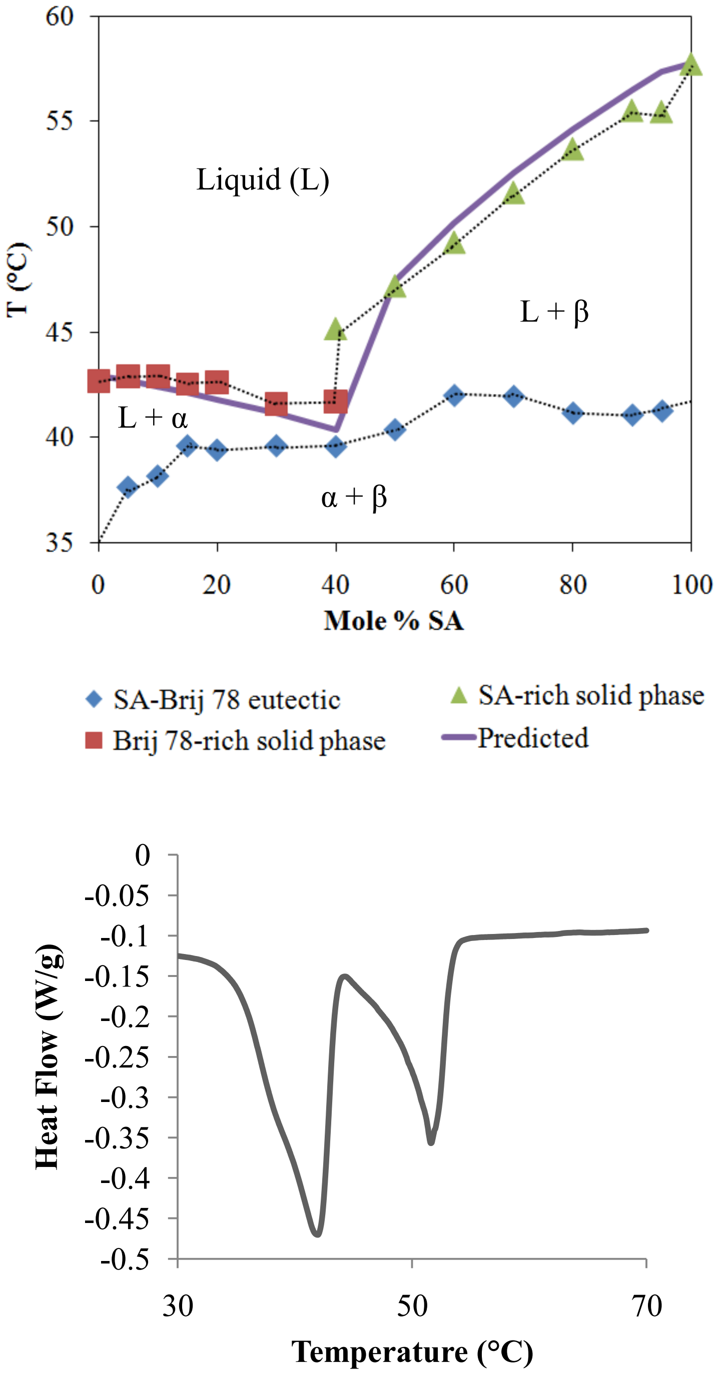

Figure 4.3. Top: SA-Brij® 78 phase diagram obtained from DSC peak maxima temperatures. Samples of different molar proportions were heated from 25-75°C; each symbol represents a peak seen in the thermograms. SA appears to dissolve in Brij® 78 up to 15 mole %. A eutectic appears at 30-40 mole % SA. Data is modeled using the van't Hoff freezing point relationship equation with good agreement (solid line). Dashed lines indicate assumed phase boundaries. α = Brij® 78-rich solid phase; β = SA-rich solid phase; L = liquid phase. Bottom: Representative SA-Brij® 78 thermogram at the ratio of interest (70.87 mole % SA, formulation 2)

The second mixture chosen for study was SA-PEG6000MS (92.21 mole % SA). The thermogram of the original mixture showed two peaks with melting temperatures significantly reduced below that of SA, and a major endotherm associated with PEG6000MS. Throughout the entire range of compositions, the same major endotherm was observed with the shoulder becoming more prominent at higher and lower concentrations (Figure 4.4). The cause for the shoulder is unknown, giving rise to the label, γ, for the intermediate region of the phase diagram. Correction of the enthalpy associated with this peak for the proportion of PEG6000MS present in the mixture (SLN concentration) produced a larger value than was seen with PEG6000MS alone (234.8 ± 1.9 J/g>170.9 ± 13.0 J/g), indicating that this peak was likely not attributable to a single phase. This agrees with the region of the phase diagram below this endotherm being bound by two solid forms, indicating the possible presence of both a PEG6000MS and an SA-PEG6000MS mixed phase.

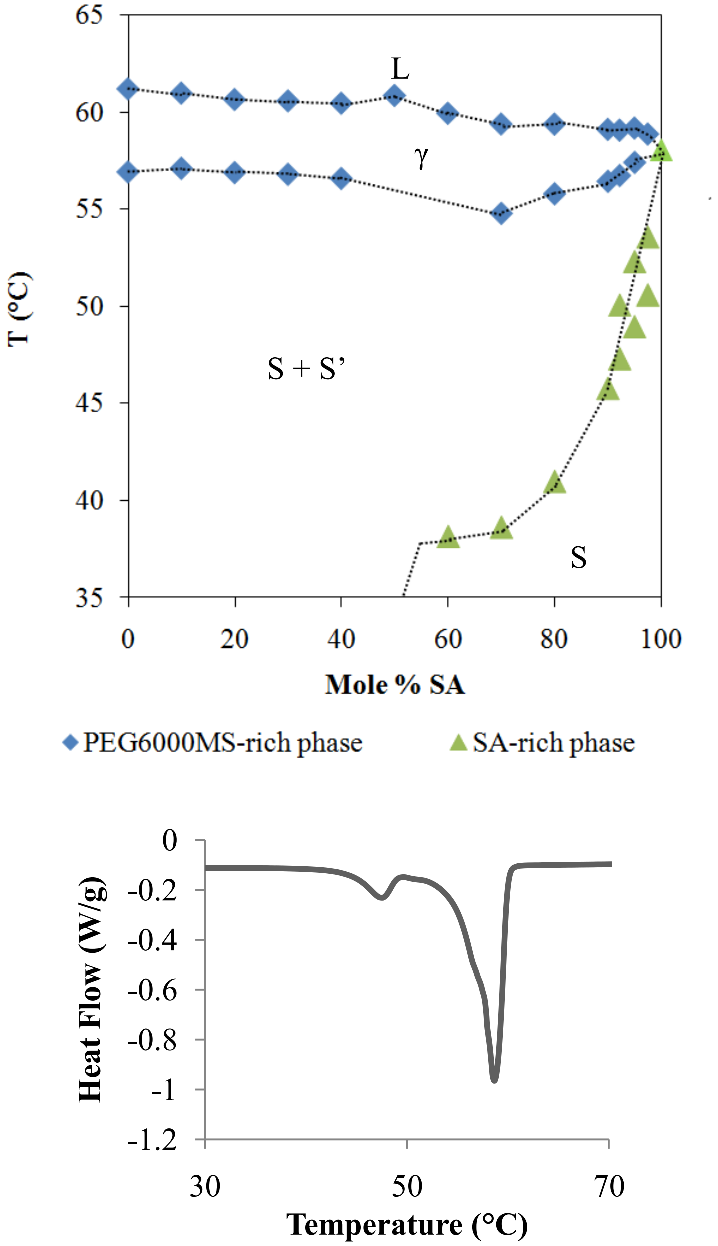

Figure 4.4. Top: SA-PEG6000MS phase diagram obtained from DSC peak maxima temperatures. Samples of different molar proportions were heated from 25-75°C; each symbol represents a peak seen in the thermograms. Dashed lines indicate assumed phase boundaries. A shoulder was observed on the PEG6000MS peak, becoming more apparent at higher and lower mole percentages (intermediate region labeled γ). The area below this region is bounded by two solid phases, indicating the likely presence of both PEG6000MS and SA-PEG6000MS phases. Assumed phases are labeled as an aide. A more complete analysis is required to verify their exact nature. S, S’= Solid phase of unknown structure; L= Liquid phase; γ = unknown. Bottom: Representative SA-PEG6000MS thermogram at the ratio of interest (92.21 mole % SA)

Brij® 78-PEG6000MS (16.44 mole % PEG6000MS) was the final mixture chosen for further analysis. The original sample displayed three endotherms: one each from Brij 78 and PEG6000MS and a smaller peak intermediate between these two. The phase diagram (Figure 4.5) showed that below 30 mole %, no crystalline Brij® 78 was detectable, indicating possible dispersion in PEG6000MS. A separate Brij® 78 phase is present above 30 mole % that upon melting leaves a PEG6000MS-rich solid phase and a liquid. At PEG6000MS mole percentages of 10-30%, the small intermediate peak was present but disappeared above these levels. Above the melting temperatures associated with this peak, a modified PEG6000MS-rich solid phase is present along with a liquid phase. The PEG6000MS peak was again characterized by a left-hand shoulder (intermediate region labeled γ in the phase diagram).

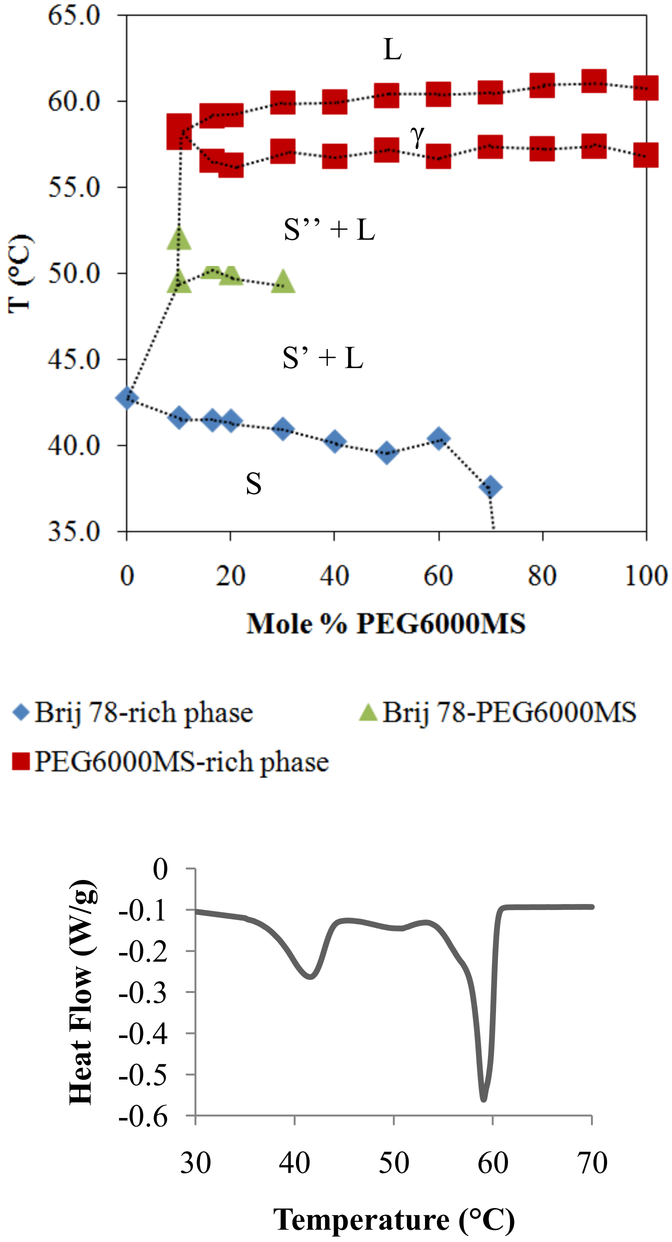

Figure 4.5. Top: Brij® 78-PEG6000MS phase diagram obtained from DSC peak maxima temperatures. Samples of different molar proportions were heated from 25-75°C; each symbol represents a peak seen in the thermograms. Dashed lines indicate assumed phase boundaries. A shoulder was again observed on the PEG6000MS peak. Brij® 78 appears to dissolve in PEG6000MS up to approximately 30 mole %. A small intermediate peak was seen at low PEG6000MS mole percentages. Overall, the materials remain as two separate phases with minimal interaction. Assumed phases are labeled as an aide. A more complete analysis is required to verify their exact nature. S, S', S''= Solid phase of unknown structure; L= Liquid phase; γ = unknown. Bottom: Representative Brij® 78-PEG6000MS thermogram at the ratio of interest (16.44 mole % PEG6000MS)

DSC and PXRD were used to evaluate the crystalline polymorph(s) present in SLNs. Since it is known that rapid cooling of melted SA can induce the formation of the metastable β-form [167], a DSC assay including a cooling cycle and a second heating cycle was developed. The generation of the β-form was confirmed with pure SA. Thermograms were then obtained for the mixtures (SA-PS60-Brij® 78 and SA-PS60-Brij® 78-PEG6000MS) using this protocol to determine where the β- and γ-forms would appear if present. These were compared to the SLN thermograms (Figure 4.6). The major SLN peaks were shown to overlap with the known γ-peaks in the mixtures. Overlayed powder X-ray diffractograms of the SLNs and their starting components are shown in Figure 4.7. Although SA peak intensity was significantly reduced in the SLNs as compared to the pure component materials, no obvious transition to the metastable form was observed. The SA peak in the SLNs was shifted slightly to the left as would be expected with the β-form [167], but as only one peak is visible, it is likely that this can be attributed to the γ-form. Neither technique was sensitive enough to conclude that the β-form was absent.

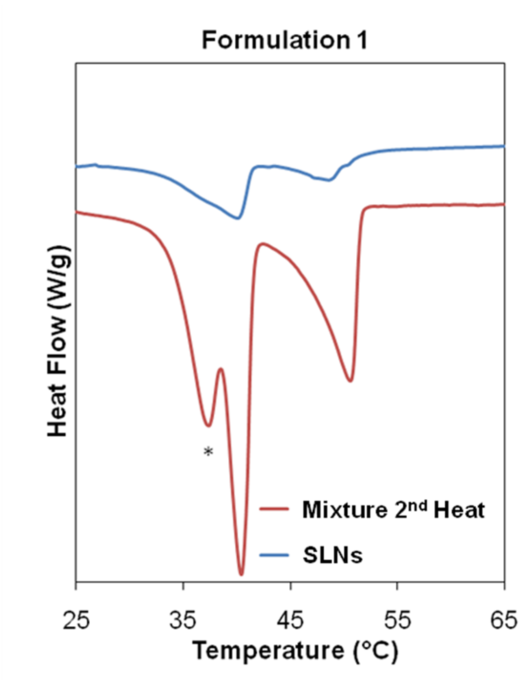

Figure 4.6. DSC thermograms comparing formulation 1 (left) and formulation 2 (right) SLNs with a second heating of their respective mixtures (SA-PS60-Brij® 78 and SA-PS60-Brij® 78-PEG6000MS) *SA β-form

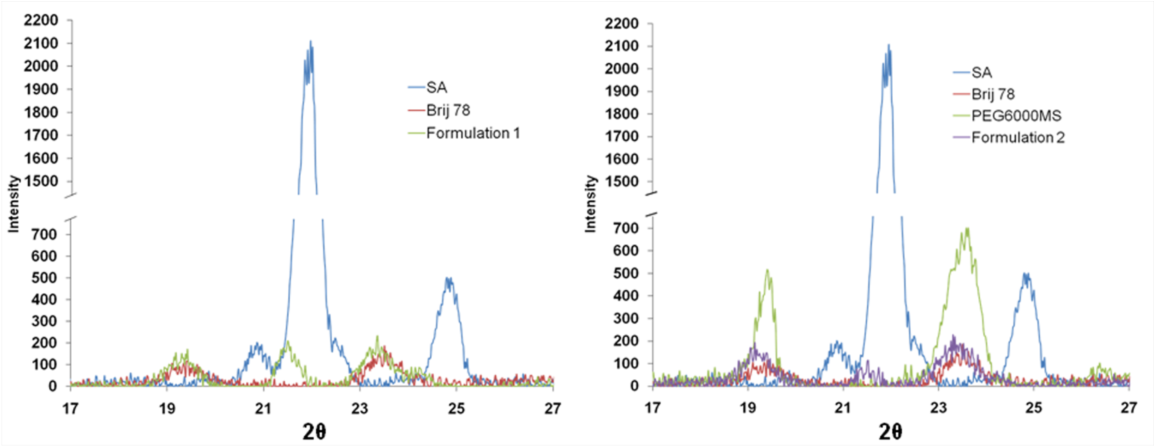

Figure 4.7. Powder X-ray diffractograms of freeze-dried SLNs in comparison to the starting materials. Formulation 1 in comparison with SA and Brij® 78 (left); Formulation 2 in comparison with SA, Brij® 78, and PEG6000MS (right).

4.3.4. SLN Temperature-Dependent Stability Study. The growth rate of SLNs increased with increasing temperature (Figure 4.8). Formulation 1 SLNs were observed to become fully destabilized at temperatures exceeding 65°C, preventing analysis at higher temperatures. The same phenomenon was not apparent in formulation 2 SLNs until 70°C. When the growth rates were plotted against temperature, a break point was observed for each formulation: 35.2°C and 43.0°C for formulation 1 and formulation 2, respectively.

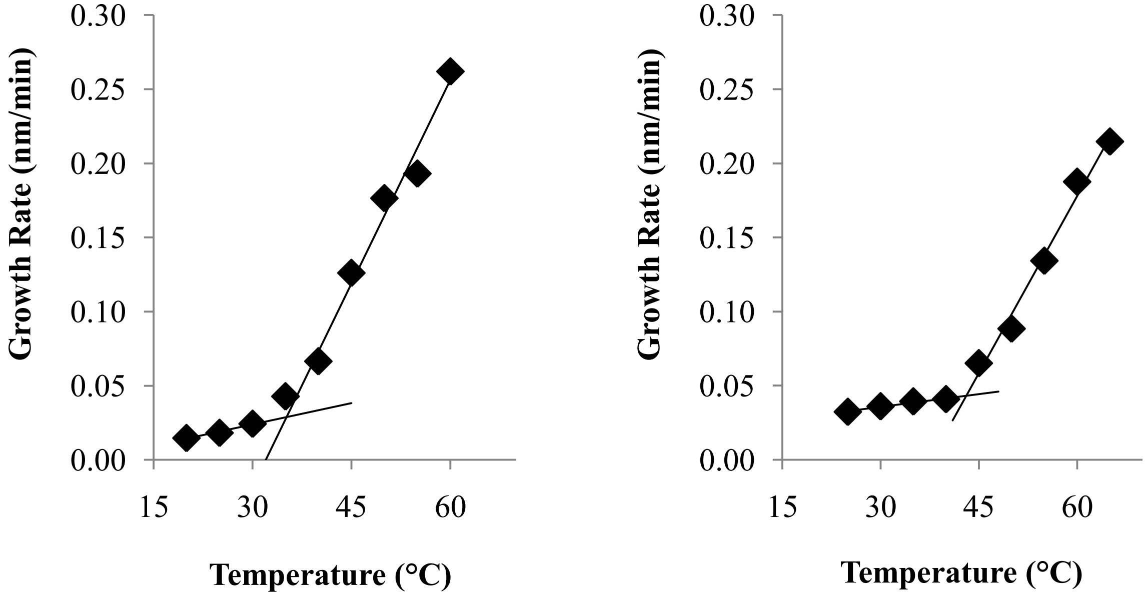

Figure 4.8. Particle size growth rates of SLNs at different temperatures. Application of the double tangent method indicated a critical temperature of 35.2°C for formulation 1 SLNs (left) and 43.0°C for formulation 2 SLNs (right).

4.4. DISCUSSION

In order to ensure the utility of SLNs as a clinically applicable drug delivery system, it is important to have a thorough understanding of their physicochemical characteristics.

These properties have been shown to have a significant effect on particle stability, including size growth [138, 139], gelation tendency [140-143], and drug retention [136-138].

DLS and TEM indicated that both NET formulations studied had a particle size of less than 100 nm, similar to SLNs produced using other methods [168-170]. Data from the two measurement techniques were in reasonable agreement though the particle sizes observed from TEM images were slightly larger than those obtained from DLS measurements. As the two techniques are based on different principles, this was an unexpected result. Measurements obtained from light scattering are based on the hydrodynamic diameter of the particle and provide an intensity-weighted average particle size, whereas measurements obtained using microscopic techniques are based on the diameter of the dry particle and give a number-weighted average particle size. As a result, particle sizes from DLS tend to be larger than those obtained by TEM [171]. The different result seen here may be attributed to the assumption of spherical particles inherent in the DLS calculations. However, the possibility of particle size and shape changes due to TEM grid preparation cannot be excluded. Non-spherical shapes have been reported for a number of SLN systems [172-174]. Anisometric particles may be a result of a crystal modification present [140] or a result of crystallization occurring non-uniformly in three dimensions [173]. Overall, it was determined that particles were within a size range appropriate to take advantage of the enhanced permeability and retention effect for tumor targeting [29]. The effect of morphology is unclear but may be expected to play a role in drug release, transport, and internalization [175].

Other groups have reported the existence of supercooled melts within a SLN formulation [136, 137]. To determine if this was present in the NET SLNs, ^{1}H-NMR spectroscopy was performed. Although supercooling of 5-10°C was observed in the two formulations under study, it was not significant enough to prohibit the formation of SLNs. Only a small proportion of the lipid remained in solution, which high T_1/T_2 ratios indicated was likely attributed to the aliphatic chains adsorbed to the particle surface.

Further structural information on the SLNs was obtained by evaluating the PEG signal arising from PS60, Brij® 78, and for formulation 2, PEG6000MS. PEG surface coverage is critical for the prevention of particle aggregation and gelation [139] and inhibiting protein adsorption [63]. Although it is presumed that PEG is present on the surface of nanoparticles in a flexible conformation, it is important to confirm this as other structures are feasible. Reverse micelles have been detected in SLNs [176], although not those possessing PEGylated surfactants. The addition of an internal standard confirmed that ~100% of the added PEG remains in solution in intact SLNs, and the low T_1/T_2 ratio found for the 3.6 ppm NMR peak indicated that it had high molecular mobility, correlating well with the expected surface localization of PEG.

To determine the physical state (e.g., crystalline vs. amorphous) of the solid phase, DSC and PXRD were performed. Changes in the crystalline nature of the SLNs were analyzed by DSC by monitoring for shifts in melting point and enthalpy from the raw materials. The crystallinity index can be determined by dividing the peak enthalpy of a processed material by that of the raw material in order to quantify the extent of crystallinity.

However, this calculation is not appropriate if the material forms a new phase not seen in the pure components (i.e., if it has formed a eutectic with another material or if it has undergone a polymorphic conversion).

DSC indicated that SLNs had reduced melting points as compared to the starting materials. A series of samples were used to evaluate the effects of the preparation procedure and the interactions among the SLN components in the bulk state. While the preparation procedure was shown to play some role in reducing the SLN melting points, the interactions among the formulation components appeared to be the primary contributors. The three samples showing the most complex thermograms (SA-Brij® 78, SA-PEG6000MS, and Brij® 78-PEG6000MS) were chosen for further study to confirm that no changes were occurring that would prohibit calculation of the crystallinity index. Specifically, phase diagrams covering the entire range of molar combinations were constructed for each mixture. It should be noted that the phase diagrams were obtained by observing phase transitions with measurable enthalpy changes, and are unlikely to identify all phase transitions that may exist in these mixtures.

The Brij® 78-PEG6000MS mixture was chosen for further study because of the additional peak observed intermediate between those of the individual components. This was assumed to be attributable to a new phase developed based on the interactions between the two materials. Based on their similar structures, it might be expected that these interactions would be significant. However, the peak was relatively small in comparison to the other two peaks (10-20% of the enthalpy of the Brij® peak), and it was of interest to see how this would change with other proportions. The phase diagram indicated that this peak remains small and is only present at 10-30 mole % PEG6000MS. At most concentrations, the materials exist as two separate phases. The lack of interaction may be of some concern if it leads to the presence of multiple nanoparticle populations. Based on the above DLS and TEM data, this does not appear to be the case, but the possibility cannot be eliminated.

The other two mixtures chosen for study were those of SA with Brij® 78 and SA with PEG6000MS. The SA-Brij® 78 mixture was chosen because of the large reduction in the SA melting point observed as compared to the starting material. The phase diagram for this mixture revealed that a eutectic was formed at 30-40 mole % SA. This prevents the calculation of crystallinity indices from the peak enthalpies because the peaks no longer represent a single component that can be compared to the starting materials. The SA-PEG6000MS (92.21 mole% SA) mixture was chosen because of the presence of multiple peaks and the large reduction in the SA melting point. The phase diagram indicated that at most temperature and concentration combinations, both PEG6000MS and an SA-PEG6000MS mixed phase exist. Thus, while the initial analysis indicated that SA crystallinity was reduced in the SLNs, the in-depth study revealed that SA is actually present in several different forms within the SLNs.

An additional drop in the melting point was observed on going from the complete mixtures to the SLNs (50.13°C to 48.50°C for formulation 1 and 51.20°C to 49.86°C for formulation 2). Three possible explanations were considered for this. The first was the presence of water in the freeze-dried SLNs. The water content was shown to be ~1% based on a Karl Fischer titration. Using this value, it was calculated that there could be up to 1 molecule of water per 6 molecules of SA if the water was present in the lipid core of the particles. This would potentially decrease the lipid melting temperature. However, it seems more likely that most of the remaining water would be associated with the hydrophilic PEG shell of the particles and would only minimally impact the lipid melting.

The second possible explanation was the Kelvin Effect, which describes why smaller particle sizes result in lower melting temperatures [177]. Numerous studies exist that have demonstrated this to play a role in the melting of SLNs [178-180]. This effect can be approximated using the Gibbs-Thomson equation [177]:

$$\ln\frac{T}{T_0} = -\frac{2\gamma_{sl}V_s}{r\Delta H_{fus}}$$

Assuming an interfacial surface tension, γ_{sl}, in the range of $10^{-2} - 10^{-3}$ mN/m (common for microemulsions, [131]), a specific volume, V_s, of the solid of 1.23 cm^3/g, a radius, r, of 45 nm (for formulation 2 SLNs), and a ΔH_{fus} of 210 J/g (bulk SA value from DSC), a T/T_0 ratio of ~0.999 was calculated. Multiplying this by the SA melting temperature found in the SA-Brij® 78-PS60-PEG6000MS combination, a reduced temperature of 51.15°C would be expected, which is higher than the experimental value obtained. However, as this is only an approximation, the actual effect may be larger.

The presence of a different polymorph represented a third possible explanation for the observed results. The β-form of SA is known to have a lower melting point than the γ-form [167]. In order to elucidate whether the third explanation was a possibility, two additional studies were performed. SLNs were compared to DSC thermograms of the mixtures that had undergone a cooling phase designed to introduce the metastable β-form of SA. Additionally, powder X-ray diffractograms of the freeze-dried SLNs were compared to those of the starting materials. Although it was difficult to conclude that the β-form of SA was absent, it did not appear to be the primary crystalline polymorph of SA present. As such, it seems likely that the small particle size of SA in the SLNs and the presence of water in the samples are the main contributors to the reduction in the SLN melting point.

Based on these results, it appeared that the SLNs under consideration have promise as a drug delivery system. The interactions among the components may lead to the decreased crystallinity desirable for high drug loading capacities [35], a goal of SLN research. For instance, liquid lipids have been added to solid lipids to generate lipid matrices with multiple defects. These so-called nanostructured lipid carriers have shown enhanced drug loading [143, 181, 182]. Nanotemplate engineered SLNs with an appropriate formulation may be able to attain a similar result. On the other hand, there may be cause for concern in terms of the stability of the SLNs. The proximity of the low melting point of the SA-Brij® 78 eutectic (38-40°C) to physiological temperatures may lead to a disruption of the particle structure under *in vivo* conditions. Enhanced mobility of the SLN components may allow for crystallization, causing changes in particle size or drug release profiles. Alternatively, it may decrease protection for biologically sensitive compounds (e.g., by making them susceptible to enzymatic attack). This was of particular concern with formulation 1 SLNs in which there is a higher concentration of Brij® 78 than in formulation 2, possibly leading to a higher proportion of SA present in this low melting form. Analysis of the SLN DSC thermograms (Figure 4.6) furthered this concern, as the SA-Brij® 78 eutectic peak was considerably more prominent in the formulation 1 SLNs than in the formulation 2 SLNs.

However, the question remained as to whether the bulk properties adequately represent the situation observed in nanoparticles. In order to determine this, growth curves were constructed for the SLNs at a variety of temperatures. At the temperature where the SLNs melt or partially melt, it might be expected that there would be a transition in their growth curves if growth is due to Ostwald ripening as has been proposed [34]. Particle size increased with time at all temperatures; higher temperatures led to higher growth rates. At 65°C and 70°C, formulation 1 and formulation 2 SLNs, respectively, became completely destabilized, preventing determination of a growth curve. In plotting the growth rates for the formulation 1 SLNs at lower temperatures, a break point was observed at the critical temperature of 35.2°C. If figure 4.6 is referenced, it can be observed that this corresponds approximately with the onset of melting of the SA-Brij® 78 eutectic, indicating that a portion of SA is present in this form even if the composition is different from that observed in the bulk state. While the low critical temperature (below 37°C) observed with these SLNs confirms that physiological stability may, in fact, be a problem for these particles, it also provides an important result in that it validates the assessment of the bulk properties of materials used in SLN preparation as a means of anticipating and/or understanding the interactions occurring within nanoparticles.

The critical temperature for the formulation 2 SLNs was higher, at 43.0°C. This corresponds approximately with the onset of melting of SA alone, indicating that little to no SA is present in the low melting eutectic form in these SLNs. As such, these SLNs are expected to exhibit considerably higher stability than formulation 1 SLNs under physiological conditions.

4.5. CONCLUSIONS

Nanotemplate engineered SLNs were shown to exhibit desirable properties for a drug delivery system. Both formulations were of a small particle size (<100 nm), ellipsoidal shape, and low polydispersity. ^{1}H-NMR spectroscopy confirmed that the SLNs have the expected solid core structure and PEGylated surface. Analysis of the bulk materials indicated that a number of complex interactions are present among the SLN components, including the formation of a SA-Brij® 78 eutectic and a mixed SA-PEG6000MS phase. The decreased crystallinity resulting from these interactions may allow for enhanced drug loading. However, physiological stability was identified and confirmed as a potential problem due to the low melting point of the eutectic. For this reason, formulation 2, in which PEG6000MS is present and the amount of Brij® 78 in the formulation is reduced, was chosen as the primary formulation for future studies.

*Reprinted with permission from Howard, M. D.; Lu, X.; Rinehart, J. J.; Jay, M.; Dziubla, T. D., Physicochemical Characterization of Nanotemplate Engineered Solid Lipid Nanoparticles. *Langmuir* **2011,** 27, (5), 1964-1971. Copyright © 2011 American Chemical Society.

Chapter 5

A Comparative Study of the Extent and Mechanism of Drug Loading in Solid Lipid Nanoparticles

5.1. INTRODUCTION

SLNs are a versatile drug delivery system capable of carrying both hydrophobic and hydrophilic small molecule drugs [131] as well as proteins [183], DNA [184], and contrast agents [185, 186]. Of these, hydrophobic small molecules have been studied most extensively. Numerous drugs, including doxorubicin [161], cyclosporine [187], and coenzyme Q10 [163, 188] have been successfully loaded into SLNs. Three main models are typically used to describe drug incorporation: 1) a solid solution model, 2) a core-shell model with a drug-enriched shell, and 3) a core-shell model with a drug-enriched core [34]. While these are useful for explaining obtained results (e.g., drug release), it can be difficult to predict and/or optimize how drug will be incorporated into the particles and to what extent.

Systematic studies considering the effects of lipid and surfactant composition have shed some light on how these parameters affect drug loading. For instance, the use of complex glycerides in lieu of pure glycerides can allow for higher drug loading due to their lower crystallinity [138]. An increase in the monoglyceride content of the lipid phase was shown to accelerate drug release; this was attributed to the ability of the monoglycerides to act as a surfactant and allow more drug to reside at the particle surface [153, 189]. High surfactant concentrations have also led to a burst release of drugs for a similar reason [190]. Our current understanding of how the physicochemical properties of the drug itself influence drug loading is more limited. Most reports on drug loading into SLNs have focused on the optimization of a system for a specific drug [149, 168]. Although a number of drugs have been reported to be loaded into SLNs, it can be difficult to compare them across different formulations and preparation methods.

Only recently has SLN research been directed toward gaining a better understanding of how the physicochemical properties of drugs are a determinant of how and to what extent they are loaded into nanoparticles. Advancements in technologies like electron paramagnetic resonance (EPR) [191] and paraelectric spectroscopy [192] have allowed for the determination of the location of probe structures within SLNs. Other studies have attempted to systematically vary drug lipophilicity and determine the effect on drug loading [153, 193]. In general, drug loading has been shown to increase with lipophilicity. Further, enhanced lipophilicity tends to slow drug release as a result of better incorporation in the lipid matrix of the nanoparticles. However, as the lipophilicity is typically increased through the addition of hydrophobic side chains that may align with SLN lipids, it may be difficult to discern whether changes are primarily associated with the change in drug lipophilicity or structure.

In our own studies, we found that the use of Dex-P , a lipophilic ester prodrug of Dex, in SLNs was able to enhance drug loading and slow drug release as compared to Dex itself [35]. As with other nanoparticle systems, it was difficult to discern whether this was primarily associated with the increased lipophilicity of the compound or whether it was due to the palmitate side chain aligning with the SLN lipids. A conformational analysis of the packing of Dex-P into liposomes showed that Dex was likely oriented toward the aqueous phase, interacting with the phospholipid head groups, while the palmitate chain was aligned with the acyl chains of phospholipids [194]. It was expected that Dex-P may align similarly in SLNs composed of a SA lipid phase and stabilized by PS60, Brij® 78, and PEG6000MS. This theory was supported by the apparent cleavage of Dex from the SLNs by the action of CE enzymes [37].

This section was focused on further evaluating the extent and mechanism of loading of Dex-P into the SLNs as well as on determining how drug loading affects the physicochemical properties of the SLNs. For comparison, two additional drugs, AP and curcumin, were chosen for study. Structures and relevant physicochemical properties of these compounds are given in Figure 5.1. Both have previously been loaded into SLNs by other groups [195, 196]. AP was chosen because it is a prodrug with the same palmitate side chain present in Dex-P. However, as ascorbic acid (AA) is considerably more hydrophilic than Dex, loading of AP should be primarily dependent on the palmitate moiety. Curcumin was chosen for study because it is lipophilic but characterized by a different structure with no hydrophobic side chains. SLNs were prepared with the three drugs of interest at loadings of 10-30% w/w SA (0.16-0.48 mg/ml drug in comparison to 1.6 mg/ml SA). Encapsulation efficiency (amount of drug associated with particles/added drug) was determined, and drug loaded particles were assessed for their size, shape, and core-shell structure. Interactions between the drugs and the nanoparticle components were analyzed in order to better understand how the drugs were loaded into the SLNs. Finally, drug release from the SLNs was monitored.

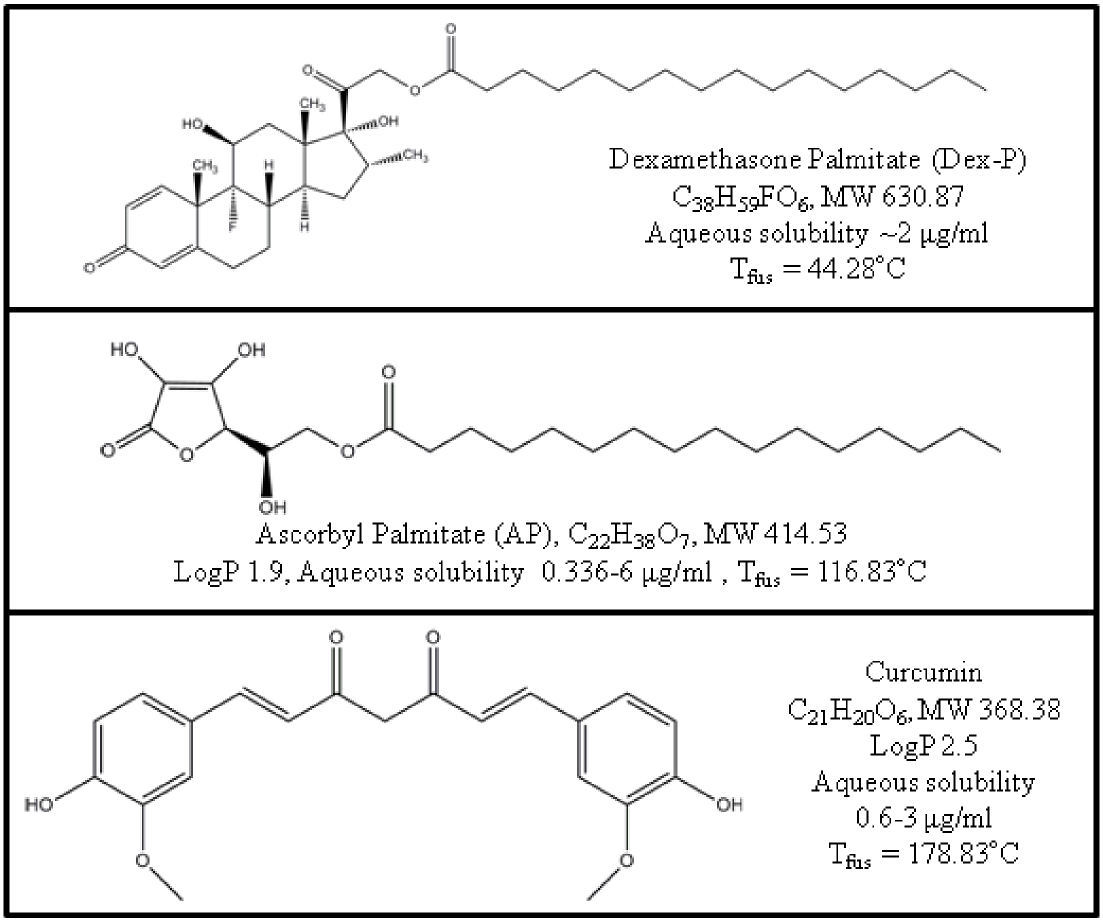

Figure 5.1. Structures of Dex-P, AP, and curcumin. MW was calculated by ChemDraw. LogP and aqueous solubility values were taken from the literature (References: Dex-P [197], AP [198-201], Curcumin [202-205]). Melting temperatures (T_{fus}) were determined by DSC.

5.2. MATERIALS AND METHODS

5.2.1. Materials. SA and polysorbate 80 were obtained from Spectrum Chemicals and Laboratory Products (Gardena, CA). PS60 and Brij® 78 were purchased from Uniqema (Chicago, IL). PEG6000MS was a gift from Stepan (Northfield, IL). AP, curcumin, deuterium oxide (D_2O), acetonitrile (ACN), methanol (MeOH), and D-Salt Polyacrylamide 6000 desalting columns were purchased from Fisher Scientific

(Pittsburgh, PA). Dex (USP) was a gift from Pfizer (Kalamazoo, MI). Palmitoyl chloride and Float-A-Lyzer G2 dialysis tubes (1 mL, 100 kD) were from Sigma-Aldrich (St. Louis, MO). Phosphate buffered saline (PBS) was purchased from Invitrogen (San Diego, CA). Water was from a Milli-Q Synthesis ultrapure water system (Millipore; Billerica, MA). Centrifugal filter devices (Microcon YM-10) were purchased from Millipore.

5.2.2. Synthesis of Dex-P. The procedure to prepare Dex-P has previously been reported [35]. In brief, 300 mg Dex was dissolved in 12 mL pyridine followed by a dropwise addition of 578 mg palmitoyl chloride. The mixture was stirred in the dark under nitrogen for 24 h. Nitrogen was used to evaporate the solvent, and the product was dissolved in dichloromethane prior to loading onto a 30 mL silica gel column. Elution of the column with a dichloromethane to dichloromethane:ethyl acetate (6:4 v/v) gradient was used to isolate the purified product. The reaction progress was monitored using silica gel thin layer chromatography (TLC) with a chloroform:ethyl acetate (7:3) mobile phase. Retention factor values were 0.10 and 0.69, for Dex and Dex-P, respectively.

5.2.3. SLN Preparation. SLNs were prepared using the nanotemplate engineering method [131]. The process used in this study consisted of 1) melting an appropriate mixture of lipids, surfactants, and drug at 70°C, 2) adding an aqueous phase to generate an oil-in-water microemulsion, and 3) cooling the microemulsion to room temperature to form a suspension of SLNs. PBS was used as the aqueous phase of the microemulsion for all studies except the NMR studies, in which D_2O was substituted. Blank SLNs (with no added drug) consisted of 1.6 mg/mL SA, 0.4 mg/mL PS60, 2.8 mg/mL Brij® 78, and

3.0 mg/mL PEG6000MS. For drug loaded SLNs, Dex-P and curcumin were added to the original mixture at 10, 20, or 30% w/w SA. As AP was degraded in a concentration-dependent manner during the preparation process, presumably largely as a result of oxidative reactions [206], the amount added initially was adjusted in order to give final drug loads of 10, 20, or 30% w/w SA (correction equation: actual load = 1.18*expected load - 10.4).

5.2.4. Drug Loading and Encapsulation Efficiency. HPLC was used to determine the concentration of drug loaded in the SLNs. The following conditions were used for Dex-P analysis: Alltech C18 column (5 μm, 250 mm×4.6 mm), 95:5 ACN:H_2O mobile phase run at 2 ml/min, and UV detection at λ=240 nm. AP was analyzed using the following parameters: Alltech Nucleosil C18 column (5 μm, 150 mm×4.6 mm), 75:10:15:0.1 MeOH:ACN:20 mM PBS:TFA mobile phase run at 1 ml/min, and UV detection at λ=254 nm. Analysis conditions for curcumin were as follows: Supelco Discovery C18 column (5 μm, 250 mm×4.6 mm), 50:50 ACN:H_20 mobile phase run at 1 ml/min, and UV detection at λ=420 nm. Standard curves for each drug were developed. Samples were prepared at 1 mg/ml and diluted with the respective mobile phase to concentrations in the range of 10-200 μg/ml. Five concentrations were chosen for each drug, and three separate samples were analyzed at each concentration.

Following preparation, each SLN suspension was passed through a 0.2 μm filter: Dex-P and AP through nylon membranes and curcumin through polytetrafluoroethylene (PTFE) membranes due to its extensive adsorption to nylon membranes. For analysis of the drug concentration in these initial and filtered SLN suspensions, 100 μl of each sample was diluted 5x with methanol, and 10 μl were injected on the HPLC column. Filtered Dex-P and AP SLNs (300 μL) were then ultrafiltered (Microcon YM-10, 10K MWCO) to remove free drug followed by three washes with PBS. Filtrates were directly injected to the HPLC column. The amount of free drug present in the filtrates was subtracted from the amount present in the filtered SLN suspension; this was compared to the initial preparation in order to calculate the encapsulation efficiency.

Due to binding of curcumin to the ultrafiltration membrane, free drug was instead removed from these SLNs using a D-salt polyacrylamide 6000 desalting column. Three hundred microliters of the filtered curcumin SLN suspensions were loaded to the column; PBS was used as the eluent. A strong yellow band was observed to travel through the column, allowing for easy collection. This band came off in the void volume of the column (as confirmed by blue dextran), providing evidence that it was associated with SLNs and not free drug. Further, particle size of the collected sample was analyzed and shown to coincide with intact SLNs. Drug concentration of the collected sample was determined following a 5x dilution with methanol. After correction for the sample dilution that occurs with running the sample through the column, the encapsulation efficiency was calculated by comparing this concentration with the concentration present in the initial preparation.

5.2.5. DLS and TEM. DLS was used to measure particle size. Samples were diluted 1:30 with Milli-Q water and analyzed in triplicate at 25°C on a Delsa™ Nano Zeta Potential and Submicrometer Particle Size Analyzer (Beckman Coulter Inc., Brea, CA). TEM images were used to provide information on the shape of SLNs. One drop (~7 µL) of a SLN suspension was incubated for 1.5 min on a carbon-coated TEM grid. The grid was then dried and stained (0.2 µm filtered 2% uranyl acetate) for an additional 1.5 min. Following 5 min of drying, the grid was imaged using a Philips Tecnai Biotwin 12 equipped with a Gatan ES 1000W CCD digital camera (FEI, Hillsboro, OR).

5.2.6. NMR Spectroscopy. ^{1}H-NMR spectra were obtained for drug loaded SLNs in D_2O using a Varian 500 MHz NMR (Varian Inc., Palo Alto, CA). Comparisons were made with images of blank SLNs previously analyzed [207]. To provide a quantifiable means of comparing the different samples, the ratios between the integrals of the main aliphatic peak at 1.3 ppm and the PEG peak at 3.6 ppm were calculated.

5.2.7. DSC. DSC analysis was performed on a TA Instruments DSC 2920 (TA Instruments, New Castle, DE). The corresponding TA Instruments Universal Analysis software was used to identify peak maxima temperatures. Mixtures of the drugs with the SLN components were prepared at the ratios found in SLNs. Dex-P and AP were used at 10, 20, or 30% w/w SA; curcumin was used at either 10 or 20% w/w SA. Materials were melted and mixed at 70°C as in the SLN preparation but without forming an aqueous dispersion and then cooled to room temperature. Following preparation, samples were allowed to sit for 24 h prior to loading of 5-7 mg in hermetically sealed aluminum pans.

Dex-P containing mixtures were run from 25-75°C at a 1°C/min heating rate. AP and curcumin containing mixtures were run using the same protocol followed by a 10°C/min ramp to 150°C and 250°C, respectively. Comparisons were made with drugs analyzed individually as well as with blank mixtures previously analyzed [207]. All measurements were performed in triplicate.

5.2.8. Drug Release. SLNs were prepared in PBS with 0.02% Polysorbate 80; the drug loading was 10% for all drugs. Following filtration using an appropriate 0.2 μm membrane, 1 mL SLNs were loaded into 100 kD Float-A-Lyzer G2 dialysis tubes preconditioned in Milli-Q water for 15 min and in PBS with 0.02% Polysorbate 80 for 30 min and dialyzed against 1 L of the same buffer at 37°C with shaking at 50 rpm. At various time points (0, 1, 3, 6, 24, and 48 h), 100 μL were withdrawn from inside the dialysis tube and immediately diluted 5x with MeOH. HPLC assay conditions were as described above. To determine if diffusion of the drug across the dialysis membrane was a rate-limiting factor, studies were repeated with free drug. Excess drug was added to solutions of PBS with 0.02% Polysorbate 80 and allowed to shake for 1 h. Following filtration (0.2 μm), samples were loaded into dialysis tubes, and the experiment was conducted in the same manner as that used for analyzing release of drug from SLNs. GraphPad Prism was used for fitting of the data; single or double phase exponential decay profiles were chosen as appropriate. The initial value was fixed at 100% drug remaining, and complete drug release was required.

5.3. RESULTS

5.3.1. Drug Loading and Encapsulation Efficiency. Linear calibration curves were obtained for all three drugs in the range of 10-200 µg/mL (Figure 5.2). Comparison with these showed that SLNs could be loaded with Dex-P or AP at 10-30% w/w SA with encapsulation efficiencies >85% (Tables 5.1-5.3). Higher drug concentrations did not result in decreased encapsulation efficiencies. Drug loss was predominantly associated with removal during the 0.2 µm filtration step. In general, only 1-2% of the drug was removed during the ultrafiltration step. In contrast, the encapsulation efficiency for SLNs containing 10% curcumin was reduced to approximately 75%, with around 10% being removed during the 0.2 µm filtration step and the other 15% removed during the column filtration step. Column filtration was required due to adsorption of curcumin to the ultrafiltration membrane.

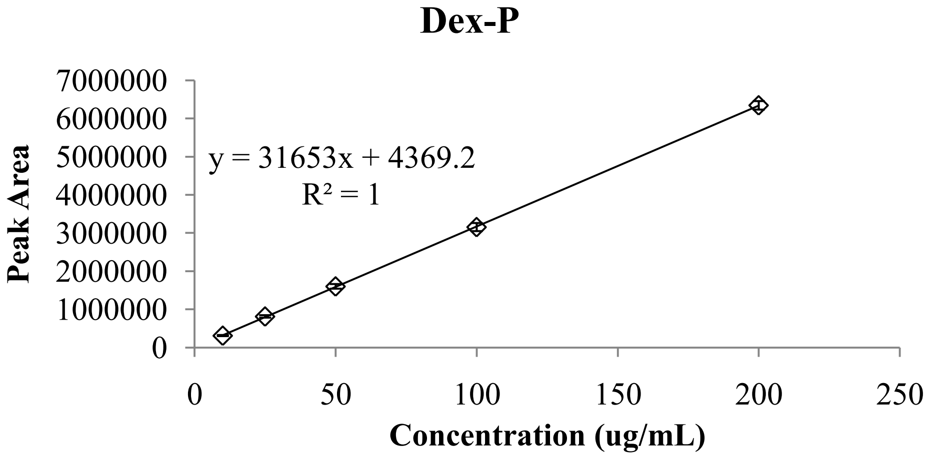

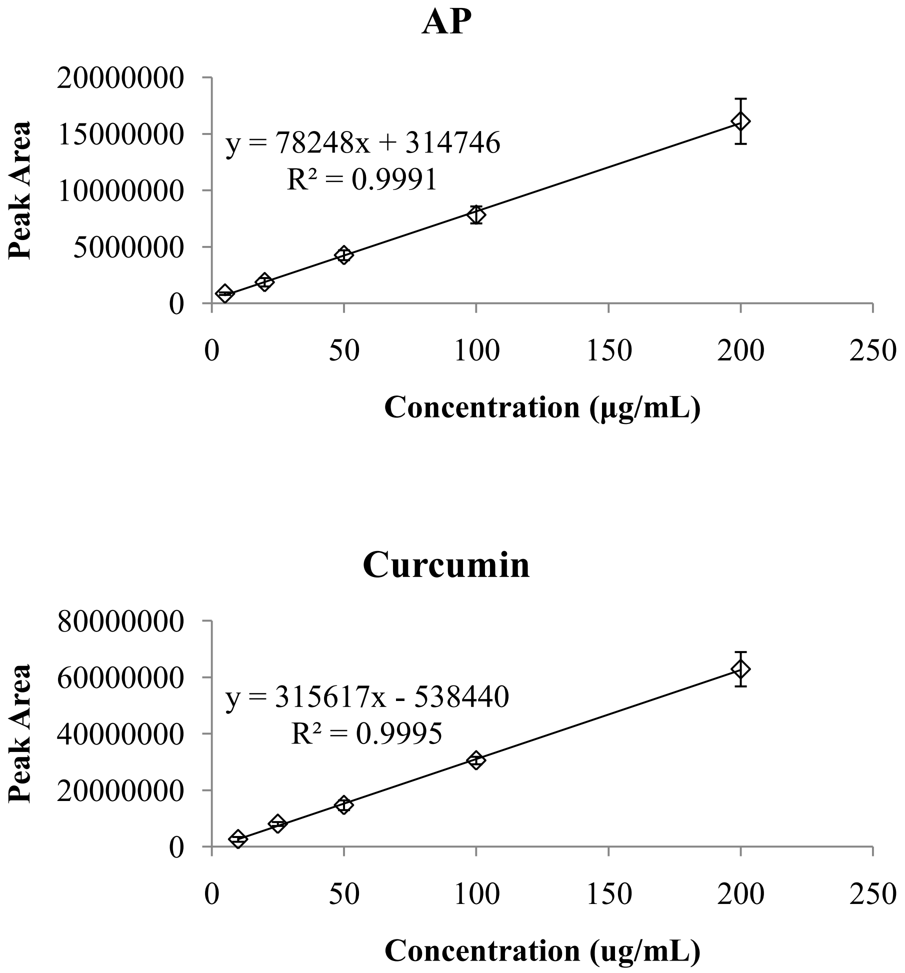

Figure 5.2. Calibration curves developed for Dex-P, AP, and curcumin using the appropriate HPLC assay (n=3)

Table 5.1. Particle size and encapsulation efficiency data for SLNs loaded with Dex-P at 10-30% w/w SA. Blank information is taken from [207].

Drug Loading	Dex-P		
	EE (%)	Size (nm)	PI
Blank	-	89.4±1.9	0.111±0.023
10%	91.56±4.48	97.7±0.1	0.069±0.027
20%	86.63±7.54	114.4±10.4	0.096±0.010
30%	91.77±6.02	132.1±3.1	0.096±0.003

Table 5.2. Particle size and encapsulation efficiency data for SLNs loaded with AP at 10-30% w/w SA. Blank information is taken from [207].

Drug Loading	AP		
	EE (%)	Size (nm)	PI
Blank	-	89.4±1.9	0.111±0.023
10%	91.84±3.86	88.5±3.0	0.069±0.013
20%	94.28±0.78	84.4±2.8	0.071±.029
30%	85.88±8.25	84.8±1.2	0.032±0.23

Table 5.3. Particle size and encapsulation efficiency data for SLNs loaded with curcumin at 10-30% w/w SA. Blank information is taken from [207].

	Curcumin		
Drug Loading	EE (%)	Size (nm)	PI
Blank	-	89.4±1.9	0.111±0.023
10%	74.62±5.05	79.4±0.5	0.078±0.051
20%	SLNs not formed		
30%			

5.3.2. DLS and TEM. The particle size of Dex-P loaded SLNs was shown to increase with higher drug loads as determined by DLS (Table 5.1). Analysis of the particle shape by TEM indicated that, at 10 and 20% loadings, SLNs retained a similar ellipsoidal shape to that observed with blank SLNs (Figure 5.3). However, both rod- and ellipsoidal-shaped particles were apparent in the SLNs with 30% Dex-P. The number and length of the rod-shaped particles differed from sample to sample.

SLNs loaded with 10% AP were similar in particle size to blank SLNs where loadings of 20 or 30% AP led to a slight reduction in particle size (Table 5.2). All drug loaded particles appeared similar in shape to blank SLNs (Figure 5.3). Inclusion of 10% curcumin led to a reduction in the particle size of SLNs by approximately 10 nm (Table 5.3). Particles also appeared slightly more spherical than blank SLNs (Figure 5.3).

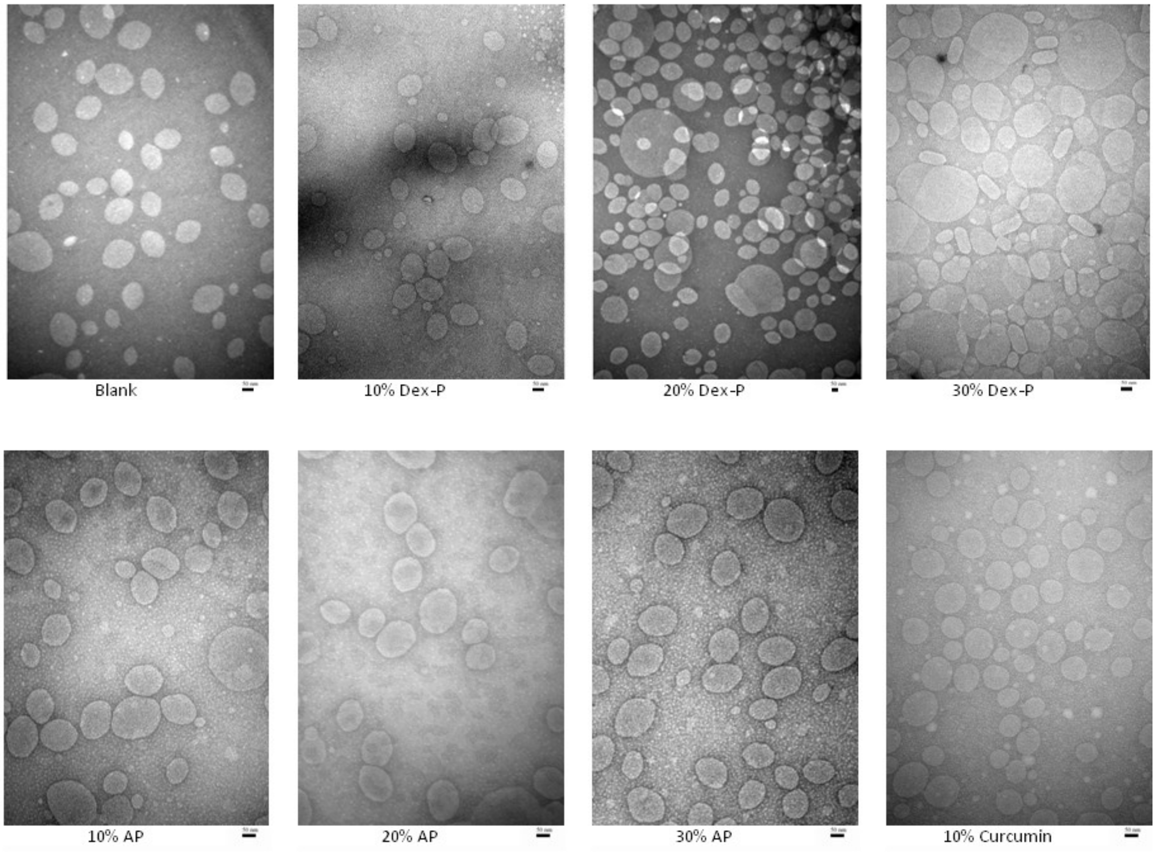

Figure 5.3. TEM images of SLNs loaded with Dex-P, AP, or curcumin in comparison with blank SLNs

5.3.3. NMR Spectroscopy. ^{1}H-NMR spectroscopy was previously used to confirm the core-shell structure of blank SLNs [207]. Comparison of the spectra of solubilized SLNs in $CDCl_3$ and intact SLNs in D_2O indicated that approximately 90.5% of the aliphatic chains of SLNs exist in the solid state with the remaining tightly adsorbed to the nanoparticle surface. Further, it was shown that essentially 100% of the added PEG is on the surface of SLNs in a flexible conformation. The ^{1}H-NMR spectra of all drug loaded SLNs in D_2O appeared similar; spectra for the Dex-P loaded SLNs are shown in Figure 5.4. For a quantifiable comparison, the ratio between the integral of the major aliphatic peak at 1.3 ppm and the PEG peak at 3.6 ppm was calculated for all samples. Results are shown in Table 5.4. Changes were minimal in comparison to blank SLNs. A slight increase was observed in AP loaded SLNs with increasing drug loading. Loading of 10 or 20% Dex-P also resulted in an increase, but 30% Dex-P resulted in a decrease. Since the PEG peak is expected to remain the same as blank SLNs, the ratio differences are likely a result of changes in the 1.3 ppm aliphatic peak. Drug-associated peaks were absent in all spectra, but this was primarily attributable to the low drug concentrations present.

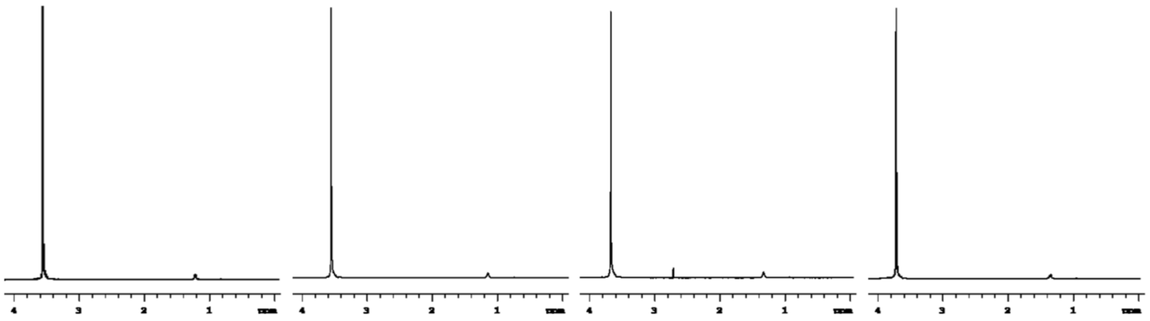

Blank 10% 20% 30%

Figure 5.4. ^{1}H-NMR spectra of Dex-P loaded SLNs in D_2O in comparison with that of blank SLNs. Spectra for AP and curcumin-loaded SLNs appeared similar.

Table 5.4. Comparison of the ^{1}H-NMR spectra of drug loaded SLNs with blank SLNs in D_2O. The 1.3 ppm aliphatic signal and 3.6 ppm PEG signal were integrated, and the 1.3 ppm/3.6 ppm ratio was calculated.

Sample	1.3 ppm/3.6 ppm
Blank	0.0868
10% Dex-P	0.1038
20% Dex-P	0.1012
30% Dex-P	0.0832
10% AP	0.0917
20% AP	0.1034
30% AP	0.1102
10% Curcumin	0.0823

5.3.4. DSC. In order to better understand the interactions occurring between the drugs and the SLN components, mixtures of each drug with the SLN matrix were prepared and thermal analysis was conducted using DSC. The blank SLN mixture exhibits three peaks in the DSC thermogram which were previously shown to be attributable to an SA-Brij® 78 eutectic (38.70±0.09°C), a separate SA phase (51.20±0.11°C), and a SA-PEG6000MS mixed phase (58.01±0.14°C) [207]. The thermograms for the mixtures containing drug were characterized by similar profiles, although transition temperatures were shifted in some cases (Figure 5.5). All three drugs caused a downward shift of the SA-Brij® 78 eutectic peak. However, whereas higher Dex-P and curcumin concentrations resulted in greater reductions in the melting temperature, the peak shift was relatively insensitive to AP concentration. The SA peak was shown to shift to lower temperatures with increasing Dex-P or AP concentrations; the change resulting from the addition of AP was larger than that of Dex-P. The addition of curcumin led to an increase in the melting temperature. The SA-PEG6000MS peak also showed a downward shift with all three drugs. The change was concentration-dependent with AP and curcumin but concentration-independent with Dex-P. A small left-hand shoulder was also present on the SA peak in all cases that was not present in the blank mixtures. This was likely a result of a certain proportion of the SA existing in the metastable β-form. Drug-associated peaks were difficult to discern in the Dex-P and AP samples. A very broad peak around 200°C was present in the mixtures containing curcumin.

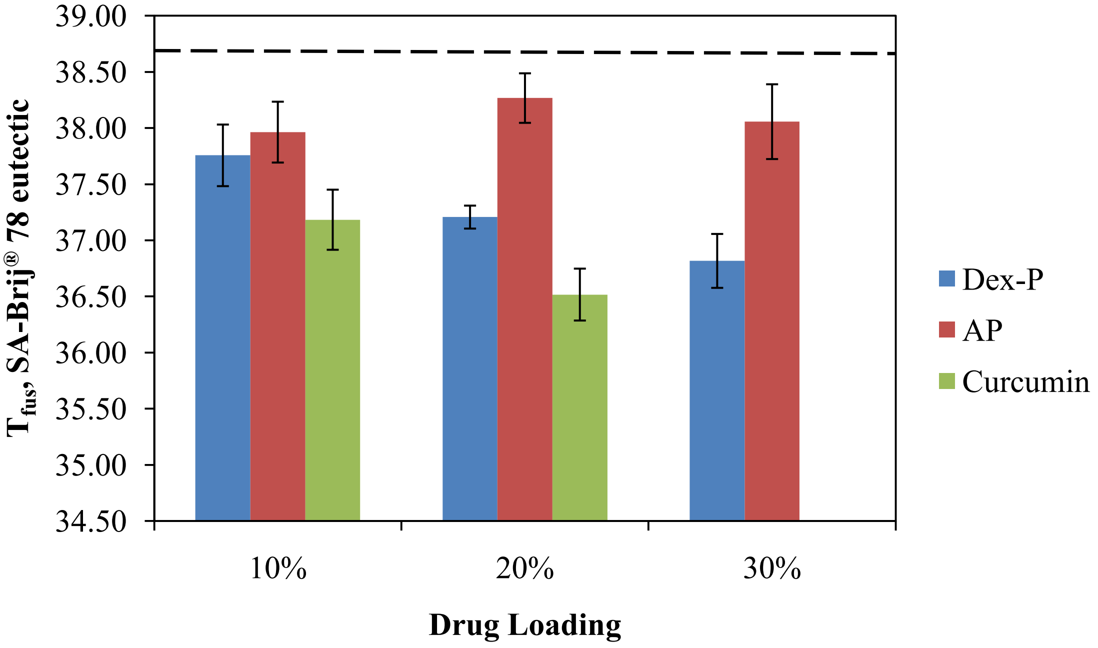
39.00
38.50
38.00
37.50
37.00
36.50
36.00
35.50
35.00
34.50
T_{fus}, SA-Brij® 78 eutectic
10%
20%
30%
Drug Loading
Dex-P
AP
Curcumin

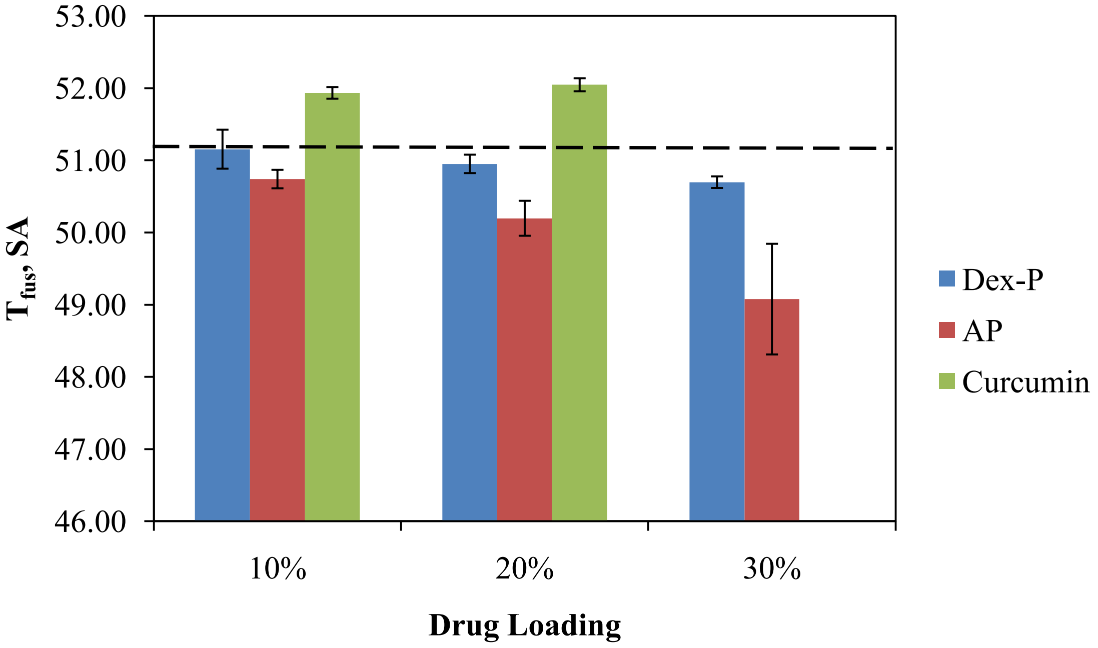
53.00
52.00
51.00
50.00
49.00
48.00
47.00
46.00
T_{fus}, SA
10%
20%
30%
Drug Loading
Dex-P
AP
Curcumin

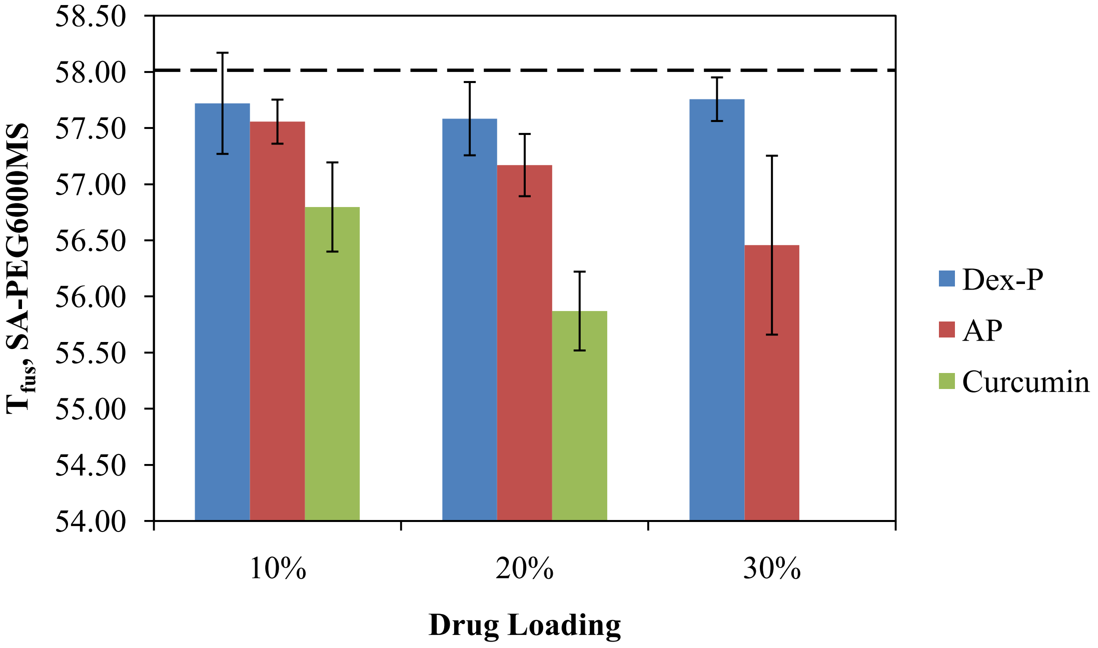

Figure 5.5. Analysis of drug containing mixtures by DSC. Results are separated by the three main peaks observed in the thermograms: SA-Brij® 78 eutectic, SA, and SA-PEG6000MS mixed phase. The peak maxima are given as the melting temperatures (T_{fus}), and the value associated with the blank mixtures is indicated by the dotted line.

5.3.5. Drug Release. Drug release profiles for Dex-P and curcumin loaded SLNs are shown in Figure 5.6. AP was shown to be unstable under the conditions of the study, and as such, drug release profiles for AP loaded SLNS could not be obtained. In both cases, release was characterized by a rapid initial phase followed by a slower secondary phase. The data could be fit using two-phase exponential decay curves: Dex-P, $y=0.1838e^{-0.3793x} + 0.8162e^{-0.003024x}$; Curcumin, $y=0.3918e^{-0.5349x} + 0.6082e^{-0.0234x}$. However, the release of curcumin was considerably faster than that of Dex-P in both phases. At 48 h, drug release of Dex-P was <30%, whereas with curcumin it was approximately 80%.

To determine the role diffusion of the drug across the dialysis membrane plays in limiting the analysis of drug release, studies were conducted using free drug. With both Dex-P and curcumin, drug was completely eliminated from within the dialysis tube by the 6 h time point. Single exponential decay curves could be used for fitting the data with the following results: Dex-P, $y=e^{-0.7832x}$; curcumin, $y=e^{-0.9510x}$ (Figure 5.6).

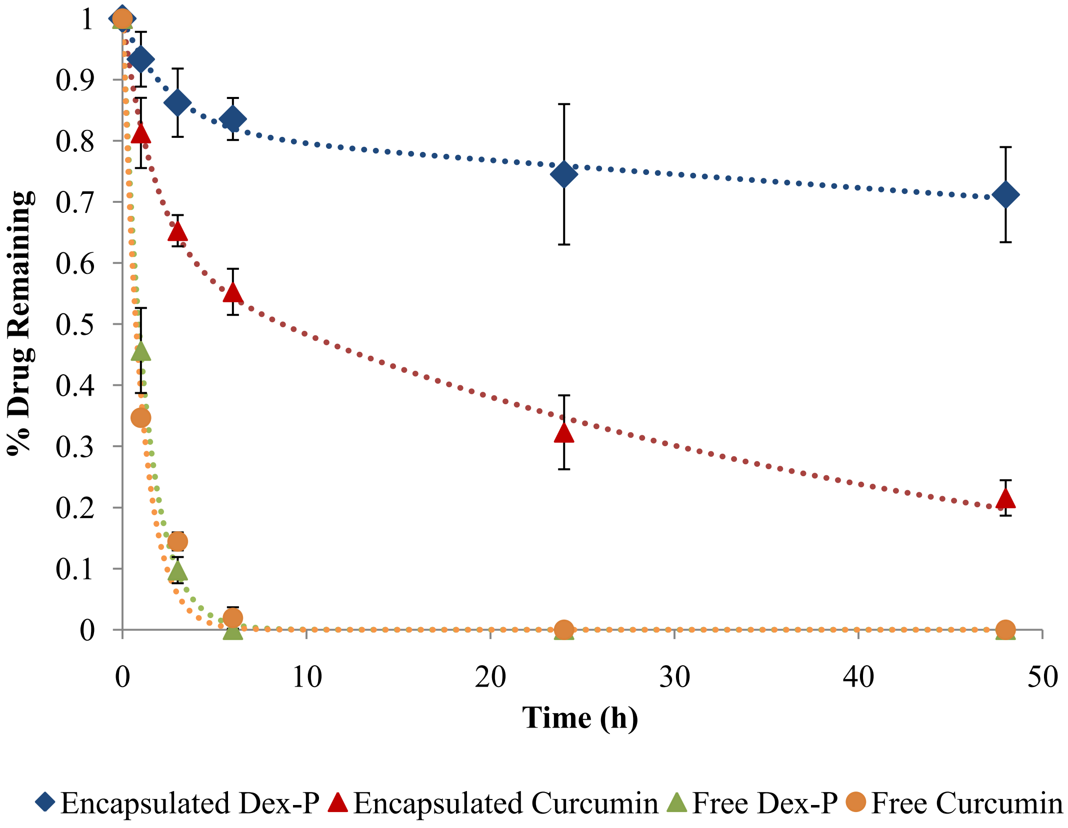

Figure 5.6. Drug release profiles for SLNs loaded with either 10% Dex-P or curcumin in comparison with diffusion of free drug across the dialysis membrane. The dotted lines represent the fit obtained using either one- or two-phase exponential decay equations: SLN-encapsulated Dex-P, $y=0.1838e^{-0.3793x} + 0.8162e^{-0.003024x}$; SLN-encapsulated Curcumin, $y=0.3918e^{-0.5349x} + 0.6082e^{-0.0234x}$; free Dex-P, $y=e^{-0.7832x}$; free curcumin, $y=e^{-0.9510x}$.

5.4. DISCUSSION

As SLNs have gained popularity as drug delivery systems, there has been increasing interest in understanding the parameters that control drug loading. While systematic studies have provided information on how the choice of lipids and surfactants as well as their concentrations may play a role in determining the extent and localization of drug loading, information on how the properties of the drug itself may affect loading remain limited. In this study, loading of Dex-P, the drug of interest, was compared with AP and curcumin. AP has a structure similar to Dex-P, but the ascorbate functionality is more hydrophilic than Dex. Curcumin is lipophilic but has no aliphatic chains that might be expected to align with the SLN lipids. In order to better understand how the drugs were loaded, the physicochemical properties of drug loaded SLNs (size, shape, and structure) and the interactions between the drugs and the SLN components were studied. Drug release from the SLNs was also monitored.

Dex-P could be loaded at 10-30% w/w SA with encapsulation efficiencies of >85%; precipitation was observed above this concentration. AP could be loaded at even higher concentrations; however, for comparative purposes, only the 10-30% drug loading data is presented. Encapsulation efficiencies for AP were also >85%. SLNs could not be prepared with curcumin loadings greater than 10%. The encapsulation efficiency was also lower (~75%) at this concentration.

Interestingly, though both Dex-P and AP exhibit high encapsulation efficiencies, SLNs loaded with these two drugs exhibit different properties. While AP loaded SLNs exhibit a particle size similar to or just smaller than blank SLNs, Dex-P loaded SLNs exhibit a concentration dependent increase in the particle size, though remaining in the size range appropriate for taking advantage of the EPR effect [29]. Particle shape appears similar to blank SLNs at all AP concentrations and at low Dex-P concentrations, but at the highest Dex-P loading (30%), a transition from ellipsoidal- to rod-shaped particles was observed. Based on the NMR studies, the overall solid core and PEGylated surface structure of the SLNs appeared to be maintained upon loading of either drug. Increases in the 1.3 ppm/3.6 ppm ratio are likely indicative of the drug inhibiting recrystallization of the lipid to the same extent as observed with blank SLNs and are to be expected. However, whereas this ratio increases in a concentration-dependent manner across the entire range of AP loadings, the addition of Dex-P increases the ratio only up to the 20% loading. Above this, the ratio is actually shifted lower than that observed with blank SLNs, echoing the transition in particle shape.

It was assumed that these differences may be attributable to how the drugs pack within the SLNs. By studying how the loading of drug affects the melting temperature of SLN component mixtures, information can be gained on drug-matrix interactions. Based on the previous modeling studies with Dex-P [129], it seems likely that this drug along with AP may reside at the interface of the solid core and PEG shell with the hydrophobic palmitate moiety anchoring the drug within the lipid phase. Evidence for this was provided in the DSC studies where the addition of Dex-P or AP was shown to decrease not only the melting temperature of the SA phase but also one of the SA-surfactant phases.

On the other hand, the fact that the two drugs predominantly impact the melting of different SA-surfactant phases may explain why the drug loaded SLNs exhibit such different properties. In the case of AP, there is a concentration-dependent decrease in the melting temperature of the SA-PEG6000MS mixed phase with little effect on the melting temperature of the SA-Brij® 78 eutectic. In contrast, the addition of Dex-P results in a concentration-dependent decrease in the melting temperature of the SA-Brij® 78 eutectic while only minimally affecting the SA-PEG6000MS phase. It is unknown why the drugs associate with the SLNs in such distinctly different manners but is likely attributable to the hydrophilicity and/or size of the parent drugs.

In contrast to both Dex-P and AP, SLNs could not be formed with curcumin loadings >10%, and encapsulation efficiency was lower at this concentration. Though ^{1}H-NMR spectroscopy indicated that the core-shell structure was maintained, the particle size was reduced by approximately 10 nm as compared to blank SLNs. Further, the particles took on a more spherical shape than blank SLNs, indicating a possible third drug packing mechanism.

In analyzing the DSC results, it appears that curcumin's interactions with SA are negligible. There was actually a slight increase in the SA melting point instead of the decrease observed with Dex-P and AP. Instead, large downward shifts in the melting temperatures of both SA-surfactant phases were observed. Based on the apparent interactions with both SA-surfactant phases, it may be tempting to conclude that curcumin resides within the PEG shell. However, caution must be used in making this conclusion. It is possible that curcumin resides within the interfacial region similarly to the Dex and ascorbic acid functionalities but lacks the aliphatic chain that extends into the lipid core of the particle.

As a final comparison, drug release from the Dex-P and curcumin loaded SLNs was evaluated; AP was unstable under the conditions of the study. Both drug release profiles appeared biphasic, demonstrating a burst release within the first 3-6 h of the study followed by a slower release over the remaining time period. The burst release may be due to an initial rapid diffusion of surface-associated drug from the SLNs, while the sustained release may be attributable to drug lost through a particle erosion mechanism. This corresponds with the assumed growth due to Ostwald ripening, which relies on the exchange of nanoparticle components. Yet, notably, release of curcumin was faster than Dex-P in both phases. Whereas nearly 80% of the encapsulated Dex-P remains associated with the nanoparticles following the 48 h time period, approximately 80% of the curcumin was found to be released. This difference was not associated with the time necessary for the drug to diffuse out of the dialysis membrane, as both drugs were eliminated from the internal compartment within 6 h. This data is in line with curcumin residing within the PEG interfacial region but not being anchored within the solid particle core as is assumed to be the case with Dex-P (and AP).

5.5. CONCLUSIONS

Overall, it appears that Dex-P loaded SLNs can be prepared with high drug loading and encapsulation efficiency while maintaining a suitable particle size, shape, and structure.

However, due to the presence of multiple particle populations with higher drug concentrations, a loading of 10% w/w SA will be used for further studies. Interestingly, comparison with AP and curcumin indicated that all three drugs showed different loading capacities and mechanisms. Release of Dex-P was shown to be slower than that of curcumin, and higher encapsulation efficiencies were achieved for both palmitate prodrugs than curcumin despite the fact that all three drugs likely reside at the core-shell interface. This was attributed to the ability of the hydrophobic side chains of Dex-P and AP to anchor the drugs within solid lipid core of the particles. Yet, even with Dex-P and AP, differences in the mechanism of drug packing were observed with corresponding changes in the properties of the SLNs.

Chapter 6

Solid Lipid Nanoparticle Stability in Human Plasma

6.1. INTRODUCTION*

Preliminary results with Dex-P loaded SLNs indicated a dependence of drug release on the CE activity of the surrounding media (Figure 6.1) [37]. In this study, nanoparticles were diluted 1:14 with 10% media in PBS and incubated at 37°C. At certain time points, samples were subjected to ultrafiltration, and filtrates were assayed for drug concentration (in the form of either Dex-P or Dex). In mouse plasma with high CE activity [208], drug release was rapid, reaching nearly 100% within 24 h. All drug assayed in the filtrates was found to be in the form of Dex, indicating that cleavage had occurred. Alternatively, in media with negligible CE activity (human plasma [208], denatured mouse plasma, mouse plasma treated with BNPP), nearly all drug was retained in the retentate and found to be in the form of Dex-P. Drug release was intermediate between these two in rat plasma, corresponding well with reported values for CE activity in rat plasma as compared to mouse or human plasma [208].

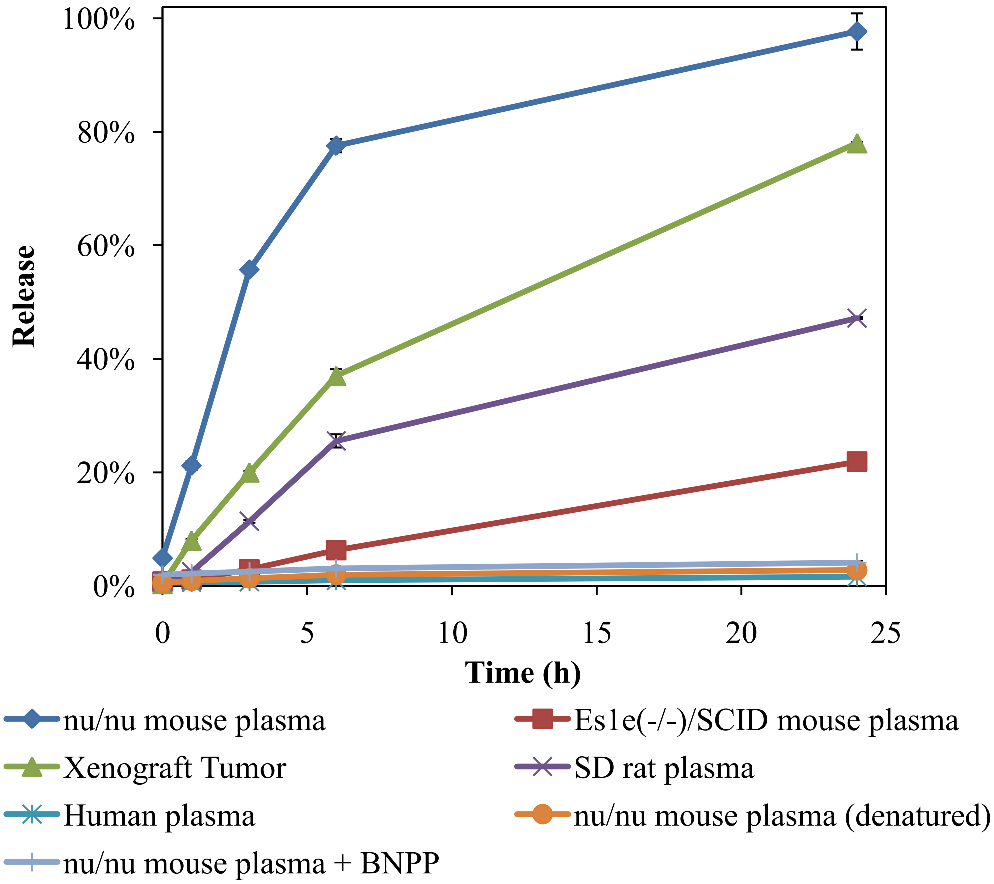

Figure 6.1. Dependence of drug release on CE activity of the surrounding environment over a 24 h incubation at 37°C (n=3). Adapted from [37]*

If drug release was in fact triggered by CE, it presented both some interesting challenges and possibilities. Because of the difference in CE activity between human plasma and plasma of typical small animal models (mice and rats), testing this drug delivery system *in vivo* may be problematic as results obtained would likely not be representative of what would be observed in humans. Carboxylesterase-deficient Es1e(-/-)/SCID mice were considered as a potential alternative. Although drug release remained higher than that seen with human plasma (Figure 6.1), it was closer than that observed with mice or rats, indicating that these animals may serve as a model more closely representative of the human situation. On the other hand, this enzymatically-triggered drug release may provide a mechanism for controlling drug release at the tumor site based on the higher CE activity levels found in human tumors than in human plasma [209, 210]. Drug may remain stably entrapped in SLNs while in circulation and then be triggered to rapidly release upon extravasation into tumors. To test this, drug release was tested in A549 human tumor xenografts that were removed from mice and homogenized (Figure 6.1). Approximately 78% of the drug was released within 24 h, and again, nearly all was in the form of Dex. To determine if any of this release was attributable to mouse plasma remaining in the homogenate, an additional study was performed using an A549 cell lysate. Release was similar at 24 h (Figure 6.2), confirming that drug release may be accelerated in human tumors over human plasma.

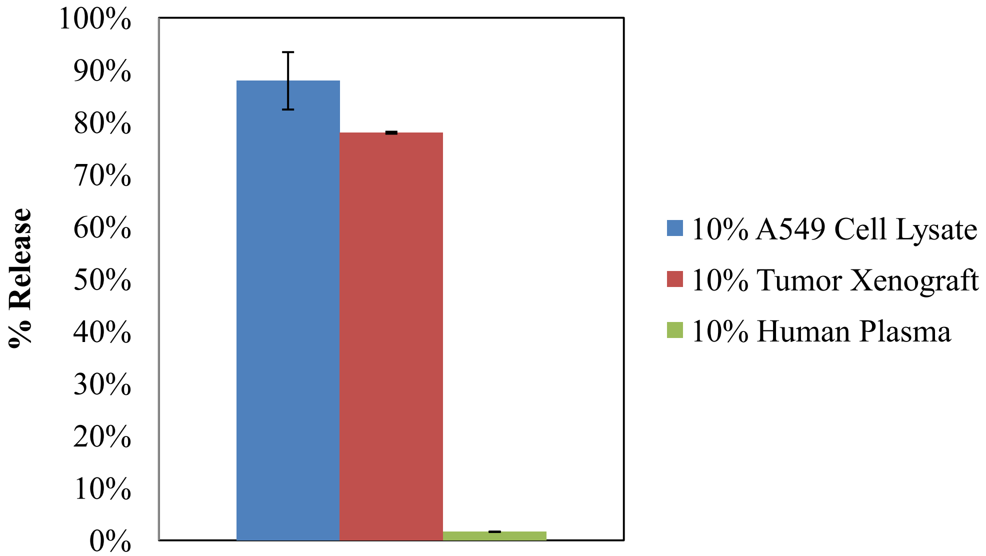

Figure 6.2. Accelerated drug release from SLNs incubated at 37°C for 24 h in homogenized human tumor xenografts or human tumor cell lysates as compared to human plasma (n=3). Adapted from [37]*

However, the caveat to this study was that it was difficult to differentiate between drug retained in SLNs and drug associated with plasma proteins. It was considered possible that Dex-P was "released" from the SLNs (either due to partitioning out of the SLNs or to general SLN instability) but remained associated with plasma proteins that would prevent its filtration. Enzymatic cleavage may then take place at the protein surface, generating free Dex that may be filtered. This is shown schematically in Figure 6.3. As such, it was important to show 1) that the SLNs remained intact and 2) that Dex-P remained stably associated with the SLNs in conditions mimicking human plasma in order to confirm the CE-dependent drug release.

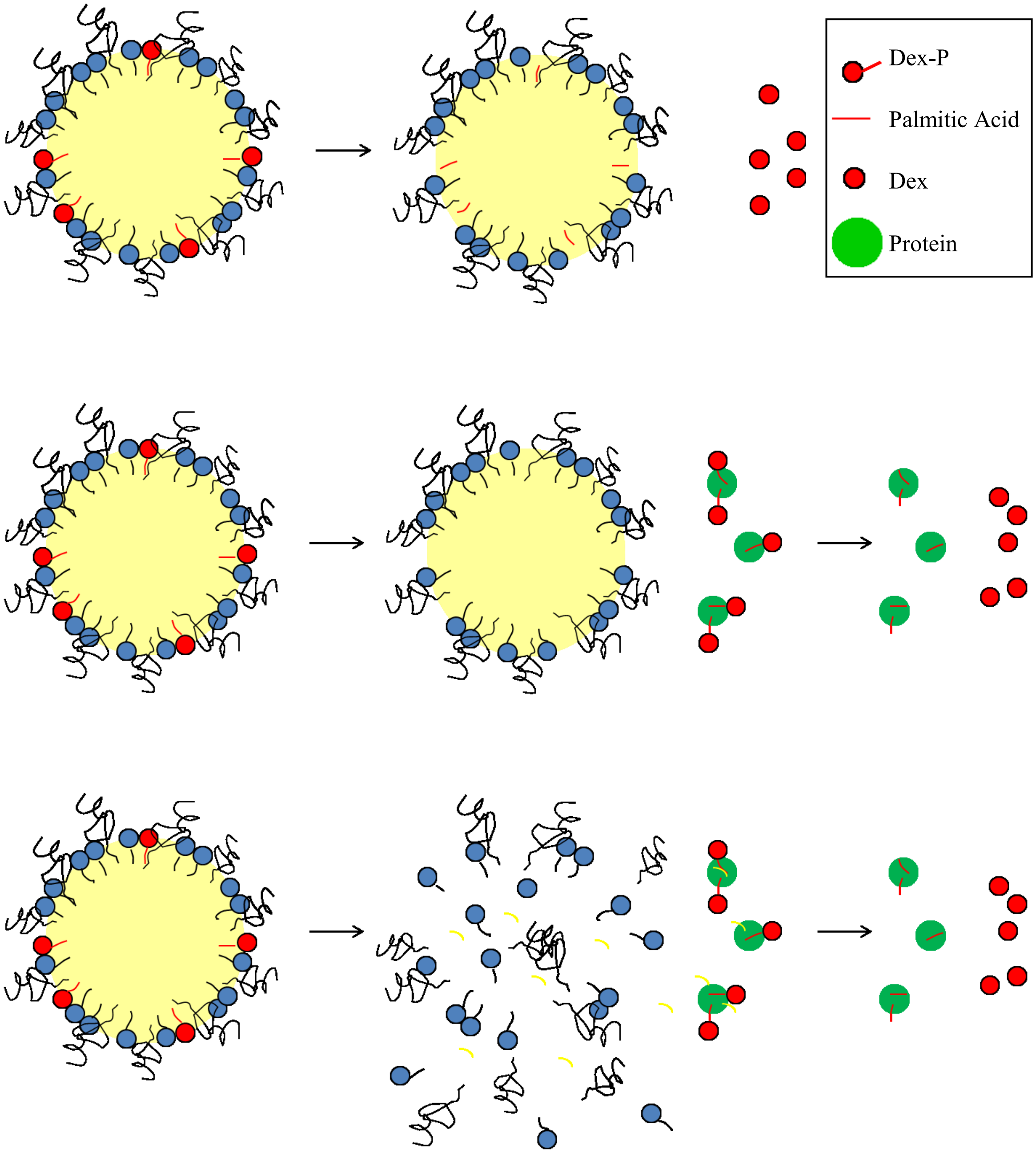

Figure 6.3. Potential mechanisms of drug release from SLNs. Top: Dex is enzymatically cleaved from surface of SLNs. Middle: Dex-P partitions out of intact SLNs onto plasma proteins prior to enzymatic cleavage. Bottom: SLNs are unstable in the presence of plasma proteins, leading to adsorption of Dex-P onto the surface of plasma proteins prior to enzymatic cleavage.

6.2. MATERIALS AND METHODS

6.2.1. Materials. SA was from Spectrum Chemicals and Laboratory Products (Gardena, CA). PS and Brij® 78 were products of Uniqema (Chicago, IL). PEG6000MS was a gift from Stepan (Northfield, IL). Tritiated dexamethasone [6,7-^{3}H(N)] (specific activity = 35-50 Ci/mmol) was purchased from American Radiolabeled Chemicals (Saint Louis, MO). PBS was obtained from Invitrogen (San Diego, CA). Centrifugal filter devices (Microcon YM-10) were purchased from Millipore (Billerica, MA). Human plasma containing sodium heparin as the anticoagulant was purchased from Innovative Research, Inc. (Novi, MI). HSA (96-99%) was a product of Sigma-Aldrich (St. Louis, MO). Liquid scintillation cocktail (Optiphase HiSafe3) was purchased from PerkinElmer (Waltham, MA).

6.2.2. Synthesis of Dex-P. Dex-P was prepared as previously described [35]. Briefly, 300 mg Dex was dissolved in 12 mL pyridine. Palmitoyl chloride (578 mg) was added dropwise to this solution. The mixture was stirred in the dark under nitrogen for 24 h. The solvent was removed by nitrogen, and the product was dissolved in dichloromethane for loading onto a 30 mL silica gel column. A dichloromethane to dichloromethane:ethyl acetate (6:4 v/v) gradient was used to elute the purified product. The reaction progress was monitored using silica gel TLC with a chloroform:ethyl acetate (7:3) mobile phase. Retention factor values were 0.10 and 0.69, for Dex and Dex-P, respectively. For the preparation of radiolabeled Dex-P, ^{3}H-Dex was used in place of Dex.

6.2.3. SLN Preparation. SLNs were prepared using the nanotemplate engineering technique as reported previously [131]. Basically, the process consisted of three steps: 1) melting an appropriate mixture of lipids and surfactants (and drug in the case of drug-loaded SLNs), 2) adding PBS to generate an oil-in-water microemulsion, and 3) cooling the microemulsion to room temperature in order to generate the SLNs. Blank SLNs with a formulation of 1.6 mg/mL SA, 0.4 mg/mL PS60, 2.8 mg/mL Brij® 78, and 3.0 mg/mL PEG6000MS were used for particle size, shape, and turbidity analyses. A second formulation (2.0 mg/mL SA, 0.5 mg/mL PS60, 3.5 mg/mL Brij® 78, 3.5 mg/mL PEG6000MS, and 0.2 mg/mL Dex-P/^{3}H-Dex-P) was used for the SEC studies and for the evaluation of the stability of the Dex-P association with SLNs.

6.2.4. SLN Stability – Physiological Temperature and pH

6.2.4.1. Temperature Effect. Samples were incubated at either 4°C or 37°C. At each time point (0, 1, 3, 6, and 24 h), 30 µL were removed and diluted to 1 mL with 0.2 µm filtered water. Particle size analysis was performed in triplicate at 25°C on a Delsa™ Nano Zeta Potential and Submicrometer Particle Size Analyzer (Beckman Coulter Inc., Brea, CA). Following the final time point, samples were collected for TEM imaging. One drop (~7 µL) of a SLN suspension was incubated for 1.5 min on a carbon-coated TEM grid. The grid was then dried and stained (0.2 µm filtered 2% uranyl acetate) for an additional 1.5 min. Excess stain was removed, and the grid was allowed to dry for 5 min. Images were obtained using a Philips Tecnai Biotwin 12 equipped with a Gatan ES 1000W CCD digital camera (FEI, Hillsboro, OR).

Three samples were analyzed per temperature, and a minimum of five images were taken per sample at different locations on the grid. Images were analyzed using ImageJ [164]. The lengths of both the major and minor axes were obtained using the manual analytical tools. Assuming a prolate spheroid shape for the ellipsoid where the minor axis is the same in the x and y directions, the volume of an ellipsoid with these dimensions was calculated using the following equation:

$$\mathrm{Volume} = \frac{4}{3}\pi r_{\mathrm{major}} r_{\mathrm{minor}}^{2}$$

where r is the radius of the relevant axis. Using this value as the volume of an equivalent sphere, the approximate particle diameter was calculated:

$$\mathrm{Diameter} = \left[\left(\frac{V}{\frac{4}{3}\pi}\right)^{\frac{1}{3}}\right]^{2}$$

In order to apply a quantitative measurement to the particle shape analysis, the aspect ratio for the particles was calculated by dividing the length of the major axis by that of the minor axis. These calculations were performed for 20 particles per image, giving a total of 100 measurements per sample. The average measurement for each sample was used in calculating the average and standard deviation for particles stored at each temperature. The PSD was also calculated using the following equation:

$$\sqrt{\mathrm{PSD}^{2}} = \sqrt{\frac{\sum_{i=1}^{k}((n_i - 1)s_i^{2})}{\sum_{i=1}^{k}(n_i - 1)}}$$

where s_i represents the standard deviations obtained from each individual sample of 100 particles, n_i represents the sample size (i.e., 100 for all 3 samples), and k represents the number of samples (i.e., 3). This differs from the standard deviation calculated above which represents the variability in the average size obtained from the three samples and is used primarily as a measurement of the homogeneity of the size distribution (comparable to the PI values obtained by DLS).

6.2.4.2. Size Recovery. SLNs were incubated at 37°C for 24 h. Following a return to refrigerated (4°C) conditions, samples were removed for measurement of the particle size at 0, 1, 3, 6, 25, 50, and 168 h. DLS analysis was performed as described above (n=3).

6.2.4.3. Concentration Effect. SLNs were diluted 10-fold or 30-fold with PBS. These SLNs along with SLNs at the original prepared concentration were incubated at 37°C for 24 h. DLS particle size measurements were performed at 0, 1, 3, 6, and 24 h (n=3). For consistency among the samples, all samples were diluted with PBS as necessary to achieve a 30-fold dilution from the original concentration prior to analysis.

6.2.5. SLN Stability – Human Plasma Proteins

6.2.5.1. Size and Shape of SLNs in Human Plasma. SLNs were diluted 1:14 (v/v) with a 10% human plasma solution in PBS. Following incubation at 37°C, 30 μL were removed and diluted to 1 mL with 0.2 μm filtered water for particle size analysis by DLS. TEM images were obtained after a 24 h incubation, using similar methods to those described above with the exception of an additional 5-fold dilution with water prior to grid preparation.

6.2.5.2. Size and Turbidity of SLNs with HSA. To replicate a 10% human plasma solution, HSA was dissolved in PBS at a concentration of 5 mg/mL. SLNs with and without HSA were incubated at 37°C with shaking at 100 rpm. At each time point (0, 1, 3, 6, and 24 h), 500 μL aliquots were removed. Four hundred and seventy microliters were used in assessing the turbidity [determined by the absorbance of the suspensions at 350 nm as measured by a Beckman DU 7500i Spectrophotometer (Beckman Coulter Inc., Brea, CA)] (n=3). The remaining 30 μL were diluted to 1 mL using 0.2 μm filtered water, and DLS particle size measurements were obtained as described above (n=3).

6.2.5.3. SEC of SLNs with HSA. A Shimadzu Prominence Ultra Fast Liquid Chromatography (UFLC) system equipped with a gel filtration-HPLC column, TSK-GEL G 3000 SW (7.5 mm i.d. x 30 cm) and coupled to a diode array detector was employed to separate SLNs from HSA. SLNs were mixed 1:1 with a 10 mg/mL HSA solution in PBS and incubated at 37°C for 2 h. The mixture at time 0 and 2 h, HSA solution (2x diluted with PBS), and SLNs (2x diluted with PBS) were injected onto the column with an injection volume of 20 μL. The elution was monitored at 280 nm (HSA λ_{max}).

6.2.6. Stability of Dex-P Association with SLNs. All radioactivity measurements were performed using a Tri-Carb liquid scintillation counter (LSC; PerkinElmer). For the determination of the protein binding of Dex-P in human plasma, 0.5 mg Dex-P/^{3}H-Dex-P were mixed with 2 mL of human plasma and incubated at 37°C for 24 h (n=2). The mixture was filtered through a 0.2 μm filter (referred to as MF filtrate), and 100 μL of each MF filtrate was measured for radioactivity. An additional 300 μL of each MF filtrate were ultrafiltered, and 50 μL of the UF filtrate measured for radioactivity. Using this data, the percentage of free drug in human plasma was calculated; this is referred to as the protein unbound ratio. Binding of Dex-P to the ultrafiltration membrane under these conditions was determined by collecting 200 μL of the UF filtrate and refiltering it through a new membrane. One hundred microliters of the second filtrate were assayed for radioactivity. The loss of radioactivity in the second UF filtrate as compared to the first was considered due to the binding of the drug to the membrane.

^{3}H-Dex-P labeled SLNs were mixed with 50% human plasma (1:14 dilution, v/v) and filtered through a 0.2 μm filter. The loss of radioactivity at this stage was assumed to be due to the precipitation of any drug aggregates. Two hundred microliters of the MF filtrate were then ultrafiltered as described above, and the UF filtrate was analyzed for radioactivity. The percent Dex-P associated with the SLNs (% SLN associated) was calculated using the equation:

$$\text{\% SLN associated} = \text{\% in MF filtrate} - \frac{\text{\% in UF filtrate}}{\text{protein unbound ratio}}$$

This process was repeated following either a 2 or 24 h incubation at 37°C, and comparisons were made with SLNs in PBS alone.

6.2.7. Statistical Analysis. All data is presented as the mean ± SD of three independent measurements. For comparison of two samples, t-tests (paired two sample for means) were used. Groups of 3 or more were compared using analysis of variance (ANOVA) one-way test with SigmaStat 3.5 software (Systat Inc., San Jose, CA). Differences were considered statistically significant when P<0.05, and the Holm-Sidak method was used to perform pairwise multiple comparisons on significant effects and interactions.

6.3. RESULTS AND DISCUSSION**

6.3.1. SLN Stability – Physiological Temperature and pH. The initial studies in this section were focused on evaluating the stability of the SLNs. Although the Dex-P release study discussed in the previous chapter indicated that SLNs likely remained intact in the presence of physiological temperature and pHs, further studies were conducted to evaluate size and shape changes. SLNs prepared in PBS were initially monitored for time- and temperature-dependent changes in size and shape. As determined by DLS, SLNs incubated at 37°C were shown to increase in size by approximately 40 nm within a 24 h time period, whereas the particle size of SLNs stored at 4°C remained approximately the same (Figure 6.4).

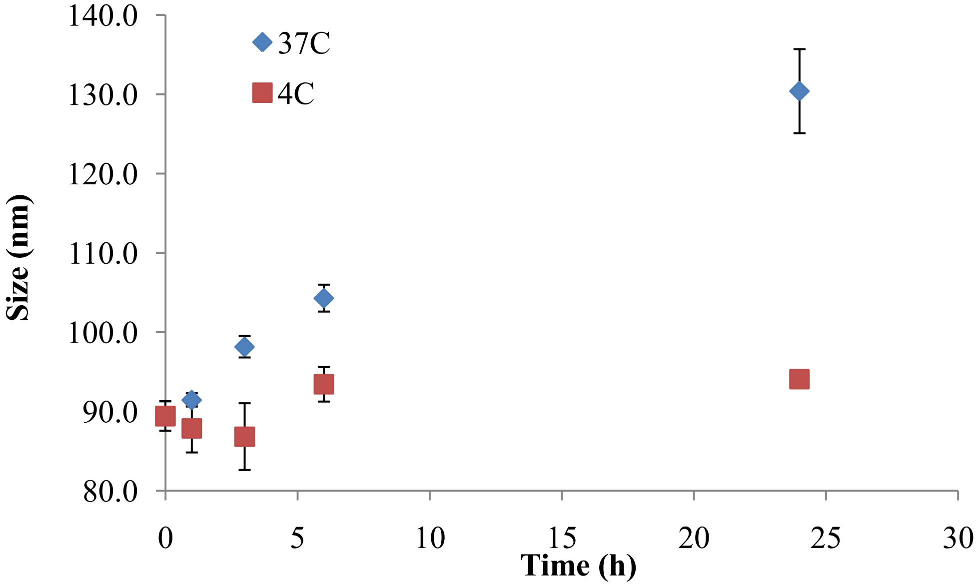

Figure 6.4. Time- and temperature-dependent growth of SLNs (n=3)

SLNs stored at either 4°C or 37°C for 24 h were also analyzed by TEM. Visually, the SLNs appeared to be similar in shape, and there was no significant difference ($P>0.05$) in the calculated aspect ratios. Particle size results obtained using this method were consistent with the DLS results, again showing a difference of approximately 40 nm between SLNs at 4°C and 37°C (Figure 6.5, Table 6.1). As in the previous chapter, the actual values obtained using TEM were slightly larger than those obtained with DLS. This may be attributable to the assumption of spherical particles inherent in the DLS calculations. Overall, no evidence for disassociation of the SLNs was observed, and the particles remained within the size range (<200 nm) deemed suitable for tumor-targeting via the EPR effect [29].

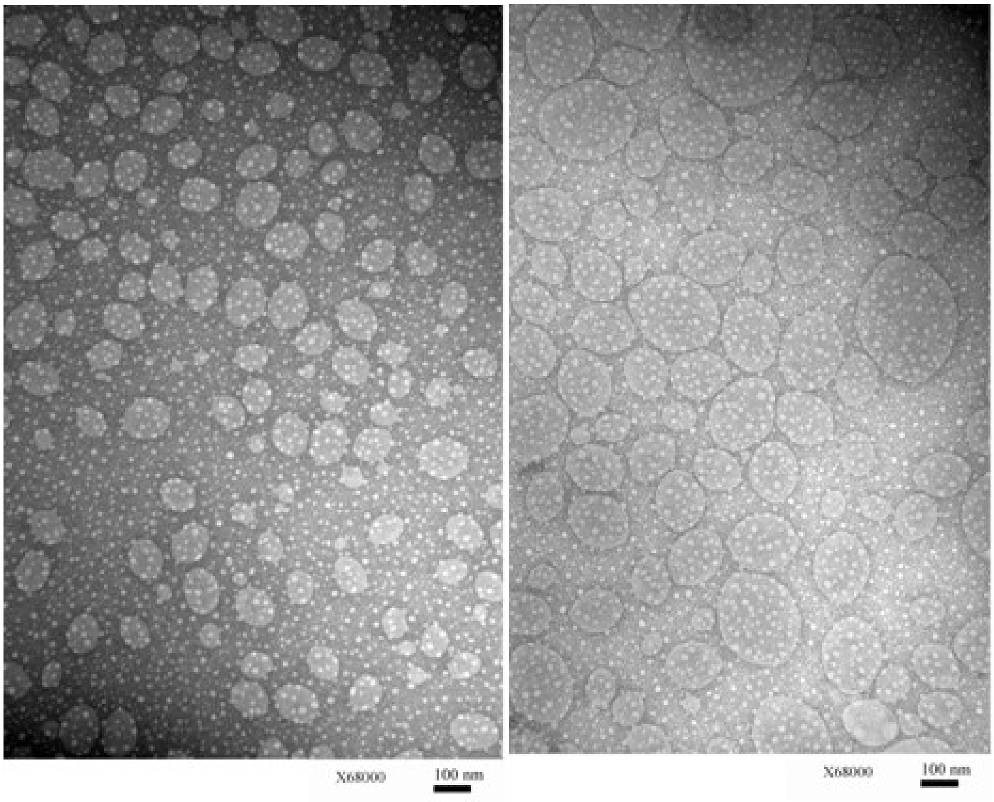

Figure 6.5. TEM images of SLNs stored for 24 h at either 4°C (left) or 37°C (right)

Table 6.1. Particle size, PSD, and aspect ratio of SLNs stored at either 4°C or 37°C for 24 h as calculated from analysis of TEM images (n=3)

Temperature (°C)	Particle Size (nm)	PSD (nm)	Aspect Ratio
4	92.9±3.7	16.4	1.30±0.02
37	131.8±5.0	43.7	1.29±0.02

Additional studies were focused on elucidating the mechanism of particle size growth. As an initial test, SLNs were returned to 4°C following a 24 h incubation at 37°C and monitored for size changes. Over a seven day period, SLNs did not exhibit any size recovery, indicating that growth was not attributable to any temperature-dependent swelling process (Figure 6.6).

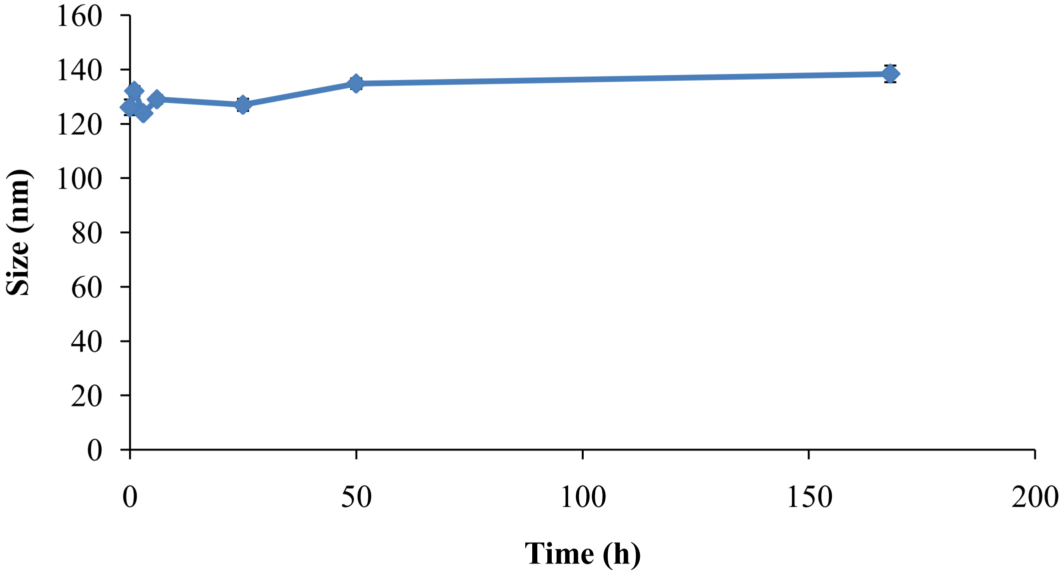

Figure 6.6. Particle size of SLNs stored at 4°C following a 24 h incubation at 37°C (n=3)

Further studies were focused on evaluating the particles for Ostwald ripening, a process whereby larger particles grow at the expense of smaller ones and which has previously been used to explain growth of SLNs [33]. The driving force is the higher surface energy and correspondingly higher solubility of the smaller particles in comparison to larger particles, as described by the Kelvin equation [211]. Small particles dissolve, generating a supersaturated solution with respect to the large particles, and the dissolved species then redeposit on the surfaces of larger particles. To test this theory, the data was fit using appropriate equations describing Ostwald ripening. The process can be divided into two steps: 1) diffusion of the solute molecules and 2) interface-controlled growth (detachment/attachment of the solute molecules to and from the particle surface) [212]. Interface-controlled growth can occur through continuous growth, surface nucleation, or spiral growth. The process can be rate-limited by either step. In the case of diffusion-controlled growth or interface-controlled growth occurring through continuous or spinal growth, the data can be fit using

$$\mathrm{d^n - d_0^n = kt}$$

where d is the average diameter at time t, d_0 is the average diameter at time t=0, and k is the growth rate. For diffusion- and spiral growth-controlled processes, the exponent n is 3, whereas for continous growth processes, the exponent n is 2 [213, 214]. In the case of surface nucleation, growth can best be fit using a logarithmic dependence on time:

$$\mathrm{d - d_0 = k \log\left(1 + \frac{t}{\tau}\right)}$$

where τ is a time constant [213]. For our system, the data was non-linear when plotted against the log time (Figure 6.7), confirming that, within this time range, growth is not likely controlled by surface nucleation. Plots of the cube and square of the mean diameter versus time were both, however, reasonably linear (Figure 6.7), preventing a conclusive determination of the growth mechanism.

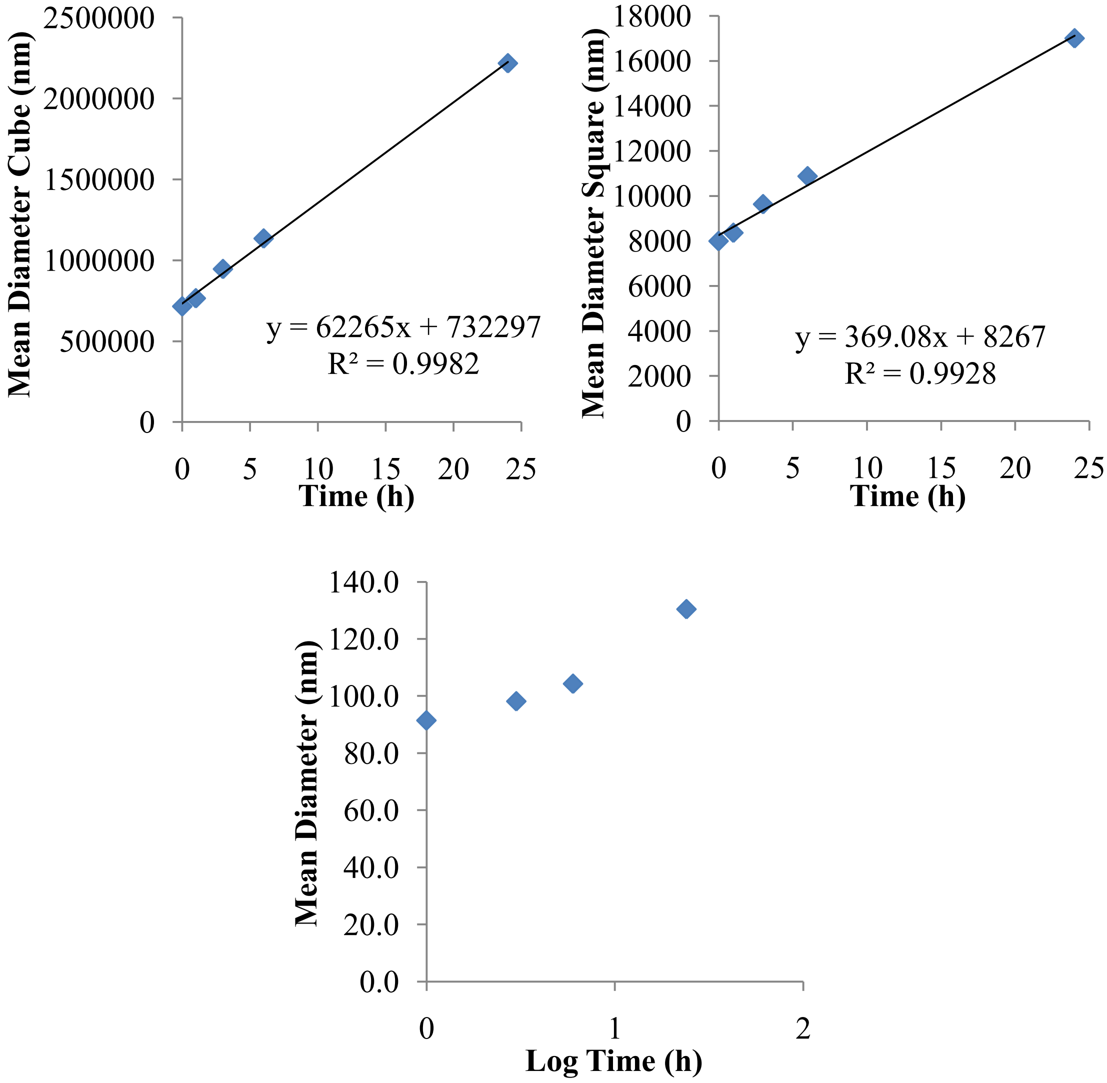

Figure 6.7. SLN 37°C growth profiles plotted as the cube of the mean diameter versus time (top left), the square of the mean diameter versus time (top right), and the diameter plotted versus the log time (bottom)

To differentiate between the two, an additional study evaluating the effect of particle concentration on growth was performed. Dilution of SLNs led to smaller particle size increases when SLNs were incubated at 37°C (Figure 6.8), corresponding with dissolution-mediated growth. However, it may be that both processes are involved or that the mechanism changes over time. It is also notable that because the various components of the SLNs are characterized by different solubilities, they may also display different rates of exchange. This may lead to particles having different compositions following growth than they did initially, though it is difficult to prove this experimentally.

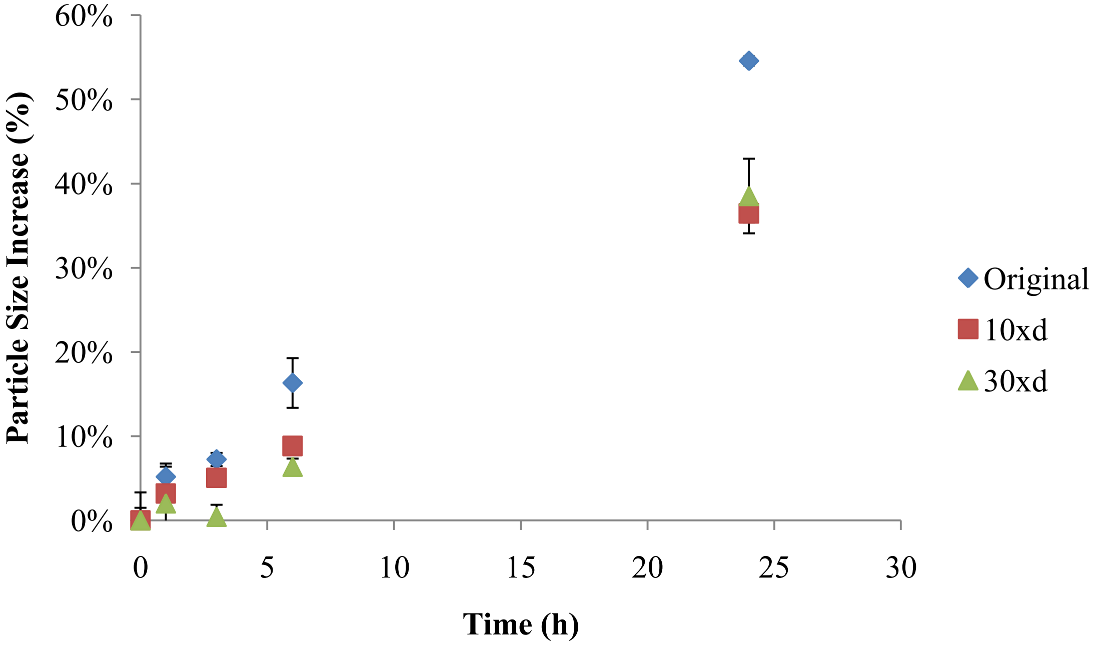

Figure 6.8. Effect of concentration on particle size growth at 37°C (n=3)

6.3.2. SLN Stability – Human Plasma Proteins. SLNs were next evaluated for their stability in the presence of human plasma proteins (excepting CE). Following incubation with 10% human plasma in PBS, SLNs were analyzed by DLS and TEM. Unfortunately, the presence of the plasma proteins obscured the SLN peak in the DLS data. SLNs appeared to remain intact in the presence of the plasma as determined by TEM imaging (Figure 6.9), but the background resulting from plasma components prevented a conclusive analysis.

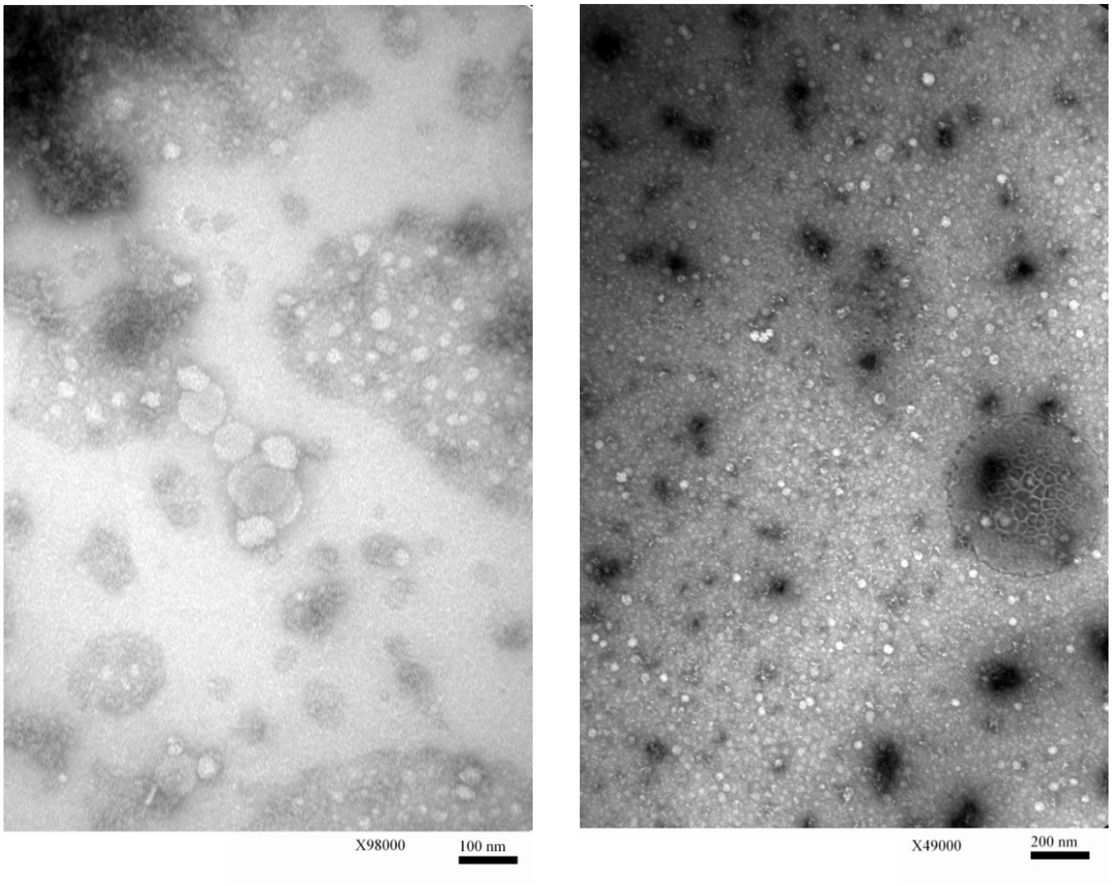

Figure 6.9. TEM images of 10% human plasma with (left) and without (right) SLNs

For this reason, further studies were conducted with HSA as representative of human plasma. The particle size growth profiles of SLNs incubated with and without 10% HSA were similar across a 24 h study (Figure 6.10), indicating that particles were remaining intact without aggregation in the presence of the protein. Only a slight increase in the particle size of SLNs incubated with the protein over that of SLNs alone was observed at the final time point, which may be attributable to some protein adsorption on the particle surface.

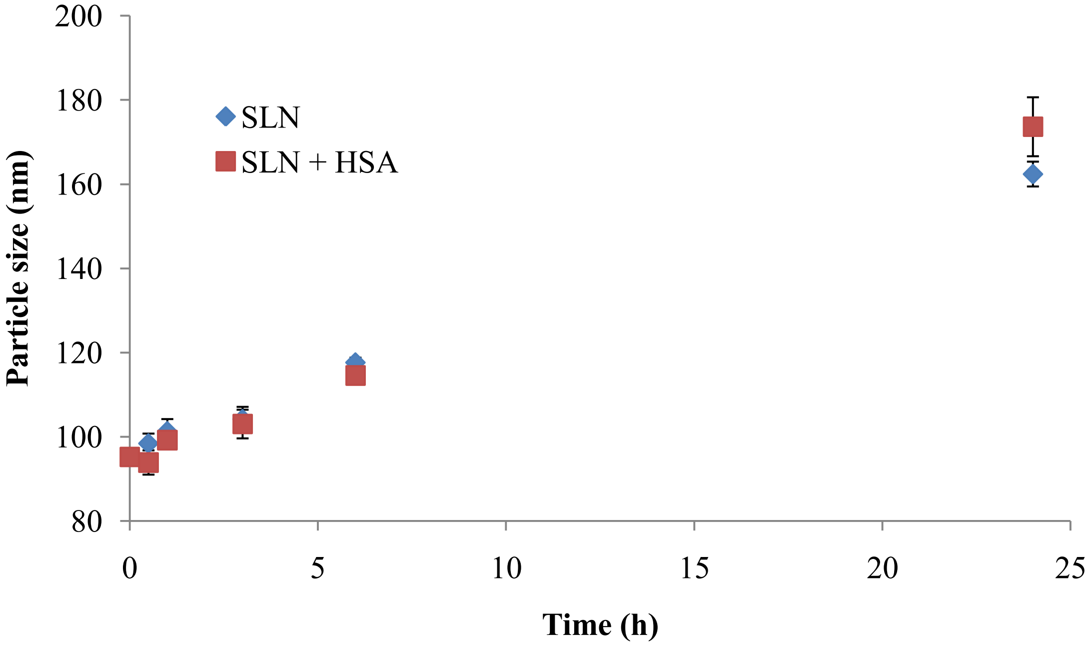

Figure 6.10. Particle size of SLNs incubated at 37°C with or without 10% HSA as a function of time (n=3)

The turbidity of SLN suspensions was assessed as a second measure of stability. Large turbidity increases would be expected with particle aggregation or disassociation (due to the insolubility of the lipid phase). Instead, both SLNs incubated with and without 10% HSA displayed only minor increases in turbidity over the time period of the study (Figure 6.11), which could be attributed to the normal particle size growth. Finally, SLNs of a similar formulation were incubated with HSA and analyzed by SEC. SLNs were eluted at 11.2 min, while HSA came off the column later at 15.5 min (dimer) and 17.5 min (monomer). Following the initial mixing of SLNs with HSA, the two components eluted similarly to their individual SEC profiles (Figure 6.12). After a 2 h incubation at 37°C, the SLN peak area was increased slightly from that observed before incubation ($P<0.05$). This was likely a result of protein adsorption. However, the amount of HSA associated with SLNs was so low that no HSA loss was identified on the basis of the HSA peak size. Overall, no evidence was seen for SLN instability in the presence of the representative plasma protein.

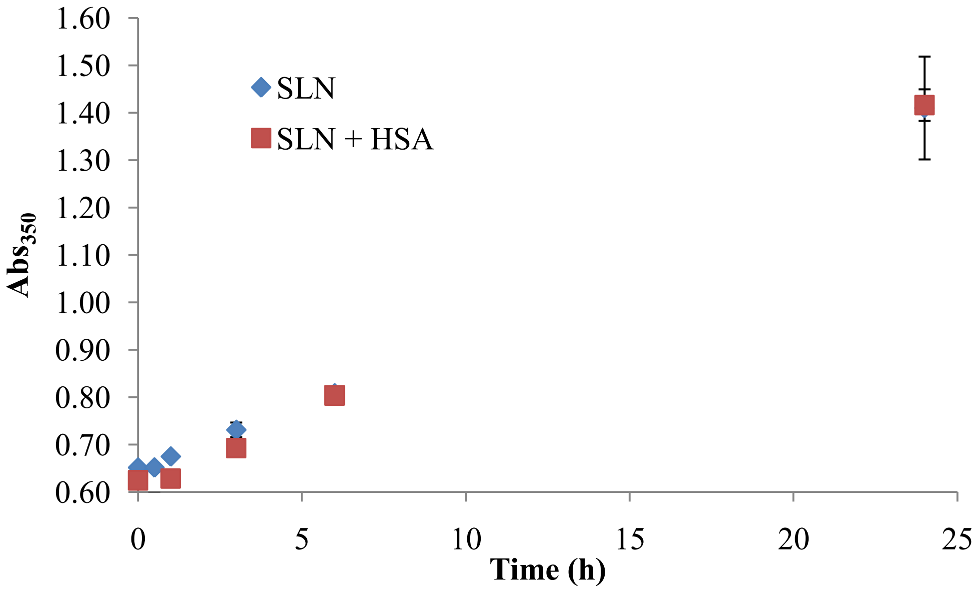

Figure 6.11. Turbidity of SLNs (as measured by the absorbance at 350 nm) incubated at 37°C with or without 10% HSA as a function of time (n=3)

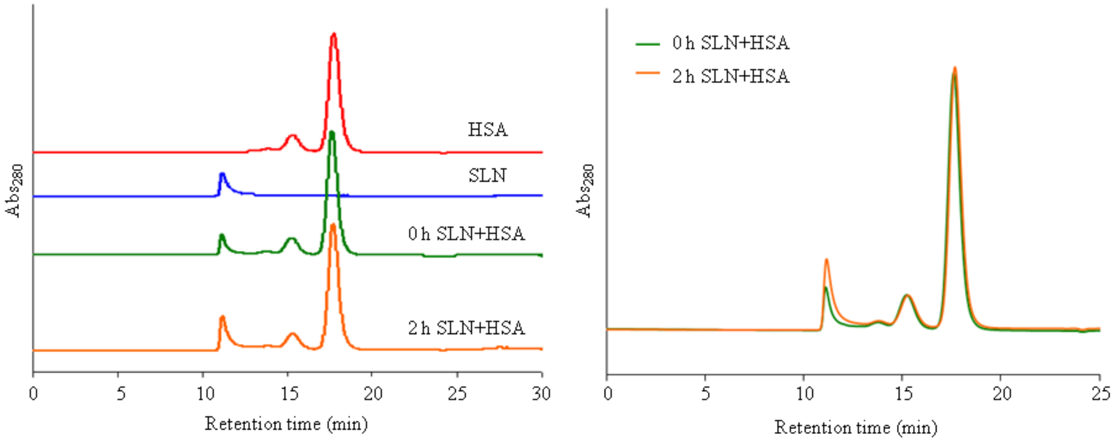

Figure 6.12. SEC profiles for HSA, SLNs, and a mixture of SLNs with HSA before and after a 2 h incubation at 37°C (left). Direct overlay of the mixture profiles at 0 and 2 h (right). Adapted from [197]**

6.3.3. Stability of Dex-P Association with SLNs. The final studies in this section were focused on confirming the stability of the association of Dex-P with SLNs in the presence of human plasma proteins. The drug release studies discussed in the previous chapter were conducted under sink conditions, and as such, should represent the drug release that would occur in the circulation. However, in addition to this study, other methods were considered to specifically evaluate drug partitioning onto plasma proteins. Centrifugation at 40,000g for 4 h failed to sediment the SLNs due to the low average density of the SLNs (1.05 g/cm^3). While SEC can be effectively used with individual proteins or possibly mixtures of a few proteins, it can be difficult to use with a complex plasma sample. As an alternative, a stepwise filtration method was used to determine the stability of Dex-P association with SLNs.

It was hypothesized that Dex-P would exist in three forms following incubation with human plasma: 1) Dex-P associated with SLNs, 2) Dex-P solubilized in plasma (including protein-bound drug), and 3) drug aggregates (unsolubilized drug). The SLN- and protein-associated Dex-P would be expected to pass through a 0.2 μm filter, but unsolubilized drug would not. Using ultrafiltration (MWCO 10 kD), free drug could then be separated from that bound to proteins or associated with SLNs. As the ratio of bound to unbound drug is constant when protein concentration is greater than drug concentration, determination of the free drug will allow for the calculation of protein bound and correspondingly SLN-associated Dex-P.

Dex-P was shown to be highly protein-bound (64%) under the conditions used in this study; sequential ultrafiltrations led to a loss of approximately 2% of the drug. Using these corrections, it was shown that greater than 96% of Dex-P remained associated with the SLNs in PBS following a 24 h incubation. When incubated in 50% human plasma, this value was reduced to 85.5% due to an increased presence of drug aggregates as well as free drug (Table 6.2). Thus, while drug release from the SLNs was slightly accelerated in the presence of plasma proteins, Dex-P remained predominantly associated with the nanoparticles.

Table 6.2. Association of Dex-P with SLNs during a 24 h incubation in PBS or 50% human plasma (n=3). Adapted from [197]**

Sample	Incubation time (h)	Unaggregated DEX-P(%) [a]	Released DEX-P (%) [b]	SLN-associated DEX-P (%) [c]
SLN in PBS	0	98.4 ± 0.5	0.8 ± 0.5	97.6 ± 0.6
	2	97.8 ± 1.4	1.2 ± 0.2	96.6 ± 1.3
	24	97.8 ± 1.5	1.6 ± 0.1	96.2 ± 1.6
SLN in plasma	0	98.1 ± 2.3	3.0 ± 0.2	95.2 ± 2.2
	2	98.1 ± 3.0	4.2 ± 0.5	93.9 ± 2.7
	24	93.2 ± 1.2	7.7 ± 0.6	85.5 ± 1.8*

[a] calculated from the recovery of DEX-P after microfiltration using a 0.2 µm syringe filter
[b] calculated from the percentage of DEX-P in the filtrate of ultrafiltration (MWCO: 10 kDa) and corrected based on 98% membrane recovery and 64% protein binding
[c] calculated from the following equation, SLN-associated DEX-P (%) = a-b
* Significantly different from 0 and 2 h time points of this sample

6.4. CONCLUSIONS

The studies described in this section were designed to confirm the stability of SLNs and the retention of Dex-P with the SLNs under conditions mimicking those found in human plasma (specifically the absence of CE activity). Although SLNs increased in size by approximately 40 nm when incubated for 24 h at physiological temperature, they appeared to retain their ellipsoidal shape. This growth may be attributable to Ostwald ripening and is unlikely to affect the ability of SLNs to achieve tumor targeting. Analysis of SLNs incubated with 10% HSA by DLS, UV/Visible spectroscopy, and SEC indicated the possibility of minor protein adsorption on the particles, but no evidence of particle disassociation or aggregation was observed. Further, using a multi-step filtration process, Dex-P was shown to remain predominantly associated with the SLNs (85.5%) during a 24 h incubation in the presence of 50% human plasma.

*Portions of the introduction, Figure 6.1, and Figure 6.2 reprinted with kind permission from Springer Science+Business Media: AAPS Journal, Nanoparticles Containing Anti-inflammatory Agents as Chemotherapy Adjuvants II: Role of Plasma Esterases in Drug Release, 11(1), 2009, 120-122, X. Lu, M.D. Howard, D.R. Talbert, J.J. Rinehart, P.M. Potter, M. Jay, M. Leggas, Copyright © 2009 Springer Science+Business Media, LLC.

**Portions of the results and discussion section, Table 6.2, and Figure 6.12 containing data from M.D. Howard reproduced with permission from Kim, J-K; Howard, M.D.; Dziubla, T.D.; Rinehart, J.J.; Jay, M.; Lu, X., Uniformity of Drug Payload and Its Effect on Stability of Solid Lipid Nanoparticles Containing an Ester Prodrug. *ACS Nano* 2010, 5, (1), 209-216. Copyright ©2011 American Chemical Society.

Chapter 7

Carboxylesterase-Triggered Hydrolysis of Nanoparticle PEGylating Agents

7.1. INTRODUCTION

The discovery that poly(ethylene glycol) (PEG) can be used as a surface coating to increase the circulation lifetime of nanoparticles has unquestionably contributed to the growth of research on nanocarrier drug delivery systems [215]. Today, PEG is considered a primary component of nearly all nanoparticle drug delivery systems with surfaces being coated through a variety of adsorption, grafting, or entrapment techniques [63]. This hydrophilic, flexible polymer acts to reduce opsonin adsorption and macrophage uptake, delaying removal of the nanoparticles by the RES [71, 85]. The extended circulation in turn provides a greater opportunity for the nanoparticles to reach the site of action, most notably tumors [216, 217].

Much research has been conducted on how to achieve optimum *in vivo* results, including studying the ideal amount, packing density, molecular weight, and structure of PEG on the surface of nanoparticles [63]. However, the other component of achieving optimal *in vivo* results that has been considered less frequently is the stability of the PEG coating. The nanoparticle drug delivery systems must not only be appropriately PEGylated upon injection, but the PEG coating must remain stably attached to the nanoparticle while in the circulation. The paucity of reports in this area may be due in part to the difficulty in characterizing PEG itself. PEG lacks a chromophore for UV detection, limiting quantitative measurements by traditional methods [218, 219]. Alternatively, as PEG is used to provide stealthiness to nanocarriers, it may be assumed that the PEG cloud surrounding the nanoparticle will sufficiently prevent interactions with proteins and enzymes that may affect its own stability.

However, recent studies may refute this assumption. PEG has been shown to desorb from nanoparticle surfaces in the presence of proteins [114, 220]. Further, the development of bioresponsive systems based on sheddable PEG coatings has led to concern over the stability of PEG derivatives against hydrolysis. These systems are designed such that upon loss of the PEG coating, nanoparticles become destabilized, accelerating drug release [221]. While hydrolysis has been triggered by stimuli such as an acidic pH [222] and a reducing environment [223, 224], PEG derivatives have also been designed for enzymatic cleavage [23, 225]. These are of the greatest concern because they indicate that the PEG cloud may not be as impenetrable to proteins as expected, at least in some cases, and warrant the study of PEG coatings previously assumed to be stable.

PEG coatings secured by ester linkages are one such example. Many PEGylating agents are linked to a lipid moiety through an ester bond; the lipid moiety is inserted into the core of the nanoparticle while PEG resides on the surface of the particle. Two of the PEGylating agents used in the SLNs under consideration – PS60 and PEG6000MS – are a case in point, and it is of interest to know if these SLN components are susceptible to hydrolysis in the presence of CE for several reasons (Figure 7.1). On a system-specific level, enzymatic degradation of these compounds may help explain the drug release results previously obtained. Previous studies have shown that release of ester prodrugs incorporated into the SLNs was dependent on CE activity [37], and while this may be attributable to the structure of the specific ester prodrug, hydrolysis of one or both of these SLN components may have contributed to the accessibility, and subsequent release, of the drug by CE. On a broader level, this knowledge may be used to design systems capable of achieving tumor-targeted drug delivery in humans by taking advantage of the negligible blood CE activity [208] in comparison to the higher tumor CE activity [37, 209]. Unfortunately, enzymatic degradation of PEGylating agents may also prevent the use of normal animal models for *in vivo* testing. Mice and rats both have significantly higher blood CE levels than humans [208, 226, 227], and studies performed in these animals may fail to give results representative of what would be seen in humans.

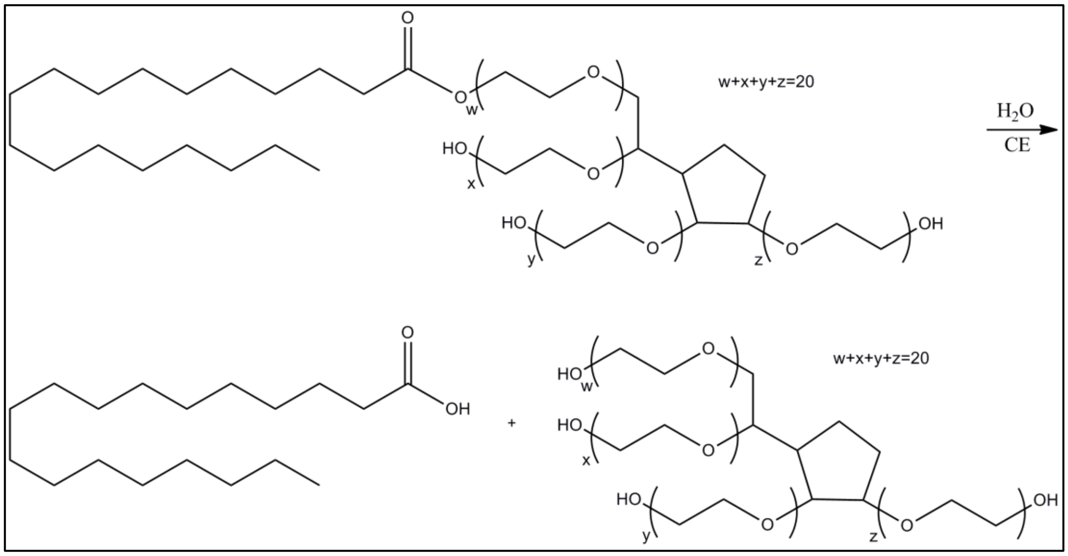

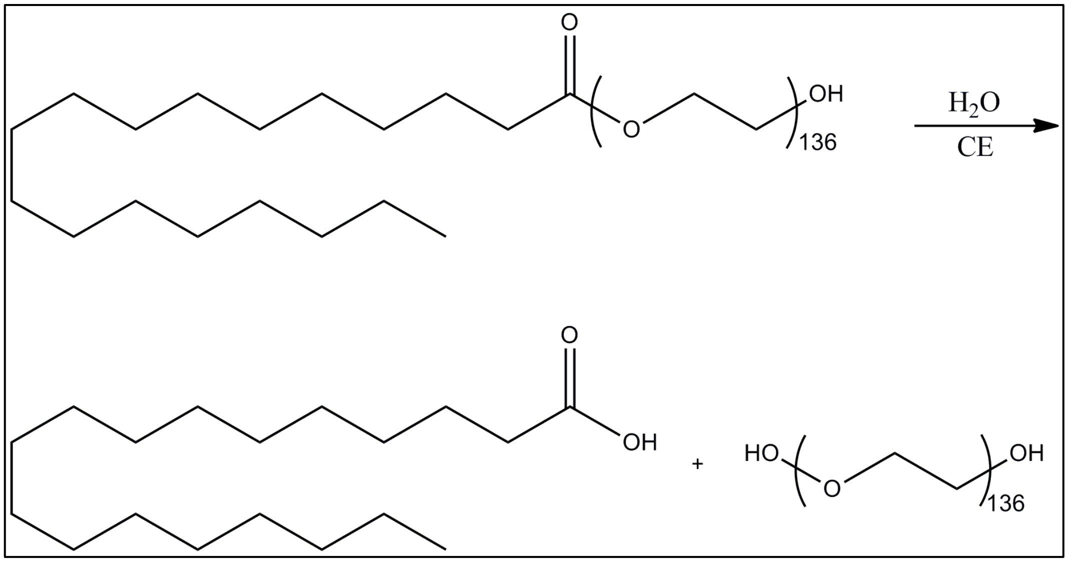

Figure 7.1. CE-catalyzed ester hydrolysis of PS60 (top) and PEG6000MS (bottom)

7.2. MATERIALS AND METHODS

7.2.1. Materials. SA was obtained from Spectrum Chemicals and Laboratory Products (Gardena, CA). PS60 and Brij® 78 were from Uniqema (Chicago, IL). PEG6000MS was a gift from Stepan (Northfield, IL). PBS was purchased from Invitrogen (San Diego, CA). NaOH was obtained from Fisher Scientific (Pittsburgh, PA). NaCl, BNPP, and CE (porcine liver esterase, 3.2 M $(NH_4)_2SO_4$ suspension, 36 mg/ml, 154 units/mg) were obtained from Sigma-Aldrich (St. Louis, MO). Water was used from a Millipore Milli-Q Synthesis ultrapure water system (Billerica, MA).

7.2.2. SLN Preparation. SLNs were prepared using NET as previously described [131]. In brief, the process consists of three steps: 1) melting an appropriate mixture of lipids and surfactants, 2) adding an aqueous phase to generate an oil-in-water microemulsion, and 3) cooling the microemulsion to form a suspension of SLNs. For this study, materials were melted at 70°C and cooled to room temperature. The aqueous phase consisted of 0.9% NaCl or PBS, as appropriate. The primary formulation (formulation 2 SLNs) consisted of 1.6 mg/mL SA, 0.4 mg/mL PS60, 2.8 mg/mL Brij® 78, and 3.0 mg/mL PEG6000MS; unless specifically noted otherwise, the term "SLN" refers to this formulation. Formulation 1 SLNs comprised of 1.6 mg/mL SA, 0.4 mg/mL PS60, and 3.5 mg/mL Brij® 78 were also used in the pH-stat experiments. PS60 (0.4 mg/mL) and PEG6000MS (3.0 mg/mL) micelles were prepared using the same process but without the addition of a lipid phase.

7.2.3. Turbidity and DLS analysis. As a measure of turbidity, UV absorbance measurements were taken at 380 nm using a Beckman DU 7500i Spectrophotometer (Beckman Coulter Inc., Brea, CA). Five samples (n=3) were incubated at 37°C in PBS with shaking at 100 rpm over a period of 48 h: SLNs, SLNs with CE, SLNs with CE and BNPP, CE, and CE with BNPP. Concentrations of CE (1.86 Units/ml, equivalent of 10% mouse plasma [208]) and BNPP (1mM, previously shown to inhibit CE [37]) were kept constant for all samples. At each time point (0, 1, 3, 6, 24, and 48 h), 500 μL aliquots were removed for turbidity measurements. PBS dilutions were performed as necessary to achieve a signal in the range of 0.2-1.0 absorbance units. The background signal associated with CE alone or the CE-BNPP combination was subtracted from the respective SLN sample for ease of analysis. An additional 30 μL were removed at each time point for measurement of the particle size and PI by DLS. These aliquots were diluted to 1 mL using 0.2 μm filtered water. Measurements were performed at 25°C on a

Delsa™ Nano Zeta Potential and Submicron Particle Size Analyzer (Beckman Coulter Inc., Brea, CA).

7.2.4. TEM. SLNs in PBS were incubated with and without CE (1.86 units/ml) at 37°C with shaking at 100 rpm. Samples were removed for TEM imaging at 1 and 24 h. Seven microliters of each were incubated for 1.5 min on a carbon-coated TEM grid. The grid was dried and stained with 0.2 µm filtered 2% uranyl acetate for an additional 1.5 min followed by an additional 5 min of drying. Images were obtained using a Philips Tecnai Biotwin 12 equipped with a Gatan ES 1000W CCD digital camera (FEI, Hillsboro, OR) and analyzed using the ImageJ processing program [164]. For each sample, five images were taken at different locations on the grid and twenty particles were measured per image. For each particle, the lengths of both the major and minor axes were obtained using the manual analytical tools. The volume of an ellipsoid with these dimensions was calculated from these values using the equation for a prolate spheroid (the assumed shape):

$$\text{Volume} = \frac{4}{3}\pi r_{\text{major}} r_{\text{minor}}^2$$

where r is the radius of the relevant axis. This value was used as the volume of an equivalent sphere to allow for the calculation of an approximate particle diameter according to the following equation:

$$\text{Diameter} = \left[\left(\frac{V}{\frac{4}{3}\pi}\right)^{\frac{1}{3}}\right]^2$$

The calculated diameters for the 100 analyzed particles were averaged to provide a mean and SD for the particle size.

7.2.5. SEC. Analysis was performed using a Shimadzu Prominence LC series equipped with a RID-10A refractive index detector. The mobile phase was 5 mM PBS, run at a rate of 0.5 mL/min. Twenty microliter samples were injected to a Shodex Asahipak GF-7M HQ column (7.5 mm x 150 mm). Molecular weight calculations were made using a calibration curve developed from PEG molecular weight standards. For concentration calculations, a calibration curve was prepared using NaOH-treated PEG6000MS. SLNs and PEG6000MS micelles were treated with 0.1 N NaOH for 3 days. Aliquots were removed and neutralized with 0.1 N HCl. Samples were centrifuged to remove any precipitate prior to analysis. To confirm complete release of free PEG, new aliquots were removed and analyzed again 24 h later. For the CE hydrolysis study, SLNs and PEG6000MS micelles (3 mg/ml) were prepared in PBS and aliquots immediately removed for the 0 h time point measurements (n=3). Samples were then treated with CE (1.86 units/mL final concentration) or a combination of CE and BNPP (5 mM) and incubated at 37°C with shaking at 100 rpm. Five hundred microliter aliquots were removed for analysis at 1, 5, 10, 15, 30, and 60 min. The CE-only aliquots were treated with BNPP upon removal in order to stop the reaction. Prior to analysis, all samples were centrifuged, and the supernatant was collected for injection onto the column. To determine the origin of the peak present in the initial samples, PEG6000MS was prepared in PBS at various concentrations (1-5 mg/mL) and analyzed without undergoing CE- or NaOH-treatment.

7.2.6. Measurement of Free Fatty Acid (FFA) Production. In addition to measuring the production of free PEG, hydrolysis of ester-containing PEGylating agents can also be analyzed by monitoring for production of FFAs. These experiments were performed using a pH-stat apparatus (Metrohm Titrando 842, Metrohm USA Inc., Riverview, FL). The pH meter was calibrated using pH 2.0, 7.0, and 10.0 standards, and all samples were degassed prior to analysis. Twenty-five milliliters of formulation 1 SLNs, formulation 2 SLNs, or PS60 micelles in 0.9% NaCl were brought to 37°C with stirring. The pH was adjusted to 7.4, and the enzyme solution was added (1.86 units/mL final concentration). The pH was kept constant by titrating the produced FFAs with a 0.01 N NaOH solution using an automated burette; the volume of NaOH added was recorded as a function of time. Samples were monitored for 2 h. Control samples for each were pre-treated with BNPP (5 mM) prior to CE exposure. Additionally, blank samples in which CE was added to 0.9% NaCl alone were analyzed. All samples were analyzed in triplicate. For comparison, the amount of NaOH added at 15 min intervals was averaged, and the measurements for all three samples were corrected for the addition of enzyme alone using their respective BNPP measurements. The SLN measurements were corrected for the hydrolysis of PEG6000MS using information (molecular weight and purity) obtained from the SEC studies. An additional study was performed in which, following the normal study period, samples with and without BNPP were titrated to pH 9.0 in order to confirm that all FFAs produced were in the detectable, ionized form. A spiking experiment was run to determine if enzyme was being inactivated. PS60 micelles with and without BNPP were run as normal; at 1 h, 1 mL of sample was removed and replaced with 1 mL of a 10 mg/mL PS60 solution. The samples were run for an additional hour.

7.2.7. Statistical Analysis. All data is presented as the mean ± SD of three independent measurements. Comparisons were made using a t-test (paired two sample for means). Results are considered statistically significant at a level of $p<0.05$.

7.3. RESULTS

7.3.1. Particle Size and Turbidity. It was assumed that hydrolysis of the SLN PEGylating agents may lead to instability of the particles, either due to particle disassociation or aggregation. If the concentration of surfactants is reduced due to degradation of PEG6000MS or PS60, particles may disassociate, leading to the release of the lipid phase. Due to the presence of Brij® 78, a non-ester-containing surfactant, and other unhydrolyzed surfactant molecules, this insoluble material may remain dispersed at least temporarily before precipitating. Alternatively, if SLNs remain intact, it is possible that they may aggregate due to the lessened concentration of PEG on their surfaces. Based on this assumption, we monitored the turbidity of the SLN suspensions; the absorbance at 380 nm was chosen as a quantifiable marker of turbidity due to the low absorbance of CE and BNPP at this wavelength. SLNs incubated with CE were compared to SLNs alone and SLNs pre-treated with BNPP prior to the addition of CE over a 48 h period (Figure 7.2). Following correction for the background signal of CE or CE and BNPP in combination, the turbidity of SLNs incubated with CE was observed to be 35-fold greater at the 0.5 h time point as compared to the two controls. Only a minimal increase in turbidity was seen with SLNs alone or SLNs incubated with CE and BNPP; no significant differences were observed between the two ($p>0.05$). Interestingly, the absorbance measurements of SLNs incubated with CE showed a decrease between 0.5 and 6 h followed by a slight increase for the remaining time period.

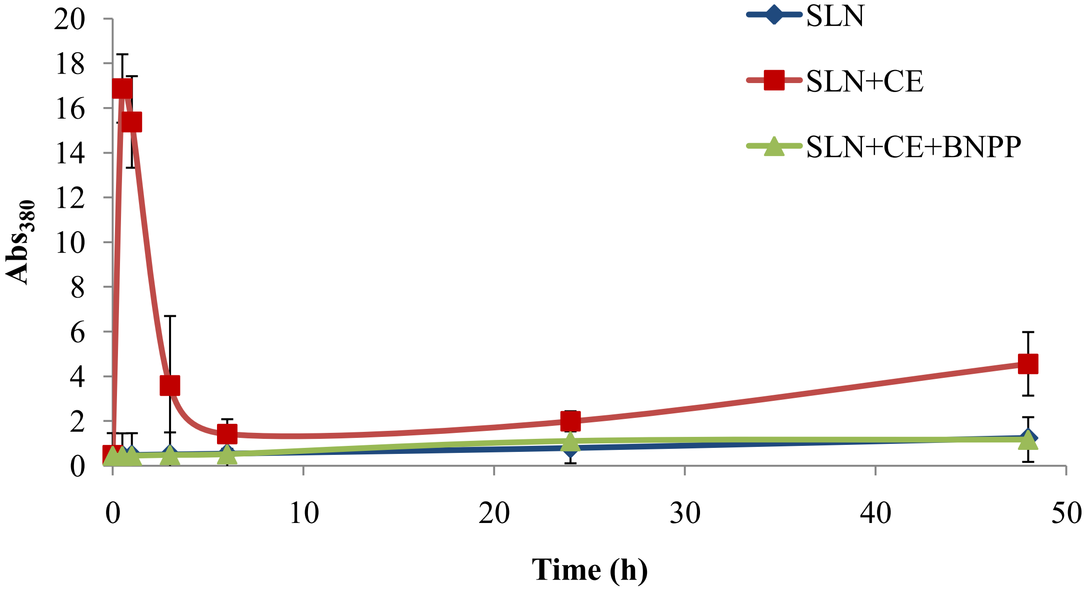

Figure 7.2. Turbidity of SLNs incubated at 37°C with CE, with BNPP-inhibited CE, or alone. Turbidity is assessed by measuring the sample absorbance at 380 nm. Samples were corrected for the background signal of CE or CE and BNPP in combination (n=3).

Throughout the turbidity study, aliquots were removed from the samples for measurement of the particle size. Control samples of CE alone or CE with BNPP failed to give the intensity necessary for particle size measurement by DLS and, as such, it was assumed that all size measurements reported were related to the SLNs themselves. The particle sizes of SLNs and SLNs with inhibited CE are similar, while SLNs with CE showed smaller sizes (Figure 7.3). This difference became especially noticeable at later time points with SLNs incubated with CE showing an average size of nearly 40 nm smaller than SLNs pre-treated with BNPP prior to exposure to CE at 48 h. SLNs with and without exposure to CE exhibited similar morphologies and homogeneities based on

TEM images taken at the 1 and 24 h time points (Figure 7.4) though analysis of the particle size using the ImageJ processing program revealed a similar trend as was observed by DLS (Table 7.1).

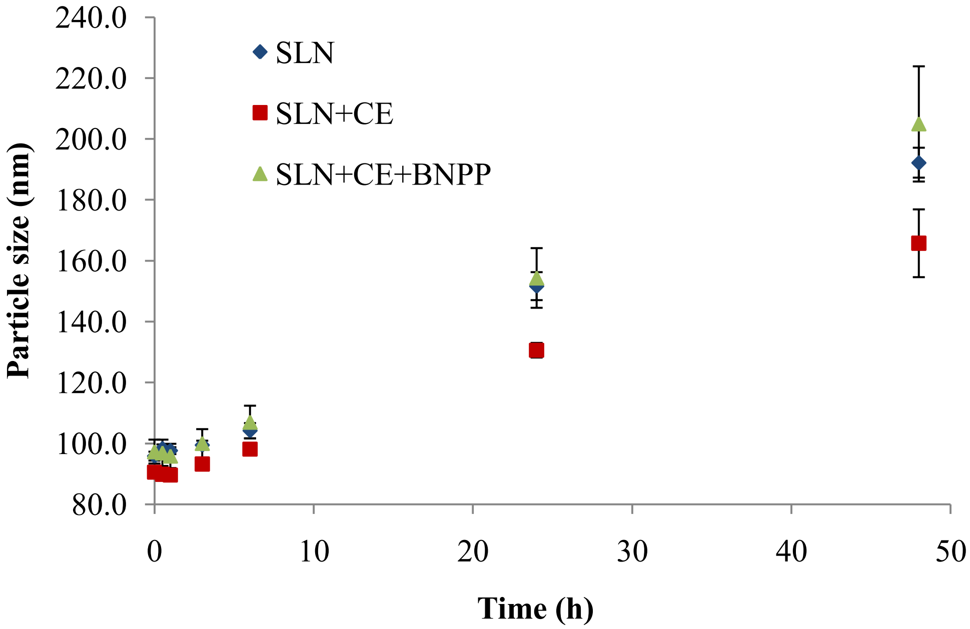

Figure 7.3. Particle size of SLNs incubated at 37°C with CE, with BNPP-inhibited CE, or alone as a function of time (n=3)

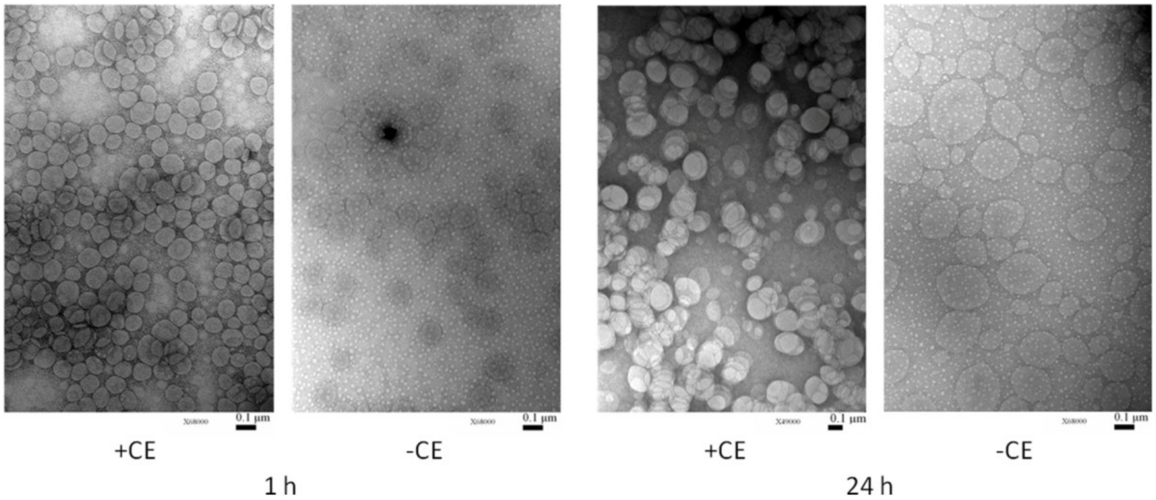

Figure 7.4. TEM images of SLNs incubated at 37°C with or without CE for 1 (left) and 24 (right) h

Table 7.1. Representative particle size distribution data obtained from SLNs incubated at 37°C with and without CE for either 1 or 24 h. Both DLS and TEM data is shown; analysis of the TEM images was performed using the ImageJ processing program.

Sample		DLS		TEM	
		Size (nm)	PI	Size (nm)	SD (nm)
1 h	-CE	93.3	0.017	98.0	15.1
	+CE	87.5	0.017	90.0	11.8
24 h	-CE	146.8	0.035	154.3	52.0
	+CE	127.9	0.101	143.1	43.9

7.3.2. SEC. While the low molecular weight of PS60 prevented its analysis by SEC, this method was deemed suitable for monitoring the hydrolysis of PEG6000MS. In analyzing this material alone, identical peaks were observed for the degradation product of PEG6000MS incubated with CE and PEG6000MS exposed to NaOH. Based on a PEG molecular weight calibration curve (Figure 7.5), it was determined that this peak was associated with a higher molecular weight than was expected (10,376 vs 6,000). As this prevented the use of an external standard for quantification, a calibration curve was developed using NaOH-treated PEG6000MS; peak height was shown to increase linearly with concentration (Figure 7.6).

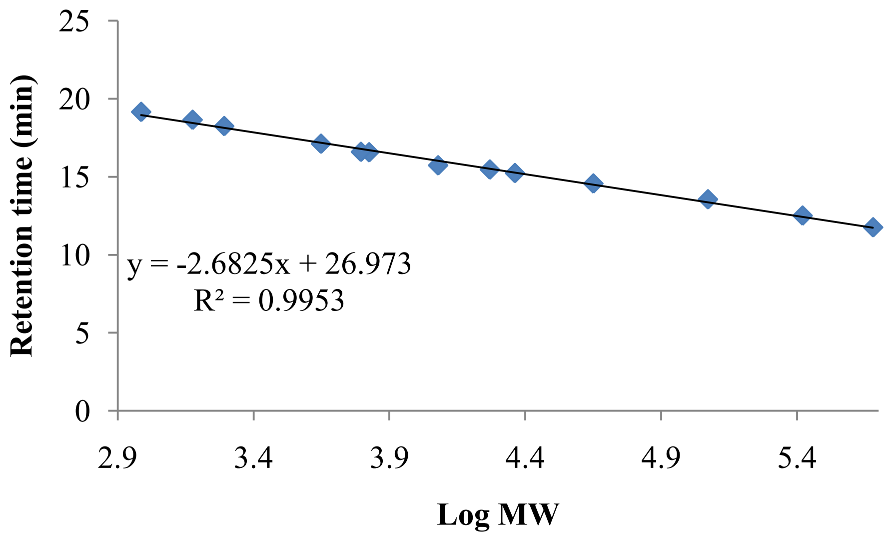

Figure 7.5. SEC molecular weight calibration curve (data from laboratory of Dr. Younsoo Bae)

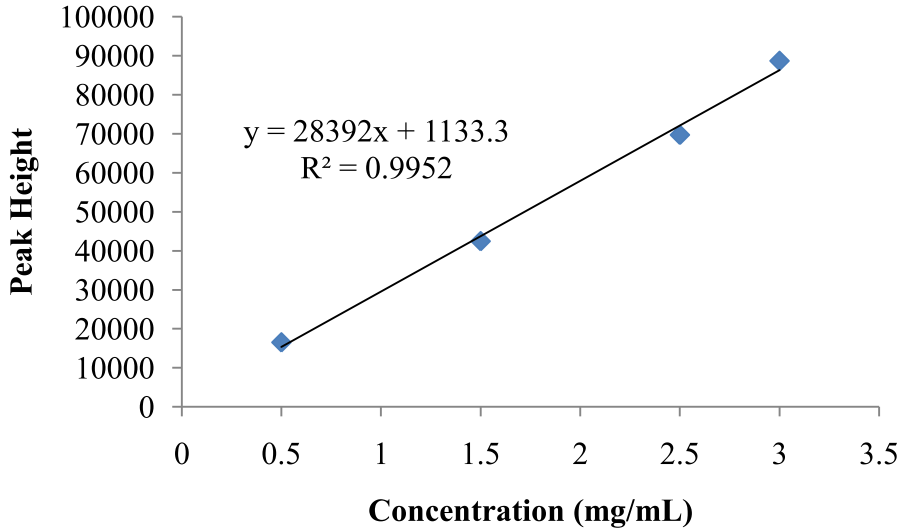

Figure 7.6. SEC concentration calibration curve developed from NaOH-treated PEG6000MS

In experiments designed to study the hydrolysis of PEG6000MS by CE, it was observed that a peak was present at the expected retention time in the SEC eluent prior to CE exposure. To determine if this was associated with an impurity in the product (PEG6000) or to free PEG6000MS, PEG6000MS was analyzed at concentrations ranging from 1-5 mg/mL. Peak height was again shown to increase linearly with concentration, indicating that the initial peak was likely due to a product impurity (Figure 7.7). A peak associated with free PEG6000MS would be expected to remain constant above the CMC (appendix C). This impurity peak was subtracted from all subsequent analyses of SEC results.

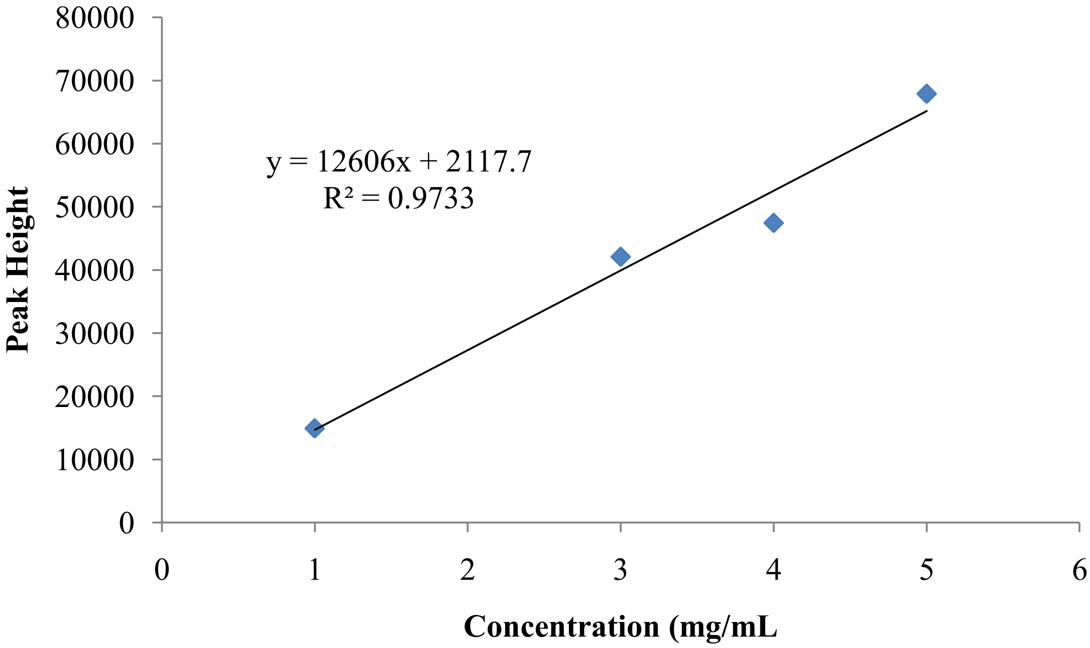

Figure 7.7. Untreated PEG6000MS peak height varies with concentration, indicating the presence of an impurity.

Inclusion in SLNs appears to delay the hydrolysis of PEG6000MS as compared to when it is in micellar form (Figure 7.8). However, almost 100% hydrolysis is still reached within 15 minutes following exposure of the SLNs to CE. When samples were pre-treated with BNPP prior to CE exposure, hydrolysis of PEG6000MS in both SLN and micellar form was negligible.

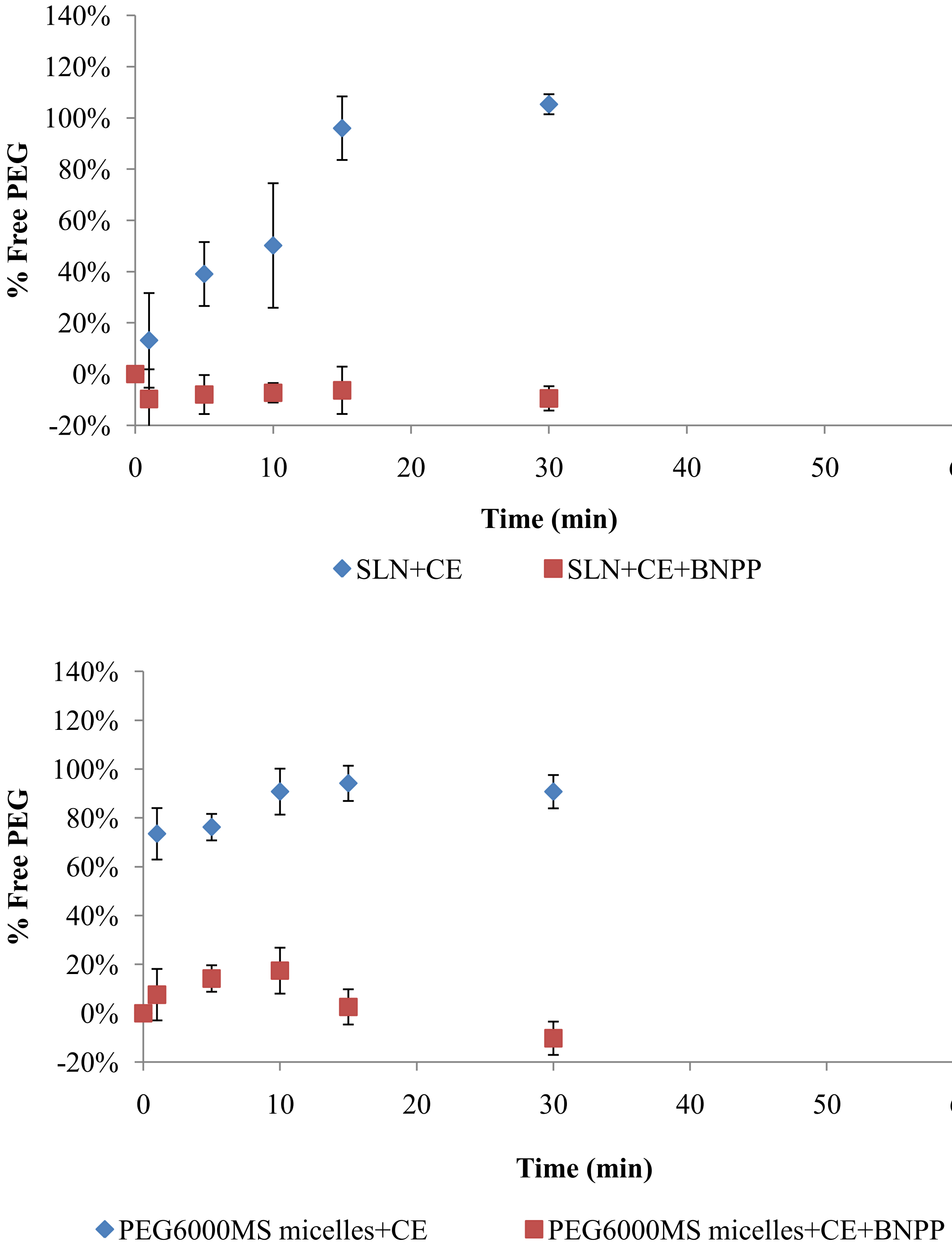

Figure 7.8. Hydrolysis of PEG6000MS as determined by SEC with RI detection. SLNs (top) and PEG6000MS micelles (bottom) were incubated with CE in the presence or absence of BNPP (n=3).

7.3.3. Measurement of FFA Production. The pH-stat technique was used to measure the change in pH induced by the formation of FFA following hydrolysis of PS60 and PEG6000MS by CE. PEG6000MS could not be monitored in its micellar form using this technique due to immediate precipitation following CE exposure. However, both SLNs and PS60 micelles were monitored for the production of FFA following the introduction of CE. To provide a direct comparison between SLNs and micelles, a second SLN formulation (formulation 1 SLNs) was analyzed in which PS60 but not PEG6000MS was included. Adjustment of pH was not required when BNPP was included in the mixture except for that required to correct for the enzyme itself (determined by blank measurements).

The average amount of NaOH added at 15 min intervals (n = 3) appears in Figure 7.9, having corrected for the amount associated with the addition of enzyme alone by subtracting out the amount added in the respective BNPP measurements at each time point (n=3). Additionally, SLN measurements were corrected for the hydrolysis of PEG6000MS, calculating the µmoles hydrolyzed using the SEC-determined molecular weight and accounting for the free material present initially. In each case, a substantial input of NaOH was required initially following CE exposure to return the pH to 7.4 followed by a slower addition over the long-term. During the initial phase, hydrolysis of PS60 appeared slower in SLNs than micelles. The addition of PEG6000MS to the SLNs appeared to retard hydrolysis even further. At later time points, the three curves become linear. If only the second hour was plotted and fitted with a linear trend line, hydrolysis rates could be obtained: PS60 micelles, 0.0036 µmol/min; formulation 1 SLNs, 0.0087 µmol/min; formulation 2 SLNs, 0.0080 µmol/min.

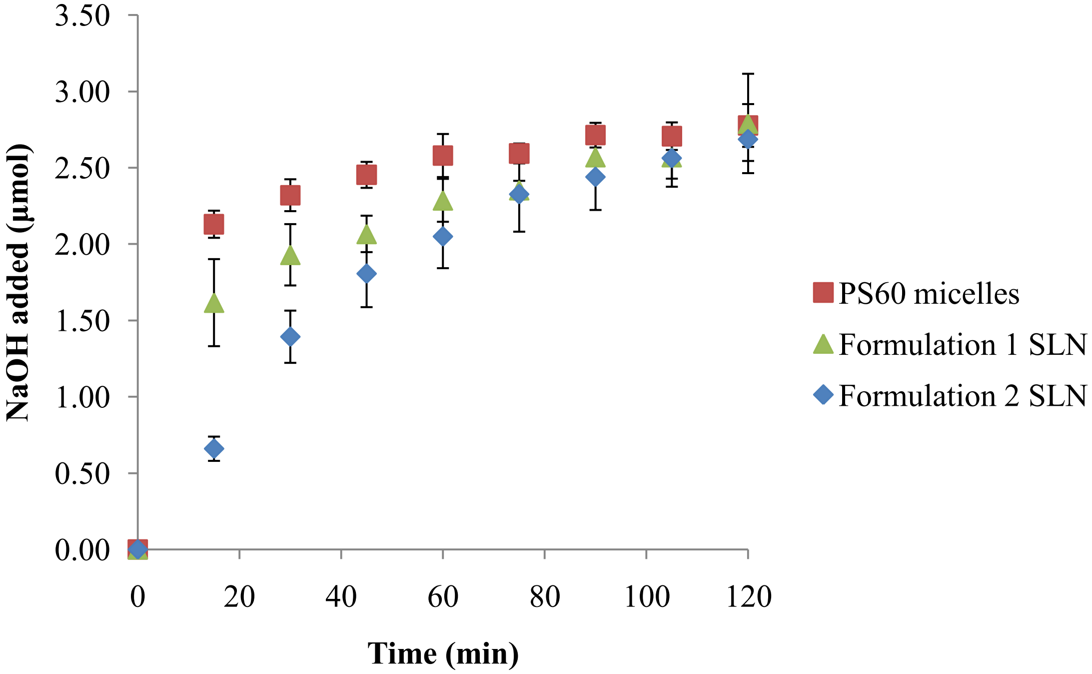

Figure 7.9. Hydrolysis of PS60 in SLNs and PS60 micelles as determined using the pH-stat technique. All three samples were corrected for the addition of enzyme; formulation 2 SLNs were also corrected for PEG6000MS hydrolysis (n=3).

To confirm that all FFAs produced were in the detectable ionized form, samples were titrated to pH 9 following a 2 h incubation. There was no difference between samples with and without BNPP (data not shown). To determine if enzyme was being inactivated over time, PS60 micelle samples with and without BNPP were run as above but spiked with additional PS60 at 1 h. Accounting for the general dilution effect using the BNPP control, hydrolysis of the spiked PS60 was 75-95% of the initial addition.

7.4. DISCUSSION

Although many PEGylated nanoparticles have been described, relatively little research has been conducted on the stability of PEG coatings [114, 220]. Most reports have focused on the therapeutic outcome involved with the use of PEGylated nanocarriers instead of the mechanism of degradation. However, loss of PEG from the surface of nanoparticles may have profound implications for drug release and *in vivo* behavior.

Ester-containing PEGylating agents have long been used in nanoparticles, some of which have achieved long circulation lifetimes and/or desirable therapeutic outcomes [228]. In the cases where such results have not been achieved, it has typically been attributed to suboptimal PEG surface coverage. However, as recent studies have described nanoparticles designed to specifically release PEG in the presence of esterases [23], it is possible that this may occur in other systems not specifically designed to do so. Loss of surface PEG may explain the sub-optimal results observed for some nanoparticle drug delivery systems.

As such, it was considered critical to evaluate the SLNs under study for their stability in the presence of CE. Both PS60 and PEG6000MS contain potentially cleavable ester bonds, and previous studies have shown that drug release from the SLNs was dependent on the CE activity of the surrounding environment [37]. As it was anticipated that cleavage of PEG from the surface of SLNs may result in particle instability (either from particle breakdown or aggregation), preliminary studies were focused on observing changes in particle stability due to the presence of CE. Turbidity studies clearly indicated a difference between SLNs incubated with and without CE. The addition of BNPP-inhibited CE as a second control showed that the turbidity increase with CE was likely due to hydrolysis of the ester bonds and not simply to a general protein effect. The minimal increase in turbidity observed with the two control samples was likely a result of the observed increase in particle size.

Interestingly, it was noted that the SLNs incubated with CE alone decreased in turbidity following a major spike at 0.5 h. Although this could be due to precipitation, the samples did not show visible signs of settling at this stage. This may instead be attributable to the formation of other colloidal structures since the SLNs also have a non-ester-containing surfactant, Brij® 78, which would not be hydrolyzed in the presence of CE.

As a second test of stability, the change in the particle size distributions of SLNs incubated with and without CE and SLNs incubated with both CE and BNPP were measured. SLNs remained detectable following exposure to CE, although the particle size was smaller than the two controls. Based on this, it did not appear that aggregation was occurring to a large extent. Instead, the produced FFAs may be released from the SLNs or a portion of the SLNs may be disassociating completely. Again, due to the presence of Brij® 78 and other unhydrolyzed surfactant, alternative colloidal structures may be formed that allow for at least temporary solubilization of the free lipid material. However, these would likely be dissolved during the dilution step necessary to achieve an intensity reading within the instrument's range, leaving only intact SLNs. The SLNs may then be smaller than the controls because a portion of the PEG has been cleaved from the surface or because the remaining SLNs had less of the ester-containing PEGylating agents initially. Preparation of test batches containing SA with Brij® 78 only, SA with Brij® 78 and PS60, and SA with Brij® 78, PS60, and free PEG6000 confirmed that particles could be detected in all cases, with sizes ranging from 100-200 nm in diameter.

TEM analysis of the SLNs provided confirmation of the DLS results. While a similar trend in size growth was seen between DLS and TEM images, the sizes obtained with TEM were slightly larger than what was measured by DLS. This atypical result is potentially a result of the non-spherical structure of the particles, which will give a slightly larger hydrodynamic radius than a perfectly spherical particle [207]. Interestingly, the SLNs remaining following CE exposure appeared to have no major morphological differences as compared to those without CE, although their image backgrounds appeared slightly different. This may be attributed to the presence of the free hydrolyzed materials in the SLN plus CE samples.

Based on these studies, it appeared that changes were occurring to SLNs incubated with CE, and further study was warranted. Methods were developed to allow for the measurement of the hydrolysis of each of the components separately. In each case, hydrolysis of the material in SLNs was compared to hydrolysis of the material in micelle form to determine if SLNs provided any protection against enzymatic cleavage.

The degradation of PEG6000MS was monitored using SEC. As no external standard was available, a reference was prepared by hydrolyzing PEG6000MS with NaOH. Repeat measurements confirmed the complete hydrolysis of PEG6000MS, and chromatographic peaks associated with the CE-hydrolyzed PEG6000MS were shown to appear with the same retention time as NaOH-hydrolyzed PEG6000MS. Thus, all data obtained with CE is expressed in reference to the NaOH-hydrolyzed PEG6000MS. A clear difference was observed between SLNs pre-treated with BNPP prior to CE exposure and those not pre-treated. Whereas untreated SLNs reached approximately 100% hydrolysis within 15 min, the addition of BNPP appeared to completely inhibit hydrolysis of the PEG-ester bonds in the SLNs.

In comparing degradation of PEG6000MS in SLNs and in micelles, we expected that SLNs may offer some protection against hydrolysis. Previous NMR studies confirmed that these nanoparticles exhibited the expected core-shell structure with the majority of lipids (from stearyl alcohol as well as the hydrophobic portion of the surfactants and PEGylating agents) solidified in the core [207]. Based on the solid nature of the particles, it was assumed that CE would have limited access to the PEG6000MS ester bond, which likely resides at the interface between the core of the nanoparticles and the PEGylated surface. Interestingly, this was observed but only to a limited extent. The increase in free PEG was more gradual with SLNs than micelles. For example, nearly 75% of PEG6000MS in micellar form was hydrolyzed within 1 min of exposure to CE; this level was not reached in SLNs until 10-15 min after exposure. However, the SLN advantage was quickly negated, with both samples reaching nearly 100% hydrolysis within 15 min.

Unfortunately, the low molecular weight of the PS60 degradation product prevented its analysis using the available SEC system. The pH-stat technique, which relies upon the analysis of FFAs produced instead of free PEG, was employed as an alternative method. As FFAs were produced, a neutralizing basic solution was automatically added to the solution in order to maintain a constant pH. The amount of NaOH added was reflective of the amount of FFA formed by hydrolysis of PS60.

Again, a clear difference was observed between SLNs exposed to CE with and without BNPP pre-treatment, with the NaOH addition being significantly greater in untreated samples. There was no difference in the profiles obtained with pre-treated samples and blank samples (CE added to 0.9% NaCl), providing a second confirmation that PEGylating agents were susceptible to hydrolysis by CE. In order to better compare PS60 hydrolysis between SLNs and micelles, formulation 1 SLNs (containing PS60 but not PEG6000MS) were also analyzed.

Interestingly, within 2 h, the hydrolysis for all samples was less than 40% of the total predicted amount. This low amount could not be traced to a pKa issue or to enzyme inactivation. Instead, it is assumed that this is attributable to the accessibility of the PS60 ester bond to attack. The rapid initial NaOH addition may be due to hydrolysis of free or easily accessible PS60, of which there appears to be less in SLN samples than micellar samples. The slower hydrolysis rates observed later may be associated with the hydrolysis of PS60 in micelles or SLNs. During this stage, the hydrolysis of PS60 in the SLN samples was more rapid than in micellar samples. This was unexpected and indicates that the PS60 micelles may pack such that the ester bond is protected from enzymatic attack. However, the rate in SLNs was still quite slow.

These results were somewhat surprising based on the hydrolysis of PEG6000MS discussed previously. Based on their structures, it was expected that PS60 and PEG6000MS would align within SLNs in a similar manner, i.e., with the ester bonds of both at the interface of the solid core of the SLNs and the PEGylated surface. If this indeed were the case, they might be expected to display similar degradation patterns. Yet, the hydrolysis of PEG6000MS occurred much more rapidly than the hydrolysis of PS60. It is possible that the PS60 ester bond is integrated more extensively into the core of the SLNs, providing it with greater protection against attack by CE. The addition of PEG6000MS to the SLNs may thus provide another barrier against enzymatic attack, explaining why hydrolysis in the SLN formulation containing PEG6000MS is even slower than in the SLNs lacking PEG6000MS. CE may have to cleave PEG6000MS from the surface of particles prior to attacking the PS60 ester bonds. Further, it was previously proposed that the SLNs lacking PEG6000MS may be in a more fluid state at 37°C than the SLNs containing PEG6000MS, thereby rendering enzymatic attack easier [207]. Alternatively, it may be the structure of PS60 itself that is less favorable to enzymatic attack than PEG6000MS. As seen in Figure 7.1, PEG6000MS consists of a single linear PEG chain, whereas PS60 is in effect a branched PEG chain. This structure may provide more steric hindrance than the linear PEG chain in PEG6000MS.

7.5. CONCLUSIONS

SLNs were evaluated for their stability in the presence of CE, specifically in regard to degradation of PS60 and PEG6000MS. Blank SLN suspensions were observed to become extremely turbid within the first 30 min following exposure to CE indicating dissociation or aggregation of at least a portion of the nanoparticles. The particle size of SLNs incubated with CE was smaller than the size of controls at all time points studied, but their morphologies appeared similar in TEM images taken following 1 and 24 h incubations. Although SLNs offered some protection over micelles, PEG6000MS was rapidly degraded within 15 min. In contrast, PS60 hydrolysis was much slower, reaching only 36% in 2 h. Based on these results, it appears that the accelerated release of Dex observed in the presence of CE may be partially attributable to increased accessibility of the prodrug to enzymes following hydrolysis of the ester-containing materials PS60 and PEG6000MS. On a broader scale, these studies reveal the importance of confirming the stability of PEG surface coatings prior to undertaking *in vivo* experiments in small animal models, which can have considerably higher plasma esterase activity than humans.

Chapter 8

Optimization of the Lyophilization Process for Long-term Stability of Solid Lipid Nanoparticles

8.1. INTRODUCTION

Long-term storage stability can be considered as a final criterion for the development of a nanoparticle drug delivery system. However, stability can be limited by a number of factors when nanoparticles are stored as aqueous suspensions. Specifically with SLNs, lipid crystallization and/or polymorphic transformations can lead to drug expulsion [136-138]. Particles can grow via Ostwald ripening processes [34], and aggregation can lead to gelation [142, 143]. Drug degradation can also occur [155, 229].

Lyophilization (freeze-drying) is one of the most effective means of improving both the physical and chemical stability of SLNs. The process consists of three main steps: freezing, primary drying, and secondary drying [230]. During the first step, water freezes into ice crystals while excluding particles and any free material (the cryo-concentrated phase). Both drying steps are conducted under vacuum. The primary drying step is conducted at low temperatures, and it is during this phase that frozen water is removed through sublimation. During the secondary drying phase, the temperature is raised to remove any unfrozen water through desorption.

Unfortunately, both the freezing and drying steps can generate various stresses that may destabilize nanoparticles. For example, the formation of ice crystals can induce mechanical stress on the particles [231]. Freezing can lead to crystallization of PEG, reducing its ability to serve as a steric stabilizer and leading to particle fusion [230]. For this reason, it is critically important to optimize the lyophilization process in order to reduce these stresses. It can also be valuable to add excipients designed to protect the nanoparticles from these stresses; such molecules are known as lyoprotectants (LPs). Sugars are the most commonly used LPs, though various polymers have been used successfully in some situations [230].

Several possible mechanisms have been proposed for the ability of LPs to prevent destabilization of the nanoparticles. The particle isolation hypothesis is based on the theory that particle aggregation is prevented simply by LPs spatially separating the particles [230]. The water replacement hypothesis is based on the ability of LPs to hydrogen bond with the components on the particle surface, effectively replacing water as it freezes. This can maintain PEG in a pseudo-hydrated state and prevent chain entanglement [230, 232]. The most popular theory, however, is the amorphous glass theory. This theory states that the LPs partition into the cryo-concentrated phase during the freezing process and then solidify into an amorphous glass around the particles. This glassy matrix can subsequently protect the particles from fusion [231, 232].

This section was designed to develop an optimized lyophilization protocol for Dex-P loaded SLNs, in terms of both the use of LPs and the lyophilization process itself. Lyophilized SLNs will be tested for their redispersibility, which is defined as their ability to be returned to their pre-dried state. Upon development of an optimized protocol, SLNs will be evaluated for their long-term storage stability. Comparisons will be made between lyophilized SLNs and SLNs stored as aqueous suspensions and between storage at 4°C and 25°C/60% RH.

8.2. MATERIALS AND METHODS

8.2.1. Materials. SA, polyvinyl alcohol (PVA), and poly(vinylpyrrolidone) (Povidone K-30, 40K average molecular weight; PVP) were obtained from Spectrum Chemicals and Laboratory Products (Gardena, CA). PS60 and Brij® 78 were purchased from Uniqema (Chicago, IL), and PEG6000MS was a gift from Stepan (Northfield, IL). Dex (USP) was a gift from Pfizer (Kalamazoo, MI). ACN and MeOH were purchased from Fisher Scientific (Pittsburgh, PA). HYDRANAL®-Coulomat AD, NaCl, fructose, glucose, maltose, mannose, sucrose, and trehalose were from Sigma-Aldrich (St. Louis, MO). Lactose was from Sheffield Bioscience (Norwich, NY, USA). PBS was from Invitrogen (San Diego, CA). Water was obtained from a Milli-Q Synthesis ultrapure water system (Millipore; Billerica, MA). Centrifugal filter devices (Amicon Ultra-0.5, Ultracel-10 Membrane, 10 kD) were purchased from Millipore (Billerica, MA).

8.2.2. Synthesis of Dex-P. The procedure to prepare Dex-P has previously been reported [35]. Briefly, 300 mg Dex was dissolved in 12 mL pyridine to which 578 mg palmitoyl chloride was added in a dropwise manner. The mixture was stirred in the dark under nitrogen for 24 h. The solvent was evaporated using a stream of nitrogen, and the dried product was dissolved in dichloromethane prior to loading onto a 30 mL silica gel column. The purified product was obtained using a dichloromethane to dichloromethane:ethyl acetate (6:4 v/v) gradient elution. The reaction progress was monitored using silica gel TLC with a chloroform:ethyl acetate (7:3 v/v) mobile phase. Retention factors for Dex and Dex-P were 0.10 and 0.69, respectively.

8.2.3. SLN Preparation. SLNs were prepared using NET as previously described [131]. The process consists of three steps: 1) melting an appropriate mixture of lipid, surfactants, long-chain PEGylating agents, and drug; 2) adding a pre-heated aqueous phase with stirring to generate an o/w microemulsion; and 3) cooling the microemulsion to form a suspension of SLNs. For this study, microemulsions were prepared at 70°C in order to ensure the melting of all components, and SLNs were cooled in a room temperature water bath. The formulation composition was 1.6 mg/mL SA, 0.4 mg/mL PS60, 2.8 mg/mL Brij® 78, and 3.0 mg/mL PEG6000MS. Where appropriate, Dex-P was added at 0.16 mg/mL, or the equivalent of a 10% drug load (w/w comparison with SA). SLNs designed for lyophilization were prepared in Milli-Q water, whereas SLNs designed to be stored as aqueous suspensions were prepared in 0.9% NaCl. SLNs were filtered using a 0.2 μm nylon membrane prior to lyophilization. SLNs were lyophilized using an FTS Systems Dura-Dry MP/Dura-Stop MP lyophilizer System (SP Scientific, Warminster, PA). Specific lyophilization protocols are described in detail below.

8.2.4. General SLN Characterization Techniques

8.2.4.1. DLS. Particle size and PI values were obtained using a Delsa™ Nano Zeta Potential and Submicron Particle Size Analyzer (Beckman Coulter Inc., Brea, CA). All measurements were performed at 25°C following a 1:30 dilution with Milli-Q water.

8.2.4.2. Drug Loading and Encapsulation Efficiency. The following HPLC conditions were used for determination of the Dex-P concentration: Alltech C18 column (5 µm, 250 mm×4.6 mm), 95:5 ACN:H_2O mobile phase run at 2 mL/min, and UV detection at λ=240 nm. A standard curve was developed in the range of 10-200 µg/mL using three samples at five concentrations (shown in chapter 5). Drug loading and encapsulation efficiency were determined using a two-step process. Drug loaded SLNs were first filtered through a 0.2 µm nylon membrane to remove any unsolubilized drug. Filtered SLNs (termed MF) were then ultrafiltered (Amicon YM-10, 10K MWCO) to remove free drug, and the retentate was collected. One hundred microliters each of the initial, MF, and retentate samples were diluted to 500 µL with MeOH, and 10 µL were injected onto the HPLC column. Encapsulation efficiencies were calculated by comparing the amount of drug remaining in the retentate to that in the initial sample.

8.2.5. Optimization of the Lyophilization Process

8.2.5.1. Effect of LP Type and Concentration: Freeze-thaw study. SLNs (1 mL) were added to 7 mL vials containing potential LPs. Nine LPs (glucose, fructose, mannose, trehalose, maltose, sucrose, lactose, PVA, and PVP) were tested at four concentrations: 0.5:1, 1:1, 2:1, and 5:1 (LP:SA weight ratio). An additional sample lacking any LP was used as a control. Following an overnight freezing at -20°C, samples were thawed at room temperature and evaluated for particle size/PI by DLS.

8.2.5.2. Effect of LP Type and Concentration: Lyophilization Study. SLNs (1 mL) were added to 7 mL vials containing fructose, mannose, maltose, or sucrose. Four LP:SA ratios were used (5:1, 10:1, 15:1, and 20:1). Three samples were prepared per condition, and an additional three control samples were prepared without LP. The following lyophilization protocol was used: freezing at -40°C on a pre-cooled shelf for 2 h, primary drying at -20°C for 24 h using a vacuum of 100 mTorr, and secondary drying at 20°C for 16 h using a vacuum of 100 mTorr. SLNs were reconstituted to their original volume with Milli-Q water using manual shaking, and the particle size and PI were determined by DLS.

8.2.5.3. Effect of SLN Concentration. SLNs were prepared at 1x, 5x, and 10x the original concentration, i.e., the 1x, 5x, and 10x samples contain 1.6, 8, and 16 mg/mL SA, respectively. Sucrose was added at either a 15:1 sucrose:SA weight ratio or at a fixed 2.4% w/v concentration (n=3 per condition). Lyophilization and reconstitution were conducted as described above, and the particle size and PI were determined by DLS.

8.2.5.4. Effect of Secondary Drying Time. SLNs were lyophilized using a 15:1 sucrose:SA weight ratio. Lyophilized samples were reconstituted to the original volume using Milli-Q water, and DLS was used for measurement of the particle size and PI (n=3). The lyophilization protocol was as follows: freezing at -40°C for 2 h on a precooled shelf, primary drying at -20°C for 24 h, and secondary drying at 20°C for either 0, 8, or 16 h. A vacuum of 100 mTorr was used during both drying steps.

8.2.5.5. Effect of Freezing Temperature and Rate. SLNs were lyophilized using a 15:1 sucrose:SA weight ratio. Lyophilized samples were reconstituted to the original volume using Milli-Q water, and DLS was used for measurement of the particle size and PI (n=3). For the evaluation of the temperature effect, temperatures of -20°C, -40°C, and -80°C were used in the 2 h freezing period; the rest of the lyophilization protocol was the same as described above. In order to compare the rate effect, SLNs were either frozen at -20°C on a precooled shelf for 2 h ("fast" freeze) or placed on a room temperature shelf, cooled to -20°C at a rate of 0.5°C/min, and then allowed to sit at -20°C for an additional 2 h ("slow" freeze). The primary and secondary drying conditions were the same as described above.

8.2.5.6. Effect of Reconstitution Media. SLNs prepared in Milli-Q water were lyophilized with a 15:1 sucrose:SA weight ratio. The lyophilization protocol was as follows: freezing at -20°C on a precooled shelf for 2 h, primary drying at -20°C for 24 h using a vacuum of 100 mTorr, secondary drying at 20°C for 16 h using a vacuum of 100 mTorr. SLNs were reconstituted to the original volume using either Milli-Q water, 0.9% NaCl, or PBS. The effects on particle size and PI were determined by DLS (n=3). Osmolality measurements (n=3) were performed using a Fiske 110 Osmometer (Advanced Instruments, Inc., Norwood, MA, USA). The instrument was calibrated with 50, 290, and 850 mOsm/kg standards.

8.2.5.7. Effect of Drug Loading. SLNs loaded with 10% Dex-P and control blank SLNs were lyophilized using a 15:1 sucrose:SA weight ratio. The lyophilization protocol was as follows: cooling from room temperature to -20°C at 0.5°C/min, a 2 h hold at -20°C, primary drying at -20°C for 24 h using a vacuum of 100 mTorr, secondary drying at 20°C for 16 h using a vacuum of 100 mTorr. SLNs were reconstituted to the original volume using Milli-Q water, and the particle size and PI were determined using DLS (n=3).

8.2.5.8. Batch-to-Batch Variability. Three batches of SLNs with and without 10% Dex-P were lyophilized on separate days (n=3/batch). A sucrose:SA weight ratio of 15:1 was used, and the lyophilization process was as follows: cooling from room temperature to -20°C at 0.5°C/min, a 2 h hold at -20°C, primary drying at -20°C for 24 h using a vacuum of 100 mTorr, secondary drying at 20°C for 16 h using a vacuum of 100 mTorr. SLNs were reconstituted to the original volume with Milli-Q water, and the particle size and PI were measured by DLS.

8.2.5.9. Evaluation of the Optimized Lyophilized Product. Prior to reconstitution, the lyophilizate was evaluated for water content using a Metrohm 684 Karl Fischer coulometer equipped with a Metrohm 703 titration stand. Lyophilized SLNs (1-3 mg) were dissolved in MeOH, and approximately 100 µL were added to the Karl Fischer reagent (HYDRANAL®-Coulumat AD). Corrections were made for the presence of water in the MeOH used to dissolve the samples. Following reconstitution, SLNs were evaluated for the presence of large aggregates using a SALD-7101 Laser Diffraction Particle Size Analyzer (Shimadzu Scientific Instruments, Columbia, MD, USA). To achieve an appropriate signal intensity, SLNs were diluted 2x with Milli-Q H_2O. Reconstituted SLNs were also analyzed by TEM. Images were obtained using a Philips Tecnai Biotwin 12 equipped with a Gatan ES 1000W CCD digital camera (FEI, Hillsboro, OR). A drop of sample (7 µL) was incubated for 1.5 min on a carbon coated

TEM grid. The grid was then dried and stained with 0.2 μm filtered 2% uranyl acetate for an additional 1.5 min. Excess stain was removed, and the grid was allowed to dry for 5 min prior to imaging. Drug loaded SLNs were also evaluated for encapsulation efficiency using the methods described above.

8.2.6. Stability Study. A 3 month stability study was conducted comparing 10% Dex-P loaded SLNs lyophilized prior to storage with those stored as aqueous suspensions. Lyophilization was conducted as follows: cooling from room temperature to -20°C at 0.5°C/min, a 2 h hold at -20°C, primary drying at -20°C for 24 h using a vacuum of 100 mTorr, secondary drying at 20°C for 16 h using a vacuum of 100 mTorr. A 15:1 sucrose:SA weight ratio was used. All vials were stoppered and crimped for storage. SLNs were stored under two conditions: 4°C or 25°C/60% relative humidity (RH). A saturated sodium bromide solution was used to control the RH [233]. At select time points [days 0, 1, 3, 7, 14, 28 (1 mo), 59 (2 mo), and 89 (3 mo)], SLNs were removed from storage for analysis (3 vials/condition). Lyophilized SLNs were reconstituted to their original volume (1 mL) with 0.9% NaCl, and all samples were tested for changes in the particle size/PI and encapsulation efficiency. These experiments were conducted as described above, with the exception that for samples that showed a particle size > 200 nm, one of the three replicates was filtered with a 0.45 μm nylon filter instead of a 0.2 μm nylon filter. This was done in an attempt to differentiate between drug loss due to the filtration of large particles and drug loss due to removal of unsolubilized drug. However, no differences were observed between the two filtration methods, and as such, data from all three samples were used in calculating average values.

8.2.7. Statistical Analysis. All data is presented as the mean ± SD of three independent measurements. For comparison of only two data sets, a t-test (paired two sample for means) was utilized. For comparison of 3 or more data sets, an analysis of variance (ANOVA, single factor) was performed. Results are considered statistically significant at a level of $p<0.05$.

8.3. RESULTS AND DISCUSSION

8.3.1. Optimization of the Lyophilization Process

8.3.1.1. Effect of LP Type and Concentration. In order to avoid numerous time-consuming lyophilization procedures, possible LPs were first evaluated by a freeze-thaw study. If the tested excipients are unable to provide protection against aggregation during the first step of the lyophilization protocol, i.e., freezing, they are unlikely to be suitable LPs. Based on previous literature reports [230], nine excipients were chosen for study: 3 monosaccharides (glucose, fructose, and mannose), 4 disaccharides (trehalose, maltose, sucrose, and lactose), and 2 polymers (PVA and PVP). Each excipient was tested at four different concentrations, all expressed as LP:SA weight ratios: 0.5:1, 1:1, 2:1, and 5:1. Following freezing at -20°C overnight, SLNs were thawed and evaluated for changes in the particle size and PI (Figure 8.1). In general, higher concentrations of excipient led to smaller increases in the particle size. It was observed that the two polymers were clearly the least effective in maintaining the particle size. Even at the highest concentrations, particles increased from approximately 95 nm to over 130 nm. Performance was better with the sugars, although there was no clear difference between the mono- and disaccharides. PI values followed a similar trend. As such, the two best performers from each sugar category were chosen for a full lyophilization study: fructose and mannose for the monosaccharides and sucrose and maltose for the disaccharides. At the highest concentrations, particle size increases were <10 nm and changes in the PI were negligible with these excipients.

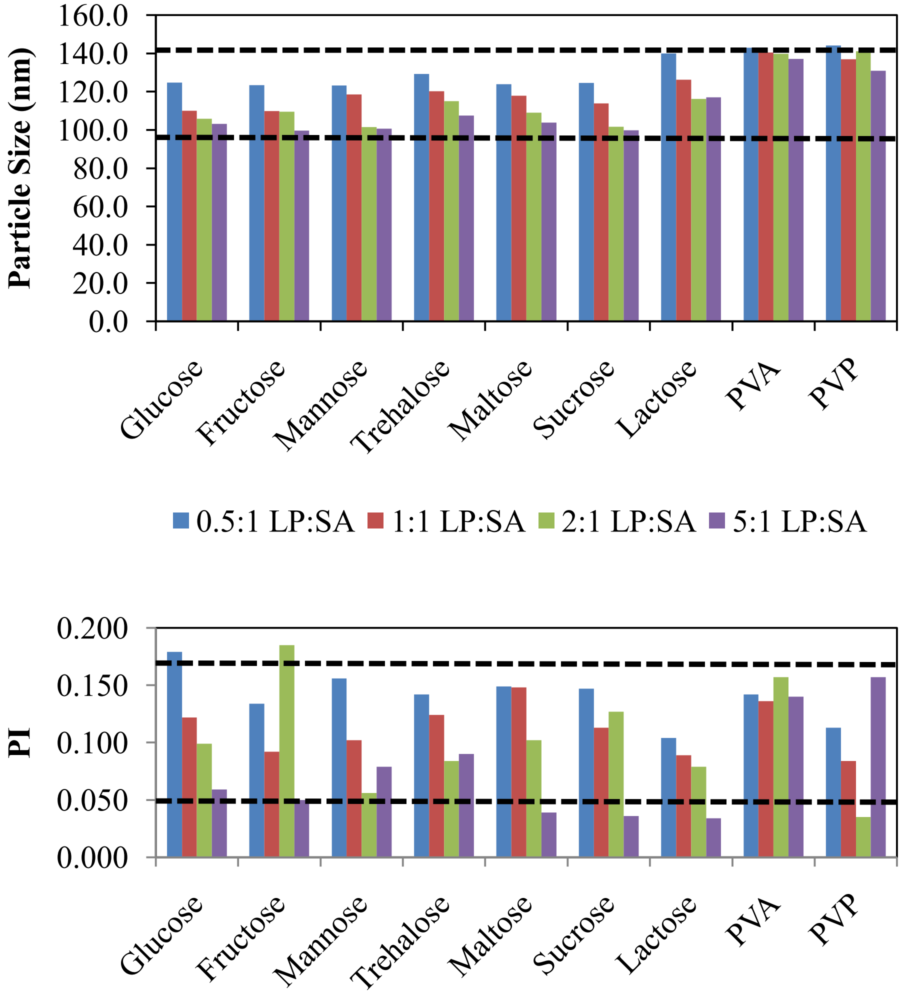

Figure 8.1. The effect of various LPs on the change in particle size (top) and PI (bottom) following an overnight freezing at -20°C and subsequent thawing. Excipients include 3 monosaccharides (glucose, fructose, and mannose), 4 disaccharides (trehalose, maltose, sucrose, and lactose), and 2 polymers (PVA and PVP). Each excipient was tested at four concentrations, all expressed in reference to SA (LP:SA weight ratio): 0.5:1, 1:1, 2:1, and 5:1. The bottom dotted line represents the original SLN condition: 95.5 nm and a PI of 0.047. The top dotted line represents the condition of SLNs frozen without any LP: 142.1 nm and a PI of 0.167.

Based on the trend of decreasing particle size with increasing LP concentration observed in the freeze-thaw study, higher concentrations were chosen for the lyophilization study. LP:SA ratios began at the 5:1 ratio used in the previous study and were raised to 10:1, 15:1, and 20:1. A basic lyophilization protocol was chosen for use: freezing at -40°C for 2 h on a precooled shelf, primary drying at -20°C/100 mTorr for 24 h, and secondary drying at 20°C/100 mTorr for 16 h. In this study, disaccharides were shown to better maintain the particle size and PI values of SLNs than monosaccharides (Figure 8.2). Specifically with fructose, particle size increases were large and variable. PI values were also higher (>0.2) than disaccharide samples (0.1-0.2). This is consistent with previous studies in which the use of disaccharides has been shown to be advantageous [146, 234]. It is thought that this is due to the ability of the disaccharides to solidify in an amorphous state while the monosaccharides crystallize upon freezing. Crystallization may decrease the ability of the excipient to interact with the SLNs and limit its ability to prevent aggregation.

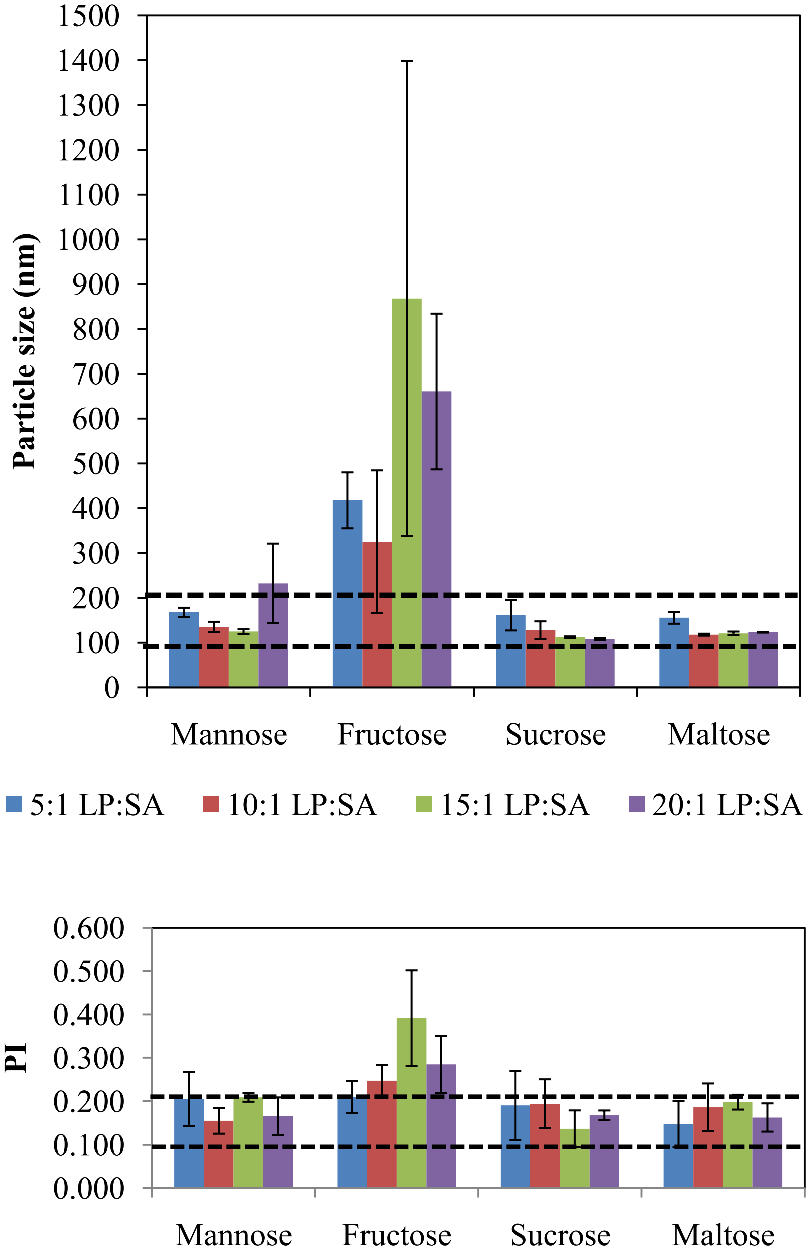

Figure 8.2. The effect of various LPs on the change in particle size (top) and PI (bottom) following lyophilization. Excipients included 2 monosaccharides (mannose and fructose) and 2 disaccharides (sucrose and maltose). Each excipient was tested at four LP:SA weight ratios: 5:1, 10:1, 15:1, and 20:1 (n=3). The bottom dashed line represents the initial SLN condition: 96.2 nm and a PI of 0.092. The top dashed line represents the condition of SLNs lyophilized without LP: 207.0 nm and a PI of 0.212.

Interestingly, increases in the LP concentration were not as clearly advantageous in the lyophilization study as they were in the freeze-thaw study. Sucrose was the only LP that showed a smaller particle size increase with higher concentration, and the reduction upon going from the 15:1 ratio to the 20:1 ratio was minimal. With all other LPs, there appeared to be a destabilization of the particles with higher LP concentrations (15:1 with fructose and maltose and 20:1 with mannose). This was somewhat surprising as most studies have reported that increasing the excipient concentration improves the maintenance of particle size [216, 235, 236]. However, there have been at least some reports of destabilization with higher LP concentrations [237, 238]. Unfortunately, there is currently a lack of understanding regarding what controls this. As has been reported, the most important parameter is the concentration of LP in the cryo-concentrated phase, which is determined by a competition between the diffusion rate of LP molecules and the freezing rate [231]. If diffusion of the LP molecules is limited (for example, because of high viscosity), the LP may be retained in the bulk frozen state as opposed to entering the cryo-concentrated phase. It may be that there is a certain critical LP concentration at which the freezing rate becomes faster than the diffusion step, and particle aggregation results. Alternatively, it has been proposed that the sugar molecules hydrogen bond with the PEGylated surfaces of nanoparticles [230], and it is possible that at high concentrations, this could lead to particle bridging.

Based on these studies, sucrose at a LP:SA ratio of 15:1 was chosen as the optimal LP concentration. This equates to 2.4% w/v and is a considerably lower LP concentration than has been used with numerous other nanoparticle systems [232, 239]. Under these conditions, particles increased in size by <17% and remained within a size range appropriate to take advantage of the EPR effect [29]. Although the particle size distribution broadened, it also remained within the range of PI values (PI<0.3) considered acceptably monodisperse [240, 241]. Additional studies were aimed at optimizing the lyophilization protocol in order to potentially limit changes to an even greater degree.

8.3.1.2. Effect of SLN Concentration. It has previously been observed with polymeric nanoparticles that a higher nanoparticle concentration can lead to improved redispersibility following reconstitution [242]. To determine whether this was the case with the SLN system under consideration, nanoparticles were prepared at 1x, 5x, and 10x the original concentration, lyophilized, and evaluated for particle size changes. Results are shown in Table 8.1. Surprisingly, only the 1x SLN sample could be easily reconstituted. All other samples remained cloudy, despite showing relatively small particle sizes. This may be partially attributed to the dilution step required for particle size measurement, during which large aggregates may dissolve. For comparison, the 5x and 10x samples were diluted to the 1x concentration and re-analyzed, but the results were not improved. Finally, to determine if it was the overall sucrose concentration and not the LP:SA ratio that led to good redispersibility, SLNs prepared at 5x and 10x were lyophilized in the presence of 2.4% w/v sucrose and evaluated for particle size changes. In this case, the samples were very cloudy following reconstitution, and the particle size increases were larger. The higher SLN concentrations may prevent the formation of the protective amorphous shell around the nanoparticles, possibly for similar reasons to those described earlier with higher LP concentrations. Results may be improved by using lower

SLN concentrations, but this would be undesirable for achieving a sufficiently high drug dose.

Table 8.1. Effect of SLN concentration on redispersibility

SLN Concentration	Initial		15:1 LP:SA Ratio		15:1 LP:SA Ratio + Dilution		2.4% LP	
	Particle size (nm)	Visual Appearance	Particle size (nm)	Visual Appearance	Particle size (nm)	Visual Appearance	Particle size (nm)	Visual Appearance
1x	97.8	clear	116.4±1.6	clear	N/A	N/A	N/A	N/A
5x	98.4	clear	125.6±2.7	cloudy	123.5±4.6	cloudy	180.1±17.0	very cloudy
10x	102.3	clear	154.5±10.3	cloudy	161.1±17.1	cloudy	424.7±108.1	very cloudy

8.3.1.3. Effect of Secondary Drying Time. The effects of the secondary drying time on the particle size and PI of the SLNs are shown in Figure 8.3. No clear trend was evident, with the 8 h drying time resulting in slightly higher (though not statistically significant, P>0.05) particle size increases and PI values than that of either the 0 h or 16 h drying time. The smallest average values were obtained for the 16 h drying time. Based on this data and a desire to ensure the least residual moisture content, a 16 h secondary drying time was chosen for further studies.

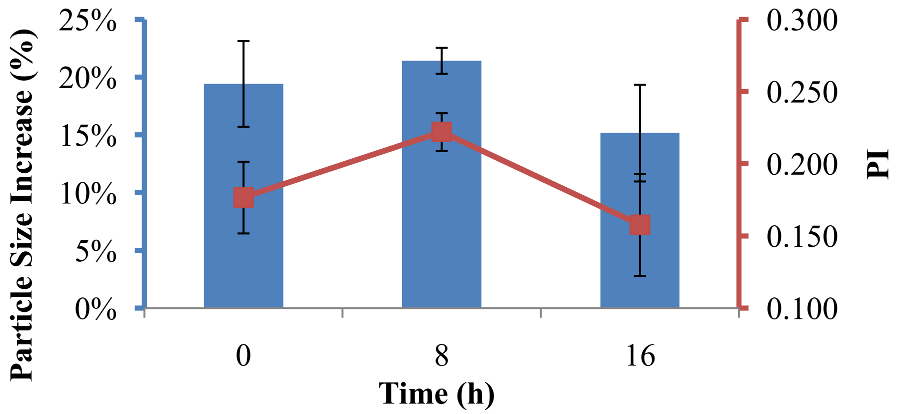

Figure 8.3. The effect of secondary drying time on the particle size and PI of SLNs following lyophilization in the presence of a sucrose:SA 15:1 weight ratio (n=3)

8.3.1.4. Effect of Freezing Temperature and Rate. The effects of freezing temperature and rate were evaluated together because they are inherently related. Lower freezing temperatures lead to faster freezing rates. However, to attempt to separate the two effects, three different temperatures were tested initially, and then direct comparisons were made between two different freezing methods at the "optimal" temperature. A clear trend in the redispersibility of the SLNs was observed with freezing temperature when the fast freeze method was employed (Figure 8.4). As the temperature decreased, both the particle size and PI increases became larger. With a -20°C freeze, the particle size increased by only 12.4±2.0%, and the average PI was 0.177±0.025. For comparison, samples were then frozen to -20°C using a slow freeze and evaluated for redispersibility (Figure 8.5). Although the fast freeze samples trended toward a smaller particle size, the difference was not statistically significant ($p>0.05$). On the other hand, the slow freeze samples exhibited a statistically significant smaller PI value ($p<0.05$).

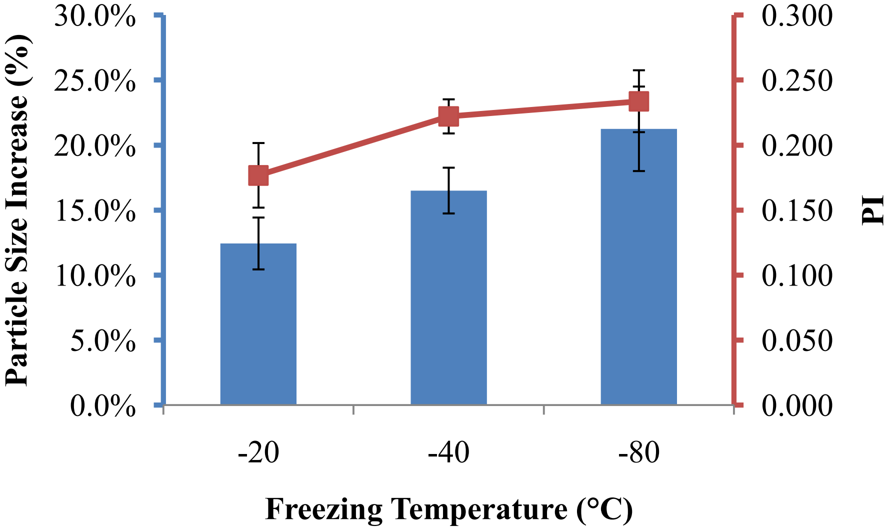

Figure 8.4. The effect of freezing temperature on the particle size and PI of SLNs following lyophilization in the presence of a sucrose:SA 15:1 weight ratio (n=3)

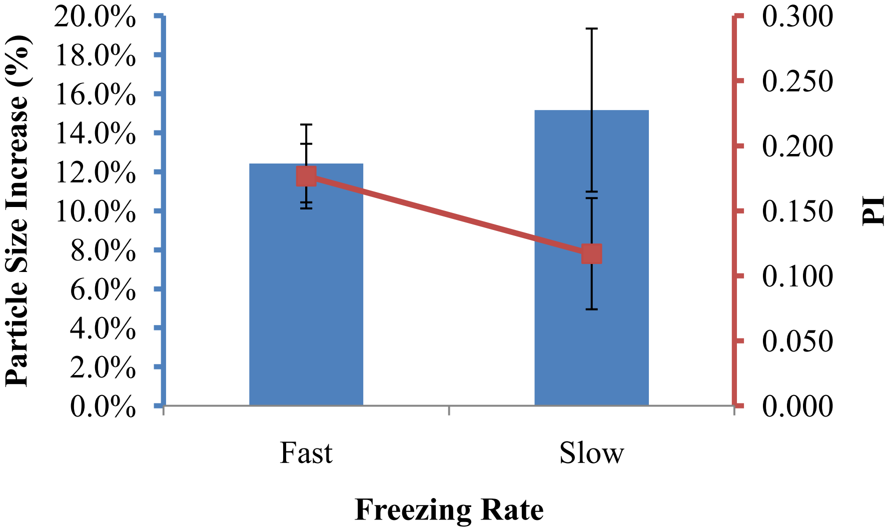

Figure 8.5. The effect of freezing rate (-20°C freeze) on the particle size and PI of SLNs following lyophilization in the presence of a sucrose:SA 15:1 weight ratio (n=3)

These results were again somewhat surprising in light of other literature reports. Most studies have reported an improvement in redispersibility with lower temperatures and faster freezing rates [231, 232, 242, 243]. This is primarily because a faster freezing rate should result in smaller ice crystals that result in less mechanical stress on the particles. However, if the freezing rate is too fast to allow partitioning of the LP molecules into the cryo-concentrated phase, this benefit may be negated, as it apparently is with these SLNs. Overall, it appeared clear that better redispersibility could be obtained with a -20°C freezing temperature, and that although a slower freezing rate at that temperature did not significantly affect the particle size change, it may reduce the change in the particle size distribution (PI of 0.117±0.043 for slow freeze vs PI of 0.177±0.025 for fast freeze).

8.3.1.5. Effect of Reconstitution Media. Although SLNs could be reconstituted with water, it may be preferable to use alternative solutions for reconstitution, either for certain lab situations or to satisfy clinical requirements. For example, a 2.4% w/v sucrose solution would be considered hypo-osmotic and may be unsuitable for injection. For this reason, SLNs reconstituted in H_2O, 0.9% NaCl (used commonly for reconstitution in clinical situations), and PBS (used commonly in lab situations to mimic physiological conditions) were compared (Table 8.2). No difference was observed among the particle size and PI values for the three solutions as determined by ANOVA, indicating that a variety of solutions could be used for reconstitution without significantly impacting the properties of the SLNs. Specifically, samples reconstituted with 0.9% NaCl were slightly hyperosmotic but remained within a clinically relevant range [244].

Table 8.2. Effect of the reconstitution media on SLN properties

Reconstitution Media	Size (nm)	PI	Osmolality (mOsm/kg)
H_2O	101.6±1.8	0.177±0.025	74.8±1.1
0.9% NaCl	104.2±4.3	0.171±0.027	350.9±2.2
PBS	102.0±2.3	0.223±0.020	382.8±4.0

8.3.1.6. Effect of Drug Loading. Drug loading has been shown to significantly impact nanoparticle redispersibility in some situations [239] but not in others [245]. The difference was primarily attributed to the presence of free drug in solution. As Dex-P loaded SLNs typically display very high encapsulation efficiencies (only 1-2% free drug following 0.2 μm filtration), this was not expected to be a limiting factor. However, in experiments designed to test this, it was observed that SLNs loaded with 10% Dex-P w/w SA showed slightly larger particle size increases and slightly higher PI values than blank SLNS (Figure 8.6). This may be a result of the small amount of free drug present in solution or to a difference in the surface properties of the SLNs with drug loading. Either way, the changes with drug loading are not expected to impair the ability of the SLNs to function as a drug delivery system. With the 22.50% increase in particle size, the particle size increased only to 123.2±0.8 nm, which is well within the 200 nm size limit considered appropriate for taking advantage of the EPR effect [29]. The PI also remained within a range considered suitably monodisperse [240, 241].

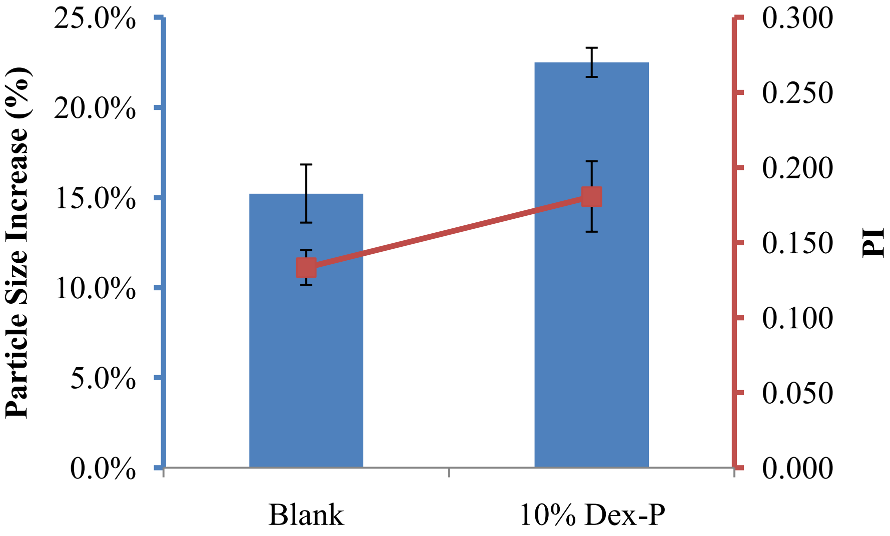

Figure 8.6. The effect of drug loading on the particle size and PI of SLNs following lyophilization in the presence of a sucrose:SA 15:1 weight ratio (n=3)

8.3.1.7. Batch-to-Batch Variability. Although intra-batch variability was minimal as evidenced by the standard deviations given above, it was important to evaluate batch-to-batch variability. As shown in Table 8.3, batches of both blank and 10% Dex-P loaded SLNs prepared on different days using the same protocol appeared to be of similar quality. ANOVA tests revealed no statistically significant differences in either the particle size or PI of SLNs prepared on different days (p>0.05).

Table 8.3. Batch-to-Batch variability

Day	Particle Size Increase (%)		PI	
	Blank	10% Dex-P	Blank	10% Dex-P
1	15.22±1.61%	22.50±0.81%	0.133±0.012	0.181±0.023
2	15.16±4.18%	24.22±1.80%	0.117±0.043	0.161±0.009
3	14.91±1.39%	27.50±0.83%	0.171±0.027	0.152±0.046

8.3.1.8. Evaluation of the Optimized Lyophilized Product. Lyophilized products were shown to have a low water content of 1.09±0.12%, a value considered acceptable for lyophilized pharmaceuticals [246]. Following reconstitution, SLNs were evaluated for the presence of large aggregates by laser diffractometry (LD) and for shape changes by TEM. Although DLS is preferable for analyzing particles in the nanometer range, it has a limited range of analysis for particles in the micrometer or millimeter range. For example, the Delsa™ Nano instrument used in these studies has an analytical range of 0.6 nm-7 μm. LD can be used as a complementary technique for evaluation of larger particles; the Shimadzu SALD-7101 instrument used in these studies was designed to study particles in the range of 0.01-300 μm. Both blank and drug-loaded SLNs appeared monodisperse with median diameters (D50%) of 247 and 257 nm, respectively. Representative particle size distributions are shown in Figure 8.7. The different particle sizes obtained from the two techniques can be explained by the different measurement principles. Of relevance for this study is that large aggregates did not appear to be present to any significant extent. Analysis of the reconstituted SLNs by TEM further indicated that the particle shape was maintained throughout the lyophilization and reconstitution process (Figure 8.8).

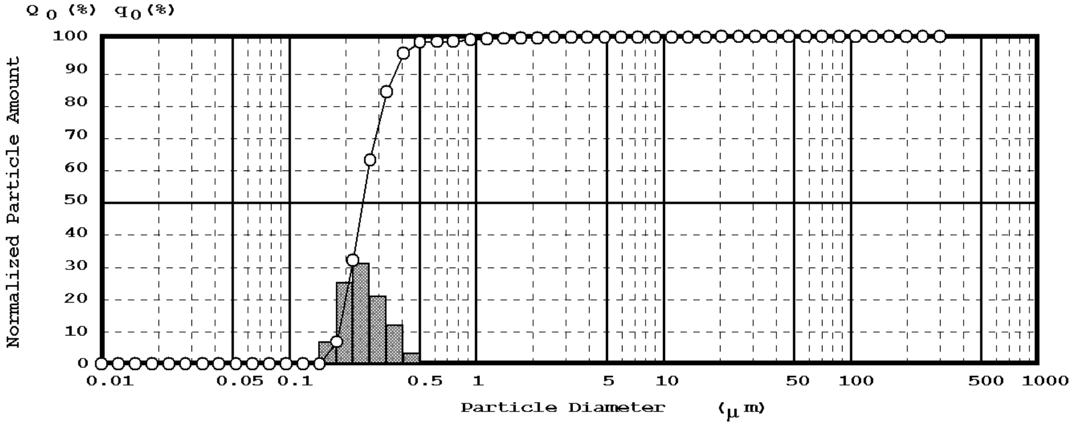

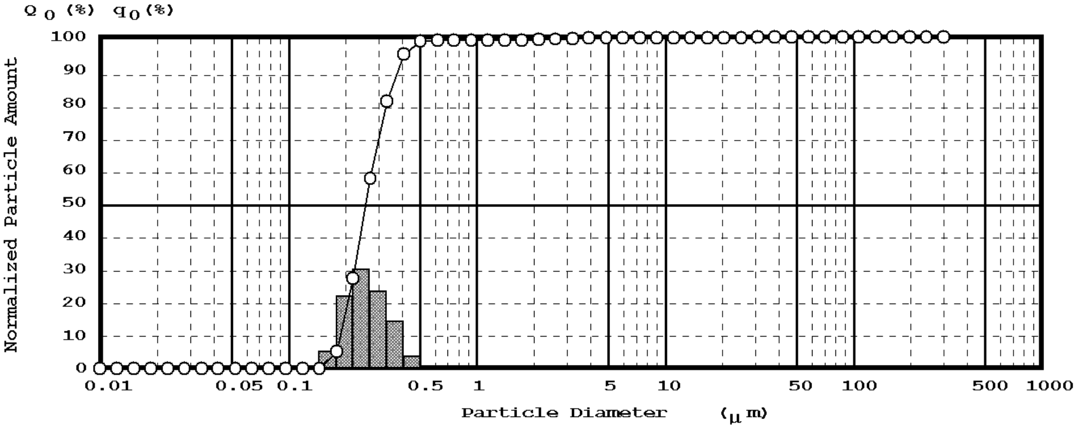

Figure 8.7. Representative particle size distributions obtained by laser diffractometry of SLNs following lyophilization and reconstitution (Blank SLNs, top; 10% Dex-P loaded SLNs, bottom)

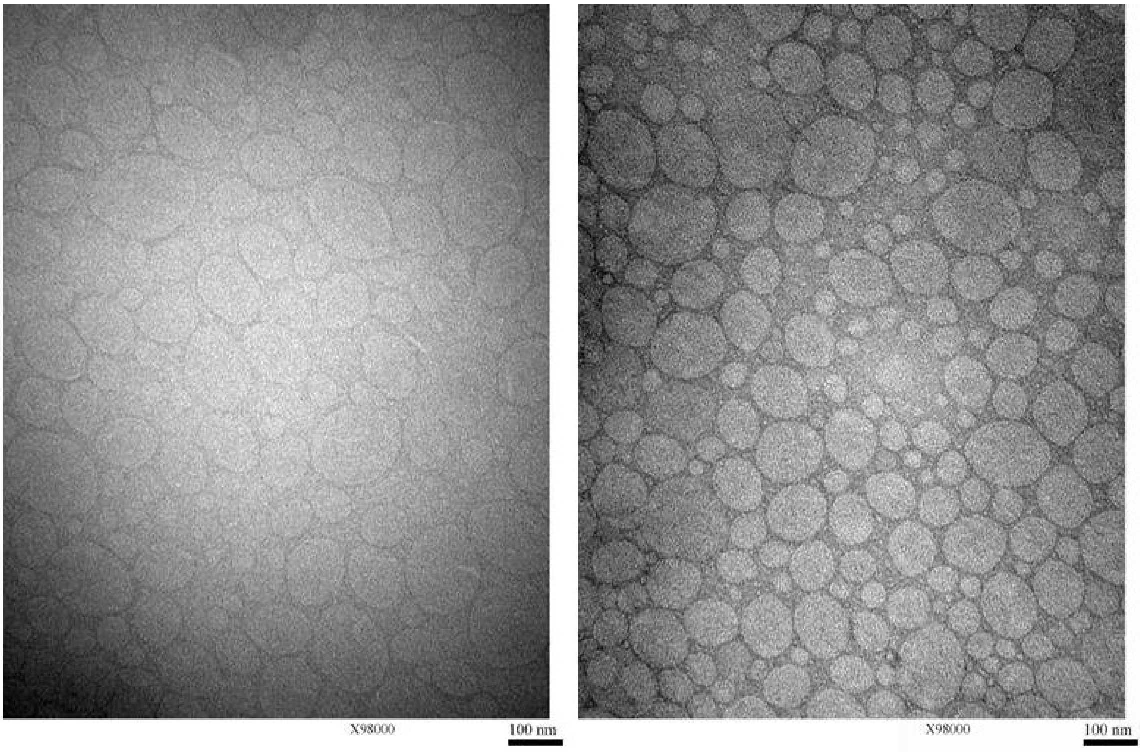

Figure 8.8. Representative TEM images of blank (left) and 10% Dex-P loaded SLNs (right) following lyophilization and reconstitution

Finally, drug loaded SLNs were evaluated for encapsulation efficiency. A number of studies have shown drug loss upon lyophilization as a result of lipid crystallization or phase transitions [235, 247]. However, this was not observed to any significant extent with the Dex-P loaded SLNs. Drug was shown to remain predominately associated with SLNs (97.98±1.83% retention), confirming that SLNs could be lyophilized using this protocol with minimal changes to the physicochemical properties of the nanoparticles.

8.3.2. Stability Study. Once the lyophilization protocol was optimized to minimize changes in the physicochemical properties of the SLNs, lyophilized SLNs were evaluated for stability over a 3 month time period. Two possible storage conditions were tested

(4°C and 25°C/60% RH), and comparisons were made with SLNs stored as aqueous suspensions. Particle size and PI data are shown in Figures 8.9 and 8.10. The most significant particle size growth was observed with the aqueous suspensions stored at 25°C/60% RH. With the particle size reaching nearly 500 nm within 3 months, the system would be considered unacceptable for use as a tumor-targeted drug delivery system in most cases. SLN suspensions stored at 4°C also showed growth, but it was much less than that observed at 25°C/60% RH. The particle size increased <40 nm, remaining well within the recommended 200 nm limit [29]. On the contrary, lyophilized SLNs showed greater consistency in their particle size measurements. The particle size of lyophilized SLNs stored at 4°C was maintained across the entire time period of the study. Lyophilized SLNs stored at 25°C/60% RH were stable up to 1 month prior to showing a slight increase in the particle size. In terms of PI values, all remained <0.3, generally considered the acceptable limit of monodispersity [240, 241]. However, increases were also observed over the 3 month time period with all conditions. Although the lowest absolute values were obtained with the aqueous suspension stored at 4°C, the increase over the time period of the study was smallest with the lyophilized SLNs stored at 4°C.

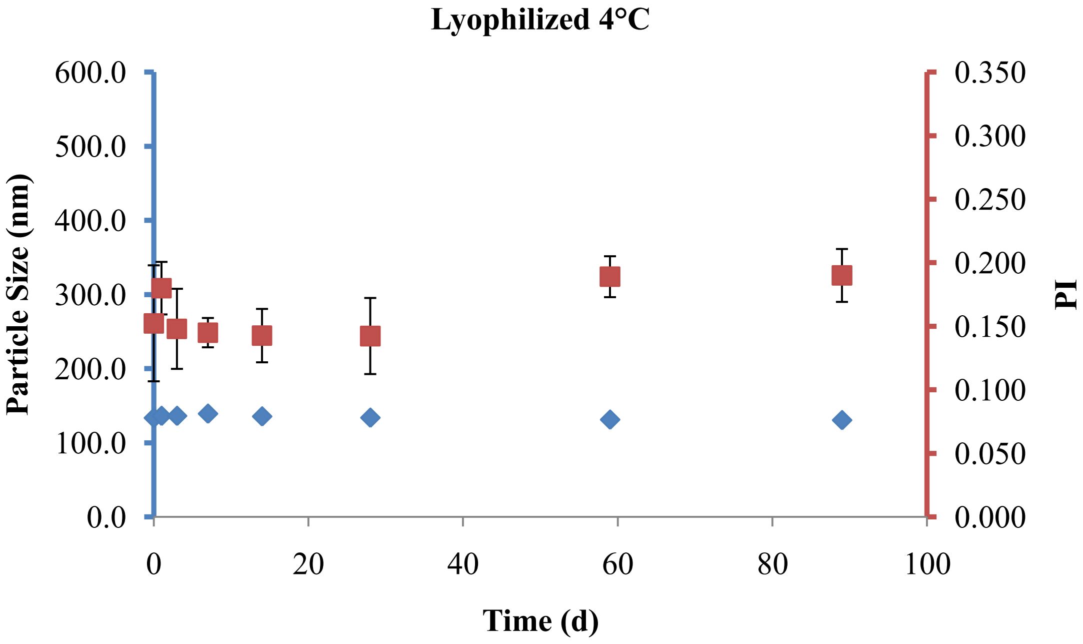

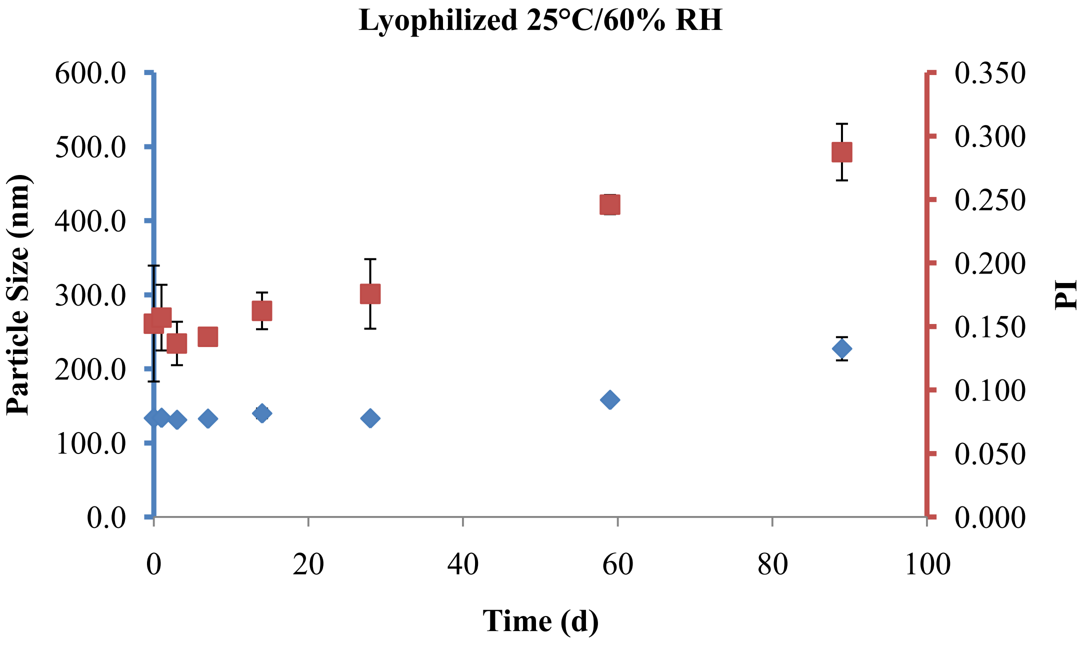

Figure 8.9. Changes in the particle size and PI of lyophilized SLNs stored at either 4°C or 25°C/60% RH over a 3 month time period (n=3)

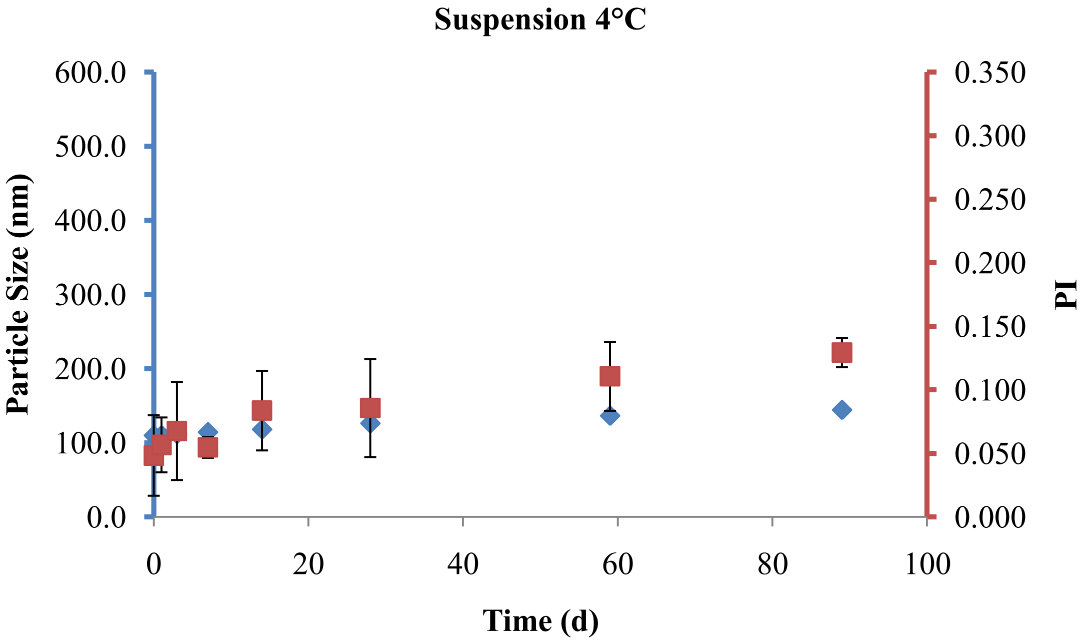

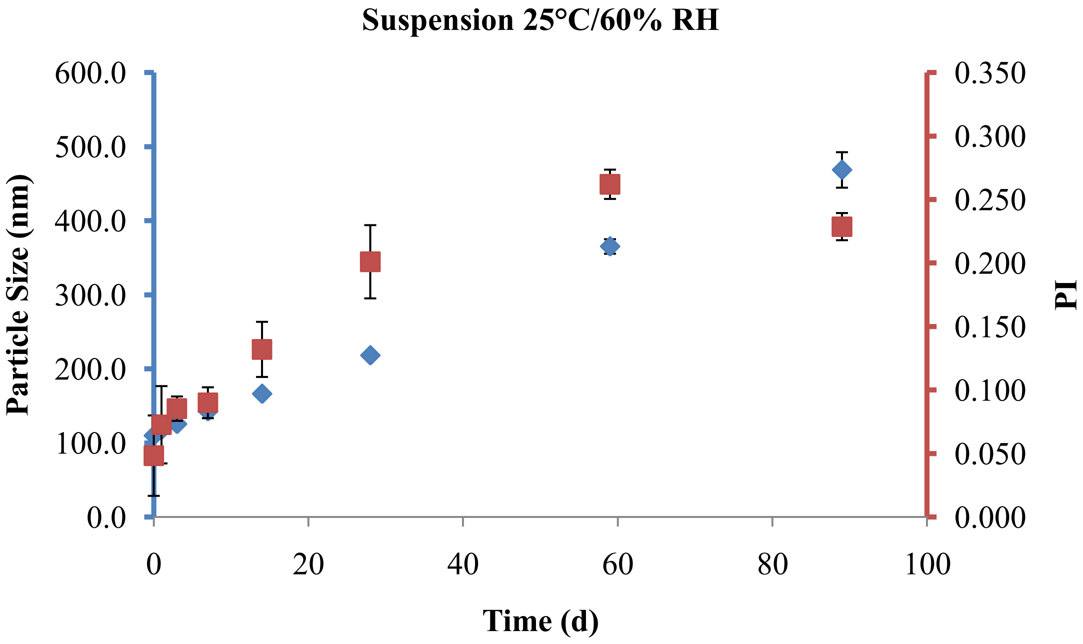

Figure 8.10. Changes in the particle size and PI of SLNs stored as aqueous suspensions at either 4°C or 25°C/60% RH over a 3 month time period (n=3)

In analyzing the drug loading, the first step was to confirm that the drug concentration in the samples remained stable across the time period of the study (Figure 8.11). Comparing drug concentrations of each sample to the day 0 sample, it appeared that virtually 100% of the drug remained in the Dex-P form with no noticeable hydrolysis. Following this confirmation, it was then necessary to determine how much Dex-P remained associated with the SLNs. A two-step process was used in which any unsolubilized drug is removed by 0.2 µm (or 0.45 µm) filtration and free drug is removed by ultrafiltration. Figures 8.12 and 8.13 provide information regarding the drug retention following each step. The data generally echoed that observed with the particle size changes. SLNs stored as aqueous suspensions at 25°C/60% RH exhibited the most significant drug loss. This drug loss was consistent across the entire time period, with the exception of the final time point. Interestingly, the other three samples seemed to exhibit a "plateau" encapsulation efficiency in the range of 75-80%. However, they differed in how long it took to achieve this plateau, how long the plateau was maintained, and whether the drug loss was primarily associated with the 0.2 µm filtration step or the ultrafiltration step. Aqueous suspensions stored at 4°C showed decreasing encapsulation efficiency up to 2 weeks and then remained approximately consistent at 75%. Lyophilized SLNs stored at 4°C showed a drop in encapsulation efficiency at the 3 day mark but then remained at approximately 80% encapsulation efficiency. Results with the lyophilized SLNs stored at 25°C/60% RH were similar but could not be maintained. As the particle size began to increase following 1 month of storage, drug loss was also accelerated. With both sets of lyophilized samples, drug loss due to the 0.2 µm filtration step was fairly consistent and less than that lost during the ultrafiltration step. The trend was opposite with the samples stored as aqueous suspensions with the drug loss being predominantly controlled by the 0.2 μm filtration step. The difference may be associated with Dex-P exhibiting varying solubility in the presence and absence of sucrose, as has been observed with other compounds [248].

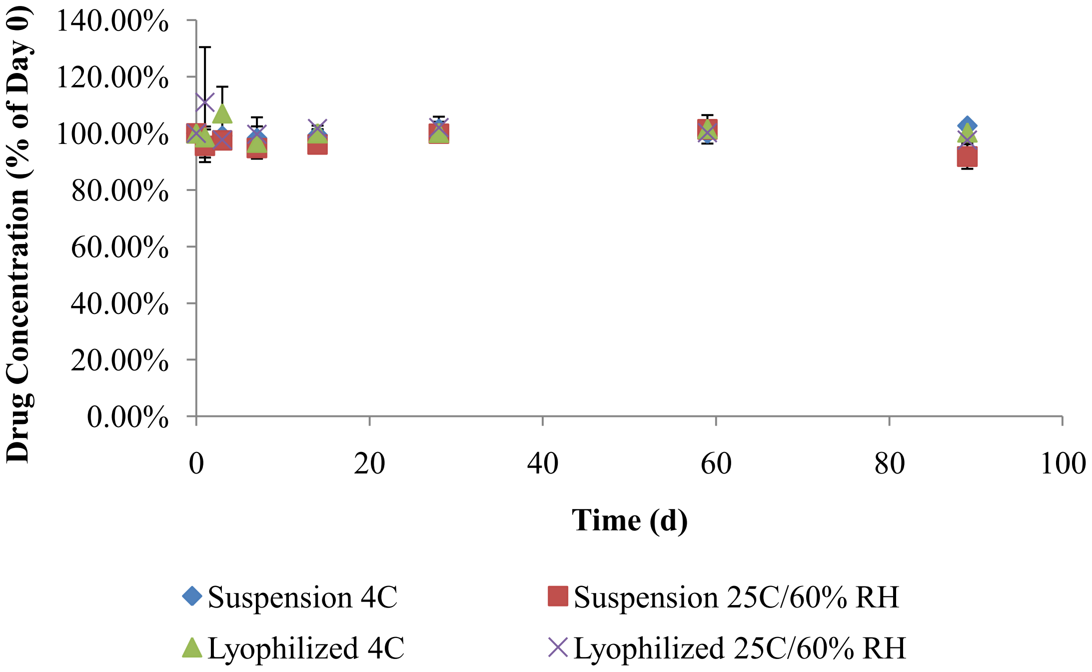

Figure 8.11. Stability of drug concentration in SLN samples over a 3 month time period (n=3)

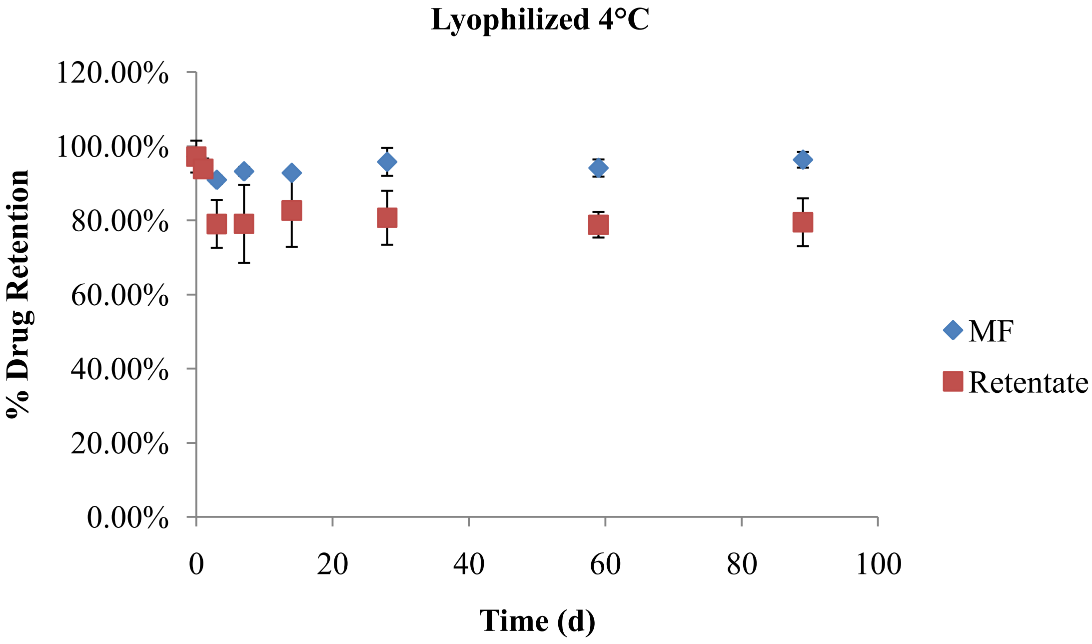

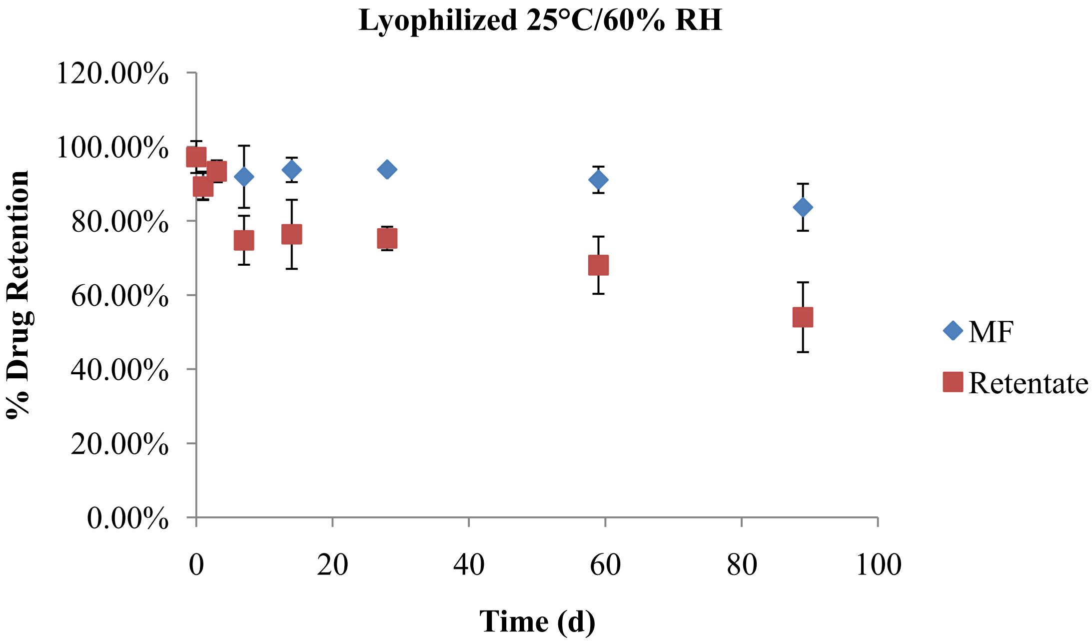

Figure 8.12. Changes in the drug encapsulation efficiency of lyophilized SLNs stored at either 4°C or 25°C/60% RH over a 3 month time period (n=3). Data is expressed as % drug retention and is separated into the Dex-P concentration found in the 0.2 µm filtrate (MF) and the retentate collected following ultrafiltration.

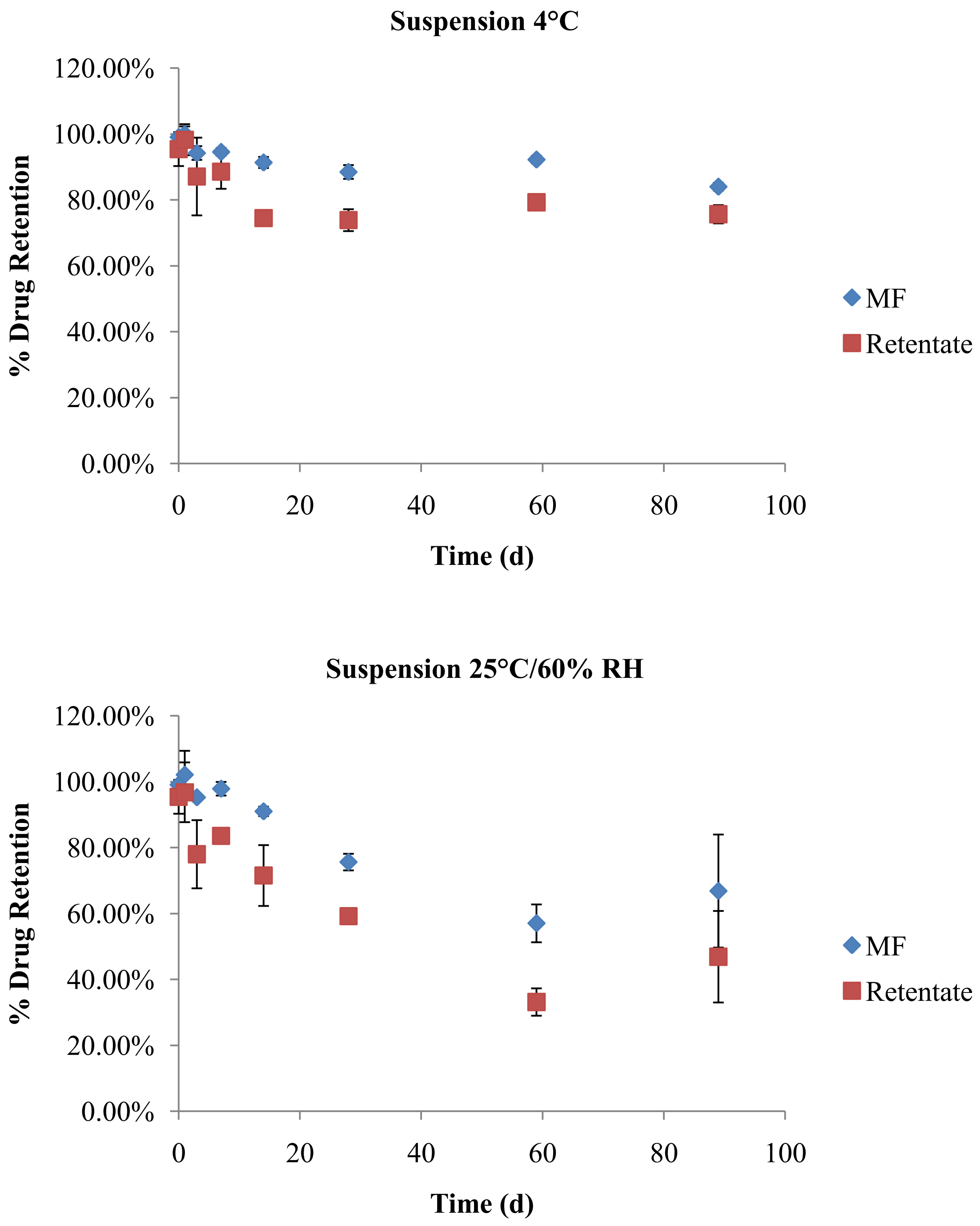

Figure 8.13. Changes in the drug encapsulation efficiency of SLNs stored as aqueous suspensions at either 4°C or 25°C/60% RH over a 3 month time period (n=3). Data is expressed as % drug retention and is separated into the Dex-P concentration found in the 0.2 µm filtrate (MF) and the retentate collected following ultrafiltration.

Overall, lyophilized SLNs stored at 4°C seemed to exhibit the greatest stability. Based on the slight decrease in encapsulation efficiency, there appeared to be some restructuring of the particle. However, this did not affect the particle size, and once it was complete, the encapsulation efficiency remained constant throughout the rest of the study. Further, with a size of approximately 130 nm and an encapsulation efficiency of around 80%, SLNs stored under these conditions could be considered suitable for use as tumor-targeted drug delivery system.

8.4. CONCLUSIONS

In this section, an optimized protocol for lyophilization of SLNs was developed, and comparisons were made between the long-term stability of aqueous and lyophilized SLNs. Of nine possible lyoprotectants tested, sucrose was shown to provide the best particle redispersibility. Specifically, a 15:1 sucrose:SA weight ratio was chosen based on the minimal increase in particle size and PI observed with this condition. A series of experiments also showed that better redispersibility could be obtained using lower SLN concentrations, higher freezing temperatures, slower freezing rates, and longer secondary drying times. The choice of reconstitution media was shown to have a negligible effect on the particle redispersibility. Larger particle size and PI increases following lyophilization were observed with drug loaded SLNs, but both parameters remained within an acceptable range for a tumor-targeted nanoparticle drug delivery system. Encapsulation efficiency and particle shape were maintained following lyophilization, and no large aggregates could be detected. Lyophilized SLNs stored at 4°C exhibited the greatest stability during the 3 month study. Particle size was maintained across the entire time period. A slight reduction in encapsulation efficiency was observed within the first 3 days of storage but then remained consistent at approximately 80%.

Chapter 9

Summary and Conclusions

The guiding hypothesis for this dissertation was that the interactions among the components of SLNs decrease the crystallinity of nanoparticle lipids resulting in enhanced drug loading and decreased nanoparticle stability. To this end, the following specific aims were identified: 1) to fully characterize nanotemplate engineered SLNs for their physicochemical properties including particle size, shape, structure, and changes in the extent or type of crystallinity from the starting materials due to interactions among the nanoparticle components, 2) to assess the degree of loading of Dex-P into nanotemplate engineered SLNs compared to other compounds of similar structure or lipophilicity, 3) to evaluate the stability of nanotemplate engineered SLNs in conditions mimicking those of human plasma as a function of time, 4) to determine if the PEGylating agents incorporated into SLNs are affected by the CE activity of the surrounding environment, and 5) to determine if the storage stability of drug loaded SLNs is enhanced when using lyophilization protocols that minimize changes in the physicochemical properties of the nanoparticles.

Based on early work from this laboratory, two formulations were chosen for evaluation. SA was used as the lipid phase with Brij® 78 and PS60 as surfactants in both formulations; the second formulation differed by the inclusion of a long-chain PEGylating agent, PEG6000MS. Both formulations exhibited a particle size of <100 nm, an ellipsoidal shape, and low polydispersity. SLNs were shown to have the expected solid core structure and PEGylated surface based on ^{1}H-NMR spectroscopy. Analysis of the bulk materials indicated that a number of complex interactions are present among the SLN components, including a eutectic between SA and Brij® 78. Unfortunately, the low melting point of the eutectic was shown to limit the physiological stability of the SLNs, specifically in the formulation lacking PEG6000MS. For this reason, formulation 2 SLNs in which PEG6000MS was included, were chosen for further studies.

Following this choice of formulation, SLNs loaded with Dex-P were prepared and evaluated for changes in their physicochemical properties. High drug loadings of up to 30% w/w SA could be obtained while maintaining drug encapsulation efficiencies >85%. The core-shell structure of the particles was maintained at all drug loadings, and although particle size was shown to increase with drug concentration, it remained within the size range considered suitable for tumor-targeting by the EPR effect. Interestingly, a transition from ellipsoidal- to rod-shaped particles was observed at the 30% drug loading. Analysis of the drug-matrix interactions by DSC indicated that Dex-P likely resided at the core-shell interface with the palmitate chain serving to anchor the drug within the solid SA and Dex interacting with the SA-Brij® 78 phase. A small burst release of Dex-P (<20%) was observed within the first 3 h of incubation at 37°C followed by a slower release over the remaining time period. For comparison, AP and curcumin were also evaluated for their extent and mechanism of drug loading as well as for their effects on SLN properties. AP interacted more favorably with the SA-PEG6000MS phase than with the SA-Brij® 78 eutectic but seemed to adopt a similar conformation to Dex-P, allowing for high drug loadings. The drug loading of curcumin was more limited, and its release from the SLNs was faster than Dex-P. This difference was attributed to the lack of interaction between curcumin and the solid SA phase of the particle. From this data, it appears that these SLNs have a great potential for high drug loading based on the decreased crystallinity of SA described above. However, this potential is modulated by the ability of the drug to interact with the SLN components, which may be correlated with its structure.

Previous studies indicated that drug release from the SLNs was dependent on the CE activity of the surrounding environment. However, additional studies were required to evaluate the stability of the nanoparticles in both the presence and absence of CE activity. When incubated at 37°C in the absence of protein, SLNs increased in diameter by approximately 40 nm within a 24 h time period but appeared to retain their ellipsoidal shape. Analysis of SLNs incubated with 10% HSA by DLS, UV/Visible spectroscopy, and SEC indicated the possibility of minor protein adsorption on the particles, but no evidence of particle disassociation or aggregation was observed. Although Dex-P association with SLNs was slightly lower in the presence of 50% human plasma than in PBS alone (85.5%<96.2% at 24 h), it appeared that the majority of enzymatic drug release was taking place at the surface of the SLNs.

Interestingly, even in the absence of Dex-P, SLNs demonstrated some instability in the presence of CE that could be attributed to hydrolysis of the PEG-ester compounds. Blank SLN suspensions became extremely turbid within the first 30 min following exposure to CE indicating dissociation or aggregation of at least a portion of the nanoparticles. The particle size of SLNs incubated with CE was smaller than the size of controls at all time points studied, although particle shape appeared similar as determined by TEM images taken following 1 and 24 h incubations. Although SLNs offered some protection over micelles, PEG6000MS was rapidly degraded within 15 min. PS60 hydrolysis was much slower, reaching only 36% in 2 h. These results indicated that the accelerated release of Dex observed in the presence of CE may be partially attributable to increased accessibility of the prodrug to enzymes following hydrolysis of the ester-containing materials PS60 and PEG6000MS.

During the last stage of this project, a lyophilization protocol designed to minimize changes in the physicochemical properties of the SLNs was developed, and the long-term storage stability of SLNs was evaluated. Sucrose was shown to provide the best particle redispersibility among the nine lyoprotectants that were evaluated. Specifically, a 15:1 weight ration of sucrose:SA was chosen based on the minimal increase in particle size and PI observed with this condition. Lower SLN concentrations, higher freezing temperatures, slower freezing rates, and longer secondary drying times were also shown to contribute to better redispersibility. A variety of both lab and clinically relevant solutions could be used to reconstitute the SLNs with negligible effects on the physicochemical properties of the particles. Larger particle size and PI increases following lyophilization were observed with drug loading, but both parameters remained within an acceptable range for a tumor-targeted nanoparticle drug delivery system. Changes in the encapsulation efficiency and particle shape following lyophilization were minimal. Also, no large aggregates were produced during the process. During the 3 month stability study, comparisons were made between lyophilized SLNs and SLNs stored as aqueous suspensions and between SLNs stored at either 4°C or 25°C/60% RH. The greatest stability was observed with lyophilized SLNs stored at 4°C. Particle size was maintained across the entire time period, and encapsulation efficiency was shown to be consistent at 80% following a reduction to this value within the first 3 days of storage.

The results of these studies support the proposed hypothesis. The interactions among the SLN components were shown to result in decreased crystallinity of the lipid phase. This was advantageous in terms of achieving a high drug load but did have negative ramifications in terms of the stability of the particles. However, for practical considerations, the stability of the SLNs could be improved by adjustments to the formulation (e.g., the addition of PEG6000MS and the reduction in the Brij® 78 concentration) and storage conditions (e.g., lyophilization). Further, instability in the presence of CE likely contributed to the accelerated drug release observed in CE-containing media and may be used as a trigger for achieving bioresponsive drug release.

In conclusion, this work yielded valuable information in regard to both the drug delivery system under study and nanoparticles in general. Several observations were reported with the nanotemplate engineered SLNs that may be of relevance to other nanoparticle systems. For instance, the in-depth crystallinity analysis led to the discovery of complex interactions among the SLN components that have a major effect on the particle behavior. This points to the importance of analyzing bulk materials in order to identify potential issues that may arise with the nanoparticles (e.g., physiological stability) prior to performing expensive and time-consuming *in vitro* or *in vivo* studies. It is also possible that these interactions may be utilized advantageously in other systems. The drug loading analysis provided information regarding the mechanism of drug packing within SLNs and outlined some tools that may be utilized to predict how and to what extent drugs can be loaded into SLNs. As another example, evidence of instability of the ester-containing PEG compounds in the presence of CE may provide an explanation for the poor *in vivo* results observed with other PEG-coated nanoparticle systems. It also provides justification for evaluating such stability prior to undertaking animal studies.

In terms of the drug delivery system itself, SLNs could be prepared using formulation 2 with desirable physicochemical properties and sufficient stability to warrant further development. Future studies must be aimed at determining the biodistribution and therapeutic efficacy of these SLNs *in vivo*. Due to the hydrolysis of Dex-P as well as the ester-containing PEGylating agents in the presence of CE, alternative animal models must be employed for these studies. Currently, the most feasible option seems to be the carboxylesterase-deficient Es1e(-/-)/SCID mouse model. Although drug was still released to a greater extent in the plasma from these animals than from human plasma, it is likely to be the most closely representative situation of the small animal models. Further, if results could be shown to be improved using this animal model as compared to normal mice or rats, it would provide validation for the CE-triggered drug release and give confidence that results in humans would be improved to an even greater extent.

Appendices

This section contains the following additional information:

Appendix A: Abbreviations

Appendix B: Analytical Techniques

Appendix C: Surfactant Micelle Evaluation

Appendix D: Polymer Micelles with Hydrazone-Ester Dual Linkers for Tunable Release of Dexamethasone

Appendix A

Abbreviations

Throughout this dissertation, abbreviations are given following the first use of a word or phrase. However, for convenience, Table A.1 includes an alphabetical list of the commonly used abbreviations.

Table A.1. Abbreviations

AA	Ascorbic acid
ACN	Acetonitrile
AP	Ascorbyl palmitate
BNPP	Bis(4-nitrophenyl) phosphate
CE	Carboxylesterase
$CHCl_3/CDCl_3$	Chloroform/Deuterated chloroform
Dex	Dexamethasone
Dex-P	Dexamethasone palmitate
DLS	Dynamic light scattering
DSC	Differential scanning calorimetry
EPR	Enhanced permeability and retention
FFA	Free fatty acid
H_2O/D_2O	Water/Deuterated water
HPH	High pressure homogenization
HPLC	High performance liquid chromatography
HSA	Human serum albumin
IFP	Interstitial fluid pressure
LD	Laser diffractometry
LP	Lyoprotectant
MDR	Multidrug resistance
MeOH	Methanol
NaCl	Sodium chloride
NaOH	Sodium hydroxide
NET	Nanotemplate engineering technology
NF-κB	Nuclear factor kappa B
NMR	Nuclear magnetic resonance
P-gp	*P*-glycoprotein
PBS	Phosphate buffered saline

Table A.1. Abbreviations (continued)

PEG	Poly(ethylene glycol)
PEG6000MS	PEG6000 monostearate
PI	Polydispersity index
PS60	Polysorbate 60
PSD	Pooled standard deviation
PVA	Polyvinyl alcohol
PVP	Poly(vinylpyrrolidone)
RES	Reticuloendothelial system
RH	Relative humidity
RI	Refractive index
SA	Stearyl alcohol
SD	Standard deviation
SEC	Size exclusion chromatography
SLN	Solid lipid nanoparticle
TEM	Transmission electron microscopy
TLC	Thin layer chromatography
UV	Ultraviolet

Appendix B

Analytical Techniques

This section is intended to provide an explanation of the analytical techniques used throughout this dissertation as well as to provide information regarding their application as appropriate.

B.1. PARTICLE SIZING TECHNIQUES

B.1.1. Dynamic Light Scattering (DLS)

Both DLS and laser diffractometry (LD, described in detail below) make use of the light scattering property of particles in determining the particle size distribution. As light waves strike the particle, the electron orbits of the included molecules are perturbed with the same frequency as the electric field of the incident wave. This generates an induced dipole within the molecule, which manifests itself as a source of electromagnetic radiation, resulting in scattered light. Basically, the end result is that the direction and intensity of the light appears changed though its wavelength/energy remain the same [249]. This scattering primarily results from diffraction, refraction, and reflection of the light (Figure B.1).

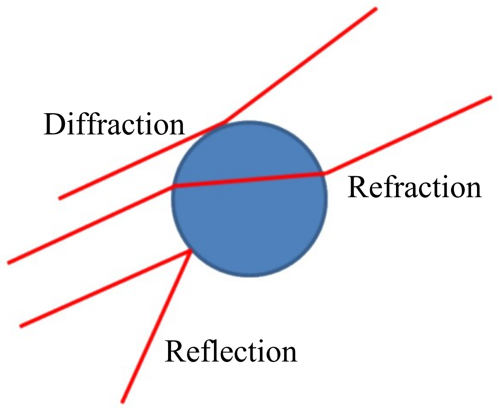

Figure B.1. Mechanisms of light scattering

DLS is a technique primarily used to determine the size of sub-micron particles suspended in a liquid [250]. It is based on the measurement of the Brownian motion of the particles, which is their random movement due to the bombardment by solvent molecules that surround them. By accounting for the viscous forces and thermal energy that affect particle movement, the particle size can be inversely correlated with particle velocity. This relationship is known as the Stokes-Einstein equation:

$$d = \frac{kT}{3\pi\eta D}$$

where d is the diameter of the particle, k is the Boltzmann's constant (1.38×10^{-23} J/K), T is the temperature in kelvins, η is the viscosity, and D is the translational diffusion coefficient. It is important to recognize that the diameter measured by this technique is the hydrodynamic diameter of the particle and can be affected by the particle's surface properties as well as the concentration and type of ions in the surrounding environment (Figure B.2).

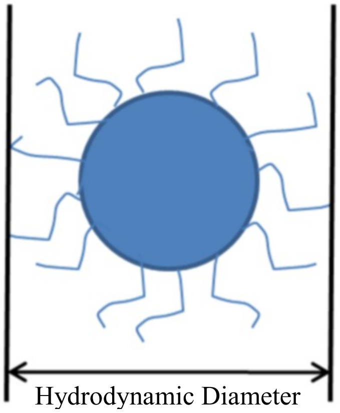

Figure B.2. The measured hydrodynamic diameter of a particle

The instrument is set up so that a laser is focused on the sample of interest. As the light passes through the dispersion, it is scattered by the particles, and the scattered light is detected. Because the particles are in motion, the intensity of the scattered light fluctuates; the rate at which these intensity fluctuations occur will depend on the size of the particles. A representative diagram of a DLS instrument set-up is shown in Figure B.3.

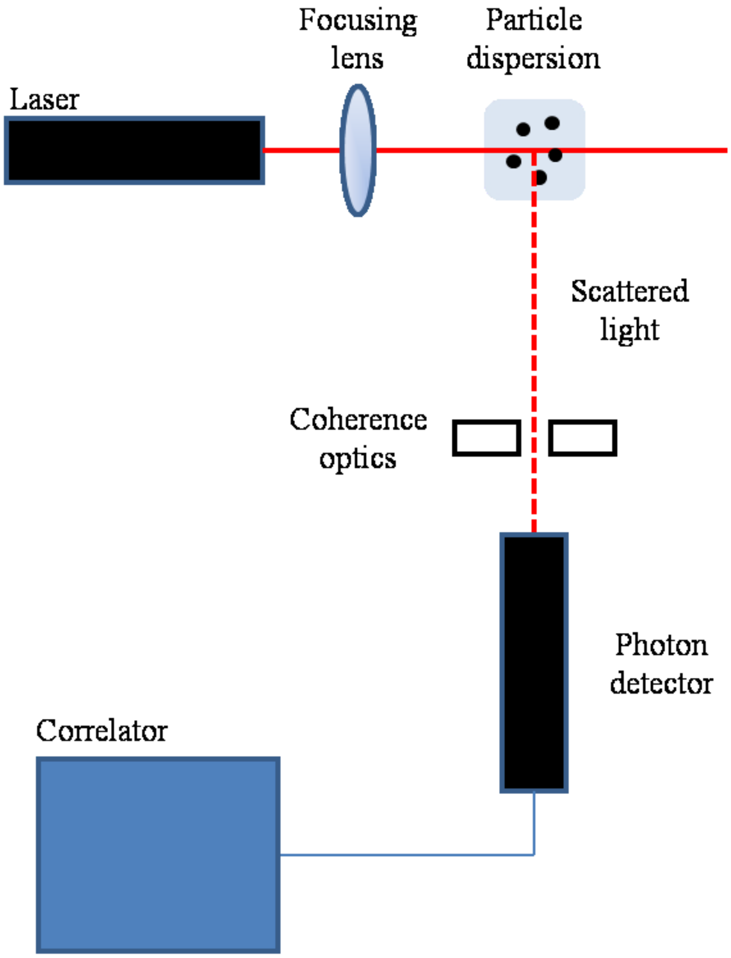

Figure B.3. Schematic diagram of a dynamic light scattering instrument

Following detection, intensity signals are compared using a correlator with the goal of generating an autocorrelation function (Figure B.4) [251]. Basically, the correlator compares the intensity, I, at time t with that at time t + τ. Similar intensities are said to exhibit high correlation. Normalization of the intensity function by average intensities allows the correlation to be expressed within a range of 0-1:

$$g^{(2)}(\tau) = \frac{< I(t) \cdot I(t+\tau) >}{< I(t) >^2}$$

where $g^{(2)}(t)$ is the normalized intensity autocorrelation function, I(t) is the intensity detected at time t, τ is the delay time, $< I(t) >^2$ is the normalization factor, and brackets (<>) indicate a time average. For small particles, in which intensity fluctuations are rapid, there is little similarity between the signals at different time points and the correlation decays quickly. For larger particles with slower intensity fluctuations, the correlation may persist for a long time.

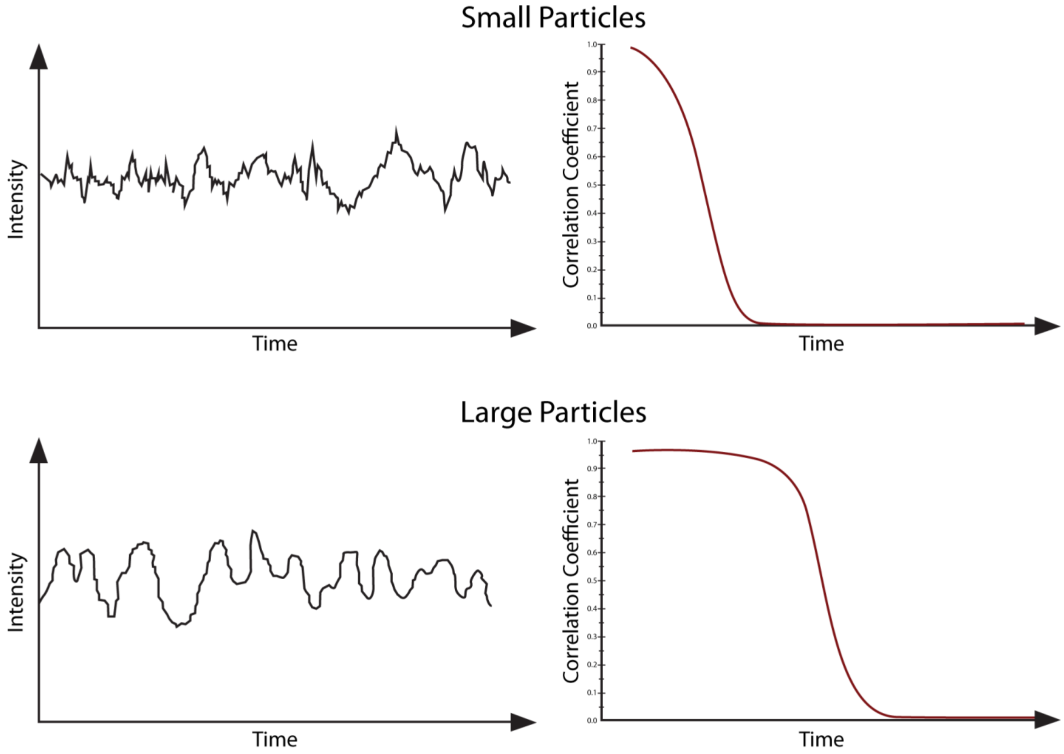

Figure B.4. Representative intensity versus time graphs (left) for small (top) and large (bottom) particles with their corresponding autocorrelation functions (right)

For particles that exhibit Brownian motion, the normalized intensity autocorrelation function will be an exponential function or a sum of exponentials. Using the Siegert relationship, the intensity autocorrelation function can be converted to the autocorrelation function of the electric field of the scattered light, $g^{(1)}(\tau)$:

$$g^{(2)}(\tau) = [g^{(1)}(\tau)]^2 + 1$$

If the particles are monodisperse, $g^{(1)}(\tau)$ will be a single exponential:

$$g^{(1)}(\tau) = Be^{-\Gamma\tau}$$

where B is a constant dependent on instrument parameters and Γ is a decay constant proportional to the diffusion coefficient:

$$\Gamma = Dq^2$$

In this equation, D is the diffusion coefficient and q is the magnitude of the scattering vector:

$$q = \frac{4\pi n \sin(\theta/2)}{\lambda}$$

where n is the refractive index of the media, λ is the wavelength of the incident light, and θ is the scattering angle. In the case of polydisperse particles, $g^{(1)}(\tau)$ will be the sum of exponentials with differing decay constants:

$$g^{(1)}(\tau) = B\sum_{i}(A_i\, e^{-\Gamma_i\tau})$$

where A_i is the relative intensity of light scattered by a particle with decay constant Γ_i and is related to the amount of such particles.

As the final step in the analysis, the correlation function is fit using various algorithms to determine the particle size. The most commonly applied analysis is the cumulants analysis. However, it is most appropriately applied only when samples are monodisperse. In this analysis, the logarithm of $g^{(1)}(\tau)$ is fit to a polynomial in τ to determine the coefficients, K_m:

$$\ln(g^{(1)}(\tau)) = \sum K_m(-\tau)^m/m!$$

The first order coefficient [or the slope of ln ($g^{(1)}(\tau)$)] is the average decay constant $<\Gamma>$ from which the diffusion coefficient and particle size (z-average diameter) can be determined. The second order coefficient $(<\Gamma-<\Gamma>)^2$ divided by $<\Gamma>^2$ is the PI, which is an estimate of the width of the particle size distribution.

In the case of multiple particle populations, a multiple exponential can be fit to the correlation function using algorithms, such as CONTIN, Marquardt, and non-negative least squares (NNLS). The NNLS technique is the simplest, solving the matrix so that only positive values for A_i are obtained. The CONTIN method also uses an NNLS technique but in combination with an eigenfunction analysis. The Marquardt method uses repeated iterations from an initial guess to fit the data.

B.1.2. Laser Diffractometry (LD)

LD is the second light scattering technique used in these studies to determine the particle size. However, it relies on different principles than DLS and is most commonly used for particle populations in the micron range (though the exact range depends on the properties of the instrument chosen). This technique is based on the fact that particles scatter light at angles that are related to their size [252]. There is a logarithmic increase in the scattering angle with a decrease in the particle size as well as a decrease in the scattering intensity. Basically, larger particles scatter light at narrow angles with high intensity while smaller particles scatter at wider angles but with less intensity. A representative instrument set-up is shown in Figure B.5.

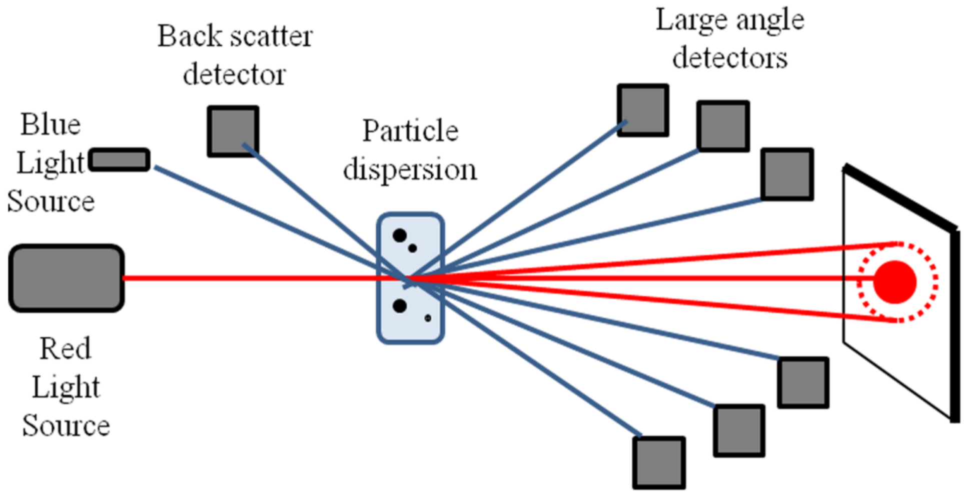

Figure B.5. Representative set-up of a laser diffractometer

Two models are used in analyzing LD data: the Fraunhofer Approximation and the Mie Theory [252]. Though the Fraunhofer Approximation was used with early LD instruments, it has since been shown to be in error when measuring particles <50 µm in size. For this reason, the Mie theory was introduced. It is based on Maxwell's electromagnetic field equations and can predict the particle size of a much wider range of particles. The calculations involved with Mie Theory are complex and will not be discussed here, but the premise is that the particle size can be calculated based on the scattering response of the particles.

B.1.3. Transmission Electron Microscopy (TEM)

TEM is a microscopic technique commonly used for the analysis of materials on the nanoscale. Because it uses electrons, which have a shorter wavelength than light, it is capable of achieving resolution a thousand times better than can be achieved with a light microscope [253]. Instruments consist of three main parts: 1) the electron gun that produces the electron beam (usually a tungsten filament coupled to a high voltage source) and the electromagnetic condenser lens that focuses it on the sample, 2) the image-producing system (consisting of the sample stage along with the electromagnetic objective, intermediate, and projector lenses that focus the electrons passing through the sample to form a highly magnified image), and 3) the image-recording system (consisting of a fluorescent screen for viewing the image and a digital camera for recording the image). A representative instrument set-up is shown in Figure B.6. Although not shown, all instruments are also equipped with a vacuum system. Samples must be analyzed under vacuum in order to minimize the collision frequency of electrons with gas atoms.

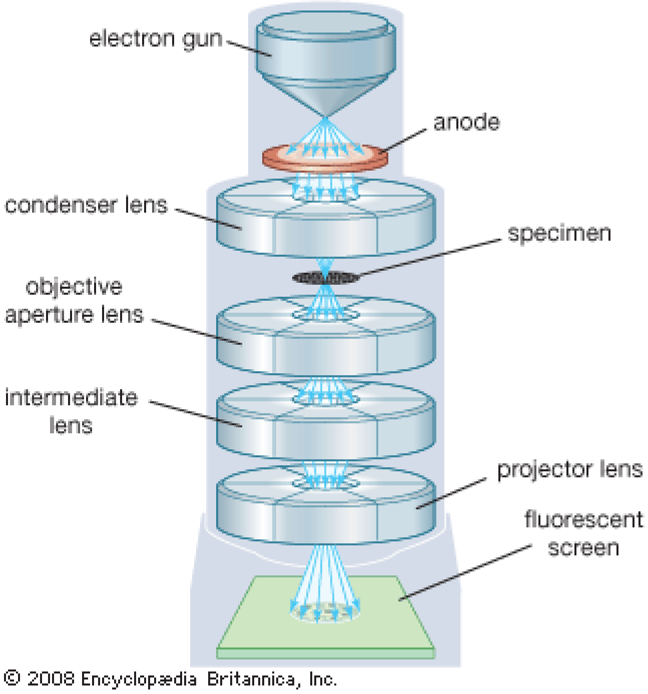

Figure B.6. Schematic diagram of a transmission electron microscope. Adapted from [253]. Reproduced with permission from Transmission Electron Microscope (TEM). *Encyclopedia Britannica. Encyclopedia Britannica Online.* Encyclopedia Britannica, 2011. <http://www.britannica.com/EBchecked/topic/602949/transmission-electron-microscope>. Copyright © 2008 Encyclopedia Britannica, Inc.

Sample preparation for nanoparticles typically consists of applying the suspended nanoparticles to a grid formed from a conductive metal and coated with carbon and allowing them to dry. The use of the conductive metal disperses the electron beam and prevents damage to the sample, while the carbon coating improves interactions with the samples. Depending on the thickness of the sample in comparison to the wavelength of the electrons, some electrons pass through the specimen while others are scattered, generating the specimen image. However, due to the insufficient contrast for most samples, stains are commonly required. In order to not obscure details of the samples, negative staining is used more frequently than positive staining. This results in staining of the background while the samples are left unstained. The most popular negative stains are salts of heavy metals known to be good electron scatterers. Their application results in the images having a dark background while the samples appear lighter.

B.2. NUCLEAR MAGNETIC RESONANCE (NMR) SPECTROSCOPY

B.2.1. ^{1}H-NMR Spectroscopy

^{1}H-NMR spectroscopy is the most commonly used analytical technique for the evaluation of molecular structures [254]. It is based on the proton having a nuclear spin of ½, which causes it to behave as a magnet. When this small “magnet” is placed within a larger magnetic field, the proton can align either with (α, lower energy state) or against (β, higher energy state) the magnetic field (Figure B.7). The energy difference between the two spin states is proportional to the strength of the magnetic field:

$$\Delta E = \gamma \frac{h}{2\pi} B_0,$$

where ΔE is the energy difference between the two spin states, h is Planck's constant (6.626×10^{-34} J·s), B_0 is the strength of the external magnetic field, and γ is the gyromagnetic ratio (26,753 sec^{-1} gauss^{-1} for a proton). Following treatment with electromagnetic radiation in the radiofrequency (RF) range, nuclei may absorb the necessary photon of energy for promotion from the lower energy state to the higher energy state. It is this absorption of energy that is detected by the NMR spectrometer. Differences in the nuclei arise from the shielding of surrounding electrons, which allows for the determination of chemical structures.

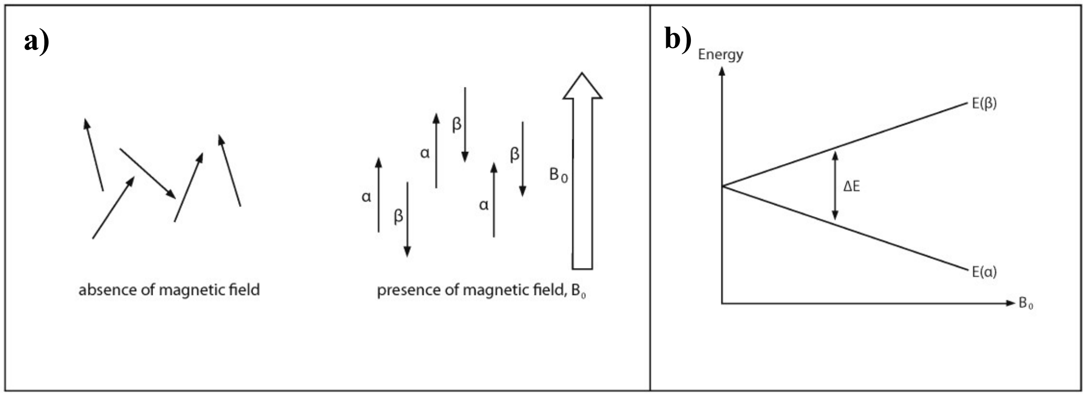

Figure B.7. (a) Nuclear spins align either with (α) or against (β) the applied magnetic field, (b) leading to an energy difference that is dependent on the strength of the external magnetic field, B_0.

B.2.2. Relaxation Time Measurements

Following the promotion of a nucleus to a higher energy state, the energy must subsequently be given off in order for the nucleus to return to the lower energy state. This is referred to as relaxation. Nuclear relaxation can be broken into two components: longitudinal or spin-lattice (T_1) and transverse or spin-spin (T_2). This is based on the fact that when a magnetic field (B_1) is applied perpendicularly to the static magnetic field (B_0), the nuclear spin experiences a different effective magnetic field (B_{eff}) (Figure B.8) [255]. The magnetization vector is correspondingly tipped from the longitudinal plane into the transverse plane, and relaxation must take place in both directions. Obtaining information on the time necessary for the relaxation process can provide valuable information regarding the environment of the molecule in question. Specifically, T_1/T_2 ratios much greater than 1 are indicative that a molecule (or portion of a molecule) is highly constrained with little flexibility, whereas T_1/T_2 ratios close to 1 indicate that a molecule (or portion of a molecule) is free in solution.

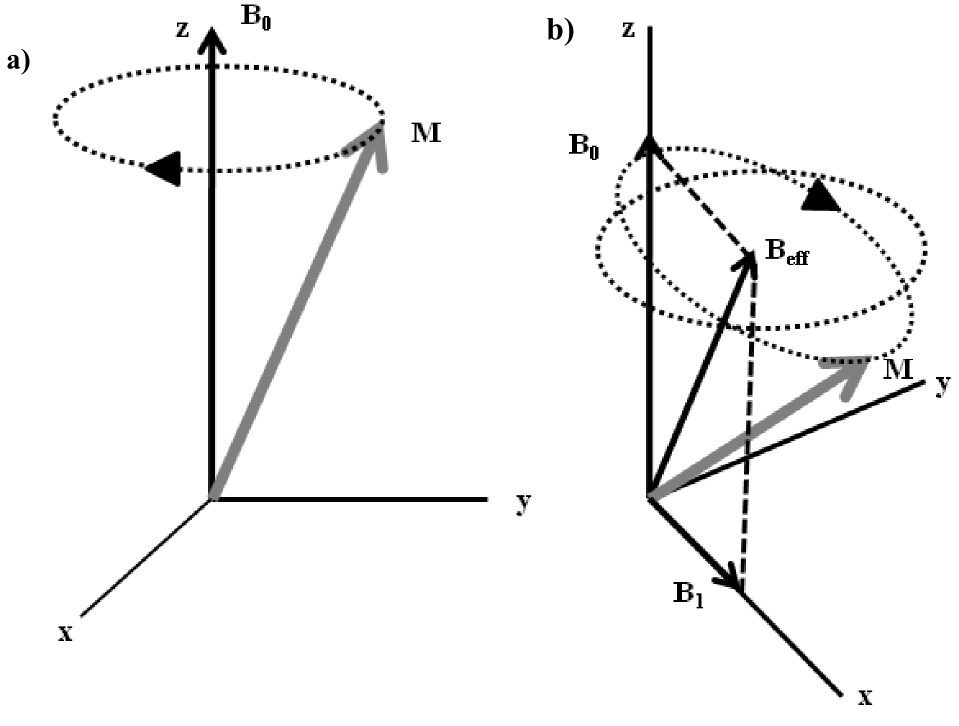

Figure B.8. Nuclei precess around the longitudinal magnetic field, B_0, with a magnetization vector, M (a). Application of a transverse magnetic field, B_1, causes the nuclear spin to experience a different effective magnetic field, B_{eff}, and a corresponding change in M (b).

Longitudinal relaxation involves an exchange of energy between the excited spins and the surrounding molecules (the lattice) as thermal motion or heat. A number of processes can be involved, including dipolar coupling, quadrapolar coupling, paramagnetic interactions, scalar coupling, chemical shift anisotropy, and spin rotation [256]. The most commonly applied experiment used for the determination of T_1 values is an inversion recovery sequence (Figure B.9). A 180° pulse is applied to invert the longitudinal magnetization (while not applying any transverse magnetization). This is followed by a delay (t) and a 90° pulse prior to detection. The sample undergoes longitudinal relaxation during the delay but does not necessarily reach equilibrium, giving a signal that is only a fraction of that obtained with the sample in its original state. The experiment is repeated numerous times with various delay periods, allowing for the generation of a curve comparing the signal intensity with the time delay. Fitting of this curve allows for the calculation of the longitudinal relaxation time (T_1), which is considered the time necessary to reduce the difference between the longitudinal magnetization and its equilibrium value by a factor of e (Figure B.10).

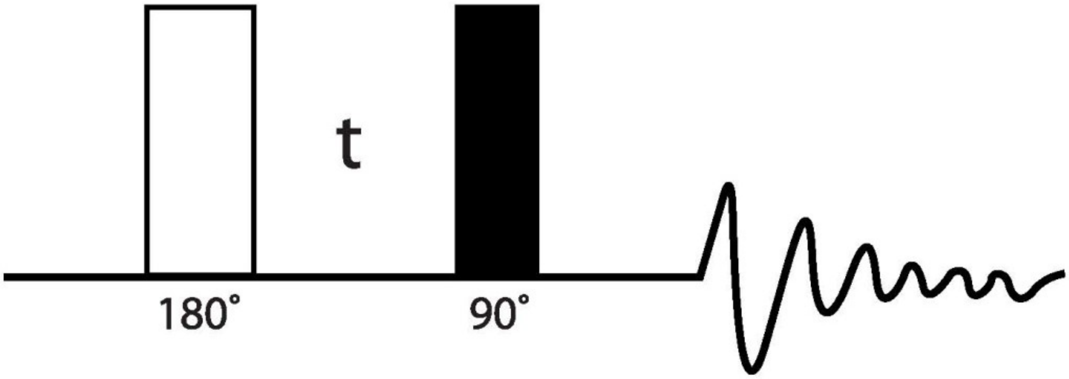

Figure B.9. Inversion recovery experiment used for the determination of T_1 relaxation times

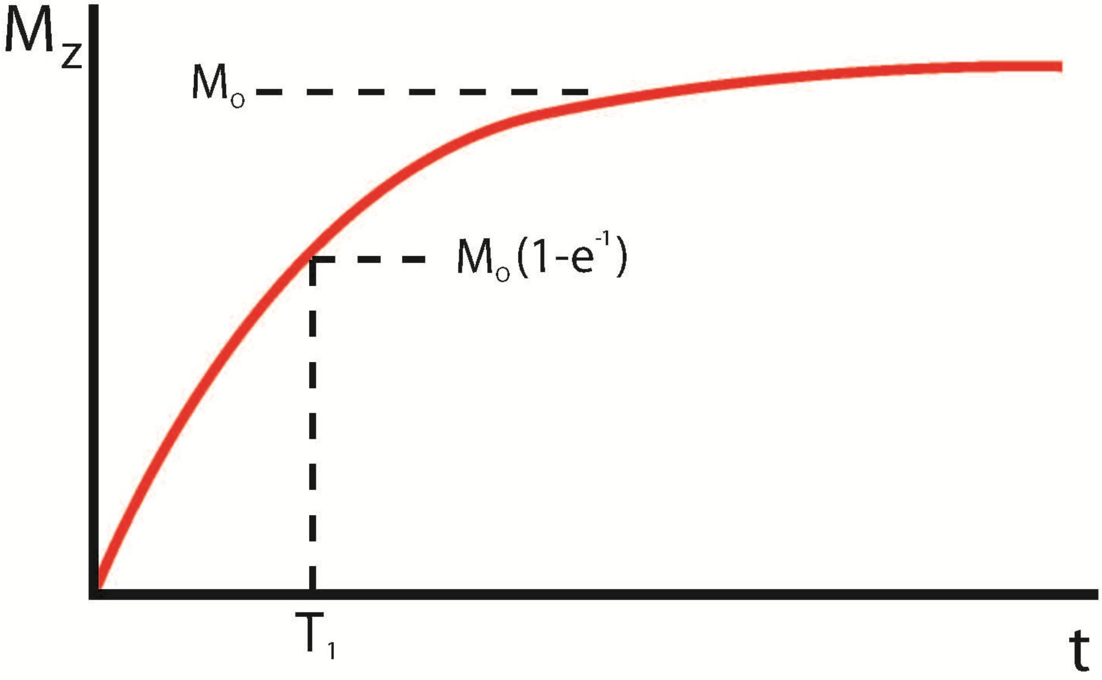

Figure B.10. The spin-lattice relaxation time, T_1, is defined as the time necessary to reduce the difference between the longitudinal magnetization (M_Z) and its equilibrium value by a factor of e.

Transverse relaxation involves excited spins exchanging energy with each other and is a shorter process than longitudinal relaxation. Relaxation mechanisms may be similar to those seen with longitudinal relaxation but may also involve spins interacting through J coupling [256]. Although in theory, T_2 values could be determined from the linewidths obtained following a 90° pulse, these can be skewed based on magnetic field inhomogeneity (resulting values are given the term T_2*). To account for this, the Carr Purcell Meiboom Gill sequence is typically employed for determination of T_2 values (Figure B.11). This sequence begins with a 90° pulse to shift the magnetization vector out of the longitudinal plane into the transverse plane. Following a delay (t), a 180° pulse is applied to flip the magnetization in the y direction. A delay of "2t" is allotted, followed by a second 180° pulse and a final delay of “t” time. The signal is then detected, and again, a curve can be prepared comparing the delay time with the signal. The time needed to reduce the transverse magnetization by a factor of e is then considered the actual T_2 relaxation time (Figure B.12).

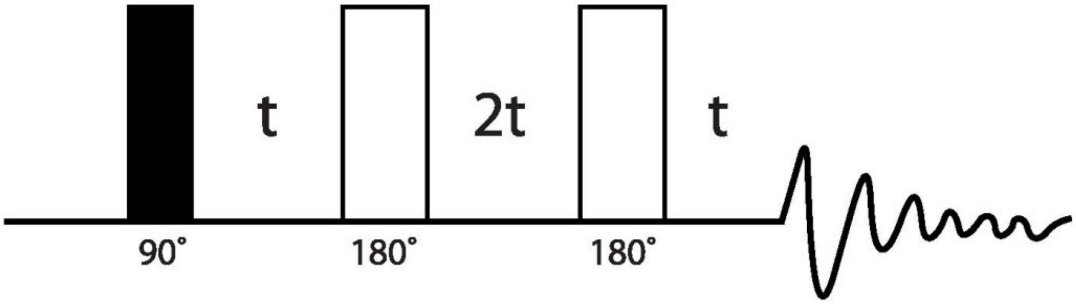

Figure B.11. The Carr Purcell Meiboom Gill sequence applied for the determination of T_2 relaxation times

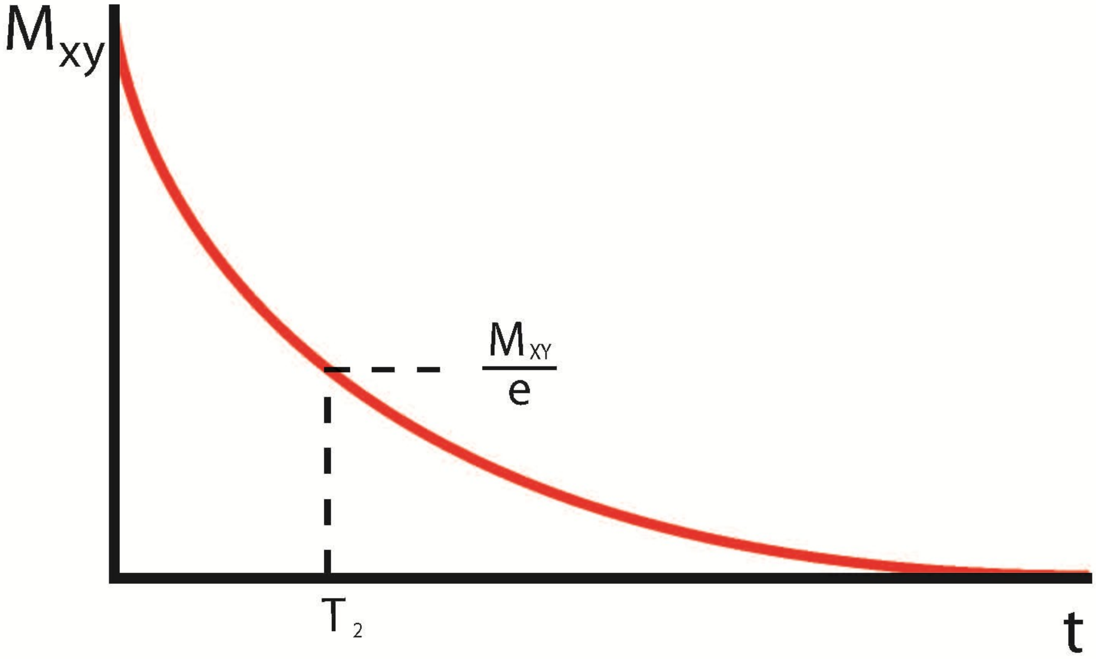

Figure B.12. The spin-spin relaxation time (T_2) is defined as the time necessary to reduce the transverse magnetization by a factor of e.

B.3. DIFFERENTIAL SCANNING CALORIMETRY (DSC)

DSC is an analytical technique based on comparing the difference in the amount of heat required to increase the temperature of a sample in comparison with a reference at the same rate [257]. A representative instrument set-up is shown in Figure B.13. Larger amounts of heat are required to keep the sample increasing in temperature at the same rate as the reference. First, the sample will have a higher heat capacity than the reference. Secondly, the sample may undergo thermal transitions (melting, recrystallization, glass transition, etc) that require large inputs of heat at certain temperatures. By plotting the heat input required versus temperature, information regarding both heat capacity and phase transitions can be obtained.

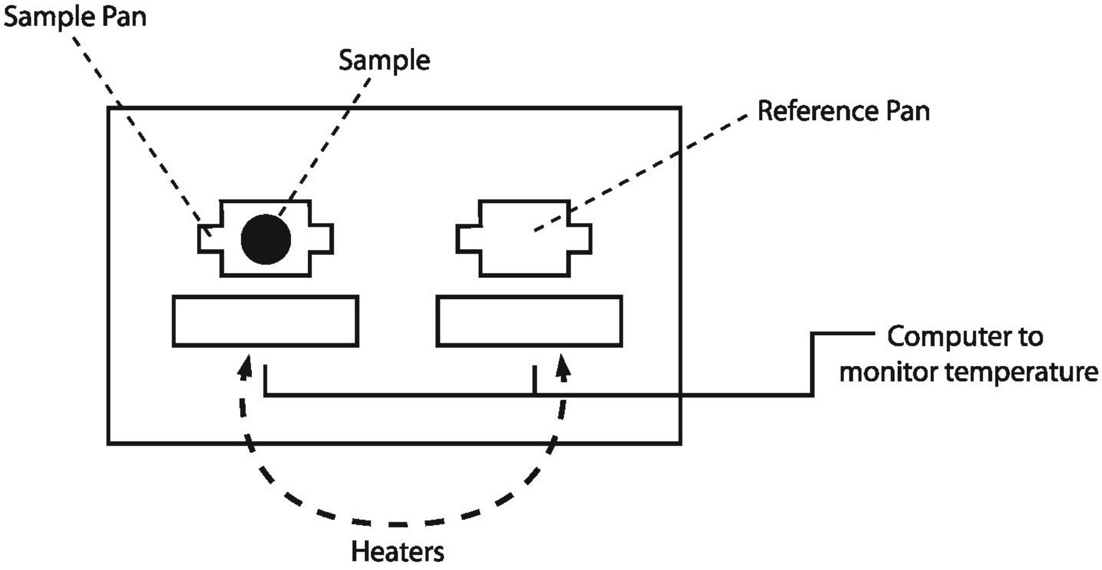

Figure B.13. Schematic of a differential scanning calorimeter

B.4. POWDER X-RAY DIFFRACTION (PXRD)

PXRD is an analytical technique primarily used for phase identification of crystalline materials; additional information may be gained on crystal structure as well [258]. It is based on the fact that as X-rays hit atoms, they are diffracted. In the absence of atomic order, the diffracted waves will be random and will interfere destructively. However, in the presence of crystalline material, there will be constructive interference in some directions (Figure B.14). This can be described by Bragg's law:

$$\lambda = 2d \sin \theta$$

where λ is the X-ray wavelength, d is the distance between crystalline planes, and θ is the angle between the incident ray and the scattering planes. Because the wavelength is fixed by the instrument, the X-ray tube and/or the detector must move in order to achieve the necessary θ angles for constructive interference (Figure B.15). The result is that each type of crystal generates a distinctive diffraction pattern.

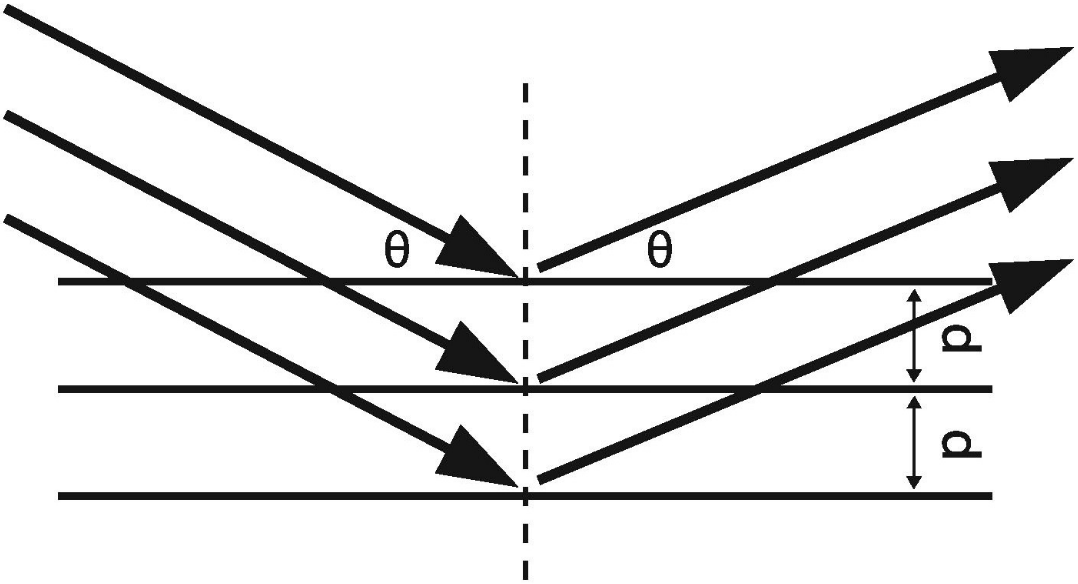

Figure B.14. Schematic depicting Bragg's Law

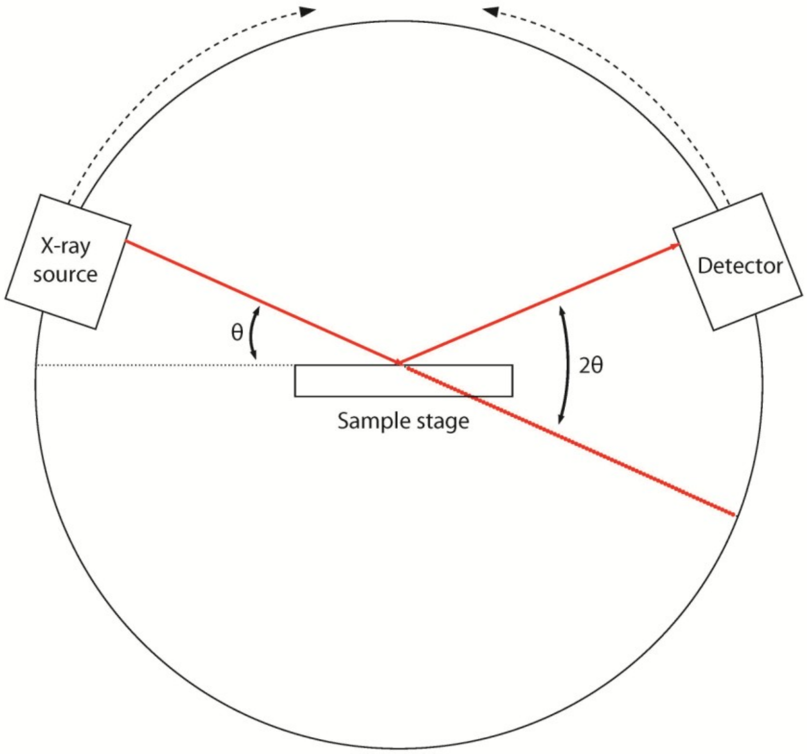

Figure B.15. Schematic of a powder X-ray diffractometer

B.5. HIGH PERFORMANCE LIQUID CHROMATOGRAPHY (HPLC)

As with all chromatography techniques, HPLC is an analytical technique designed to separate mixtures [259]. It involves the flow of solvent (mobile phase) through a column (stationary phase) at high pressures. Samples are injected onto the column, and molecules within the sample are separated based on their properties. In this dissertation, reversed phase HPLC is employed in which the stationary phase is non-polar and the mobile phase is more polar. Separation is based on the hydrophobicity of the molecules with more polar compounds coming off the column more quickly. Detection techniques can be chosen as appropriate.

B.6. SIZE EXCLUSION CHROMATOGRAPHY (SEC)

SEC is a chromatographic technique designed to separate materials (molecules, macromolecules, colloids) based on their size [260]. Similarly to HPLC, samples are added to a column through which mobile phase is flowing. Mobile phase can be pumped through the column or run through using gravity flow. Larger materials fail to enter the pores of the column and pass through the column quickly, whereas smaller materials enter the pores of the column and are retained for a longer period of time. When an aqueous solution is used as the mobile phase, SEC is referred to as gel filtration chromatography (GFC). When an organic solvent is employed, SEC is termed gel permeation chromatography (GPC). Detection techniques can be chosen as appropriate.

B.7. KARL FISCHER COULOMETRIC TITRATION

The Karl Fischer titration is a commonly used titrimetric method for the determination of trace amounts of water in a sample [261]. The titration is based on two reactions. In the first, an alcohol (ROH), sulfur dioxide (SO_2), and a base (R'N) react to form an alkylsulfite intermediate:

$$ROH + SO_2 + R'N \leftrightarrow [R'NH]SO_3R$$

During the second reaction, this intermediate reacts with iodine (I_2) and water from the sample:

$$[R'NH]SO_3R + I_2 + H_2O + 2R'N \leftrightarrow [R'NH]SO_4R + 2[R'NH]I$$

Because water and iodine are consumed in equimolar amounts during the second reaction, the consumption of iodine can be monitored to provide information on the presence of water in the sample. In the volumetric method, iodine is included with the reagents. However, with the coulometric method, which is used in this study, iodine is generated at an electrode.

The extent of reaction is monitored bipotentiometrically, meaning that electrical conductivity changes of the reaction solution are measured. As sulfur is oxidized in the second reaction, two electrons are produced that react with iodine:

$$I_2 + 2e^- \rightarrow 2I^-$$

This changes the electrical potential of the system, and the change is detected by an electrode.

Practically speaking, the alcohol generally used for the reaction solution is methanol. Substitutions have been made in the case of sample insolubility in methanol or side reactions with methanol. Pyridine was originally used as the base but has been replaced by imidazole (Figure B.16). As a stronger base, imidazole serves to shift the balance of reaction 1 to the right. Further, it lacks the unpleasant odor and toxicity associated with pyridine.

Figure B.16. Structures of bases used in Karl Fischer Titration: Pyridine (left) and Imidazole (right)

Appendix C

Surfactant Micelle Evaluation

C.1. INTRODUCTION

A careful evaluation of the uniformity of any drug delivery system is important, specifically in the case of SLNs where the low molecular weight surfactants used for stabilization are known to form other structures, such as micelles [34]. As such, it was deemed important to gain background information on the potential self-assembly of all components used in the formation of the SLNs under study.

C.2. PYRENE CMC ASSAY

C.2.1. Background

Pyrene is a polynuclear aromatic compound with a strong fluorescence spectrum (Figure C.1). Due to its different, non-planar structure in its excited state as compared to its ground state, certain emission bands in its fluorescence emission spectrum are very sensitive to the solvent's polarity [262]. This makes it a valuable probe molecule for CMC determination because, as micelles form, they entrap pyrene, causing it to experience a more hydrophobic environment than when it is free in the aqueous solution. This results in a corresponding change in its emission spectrum [263].

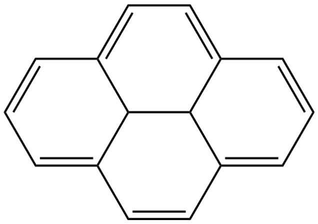

Figure C.1. Structure of pyrene

C.2.2. Experimental Method

The assay consisted of adding pyrene (67.6 µL of a 0.1 mg/mL acetone solution) to clean 7 mL vials and allowing it to evaporate. Five milliliter surfactant samples prepared in Milli-Q water at relevant concentrations were then added to the vials and allowed to shake overnight at 100 rpm in the dark. Two milliliters of each sample were then added to a quartz cuvette and analyzed by a Varian Cary Eclipse Fluorescence Spectrophotometer (Agilent Technologies, Santa Clara, CA, USA). The following conditions were used: excitation wavelength, 335 nm; emission spectra, 350-500 nm; excitation slit width, 5 nm; emission slit width, 1.5 nm; slow setting. Before the first sample was loaded into the quartz cuvette and between every sample, the cuvette was washed with acetone to eliminate any pyrene residue and then subsequently washed with deionized water to remove any remaining acetone. Samples were analyzed to retrieve the peak intensities using the Cary Eclipse software. The ratio of the first (I1 ~ 372 nm) and third (I3 ~ 383nm) peak intensities was plotted against the surfactant concentration. Concentration is expressed in mM values for comparison with the literature. Manufacturer reported molecular weight values were used for Brij® 78 (1151.56 g/mol) and PS60 (1311.67 g/mol). A value of 10,643 g/mol was used for PEG6000MS based on the SEC-determined molecular weight of free PEG (chapter 7). Two different methods were used for computing the CMC [264]. For the tangent method, the curve was fit using two linear equations (one for the rapidly varying part and one for the nearly horizontal part), and the point of intersection was defined as the CMC. For the inflection method, the OriginPro8.5 program was used to fit the curve using a Boltzmann-type sigmoid, and the inflection point was used as the CMC. Each experiment was repeated twice to provide an average and standard deviation. Experimentally determined values were compared to literature values where available.

C.2.3. Results and Discussion

Representative curves for Brij® 78, PS60, and PEG6000MS are shown in Figure C.2. Experimentally determined CMC values are given in Table C.1. The results from the inflection and tangent methods are shown. Both have been used in the literature, though the inflection method is more commonly applied for nonionic surfactants with low CMC values (<1 mM) [264]. In this case, the PS60 literature values agreed better with the $\text{CMC}_{\text{tangent}}$ value, whereas the Brij® 78 literature value agreed more closely with the $\text{CMC}_{\text{inflection}}$ method. No literature data was available for PEG6000MS. Of greatest importance for this study was the observation that the three surfactants can all form micelles at the concentrations used in SLN preparation [PS60, 0.4 mg/ml≈0.3050 mM (> 12 times the CMC); Brij® 78, 2.8 mg/ml≈2.4315 mM (> 180 times the CMC); PEG6000MS, 3.0 mg/ml≈0.2819 mM (>10 times the CMC)]. Preparations of SA and Dex-P were also analyzed, but I1/I3 ratios were consistent across the entire concentration range.

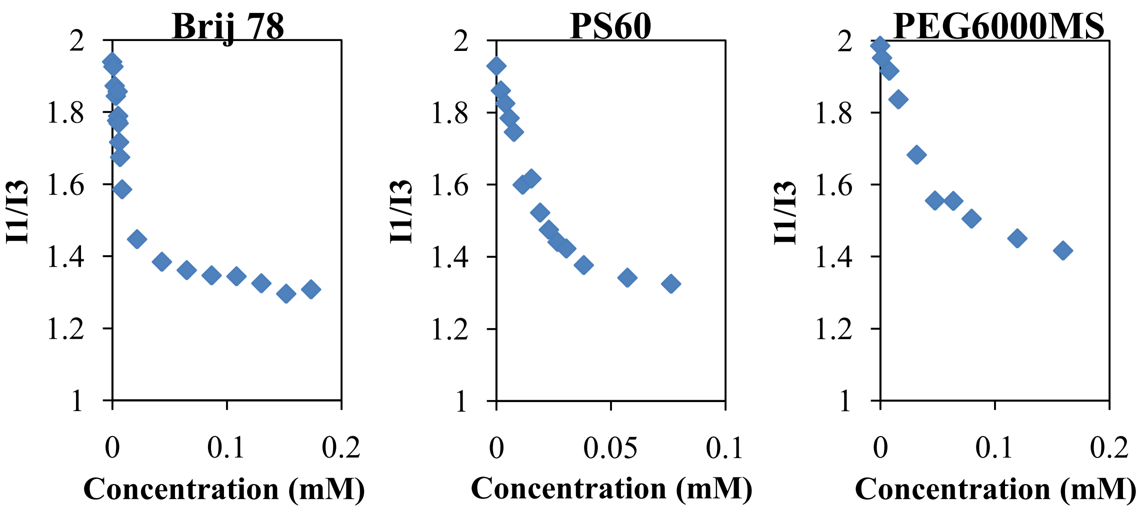

Figure C.2. Representative plots of the variation in the I1/I3 ratio of pyrene peak intensities (I1 ~ 372 nm, I3 ~ 383nm) with concentration for Brij® 78, PS60, and PEG6000MS

Table C.1. CMC values of Brij® 78, PS60, and PEG6000MS

Sample	**Experimental Values**		**Literature**	
	$\text{CMC}_{\text{inflection}}$ (mM)	$\text{CMC}_{\text{tangent}}$ (mM)	CMC (mM)	Method
Brij® 78	0.0092±0.0023	0.0135 ± 0.0006	0.0050 [265]	Surface tension
PS60	0.0135±0.0006	0.0240 ± 0.0005	0.0206 [266]	Surface tension
			0.0209 [266]	Iodine absorbance
PEG6000MS	0.0178±0.0007	0.0271 ± 0.0001	Previously unreported	

C.3. TEM

DLS is one technique that can be used in analyzing nanoparticle suspensions for the presence of micelles. The SLNs under study appear monodisperse (Figure C.3) and are characterized by low PI values (<0.1). Representative formulation 1 SLNs were characterized by a D10% of 45.4 nm, a D50% of 58.4 nm, and a D90% of 75.3 nm. Representative formulation 2 SLNs exhibited a D10% of 67.8 nm, a D50% of 85.6 nm, and a D90% of 109.9 nm. However, in this case, a dilution step was required to bring the SLN sample intensity within the range appropriate for the instrument, which would dilute PS60 and PEG6000MS micelles below their CMC values. This makes it difficult to conclude the absence of micelles from the DLS analysis.

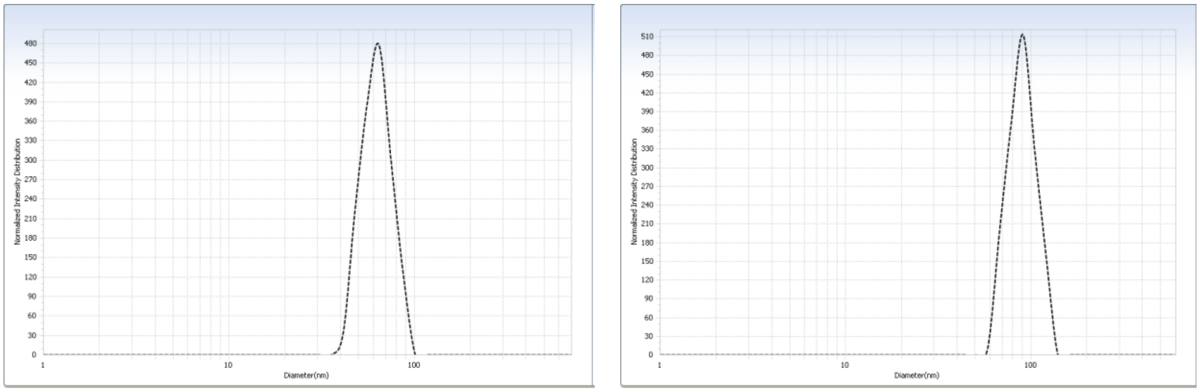

Figure C.3. Representative DLS intensity distributions for formulation 1 (left) and formulation 2 (right) SLNs

TEM was chosen as an alternative technique for analysis. Brij® 78, PS60, and PEG6000MS were prepared at the concentrations used in SLN preparation and imaged using the same protocol as described in chapter 4 (Figure C.4). Brij® 78 and PS60 had a dense population of small dots. When analyzed using ImageJ, the sizes were determined to be 13.3±4.2 nm and 23.1±3.4 nm (mean ± SD of 10 micelles), respectively. PEG6000MS micelles appeared larger at a size of 37.7±8.8 nm. In the majority of SLN images (e.g., those in chapter 4), particles in this size range cannot be observed, indicating the absence of micelles. In some SLN images, there were some dots intermediate within this size range (17.3±2.1 nm), but these could be traced to the background associated with the stain itself (18.5±4.4 nm). Overall, it appeared likely that micelles were not present to any great extent within SLN suspensions.

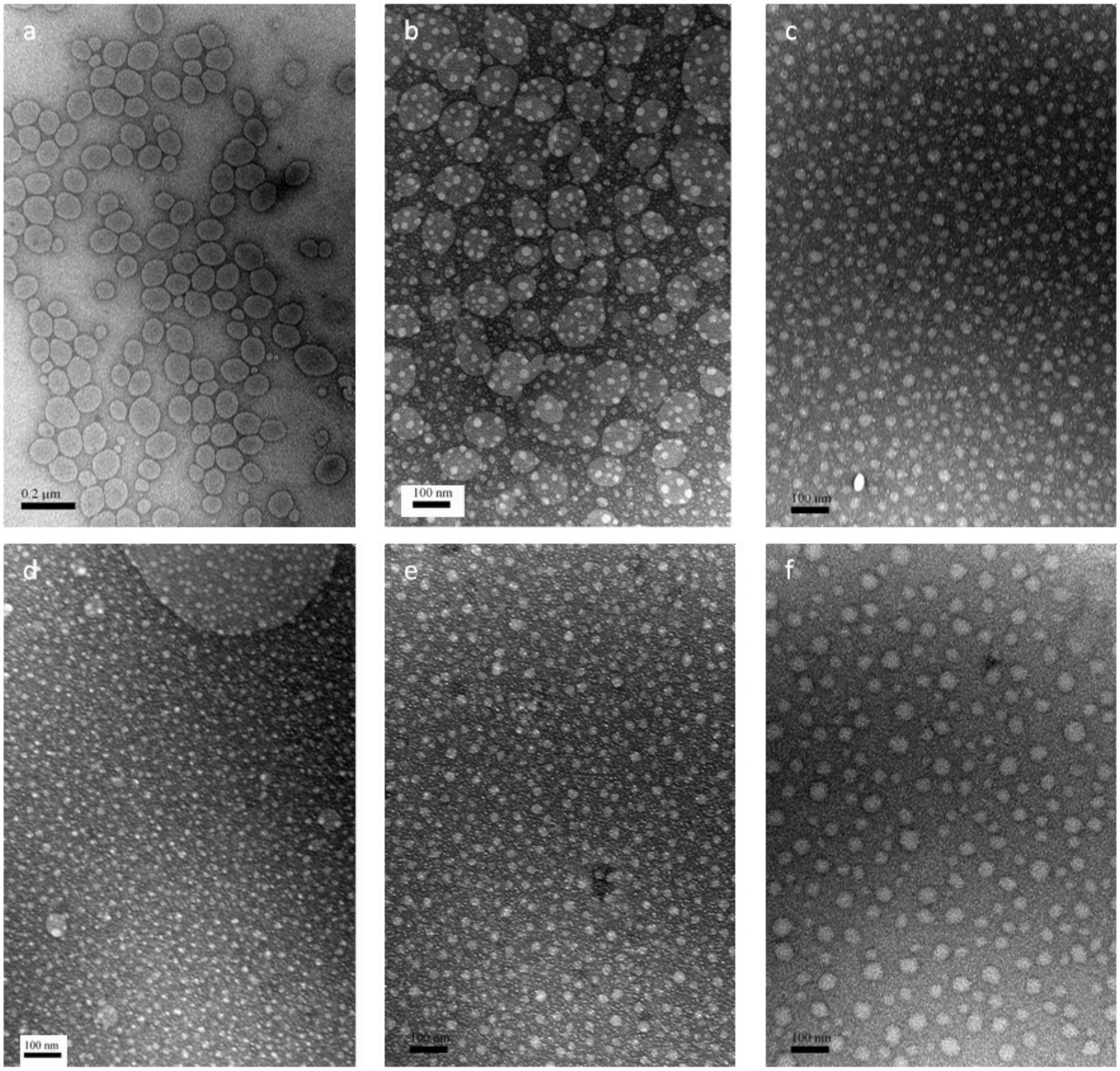

Figure C.4. TEM images of formulation 2 SLNs without background dots (a), formulation 2 SLNs with background dots (b), uranyl acetate stain (c), Brij® 78 micelles (d), PS60 micelles (e), and PEG6000MS micelles (f)

Appendix D

Polymer Micelles with Hydrazone-Ester Dual Linkers for Tunable Release of Dexamethasone*

D.1. INTRODUCTION

Polymer micelles are polymer nanoassemblies with a distinctive core-shell structure. They have been touted as promising drug carriers because they can protect drug payloads from the *in vivo* environment by entrapping drugs in a hydrophobic core enveloped by a hydrophilic shell [267]. Several preclinical and clinical studies have shown that polymer micelles improve the bioavailability and tumor-targeted delivery of various therapeutic agents while allowing chemical modifications to the core and shell for multifunctional applications [268].

Furthermore, these systems can be designed so that drugs are released in tumors in response to a biological stimulus [269-271]. For example, in a process known as the Warburg effect, cancer cells consume glucose inefficiently and produce a large amount of lactic acid that acidifies tumor tissues [272]. Drug conjugation through acid-sensitive hydrazone bonds may then lead to accelerated drug release at the tumor site [273]. In addition to providing a second method for tumor-targeting, this technique also provides opportunities for tuning drug release to achieve an appropriate profile. By modifying the chemistry surrounding the drug linker, drug release can be modulated so that tumors are treated with the appropriate drug concentration and schedule [274].

For these reasons, pH-sensitive polymer micelles were investigated as an alternative delivery system for Dex. Poly(ethylene glycol)-poly(amino acid) block copolymers were chosen because they have been shown to be a versatile drug delivery platform to design multifunctional drug carriers [275]. Dex was entrapped using hydrazone-ester dual linkers to achieve pH-controlled drug release in a tunable manner (Figure D.1A). The dual linkers consist of acid-labile hydrazone (a) and enzymatically degradable ester (b) linkages while spacers (X) modulate Dex release patterns and stability of the micelles. The dual linker micelles can achieve tunable release of Dex in tumors (Figure D.1B), reducing the IFP that limits tumor accumulation of other drugs (Figure D.1C). Micelles with single hydrazone or ester linkers were also tested for acid-sensitive Dex release. The physicochemical properties of the micelles, including particle size and Dex release patterns, were characterized at different pH values corresponding to the normal physiological condition (pH 7.4) and the acidic tumor tissues (pH 5.0). Stability of Dex loaded micelles was also tested in the presence of CE. In addition to providing information on a possible Dex delivery system, our characterization of these polymer micelles provides valuable insight into the design of drug-binding linkers and drug carriers for tunable release.

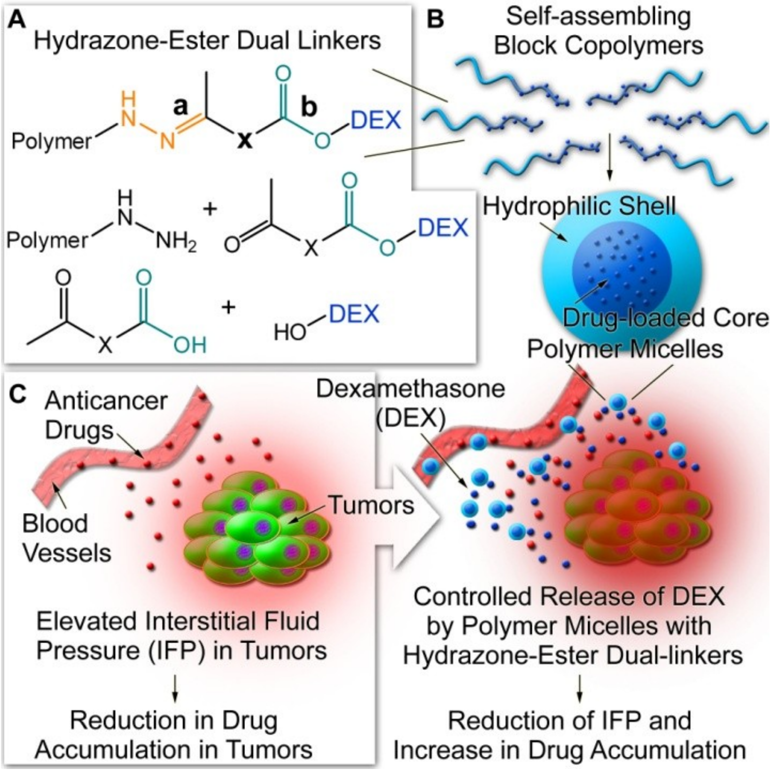

Figure D.1. Mechanism of tumor-preferential tunable release of Dex from polymer micelles. Polymer micelles entrap Dex through hydrazone-ester dual linkers (A). The dual linkers consist of acid-labile hydrazone linkages (a) and enzymatically degradable ester linkages (b) while spacers (X) modulate Dex release patterns and stability of the micelles. The dual linker micelles can achieve tunable release of Dex in tumors (B), reducing the IFP that limits tumor accumulation of other drugs (C).

D.2. MATERIALS AND METHODS

D.2.1. Materials. α-Methoxy-ω-amino poly(ethylene glycol) (PEG-NH_2, MW=12,266) was purchased from NOF Corporation (Shibuya-ku, Tokyo, Japan). L-aspartic acid β-benzyl ester, triphosgene, 4,4-diphenyl-cyclohexa-2,5-dienone, 2-hydroxy-1-(1-hydroxycyclohexyl)ethanone, 4-acetylbutyric acid (ABA), 6-oxoheptanoic acid (OHA), 7-oxooctanoic acid (OOA), Dex, prednisolone, N,N'-diisopropylcarbodiimide (DIC), 4-(dimethylamino)pyridine (DMAP), ACN, benzene, N,N-dimethylformamide, anhydrous N,N-dimethylformamide (DMF), anhydrous dimethyl sulfoxide (DMSO), DMSO-*d6*,

D_2O, anhydrous ethyl ether, anhydrous hexane, anhydrous hydrazine, anhydrous tetrahydrofuran (THF), acetate buffer solution, and phosphate buffer solution were purchased from Sigma-Aldrich (St. Louis, MO). Regenerated cellulose dialysis bags with molecular weight cut off (MWCO 6-8,000 Da) and Slide-A-Lyzer G2 dialysis cassettes with MWCO 10,000 were purchased from Fisher Scientific (Pittsburgh, PA). Amicon-Ultra centrifugal ultrafiltration devices with MWCO 10,000 were purchased from Millipore (Billerica, MA).

D.2.2. PEG-PBLA Block Copolymer Synthesis. Our synthesis protocol is shown in Figure D.2. β-Benzyl-L-aspartate N-carboxy anhydride (BLA-NCA, **2**) was prepared using the Fuchs-Farthing method as described elsewhere [276]. Triphosgene (2.88 g, 9.7 mmol) and β-benzyl-L-aspartate (5.0 g, 22.4 mmol) were mixed in dry THF (100 mL). The reaction was conducted in N_2 at 45°C until the solution turned clear. Anhydrous hexane was slowly added to the reaction solution for recrystallization of BLA-NCA in -20°C. Purified BLA-NCA was polymerized in anhydrous DMSO at 45°C for 2 days by using amino-terminated PEG as a macroinitiator. The amount of BLA-NCA was adjusted with respect to PEG to prepare PEG-PBLA block copolymers with 35 units of aspartic acid, **3**. The reaction solution was precipitated in anhydrous ethyl ether. White PEG-PBLA was collected by freeze-drying from benzene.

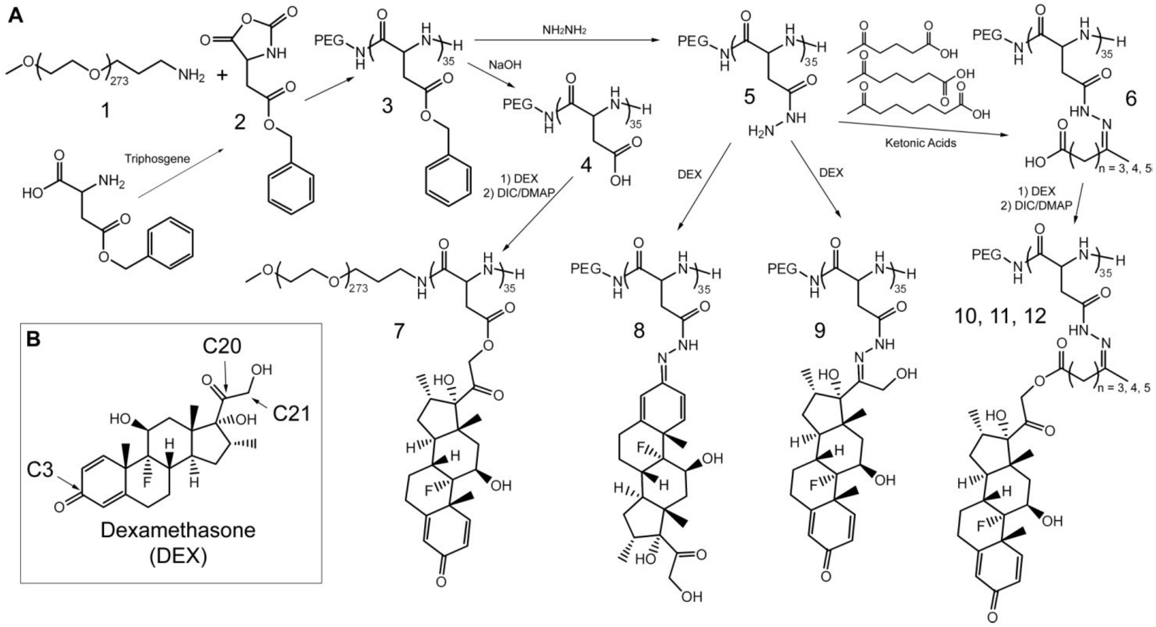

Figure D.2. (A) Synthesis of block copolymers. PEG-PBLA, 3, was prepared from 12 kDa PEG, 1, and 35 units of BLA-NCA, 2. PEG-pAsp, 4, was produced by complete deprotection of 3 in 0.1 N NaOH. Dex was conjugated to 4 through an ester linkage by an esterification reaction between the hydroxyl group at the C21 moiety of DEX and carboxyl groups of 4 to give 7. Dex was conjugated at its C3 and C20 positions to PEG-p(Asp-Hyd), 5, through ketone linkages to produce 8 and 9, respectively. Reactions between 5 and various ketonic acids (ABA, OHA, and OOA) produced 6 in which the ketonic acids served as spacers. Dex was conjugated to 6 through an esterification reaction to give three polymer compositions with hydrazone-ester dual linkers (10, 11, and 12). (B) Structure of Dex with relevant conjugate sites numbered

D.2.3. PEG-p(Asp-Est-Dex) Synthesis. PEG-PBLA was dissolved in 0.1 N NaOH to deprotect benzyl ester groups. The solution was dialyzed against deionized water using MWCO 6-8,000 Da until NaOH was removed completely. PEG-poly(aspartate) [PEG-p(Asp), **4**] was collected by freeze drying. Dex was conjugated to PEG-p(Asp) through an ester bond in DMSO at room temperature. DIC and DMAP were used for the esterification reaction. The reaction solution was precipitated in anhydrous ethyl ether. The product was freeze dried from benzene to collect PEG-poly(aspartate ester

Dexamethasone) [PEG-p(Asp-Est-Dex), **7**]. Sample aliquots were filled with nitrogen to minimize hydrolytic degradation.

D.2.4. PEG-p(Asp-Hyd-Dex) Synthesis. Hydrazide groups were introduced to PEG-PBLA through aminolysis reactions as previously reported [273]. PEG-PBLA and anhydrous hydrazine were reacted in DMSO at 45°C for 1 h (50-100 mg polymer/mL DMSO) to prepare PEG-poly(aspartate hydrazide) [PEG-p(Asp-Hyd), **5**]. PEG-p(Asp-Hyd) was precipitated in anhydrous ethyl ether and freeze dried from benzene. Dex and PEG-p(Asp-Hyd) were mixed in DMSO at 40°C for 72 h. The reaction solution was precipitated in anhydrous ethyl ether repeatedly. The precipitates were collected from benzene to provide PEG-poly(aspartate hydrazone Dexamethasone) [PEG-p(Asp-Hyd-Dex), **8** and **9**].

D.2.5. PEG-p(Asp-Hyd-X-Est-Dex) Synthesis ('X' indicates ketonic acids as spacers). PEG-p(Asp-Hyd) block copolymers were reacted with three ketonic acids (ABA, OHA and OOA) separately in DMSO at 40°C for 3 days. Reaction solutions were precipitated in anhydrous ethyl ether, followed by freeze drying from benzene. Each PEG-p(Asp-Hyd) modified with ketonic acids, **6**, was reacted with Dex in DMSO at room temperature by adding DIC and DMAP. The reactions were conducted for 24 h, followed by precipitation in anhydrous ethyl ether and freeze drying from benzene. The ketonic acids provided spacers of 3, 4 and 5 methylene groups ('X') between PEG-p(Asp-Hyd) and Dex in the final products [PEG-p(Asp-Hyd-X-Est-Dex), **10**, **11** and **12**].

D.2.6. Polymer Micelle Preparation. Polymer micelles were prepared from **7**, **8**, **9**, **10**, **11** and **12**. Either reconstitution or freeze drying methods were used to prepare the micelles. The reconstitution method was conducted by dissolving drug-conjugated polymer powders directly in aqueous solutions and sonicating the solution. For the freeze drying method, block copolymers were dissolved in ACN first and diluted with deionized water, adjusting the final ACN content to 20%. The block copolymer solutions were freeze dried, following dry ice freezing. Freeze-dried micelle powders were reconstituted in aqueous solutions. All micelles were filtered through 0.2 μm filters prior to further experiments. Polymer micelles from Dex-conjugated block copolymers are abbreviated according to the drug-binding linkers used, which include hydrazone (HYD-M), ester (EST-M), hydrazone-ABA-ester (ABA-M), hydrazone-OHA-ester (OHA-M) and hydrazone-OOA-ester (OOA-M).

D.2.7. Analytical Methods. Particle size of polymer micelles in water was determined by DLS measurements using a Zetasizer Nano-ZS (Malvern; Worcestershire, UK). The instrument was equipped with a He-Ne laser (4 mW, 633 nm) and set up to collect 173° angle scattered light. Number distributions are presented as the mean particle size. ^{1}H-NMR experiments were performed on a Varian 500 MHz NMR (Varian Inc., Palo Alto, CA) at 25°C. Products were dissolved in DMSO-*d6* and analyzed following each step in the synthetic pathway. NMR spectra were also obtained for freeze-dried micelles reconstituted in D_2O. Where appropriate, SEC was additionally used to confirm the success of reactions. The system was a Shimadzu Prominence HPLC series equipped with a Shodex Asahipack GF-7M HQ column and an RID-10A refractive index detector.

The mobile phase was 5 mM PBS run at 0.5 mL/min; the column temperature was held at 35°C. Molecular weight was calculated through comparison with a calibration curve based on PEG standards. The PI was calculated by dividing the weight average molecular weight by the number average molecular weight. Dex loading was confirmed by ^{1}H-NMR spectroscopy and quantified by HPLC. Ester-containing micelles were prepared at 2 mg/mL in either acetate buffer (10 mm pH 5.0, n=3) or phosphate buffer (10 mM pH 7.4, n=3). One hundred microliters of each sample were combined with 100 μL prednisolone (0.1 mg/mL) as an internal standard and 10 μL NaOH (0.1 N). The mixed solutions were incubated at 37°C overnight with shaking at 100 rpm. Samples were neutralized with 10 μL HCl (0.1 N). One hundred microliters of the neutralized samples were mixed with ACN (45% ACN/55% H_2O) and ultrafiltered. Filtrates were analyzed by HPLC according to the following conditions. The system was a Shimadzu Prominence HPLC series equipped with a SPD-M20A Photodiode Array Detector. Five microliter samples were injected to an Eclipse XDB-C18 (4.6 mm×150 mm, 5 micron, Agilent Technologies) column at 40°C. The mobile phase (45% ACN/55% H_2O) was run at a flow rate of 1 mL/min. Concentrations were calculated based on peak area calibration curves prepared for Dex and Prednisolone at 254 nm from 1 to 500 μg/mL.

D.2.8. pH-Dependent Drug Release Study. Drug release studies were conducted in acetate (10 mM, pH 5.0) and phosphate (10 mM, pH 7.4) buffers under sink conditions. Samples were removed at 0 h from initial preparations. Dialysis cassettes were loaded with 400 μL of 2 mg/mL micelle solutions and placed into 5 L of buffer solutions at 37°C. At each time point (1, 3, 6, and 24 h), the entire internal solution was collected from three dialysis cassettes and stored at room temperature until all samples had been collected. Samples were treated as described above to determine drug loading by HPLC analysis. Data are presented as percent drug remaining, using 0 hr concentrations as the standard. The area under the curve ($AUC_{0\text{-}t}$: where 't' represents a time point) was determined by using the trapezoidal rule for % Dex released (% Dex released = 100 - % DEX remaining) with respect to time. AUC values were compared for the early (0-3 h) and late (3-24 h) periods.

D.2.9. CE-Dependent Drug Release Study. Polymer micelles (2 mg/mL) were incubated under non-sink conditions at 37°C/pH 7.4 in media with varying levels of CE activity: 1) RPMI cell culture medium; 2) RPMI with 10% fetal serum bovine (FBS); 3) RPMI with 10% mouse plasma (MP); 4) RPMI with 10% human plasma (HP); 5) RPMI with 10% FBS and 10% MP; and 6) RPMI with 10% FBS and 10% HP. Mouse plasma is known to have higher levels of CE activity than human plasma (46). RPMI was used as a control to determine the effects of ions and small molecules (vitamins and amino acids) on micelle stability. FBS was used as a control for general protein effects on micelle stability. All combinations were prepared on a volume basis. Plasma samples contained sodium heparin as the anti-coagulant. One hundred microliter aliquots (n=3) were collected at 0 and 24 h, followed by ultrafiltration and HPLC analysis as described above. Drug release patterns were determined by quantifying cleaved Dex and Dex-ketonic acid conjugates.

D.2.10. Statistical Analysis. Statistical analyses were performed using ANOVA (single factor) at the 5% significance level. Data were recorded as mean ± SD. All experiments were done in triplicate as specified in the results section. Data analyses were performed using Microsoft Excel (2007).

D.3. RESULTS

D.3.1. Block Copolymer Synthesis. Figure D.2 summarizes the synthetic pathways for all materials used in the research. Using the PEG peak as a reference, ^{1}H-NMR indicated that the polymerization reaction between 12 kDa PEG, **1**, and BLA-NCA, **2**, had proceeded to give PEG-PBLA, **3**, with 35 units of aspartic acid. GPC further showed neither unreacted PEG nor PBLA homopolymers after purification. Molecular weight distribution of the block copolymers was homogeneous with a polydispersity index smaller than 1.3. The results were consistent with what we observed previously. PEG-p(Asp), **4**, was produced by complete deprotection of **3** in 0.1 N NaOH. Dex was conjugated to **4** through an ester linkage by an esterification reaction between the hydroxyl group at the C21 moiety of Dex and carboxyl groups of **4** to give **7**. Dex loading was 8.67±0.86 wt% (n=6). Dex was conjugated at its C3 and C20 positions to PEG-p(Asp-Hyd), **5**, through ketone linkages to produce **8** and **9**, respectively. Drug loading for these two products together appeared low by ^{1}H-NMR and could not be quantified by HPLC due to difficulties in cleaving the drug from the polymer. Reactions between **5** and various ketonic acids (ABA, OHA, and OOA) produced **6** in which the ketonic acids served as spacers containing 3, 4 and 5 methylene groups. Dex was subsequently conjugated to **6** through esterification to give three polymer compositions with hydrazone-ester dual linkers, **10**, **11**, and **12**. Dex loadings were 4.63±0.75, 5.57±0.61, and 4.50±0.28 wt% for **10**, **11**, and **12**, respectively (n=6).

D.3.2. Polymer Micelle Preparation. All Dex-conjugated block copolymers formed polymer micelles irrespective of the composition. Freeze-dried micelles were readily reconstituted in aqueous solutions at concentrations >2 mg/mL; no precipitate was observed. Prepared micelles were smaller than 100 nm: EST-M (85.74 nm), ABA-M (61.50 nm), OHA-M (43.82 nm), and OOA-M (37.84 nm). ^{1}H-NMR spectra of the micelles in DMSO-*d6* (Figure D.3) showed the characteristic peaks of Dex [dienone (7.3, 6.2 and 6.0 ppm) and hydroxyethanone (5.2 ppm)] and PEG (3.6 ppm). A complete reduction of Dex peaks was seen in the micellar spectra in D_2O while the PEG peak remained, indicating that Dex is primarily entrapped within the micelles.

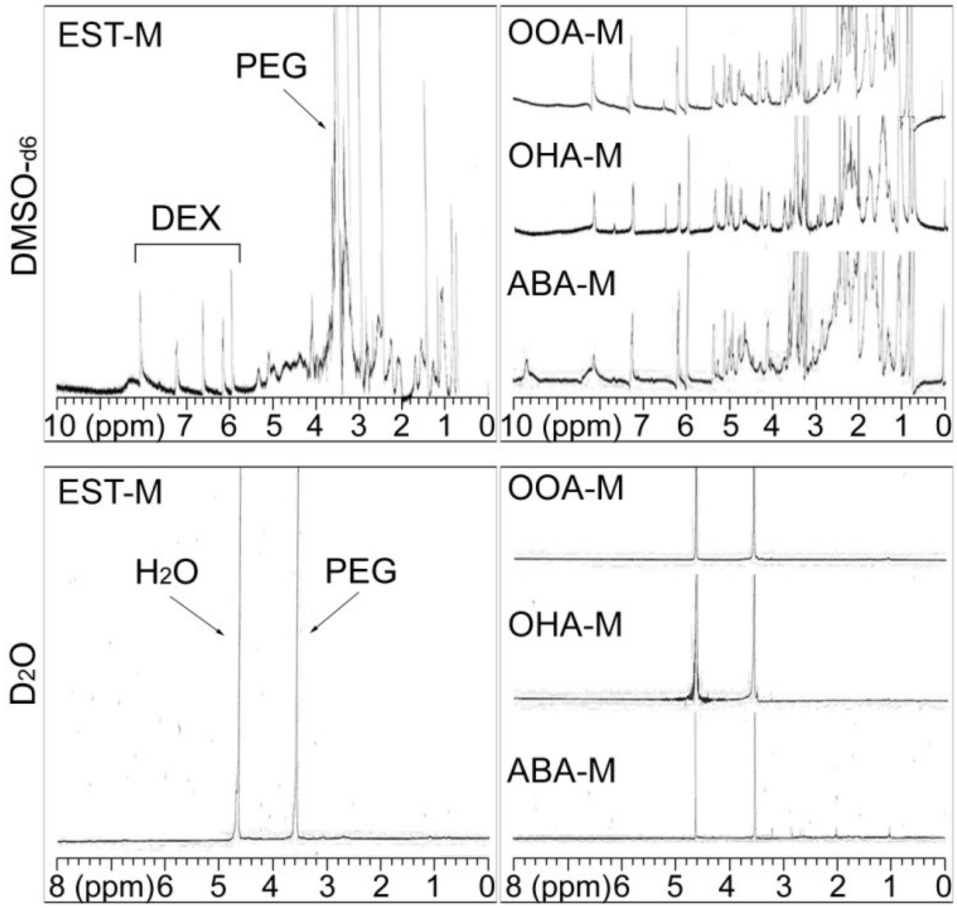

Figure D.3. ^{1}H-NMR spectra of polymer micelles in DMSO-*d6* and D_2O. ^{1}H-NMR spectra of the micelles in DMSO-*d6* showed the characteristics peaks of Dex [dieneone (7.3, 6.2 and 6.0 ppm) and hydroxyethanone (5.2 ppm)] and PEG (3.6 ppm). A complete reduction of Dex peaks was seen in the micellar spectra in D_2O while the PEG peak remained, indicating that Dex was entrapped within the micelles.

HYD-M, a mixture of **8** and **9**, did not form homogeneous polymer micelles. We were unable to determine the particle size of HYD-M because it varied between batches (4.50 - 2187.20 nm). Our preliminary experiments showed that drug release from HYD-M (**8** and **9**) was negligible even under strongly acidic conditions (pH<2) and at elevated temperatures (>60°C). To elucidate the mechanism, PEG-p(Asp-Hyd) was reacted with two model ketone compounds, 4,4-diphenyl-cyclohexa-2,5-dienone and 2-hydroxy-1-(1-

hydroxycyclohexyl)ethanone, which represent the C3 and C20 moieties of Dex, respectively. HPLC analysis revealed that hydrazone formation at the C3 ketone of Dex is favorable and highly stable compared to the hydrazone at the C20 ketone of Dex. Based on these results, we concluded that direct conjugation of Dex to PEG-p(Asp) through the hydrazone would be inappropriate to design our polymer micelles for the delivery and pH-sensitive release of Dex in tumors. We did not pursue further experiments with HYD-M accordingly.

D.3.3. pH-Dependent Dex Release from the Micelles. Drug release patterns showed that EST-M was unstable at pH 7.4 while it was more stable at pH 5.0 (Figure D.4). 51.39% and 32.37% of Dex were released from EST-M in 6 h at pH 7.4 and pH 5.0, respectively. Polymer micelles with hydrazone-ester dual linkers showed the opposite drug release patterns. In all cases (ABA-M, OHA-M, and OOA-M), Dex release from the micelles was suppressed at pH 7.4 and accelerated at pH 5.0. The results suggest that polymer micelles with hydrazone-ester dual linkers may remain stable in blood and release more Dex in acidic tumor tissues. Dex release was reduced at pH 5.0 as the chain length of the spacer increased. Interestingly, Dex release was less dependent on the spacer at pH 7.4. To suppress Dex release at pH 7.4, we also attempted to test ketonic acids longer than OOA, but the block copolymers precipitated forming no micelles (data not shown).

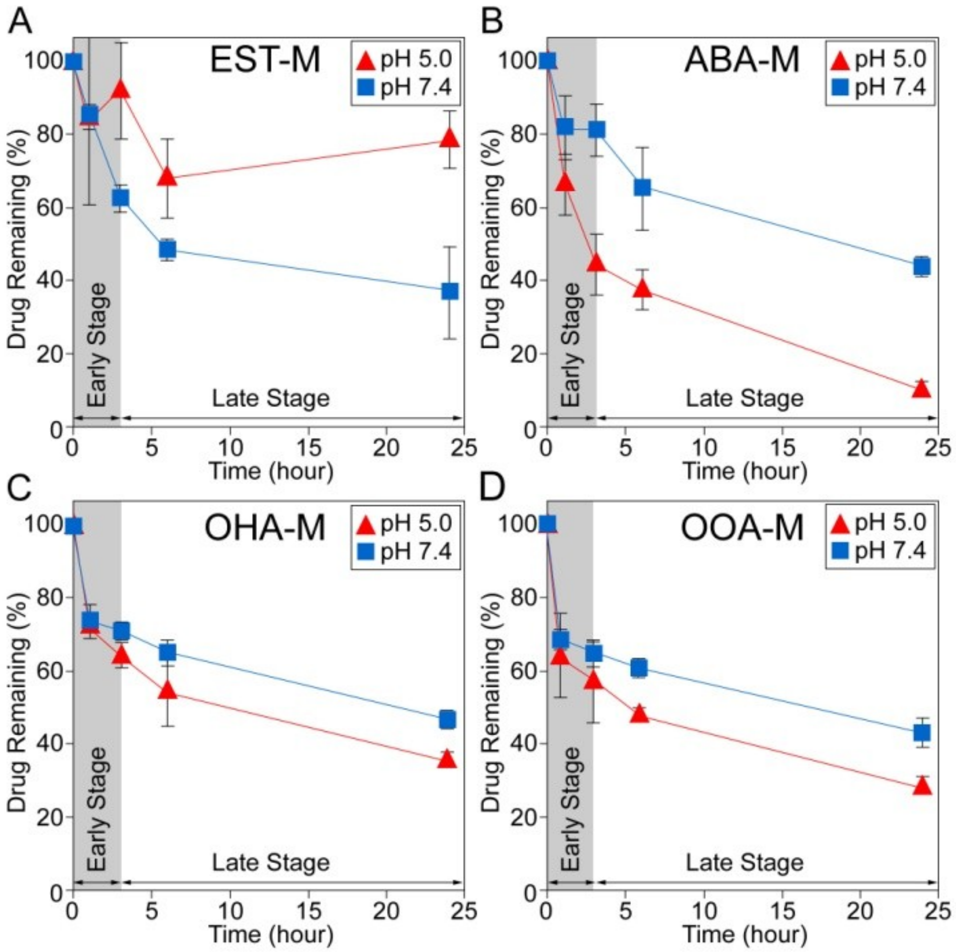

Figure D.4. Time- and pH-dependent release of Dex from polymer micelles at 37°C. EST-M was unstable at pH 7.4 while it was more stable at pH 5.0. Polymer micelles with hydrazone-ester dual linkers showed the opposite drug release patterns with drug release being accelerated at pH 5.0 and suppressed at pH 7.4. Dex release was reduced at pH 5.0 as the chain length of the spacer increased but was less dependent on the spacer at pH 7.4.

Dex release profiles were compared by calculating the AUC values of Dex released at different pH conditions. Data were analyzed by separating the AUC values for the early (0-3 hr) and late (3-24 hr) time periods (Table D.1). The $AUC_{0\text{-}3}$ showed that ABA-M suppressed drug release at pH 7.4 effectively with respect to EST-M. OHA-M and OOA-M released slightly more drugs than EST-M in the same time period. At pH 5.0 (0-3 h), all micelles released Dex in a pH-dependent manner. At later time periods ($AUC_{3\text{-}24}$), Dex release at pH 7.4 was slower and more sustained in all micelles with dual linkers compared to EST-M. The AUC_{3-24} at pH 5.0 showed that ABA-M released more Dex than either OHA-M or OOA-M. It is intriguing that OOA-M, containing longer and more hydrophobic spacers, released more Dex than OHA-M. Among the micelles with dual linkers, ABA-M released the least amount of Dex at pH 7.4 and the greatest amount of drug at pH 5.0 during the early time period (0-3 h). In the later time period (3-24 h), all micelles showed similar Dex release patterns at pH 7.4. However, ABA-M still released more Dex than OHA-M and OOA-M at pH 5.0. Based on the pH-dependent drug release studies, ABA-M was chosen as the lead composition for further studies.

Table D.1. Accumulated Dex release from polymer micelles

pH	Micelles	AUC [a]					
		% Dex released × hour [b]		Micelles/EST-M [c]		Micelles/ABA-M [c]	
		0-3 hr	3-24 hr	0-3 hr	3-24 hr	0-3 hr	3-24 hr
7.4	EST-M	59.62	1162.83	1	1	-	-
	ABA-M	45.20	893.03	0.76	0.77	1	1
	OHA-M	70.02	893.24	1.17	0.77	1.55	1.00
	OOA-M	83.86	983.39	1.41	0.85	1.86	1.10
5.0	EST-M	30.29	540.59	1	1	-	-
	ABA-M	105.38	1536.74	3.48	2.84	1	1
	OHA-M	76.27	1106.28	2.52	2.05	0.72	0.72
	OOA-M	97.17	1254.63	3.21	2.32	0.92	0.82

[a] AUC denotes the area under the curve of Dex released from the micelles.
[b] The unit for AUC is defined as % Dex released × hour.
[c] The ratios show Dex released from each micelle with respect to either EST-M or ABA-M.

D.3.4. CE-Dependent Drug Release. In addition to pH, we tested stability of ABA-M in the presence of CE to confirm that polymer micelles can protect Dex and the ester linkers from enzymatic degradation. The micelles were incubated at 37°C under six different conditions as described in the Materials and Methods section. Total Dex released from ABA-M is summarized in Figure D.5. No dissociation of micelles was seen in all incubation conditions at 0 h. Dex release was minimal ($<5\%$) at the initial time point. An ANOVA analysis indicated no significant differences among the six samples at 0 h ($p>0.05$). It is noticeable that ABA-M remained stable in RPMI, FBS, MP and HP alone or in combination, suggesting that the micelles protected Dex and the dual linkers in the solutions that contain various additives such as ions, small molecules, amino acids, proteins and digestive enzymes. Following 24 h incubations, Dex release was slightly higher (10 - 15%) in samples containing mouse plasma compared to the samples lacking CE activity ($p<0.05$). A slight difference in release was also observed between drug release in this study and the pH-dependent study described above, which may be attributable to the non-sink versus sink conditions employed.

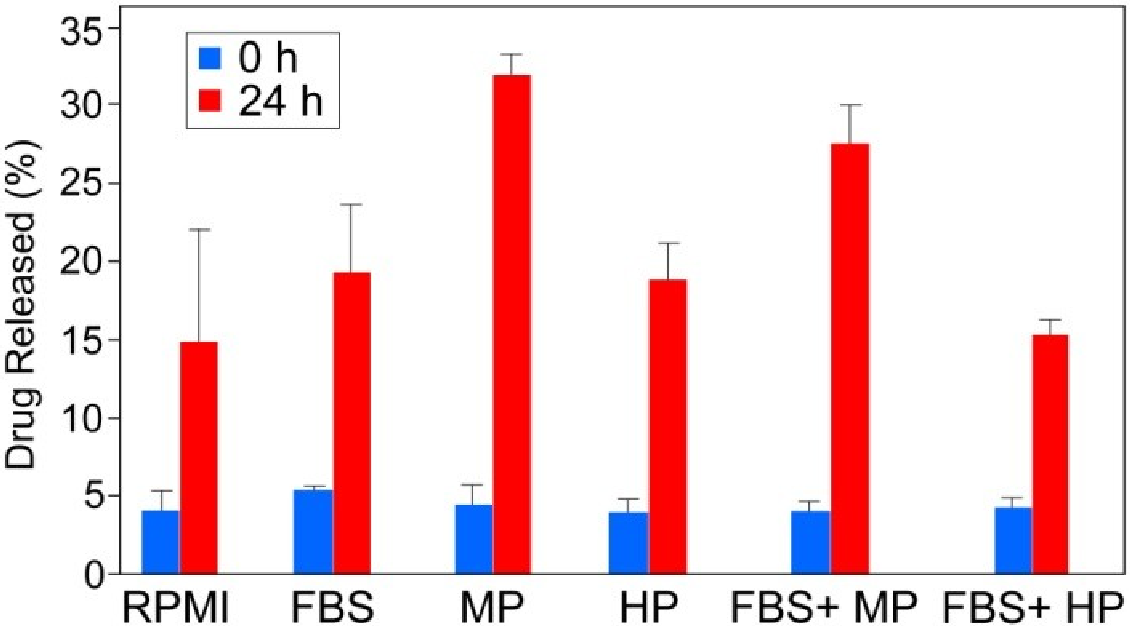

Figure D.5. Stability of polymer micelles (ABA-M) in cell culture medium (RPMI), 10% fetal bovine serum (FBS), 10% mouse plasma (MP), 10% human plasma (HP), and in combinations of these. Drug release was low at the initial time point, indicating that polymer micelles are stable in the presence of biological media. Drug release was slightly elevated in media containing CE at 24 h as compared to media lacking CE.

D.4. DISCUSSION

D.4.1. Polymer Synthesis and Dex Conjugation. Dex was conjugated to PEG-p(Asp) block copolymers through hydrazone-ester dual linkers to prepare polymer micelles that can release the drug preferentially in acidic tumor tissues (pH<7.0). We initially tested Dex conjugation to PEG-pAsp block copolymers using single hydrazone and ester linkers. While Dex could be conjugated to block copolymers directly through a hydrazone linker, the drug loading was low and the hydrazone bond appeared too stable to release the drug in a physiologically relevant time period. Further, micelles from this composition were not homogenous in size, which may result from both **8** and **9** being present or from the polymers having an insufficiently hydrophobic section due to the low drug load. The results also indicated that Dex conjugation through ester linkers had limited stability. Polymer micelles entrapping Dex through an ester linkage would be unsuitable for drug delivery to tumors because more drug would be released in blood (pH 7.4) than in acidic tumor tissues (<pH 6.5). In spite of these apparent failures at achieving pH-dependent Dex release, each linkage still showed successful reaction yields (hydrazone formation) and high drug conjugation (ester formation) between Dex and block copolymers. To take advantage of these possibilities, Dex was conjugated to the block copolymers using a hydrazone-ester dual linker with ketonic acids of varying carbon chain lengths introduced as spacers. Dex loading (4.50 - 5.57 wt%) was high enough to prepare polymer micelles that can carry the drug at concentrations even greater than the effective dose (<1 mg/kg) [277] for future *in vivo* applications.

D.4.2. Preparation of Dex Loaded Micelles. Block copolymers with hydrazone-ester dual linkers formed polymer micelles smaller than 100 nm, which is clinically relevant for tumor-preferential drug delivery by the EPR effect [278]. Interestingly, particle size of the micelles with dual linkers decreased as hydrophobicity of ketonic acids increased in comparison to EST-M. This may be attributable to how the different polymer compositions assemble into micelles with differences in hydrophobicity leading to a change in the micellar aggregation number. ^{1}H-NMR analysis in DMSO-*d6* confirmed Dex conjugation to polymers (Figure D.3). The NMR spectra of the micelles in D_2O showed a complete reduction of peaks from free Dex and the core-forming segment of PEG-p(Asp) block copolymers. Only the PEG peak was observed in all micelle compositions. These results indicate that micelles exhibited the expected core-shell structures with PEG on the surface and the hydrophobic portion of the polymers forming the core to which Dex was entrapped with limited molecular mobility. It is noted that polymer micelles were readily prepared by reconstituting freeze-dried powders, which would facilitate the pharmaceutical development of Dex loaded polymer micelles.

D.4.3. pH-Dependent Dex Release from the Micelles. Polymer micelles with hydrazone or ester single linkers were unsuitable to achieve Dex release in the acidic environment of tumors. The hydrazone linker was too stable to release Dex in both pH 7.4 and 5.0 solutions likely as a result of the multiple double bonds present around the hydrolytic site when Dex is conjugated at the C3 position. Dex release from HYD-M was negligible in 72 h. Ester linkers caused undesirable Dex release from the micelles at pH 7.4 while suppressing drug release at pH 5.0. *In vivo* applications of our polymer micelles with single linkers appeared unlikely for parenteral delivery of Dex. Ester linker micelles may alternatively be suitable for oral delivery of Dex as they may remain stable in acidic gastric fluids until they reach the small intestine.

Polymer micelles with hydrazone-ester dual linkers achieved Dex release suitable for tumor-preferential delivery of Dex. As Dex is conjugated to these polymers following the insertion of a spacer, the hydrazone linker regains its susceptibility to pH-dependent hydrolysis that was lost in the HYD-M composition. In comparison to EST-M, the dual linker micelles suppressed Dex release at pH 7.4 while accelerating Dex release at pH 5.0. Similarly to the hydrazone linker, the difference in ester stability between the single and dual linkers can be attributed to the surrounding chemical structure. Importantly, the results suggest that polymer micelles with dual linkers will remain stable in blood and release more Dex in acidic tumor tissues. Dex release at pH 5.0 was dependent on the chain length of ketonic acid spacers for the dual linker micelles. Dex remaining in OHA-M and OOA-M at 24 h were greater than ABA-M. The suppressed drug release at pH 5.0 with longer ketonic acids may be attributed to the increased hydrophobicity stabilizing the micelle core. The difference in Dex release between OHA-M and OOA-M was not significant. There was no difference in Dex release at pH 7.4, irrespective of the spacer length. These results suggest that the hydrazone is responsible for drug release at pH 5.0 while ester hydrolysis contributes to Dex release at pH 7.4.

It is unknown why polymer micelles did not prevent linkers from hydrolysis at pH 7.4. Our initial expectation was that more hydrophobic spacers would make the micelle cores more stable, and thus suppress drug release further. However, even though Dex molecules are tightly entrapped in the micelle core (as seen in the ^{1}H-NMR analysis), the polymer micelle cores may be porous enough to allow water molecules to penetrate and attack both bonds. Previous results have shown that hydrolysis of small molecule prodrugs with ester linkages can be suppressed as the chain length of tail groups is extended [279]. In contrast, our results showed that the chain length of spacers did not seem to affect the stability of ester linkages in the micelle core. The difference may be attributable to the fact that the mobility of spacers is restricted in the micelle core, offsetting the effects of chain extension, whereas tail groups of prodrugs can move freely in solutions, leading to extended degradation half-lives of ester bonds. It is also possible that the surrounding micelle environment, including the hydrophilic PEG shell, might have attracted water molecules close to the ester linkages in polymer cores, and therefore, hydrolysis reactions took place.

D.4.4. Tunable Dex Release from the Micelles. We analyzed the AUC of Dex release patterns to confirm tunable drug release from the micelles. Tunable drug release is important to control Dex distribution in tumors at different time points after the injection of polymer micelles. Tumor accumulation of polymer micelles was previously shown to reach its maximum level after 3 hours post-injection [280]. For this reason, the AUC values were analyzed both in the early (0-3 h) and late (3-24 h) stages of the drug release study (Figure D.4). Table D.1 summarizes the results.

The $AUC_{0\text{-}3}$ showed that ABA-M (45.20) effectively suppressed drug release at pH 7.4 with respect to EST-M (59.62). OHA-M (70.02) and OOA-M (83.86) released slightly more Dex than EST-M in the same period. At pH 5.0 (0-3 h), all micelles released Dex in a pH-dependent manner [ABA-M (105.38), OHA-M (76.27) and OOA-M (97.17)] compared to EST-M (30.29). At later time periods ($AUC_{3\text{-}24}$), Dex release at pH 7.4 was slower and more sustained in all dual linker micelles compared to EST-M (1162.83): ABA-M (893.03), OHA-M (893.24), and OOA-M (983.39). The $AUC_{3\text{-}24}$ at pH 5.0 showed that ABA-M (1536.74) released more Dex than either OHA-M (1106.28) or OOA-M (1254.63). It is interesting that OOA-M, containing longer and more hydrophobic spacers, released more DEX than OHA-M. Among the dual linker micelles, ABA-M released the least drugs at pH 7.4 and the most drugs at pH 5.0 during the early time period (0-3 h). Using Dex release from ABA-M (100%) as the reference, release from OHA-M (155%) and OOA-M (186%) was greater at pH 7.4 between 0-3 h. OHA-M (72%) and OOA-M (92%) suppressed DEX release at pH 5.0 in the early period compared to ABA-M (100%). In the later time period (3-24 h), Dex release patterns at pH 7.4 were similar in all micelles [ABA-M (100%), OHA-M (100.0%) and OOA-M (110%)]. At pH 5.0, however, ABA-M (100%) still released more Dex than OHA-M (72%) and OOA-M (82%).

These multi-step drug release profiles are desirable for achieving the necessary Dex concentrations at the tumor site. In the early stages following micelle accumulation in tumors, micelles are expected to exhibit a prompt drug release, bringing Dex concentrations up to the required level rapidly. The slower drug release at later time points will allow for Dex concentration levels to be maintained over an extended period of time, reducing the need for multiple doses. It remains challenging for OHA-M and OOA-M to suppress Dex release at pH 7.4 while achieving tunable DEX release in acidic tumor environment. Based on these results, we considered ABA-M the optimal composition that would remain stable in blood and release Dex quickly in tumor tissues.

D.4.5. Enzymatic Stability of Dex Loaded Micelles. Ester linkers can undergo enzymatic degradation in addition to hydrolysis. We tested stability of ABA-M in the presence of CE, a digestive enzyme of esters. We also investigated the influence of ions, small molecules (glucose, vitamins and amino acids), and proteins by testing stability of micelles in cell culture medium (RPMI) and FBS. Such investigation is of importance because the micelles will be exposed to various materials in the blood following injection. Instability in the presence of CE is critically important to be aware of because the CE activity of mouse plasma is significantly higher than human plasma, and studies performed in these animals may not give results representative of what would be observed in humans. Total drug release patterns (free Dex plus Dex-ABA) were compared at 0 and 24 h (Figure D.5). We observed no significant differences among the samples at the initial time point ($p>0.05$). However, the micelles in mouse plasma containing CE showed a slight increase in Dex release at 24 h as compared to the RPMI control. Human plasma lacking CE activity caused no increase in Dex release. As ^{1}H-NMR of the micelles indicated that Dex was entrapped in the micelle core, it seemed unlikely that a 60-70 kDa CE enzyme could penetrate the micelle to this extent. However, this possibility cannot be excluded completely because no general protein destabilization effects on our polymer micelles were observed. Despite this, it is still reasonable to surmise that this minimal increase in Dex release (10 - 15% at 24 h) may not significantly impact the outcome of future *in vivo* studies using ABA-M. This apparent stability of polymer micelles in the presence of CE indicates that Dex-ABA should be primarily released in a pH-dependent manner at the tumor site followed by CE-associated regeneration of free Dex.

D.5. CONCLUSIONS

In exploring polymer micelles as a second possible tumor-targeted drug delivery system, Dex was conjugated to poly(ethylene glycol)-poly(aspartate) block copolymers using hydrazone, ester, or hydrazone-ester dual linkers. Ketonic acids containing 3, 4, and 5 methylene groups were used as spacers to separate the dual linkers. DLS measurements and ^{1}H-NMR analysis confirmed that all Dex loaded micelles were <100 nm with a core-shell structure. Single linker micelles appeared unsuitable to release Dex preferentially in acidic tumor tissues. Hydrazone linkages between Dex and polymers were non-degradable at both pH 7.4 and 5.0. Ester linkages that were stable at pH 5.0 were unstable at pH 7.4. Hydrazone-ester dual linkers suppressed Dex release at pH 7.4, while accelerating drug release at pH 5.0. Dex release decreased at pH 5.0 as the length of the ketonic acid increased but was independent of spacer length at pH 7.4. The dual linker micelles were also stable in the presence of CEs, suggesting that Dex release was primarily due to pH-dependent hydrolysis. Overall, it appears that PEG-poly(aspartate) block copolymer micelles with hydrazone-ester dual linkers are a promising drug delivery platform for tunable release of Dex in tumors. In comparison to single hydrazone or ester linkers, hydrazone-ester dual linkers using ketonic acid spacers are convenient and effective in changing the hydrophobicity of the micelle cores, chemical stability of drug conjugation linkages, and drug release patterns. Such dual linkers may also be useful for other drug delivery platforms to achieve pH-dependent tunable drug release, especially for prodrugs that have been developed based only on ester chemistry. Tunable drug release using hydrazone-ester dual linkers may bring a variety of options for combination chemotherapy and mixed drug delivery using polymer drug carriers in the pharmaceutical research area.

*Reproduced with kind permission from Springer Science+Business Media: Pharmaceutical Research, Polymer Micelles with Hydrazone-Ester Dual Linkers for Tunable Release of Dexamethasone, DOI 10.1007/s11095-011-0470-1, M.D. Howard, A. Ponta, A. Eckman, M. Jay, Y. Bae, Copyright © 2011 Springer Science+Business Media, LLC.

REFERENCES

[1] R.K. Jain, Delivery of molecular medicine to solid tumors: lessons from in vivo imaging of gene expression and function. J. Controlled Release 74(1-3) (2001) 7-25.

[2] R. Perez-Tomas, Multidrug resistance: retrospect and prospects in anti-cancer drug treatment. Curr. Med. Chem. 13(16) (2006) 1859-1876.

[3] D. Franchimont, Overview of the actions of glucocorticoids on the immune response: a good model to characterize new pathways of immunosuppression for new treatment strategies. Ann. N. Y. Acad. Sci. 1024 (2004) 124-137.

[4] D. Czock, F. Keller, F. Franz Maximilian Rasche, U. Häussler, Pharmacokinetics and Pharmacodynamics of Systemically Administered Glucocorticoids. Clin. Pharmacokinet. 44(1) (2005) 61-98.

[5] H. Wang, M. Li, J.J. Rinehart, R. Zhang, Pretreatment with Dexamethasone Increases Antitumor Activity of Carboplatin and Gemcitabine in Mice Bearing Human Cancer Xenografts: In Vivo Activity, Pharmacokinetics, and Clinical Implications for Cancer Chemotherapy. Clin. Cancer Res. 10(5) (2004) 1633-1644.

[6] H. Wang, M. Li, J.J. Rinehart, R. Zhang, Dexamethasone as a chemoprotectant in cancer chemotherapy: hematoprotective effects and altered pharmacokinetics and tissue distribution of carboplatin and gemcitabine. Cancer Chemother. Pharmacol. 53(6) (2004) 459-467.

[7] J. Rinehart, L. Keville, J. Neiddhart, L. Wong, L. DiNunno, P. Kinney, M. Aberle, L. Tadlock, G. Cloud, Hematopoietic Protection by Dexamethasone or Granulocyte-Macrophage Colony-Stimulating Factor (GM-CSF) in Patients Treated with Carboplatin and Ifosfamide. Am. J. Clin. Oncol. 26(5) (2003) 448- 458.

[8] M. Leggas, K.L. Kuo, F. Robert, G. Cloud, M. deShazo, R. Zhang, M. Li, H. Wang, S. Davidson, J. Rinehart, Intensive anti-inflammatory therapy with dexamethasone in patients with non-small cell lung cancer: effect on chemotherapy toxicity and efficacy. Cancer Chemother. Pharmacol. 63(4) (2009) 731-743.

[9] N. Auphan, J.A. DiDonato, C. Rosette, A. Helmberg, M. Karin, Immunosuppression by Glucocorticoids: Inhibition of NF-kB Activity Through Induction of IkB Synthesis. Science 270(5234) (1995) 286-290.

[10] R.I. Scheinman, P.C. Cogswell, A.K. Lofquist, J. Albert S. Baldwin, Role of Transcriptional Activation of I kappa B alpha in Mediation of Immunosuppression by glucocorticoids. Science 270(5234) (1995) 283-286.

[11] H. Wang, Y. Wang, E.R. Rayburn, D.L. Hill, J.J. Rinehart, R. Zhang, Dexamethasone as a chemosensitizer for breast cancer chemotherapy: potentiation of the antitumor activity of adriamycin, modulation of cytokine expression, and pharmacokinetics. Int. J. Oncol. 30(4) (2007) 947-953.

[12] P.G. Braunschweiger, L.M. Schiffer, Effect of Dexamethasone on Vascular Function in RIF-1 Tumors. Cancer Res. 46(7) (1986) 3299-3303.

[13] P.E.G. Kristjansen, Y. Boucher, R.K. Jain, Dexamethasone Reduces the Interstitial Fluid Pressure in a Human Colon Adenocarcinoma Xenograft. Cancer Res. 53(20) (1993) 4764-4766.

[14] C. Wilson, P. Scullin, J. Worthington, A. Seaton, P. Maxwell, D. O'Rourke, P.G. Johnston, S.R. McKeown, R.H. Wilson, J.M. O'Sullivan, D.J.J. Waugh, Dexamethasone

potentiates the antiangiogenic activity of docetaxel in castration-resistant prostate cancer. Br. J. Cancer 99(12) (2008) 2054-2064.

[15] W. Wu, T. Pew, M. Zou, D. Pang, S.D. Conzen, Glucocorticoid Receptor-induced MAPK Phosphatase-1 (MPK-1) Expression Inhibits Paclitaxel-associated MAPK Activation and Contributes to Breast Cancer Cell Survival. J. Biol. Chem. 280(6) (2005) 4117-4124.

[16] D. Pang, M. Kocherginsky, T. Krausz, S.Y. Kim, S.D. Conzen, Dexamethasone decreases xenograft response to Paclitaxel through inhibition of tumor cell apoptosis. Cancer Biol. Ther. 5(8) (2006) 933-940.

[17] M. Sui, F. Chen, Z. Chen, W. Fan, Glucocorticoids interfere with therapeutic efficacy of paclitaxel against human breast and ovarian xenograft tumors. Int. J. Cancer 119(3) (2006) 712-717.

[18] S. Meyer, T. Eden, H. Kalirai, Dexamethasone protects against Cisplatin-induced activation of the mitochondrial apoptotic pathway in human osteosarcoma cells. Cancer Biol. Ther. 5(8) (2006) 915-920.

[19] D. Franchimont, J. Galon, M. Gadina, R. Visconti, Y.J. Zhou, M. Aringer, D.M. Frucht, G.P. Chrousos, J.J. O'Shea, Inhibition of Th1 Immune Response by Glucocorticoids: Dexamethasone Selectively Inhibits IL-12-Induced Stat4 Phosphorylation in T Lymphocytes. J. Immunol. 164(4) (2000) 1768-1774.

[20] V.P. Torchilin, A.N. Lukyanov, Z. Gao, B. Papahadjopoulos-Sternberg, Immunomicelles: Targeted pharmaceutical carriers for poorly soluble drugs. PNAS 100(10) (2003) 6039-6044.

[21] F. Ahmed, R.I. Pakunlu, G. Srinivas, A. Brannan, F. Bates, M.L. Klein, T. Minko, D.E. Discher, Shrinkage of a Rapidly Growing Tumor by Drug-Loaded Polymersomes: pH-Triggered Release through Copolymer Degradation. Mol. Pharmaceutics 3(3) (2006) 340-350.

[22] N. Tirelli, (Bio)Responsive nanoparticles. Current Opinion in Colloid & Interface Science 11(4) (2006) 210-216.

[23] H. Xu, Y. Deng, D. Chen, W. Hong, Y. Lu, X. Dong, Esterase-catalyzed dePEGylation of pH-sensitive vesicles modified with cleavable PEG-lipid derivatives. J. Controlled Release 130(3) (2008) 238-245.

[24] S. Ganta, H. Devalapally, A. Shahiwala, M. Amiji, A review of stimuli-responsive nanocarriers for drug and gene delivery. J. Controlled Release 126(3) (2008) 187-204.

[25] D. Kim, E.S. Lee, K.T. Oh, Z.G. Gao, Y.H. Bae, Doxorubicin-Loaded Polymeric Micelle Overcomes Multidrug Resistance of Cancer by Double-Targeting Folate Receptor and Early Endosomal pH. Small 4(11) (2008) 2043-2050.

[26] X. Dong, C.A. Mattingly, M.T. Tseng, M.J. Cho, Y. Liu, V.R. Adams, R.J. Mumper, Doxorubicin and Paclitaxel-Loaded Lipid-Based Nanoparticles Overcome Multidrug Resistance by Inhibiting P-Glycoprotein and Depleting ATP. Cancer Res. 21 (2009) 21.

[27] E.A. Simone, T.D. Dziubla, F. Colon-Gonzalez, D.E. Discher, V.R. Muzykantov, Effect of polymer amphiphilicity on loading of a therapeutic enzyme into protective filamentous and spherical polymer nanocarriers. Biomacromolecules 8(12) (2007) 3914-3921.

[28] Y. Matsumura, H. Maeda, A new concept for macromolecular therapeutics in cancer chemotherapy: mechanism of tumoritropic accumulation of proteins and the antitumor agent smancs. Cancer Res. 46 (1986) 6387 - 6392.

[29] S.K. Hobbs, W.L. Monsky, F. Yuan, W.G. Roberts, L. Griffith, V.P. Torchilin, R.K. Jain, Regulation of transport pathways in tumor vessels: Role of tumor type and microenvironment. PNAS 95(8) (1998) 4607-4612.

[30] T. Lammers, V. Subr, K. Ulbrich, P. Peschke, P.E. Huber, W.E. Hennink, G. Storm, Simultaneous delivery of doxorubicin and gemcitabine to tumors in vivo using prototypic polymeric drug carriers. Biomaterials 30(20) (2009) 3466-3475.

[31] E. Ambegia, S. Ansell, P. Cullis, J. Heyes, L. Palmer, I. MacLachlan, Stabilized plasmid-lipid particles containing PEG-diacylglycerols exhibit extended circulation lifetimes and tumor selective gene expression. Biochim. Biophys. Acta (BBA) - Biomembranes 1669(2) (2005) 155-163.

[32] M. Uner, G. Yener, Importance of solid lipid nanoparticles (SLN) in various administration routes and future perspectives. Int. J. Nanomedicine 2(3) (2007) 289-300.

[33] W. Mehnert, K. Mäder, Solid lipid nanoparticles: Production, characterization and applications. Adv. Drug Deliv. Rev. 47(2-3) (2001) 165-196.

[34] R.H. Muller, K. Mader, S. Gohla, Solid lipid nanoparticles (SLN) for controlled drug delivery - a review of the state of the art. Eur. J. Pharm. Biopharm. 50(1) (2000) 161-177.

[35] X. Lu, M. Howard, M. Mazik, J. Eldridge, J. Rinehart, M. Jay, M. Leggas, Nanoparticles Containing Anti-inflammatory Agents as Chemotherapy Adjuvants: Optimization and In Vitro Characterization. AAPS J. 10(1) (2008) 133-140.

[36] K. Yokoyama, M. Watanabe, Limethason as a lipid microsphere preparation: An overview. Adv. Drug Deliv. Rev. 20(2-3) (1996) 195-201.

[37] X. Lu, M.D. Howard, D.R. Talbert, J.J. Rinehart, P.M. Potter, M. Jay, M. Leggas, Nanoparticles Containing Anti-inflammatory Agents as Chemotherapy Adjuvants II: Role of Plasma Esterases in Drug Release. AAPS J. 11(1) (2009) 120-122.

[38] S.-S. Feng, S. Chien, Chemotherapeutic engineering: Application and further development of chemical engineering principles for chemotherapy of cancer and other diseases. Chemical Engineering Science 58(18) (2003) 4087-4114.

[39] A.C. Society, Cancer Statistics 2010. 2010.

[40] I. Fischer, K. Aldape, Molecular Tools: Biology, Prognosis, and Therapeutic Triage. Neuroimaging Clin. N. Am. 201(3) (2010) 273-282.

[41] R. Salgia, T. Hensing, N. Campbell, A.K. Salama, M. Maitland, P. Hoffman, V. Villaflor, E.E. Vokes, Personalized Treatment of Lung Cancer. Semin. Oncol. 38(2) (2011) 274-283.

[42] R.K. Jain, Transport of Molecules in the Tumor Interstitium: A Review. Cancer Res. 47(12) (1987) 3039-3051.

[43] P. Carmeliet, R.K. Jain, Angiogenesis in cancer and other diseases. Nature 407(6801) (2000) 249-257.

[44] C.-H. Heldin, K. Rubin, K. Pietras, A. Ostman, High interstitial fluid pressure - an obstacle in cancer therapy. Nat. Rev. Cancer 4(10) (2004) 806-813.

[45] M.M. Mueller, N.E. Fusenig, Friends or foes - bipolar effects of the tumour stroma in cancer. Nat. Rev. Cancer 4(11) (2004) 839-849.

[46] K. Yang, J. Wu, X. Li, Recent advances in the research of P-glycoprotein inhibitors. Biosci. Trends 2(4) (2008) 137-146.

[47] M.E. Lippman, Glucocorticoid receptors and effects in human lymphoid and leukemic cells. Monogr. Endocrinol. 12 (1979) 377-397.

[48] E.B. Thompson, J.R. Smith, S. Bourgeois, J.M. Harmon, Glucocorticoid receptors in human leukemias and related diseases. Klin. Wochenschr. 63(15) (1985) 689-698.

[49] D.T. Chua, J.S. Sham, D.L. Kwong, C.C. Kwok, A. Yue, Y.C. Foo, R. Chan, Comparative efficacy of three 5-HT3 antagonists (granisetron, ondansetron, and tropisetron) plus dexamethasone for the prevention of cisplatin-induced acute emesis: a randomized crossover study. Am. J. Clin. Oncol. 23(2) (2000) 185-191.

[50] E.M. Ibrahim, H.Y. Al-Idrissi, A. Ibrahim, G. Absood, E. Al-Dossary, A. Al-Jammaa, S. Al-Ethan, A. Eliopoulos, Antiemetic efficacy of high-dose dexamethasone: randomized, double-blind, crossover study with high-dose metoclopramide in patients receiving cancer chemotherapy. Eur. J. Cancer Clin. Oncol. 22(3) (1986) 283-288.

[51] A.B. Kriegler, D. Bernardo, S.M. Verschoor, Protection of murine bone marrow by dexamethasone during cytotoxic chemotherapy. Blood 83(1) (1994) 65-71.

[52] A.L. Rose, B.E. Smith, D.G. Maloney, Glucocorticoids and rituximab in vitro: synergistic direct antiproliferative and apoptotic effects. Blood 100(5) (2002) 1765-1773.

[53] A.C. Bharti, B.B. Aggarwal, Nuclear factor-kappa B and cancer: its role in prevention and therapy. Biochem. Pharmacol. 64(5-6) (2002) 883-888.

[54] M.A. Altinoz, R. Korkmaz, NF-kappaB, macrophage migration inhibitory factor and cyclooxygenase-inhibitions as likely mechanisms behind the acetaminophen- and NSAID-prevention of the ovarian cancer. Neoplasma 51(4) (2004) 239-247.

[55] I. Herr, E. Ucur, K. Herzer, S. Okouoyo, R. Ridder, P.H. Krammer, M. von Knebel Doeberitz, K.-M. Debatin, Glucocorticoid Cotreatment Induces Apoptosis Resistance toward Cancer Therapy in Carcinomas. Cancer Res. 63(12) (2003) 3112-3120.

[56] C.J. Vecht, A. Hovestadt, H.B. Verbiest, J.J. van Vliet, W.L. van Putten, Dose-effect relationship of dexamethasone on Karnofsky performance in metastatic brain tumors: a randomized study of doses of 4, 8, and 16 mg per day. Neurology 44(4) (1994) 675-680.

[57] O.C. Farokhzad, R. Langer, Impact of Nanotechnology on Drug Delivery. ACS Nano 3(1) (2009) 16-20.

[58] J.-H. Kim, Y.-S. Kim, S. Kim, J.H. Park, K. Kim, K. Choi, H. Chung, S.Y. Jeong, R.-W. Park, I.-S. Kim, I.C. Kwon, Hydrophobically modified glycol chitosan nanoparticles as carriers for paclitaxel. J. Controlled Release 111(1-2) (2006) 228-234.

[59] Z. Zhang, D.W. Grijpma, J. Feijen, Poly(trimethylene carbonate) and monomethoxy poly(ethylene glycol)-block-poly(trimethylene carbonate) nanoparticles for the controlled release of dexamethasone. J. Controlled Release 111(3) (2006) 263-270.

[60] K. Kataoka, T. Matsumoto, M. Yokoyama, T. Okano, Y. Sakurai, S. Fukushima, K. Okamoto, G.S. Kwon, Doxorubicin-loaded poly(ethylene glycol)-poly([beta]-benzyl--aspartate) copolymer micelles: their pharmaceutical characteristics and biological significance. J. Controlled Release 64(1-3) (2000) 143-153.

[61] K. Dongin, L. Eun Seong, O. Kyung Taek, G. Zhong Gao, B. You Han, Doxorubicin-Loaded Polymeric Micelle Overcomes Multidrug Resistance of Cancer by

Double-Targeting Folate Receptor and Early Endosomal pH. Small 4(11) (2008) 2043-2050.

[62] M.E. Davis, Z. Chen, D.M. Shin, Nanoparticle therapeutics: an emerging treatment modality for cancer. Nat. Rev. Drug Discov. 7(9) (2008) 771-782.

[63] M.D. Howard, M. Jay, T.D. Dziubla, X. Lu, PEGylation of Nanocarrier Drug Delivery Systems: State of the Art. J. Biomed. Nanotechnol. 4 (2008) 133-148.

[64] Y. Matsumura, H. Maeda, A New Concept for Macromolecular Therapeutics in Cancer Chemotherapy: Mechanism of Tumoritropic Accumulation of Proteins and the Antitumor Agent Smancs. Cancer Res. 46(12_Part_1) (1986) 6387-6392.

[65] T. Ishihara, T. Kubota, T. Choi, M. Higaki, Treatment of Experimental Arthritis with Stealth-Type Polymeric Nanoparticles Encapsulating Betamethasone Phosphate. J. Pharmacol. Exp. Ther. 329(2) (2009) 412-417.

[66] D. Wang, S. Miller, X.-M. Liu, B. Anderson, X.S. Wang, S. Goldring, Novel dexamethasone-HPMA copolymer conjugate and its potential application in treatment of rheumatoid arthritis. Arthritis Res. Ther. 9(1) (2007) R2.

[67] X.M. Liu, L.D. Quan, J. Tian, Y. Alnouti, K. Fu, G.M. Thiele, D. Wang, Synthesis and evaluation of a well-defined HPMA copolymer-dexamethasone conjugate for effective treatment of rheumatoid arthritis. Pharm. Res. 25(12) (2008) 2910-2919.

[68] M.O. Oyewumi, R.A. Yokel, M. Jay, T. Coakley, R.J. Mumper, Comparison of cell uptake, biodistribution and tumor retention of folate-coated and PEG-coated gadolinium nanoparticles in tumor-bearing mice. J. Controlled Release 95(3) (2004) 613-626.

[69] J.E. Schnitzer, Vascular Targeting as a Strategy for Cancer Therapy. N. Engl. J. Med. 339(7) (1998) 472-474.

[70] D.E. Owens III, N.A. Peppas, Opsonization, biodistribution, and pharmacokinetics of polymeric nanoparticles. Int. J. Pharm. 307(1) (2006) 93-102.

[71] A. Vonarbourg, C. Passirani, P. Saulnier, J.-P. Benoit, Parameters influencing the stealthiness of colloidal drug delivery systems. Biomaterials 27(24) (2006) 4356-4373.

[72] S.M. Moghimi, H.M. Patel, Serum-mediated recognition of liposomes by phagocytic cells of the reticuloendothelial system - The concept of tissue specificity. Adv. Drug Deliv. Rev. 32(1-2) (1998) 45-60.

[73] H. Harashima, S. Komatsu, S. Kojima, C. Yanagi, Y. Morioka, M. Naito, H. Kiwada, Species Difference in the Disposition of Liposomes Among Mice, Rats, and Rabbits: Allometric Relationship and Species Dependent Hepatic Uptake Mechanism. Pharm. Res. 13(7) (1996) 1049-1054.

[74] D. Liu, Q. Hu, Y.K. Song, Liposome clearance from blood: different animal species have different mechanisms. Biochim. Biophys. Acta 1240 (1995) 277-284.

[75] F. Liu, D. Liu, Serum independent liposome uptake by mouse liver. Biochim. Biophys. Acta (BBA) 1278 (1996) 5-11.

[76] H. Harashima, H. Matsuo, H. Kiwada, Identification of proteins mediating clearance of liposomes using a liver perfusion system. Adv. Drug Deliv. Rev. 32(1-2) (1998) 61-79.

[77] D.V. Devine, K. Wong, K. Serrano, A. Chonn, P.R. Cullis, Liposome-complement interactions in rat serum: implications for liposome survival studies. Biochim. Biophys. Acta - Biomembranes 1191(1) (1994) 43-51.

[78] D. Liu, F. Liu, Y.K. Song, Recognition and clearance of liposomes containing phosphatidylserine are mediated by serum opsonin. Biochim. Biophys. Acta 1235(1) (1995) 140-146.

[79] A. Chonn, S.C. Semple, P.R. Cullis, Association of blood proteins with large unilamellar liposomes in vivo. Relation to circulation lifetimes. J. Biol. Chem. 267(26) (1992) 18759-18765.

[80] A. Chonn, P.R. Cullis, D.V. Devine, The role of surface charge in the activation of the classical and alternative pathways of complement by liposomes. J. Immunol. 146(12) (1991) 4234-4241.

[81] S.C. Semple, A. Chonn, P.R. Cullis, Interactions of liposomes and lipid-based carrier systems with blood proteins: Relation to clearance behaviour in vivo. Adv. Drug Deliv. Rev. 32(1-2) (1998) 3-17.

[82] R. Gref, M. Luck, P. Quellec, M. Marchand, E. Dellacherie, S. Harnisch, T. Blunk, R.H. Muller, `Stealth' corona-core nanoparticles surface modified by polyethylene glycol (PEG): influences of the corona (PEG chain length and surface density) and of the core composition on phagocytic uptake and plasma protein adsorption. Colloids Surf. B Biointerfaces 18(3-4) (2000) 301-313.

[83] L. Ilium, I.M. Hunneyball, S.S. Davis, The effect of hydrophilic coatings on the uptake of colloidal particles by the liver and by peritoneal macrophages. Int. J. Pharm. 29(1) (1986) 53-65.

[84] G.R. Llanos, M.V. Sefton, Review Does polyethylene oxide possess a low thrombogenicity? J. Biomater. Sci. Polym. Ed. 4 (1993) 381-400.

[85] T.M. Allen, The use of glycolipids and hydrophilic polymers in avoiding rapid uptake of liposomes by the mononuclear phagocyte system. Adv. Drug Deliv. Rev. 13(3) (1994) 285-309.

[86] S. Nagaoka, Y. Mori, H. Takiuchi, K. Yokota, H. Tanzawa, S. Nishiumi, in: S. Shalaby, A. S. Hoffman, B. D. Ratner and T. A. Horbett (Eds.), Polymers as Biomaterials, Plenum Press, New York, 1984, pp. 361-371.

[87] E. Kiss, C. Gölander, J. Eriksson, Surface Forces and Surfactant Systems, 1987, pp. 113-119.

[88] V.P. Torchilin, Polymer-coated long-circulating microparticulate pharmaceuticals. J. Microencapsul. 15(1) (1998) 1-19.

[89] V.P. Torchilin, V.G. Omelyanenko, M.I. Papisov, A.A. Bogdanov, Jr., V.S. Trubetskoy, J.N. Herron, C.A. Gentry, Poly(ethylene glycol) on the liposome surface: on the mechanism of polymer-coated liposome longevity. Biochim. Biophys. Acta 1195(1) (1994) 11-20.

[90] B. Jansen, G. Ellinghorst, Modification of polyetherurethane for biomedical application by radiation induced grafting. II. Water sorption, surface properties, and protein adsorption of grafted films. J. Biomed. Mater. Res. 18(6) (1984) 655-669.

[91] D.L. Coleman, D.E. Gregonis, J.D. Andrade, Blood-materials interactions: The minimum interfacial free energy and the optimum polar/apolar ratio hypotheses. J. Biomed. Mater. Res. 16(4) (1982) 381-398.

[92] S.I. Jeon, J.H. Lee, J.D. Andrade, P.G. DeGennes, Protein-surface interactions in the presence of polyethylene oxide I. Simplified Theory. J. Colloid Interface Sci. 142(1) (1991) 149-158.

[93] S.M. Moghimi, H.M. Patel, Tissue specific opsonins for phagocytic cells and their different affinity for cholesterol-rich liposomes. FEBS Lett. 233(1) (1988) 143-147.

[94] S.M. Moghimi, H.M. Patel, Serum opsonins and phagocytosis of saturated and unsaturated phospholipid liposomes. Biochim. Biophys. Acta 984(3) (1989) 384-387.

[95] S.M. Moghimi, H.M. Patel, Differential properties of organ-specific serum opsonins for liver and spleen macrophages. Biochim. Biophys. Acta 984(3) (1989) 379-383.

[96] S.M. Moghimi, H.M. Patel, Serum factors that regulate phagocytosis of liposomes by Kupffer cells. Biochem. Soc. Trans. 21(2) (1993) 128S.

[97] S.M. Moghimi, J. Szebeni, Stealth liposomes and long circulating nanoparticles: critical issues in pharmacokinetics, opsonization and protein-binding properties. Prog. Lipid Res. 42(6) (2003) 463-478.

[98] S.M. Moghimi, I.S. Muir, L. Illum, S.S. Davis, V. Kolb-Bachofen, Coating particles with a block co-polymer (poloxamine-908) suppresses opsonization but permits the activity of dysopsonins in the serum. Biochim. Biophys. Acta 1179(2) (1993) 157-165.

[99] I.S. Muir, S.M. Moghimi, L. Illum, S.S. Davis, M.C. Davies, The effect of block co-polymers on the uptake of model polystyrene microspheres by Kupffer cells--in vitro and in vivo studies. Biochem. Soc. Trans. 19(3) (1991) 329S.

[100] S.E. Dunn, A. Brindley, S.S. Davis, M.C. Davies, L. Illum, Polystyrene-Poly (Ethylene Glycol) (PS-PEG2000) Particles as Model Systems for Site Specific Drug Delivery. 2. The Effect of PEG Surface Density on the *in Vitro* Cell Interaction and *in Vivo* Biodistribution. Pharm. Res. 11(7) (1994) 1016-1022.

[101] V.C. Mosqueira, P. Legrand, R. Gref, B. Heurtault, M. Appel, G. Barratt, Interactions between a macrophage cell line (J774A1) and surface-modified poly (D,L-lactide) nanocapsules bearing poly(ethylene glycol). J. Drug Target. 7(1) (1999) 65-78.

[102] G. Storm, S.O. Belliot, T. Daemen, D.D. Lasic, Surface modification of nanoparticles to oppose uptake by the mononuclear phagocyte system. Adv. Drug Deliv. Rev. 17(1) (1995) 31-48.

[103] J.K. Gbadamosi, A.C. Hunter, S.M. Moghimi, PEGylation of microspheres generates a heterogeneous population of particles with differential surface characteristics and biological performance. FEBS Lett. 532(3) (2002) 338-344.

[104] P.J. Photos, L. Bacakova, B. Discher, F.S. Bates, D.E. Discher, Polymer vesicles in vivo: correlations with PEG molecular weight. J. Controlled Release 90(3) (2003) 323-334.

[105] A.S. Zahr, C.A. Davis, M.V. Pishko, Macrophage Uptake of Core-Shell Nanoparticles Surface Modified with Poly(ethylene glycol). Langmuir 22(19) (2006) 8178-8185.

[106] K. Bergstrom, E. Osterberg, K. Holmberg, A.S. Hoffman, T.P. Schuman, A. Kozlowski, J.H. Harris, Effects of branching and molecular weight of surface-bound poly(ethylene oxide) on protein rejection. J. Biomater. Sci. Polym. Ed. 6(2) (1994) 123-132.

[107] S. Stolnik, L. Illum, S.S. Davis, Long circulating microparticulate drug carriers. Adv. Drug Deliv. Rev. 16(2-3) (1995) 195-214.

[108] B. Shi, C. Fang, Y. Pei, Stealth PEG-PHDCA niosomes: Effects of chain length of PEG and particle size on niosomes surface properties, in vitro drug release, phagocytic

uptake, in vivo pharmacokinetics and antitumor activity. J. Pharm. Sci. 95(9) (2006) 1873-1887.

[109] M. Vittaz, D. Bazile, G. Spenlehauer, T. Verrecchia, M. Veillard, F. Puisieux, D. Labarre, Effect of PEO surface density on long-circulating PLA-PEO nanoparticles which are very low complement activators. Biomaterials 17(16) (1996) 1575-1581.

[110] S.J. Sofia, V. Premnath, E.W. Merrill, Poly(ethylene oxide) Grafted to Silicon Surfaces: Grafting Density and Protein Adsorption. Macromolecules 31(15) (1998) 5059-5070.

[111] W.R. Gombotz, G.H. Wang, T.A. Horbett, A.S. Hoffman, Protein adsorption to poly(ethylene oxide) surfaces. J. Biomed. Mater. Res. 25(12) (1991) 1547-1562.

[112] D.D. Lasic, in: J. M. Harris and S. Zalipsky (Eds.), Poly(ethylene glycol) Chemistry and Biological Applications, American Chemical Society, Washington, D.C., 1997, pp. 31-44.

[113] R. Gref, Y. Minamitake, M.T. Peracchia, V. Trubetskoy, V. Torchilin, R. Langer, Biodegradable Long-Circulating Polymeric Nanospheres. Science 263(5153) (1994) 1600-1603.

[114] J.C. Neal, S. Stolnik, E. Schacht, E.R. Kenawy, M.C. Garnett, S.S. Davis, L. Illum, In vitro displacement by rat serum of adsorbed radiolabeled poloxamer and poloxamine copolymers from model and biodegradable nanospheres. J. Pharm. Sci. 87(10) (1998) 1242-1248.

[115] S.R. Sheth, D. Leckband, Measurements of attractive forces between proteins and end-grafted poly(ethylene glycol) chains. PNAS 94(16) (1997) 8399-8404.

[116] G.R. Harper, M.C. Davies, S.S. Davis, T.F. Tadros, D.C. Taylor, M.P. Irving, J.A. Waters, Steric stabilization of microspheres with grafted polyethylene oxide reduces phagocytosis by rat Kupffer cells in vitro. Biomaterials 12(7) (1991) 695-700.

[117] D. Bazile, C. Prud'homme, M.-T. Bassoullet, M. Marlard, G. Spenlehauer, M. Veillard, Stealth Me.PEG-PLA nanoparticles avoid uptake by the mononuclear phagocytes system. J. Pharm. Sci. 84(4) (1995) 493-498.

[118] S.D. Li, Y.C. Chen, M.J. Hackett, L. Huang, Tumor-targeted Delivery of siRNA by Self-assembled Nanoparticles. Mol. Ther. 16(1) (2008) 163-169.

[119] C. Bocca, O. Caputo, R. Cavalli, L. Gabriel, A. Miglietta, M.R. Gasco, Phagocytic uptake of fluorescent stealth and non-stealth solid lipid nanoparticles. Int. J. Pharm. 175(2) (1998) 185-193.

[120] A. Fundaro, R. Cavalli, A. Bargoni, D. Vighetto, G.P. Zara, M.R. Gasco, Non-stealth and stealth solid lipid nanoparticles (SLN) carrying doxorubicin: pharmacokinetics and tissue distribution after i.v. administration to rats. Pharmacol. Res. 42(4) (2000) 337-343.

[121] Y.-P. Li, Z.-H. Zhou, Y.-Y. Pei, X.-Y. Zhang, Z.-H. Gu, W.-F. Yuan, PEGylated polycyanoacrylate nanoparticles as salvicine carriers: synthesis, preparation, and in vitro characterization. Acta Pharmacologica Sinica 22(7) (2001) 645-650.

[122] E.F. Craparo, G. Cavallaro, M.L. Bondi, D. Mandracchia, G. Giammona, PEGylated Nanoparticles Based on a Polyaspartamide. Preparation, Physico-Chemical Characterization, and Intracellular Uptake. Biomacromolecules 7(11) (2006) 3083-3092.

[123] G. Loch-Neckel, D. Nemen, A.C. Puhl, D. Fernandes, M.A. Stimamiglio, M. Alvarez Silva, M. Hangai, M.C. Santos Silva, E. Lemos-Senna, Stealth and non-stealth

nanocapsules containing camptothecin: in-vitro and in-vivo activity on B16-F10 melanoma. J. Pharm. Pharmacol. 59(10) (2007) 1359-1364.

[124] L. Zhang, F.X. Gu, J.M. Chan, A.Z. Wang, R.S. Langer, O.C. Farokhzad, Nanoparticles in Medicine: Therapeutic Applications and Developments. Clin. Pharmacol. Ther. (2007).

[125] D.W. Northfelt, B.J. Dezube, J.A. Thommes, B.J. Miller, M.A. Fischl, A. Friedman-Kien, L.D. Kaplan, C. Du Mond, R.D. Mamelok, D.H. Henry, Pegylated-liposomal doxorubicin versus doxorubicin, bleomycin, and vincristine in the treatment of AIDS-related Kaposi's sarcoma: results of a randomized phase III clinical trial. J. Clin. Oncol. 16(7) (1998) 2445-2451.

[126] C. Gomez-Gaete, N. Tsapis, M. Besnard, A. Bochot, E. Fattal, Encapsulation of dexamethasone into biodegradable polymeric nanoparticles. Int. J. Pharm. 331(2) (2007) 153-159.

[127] M.J. Heffernan, N. Murthy, Polyketal Nanoparticles: A New pH-Sensitive Biodegradable Drug Delivery Vehicle. Bioconjugate Chem. 16(6) (2005) 1340-1342.

[128] M. Banciu, M.H.A.M. Fens, G. Storm, R.M. Schiffelers, Antitumor activity and tumor localization of liposomal glucocorticoids in B16 melanoma-bearing mice. J. Controlled Release 127(2) (2008) 131-136.

[129] H. Benameur, G.D. Gand, R. Brasseur, J.P.V. Vooren, F.J. Legros, Liposome-incorporated dexamethasone palmitate: Chemical and physical properties. Int. J. Pharm. 89 (1993) 157-167.

[130] M. Uner, Preparation, characterization and physico-chemical properties of solid lipid nanoparticles (SLN) and nanostructured lipid carriers (NLC): their benefits as colloidal drug carrier systems. Pharmazie 61(5) (2006) 375-386.

[131] R.J. Mumper, Z. Cui, M.O. Oyewumi, Nanotemplate Engineering of Cell Specific Nanoparticles. J. Dispers. Sci. Technol. 24(3) (2003) 569 - 588.

[132] A. Dingler, R.P. Blum, H. Niehus, R.H. Muller, S. Gohla, Solid lipid nanoparticles (SLN/Lipopearls)-a pharmaceutical and cosmetic carrier for the application of vitamin E in dermal products. J. Microencapsul. 16(6) (1999) 751.

[133] M.R. Gasco, Solid lipid nanospheres from warm micro-emulsions. Pharmaceutical Technology Europe 9 (1997) 52-58.

[134] R.J. Mumper, M. Jay, Microemulsions as precursors to solid nanoparticles, USA Patent 71535252006.

[135] R.H. Müller, M. Radtke, S.A. Wissing, Nanostructured lipid matrices for improved microencapsulation of drugs. Int. J. Pharm. 242(1-2) (2002) 121-128.

[136] K. Westesen, H. Bunjes, M.H.J. Koch, Physicochemical characterization of lipid nanoparticles and evaluation of their drug loading capacity and sustained release potential. J. Controlled Release 48(2-3) (1997) 223-236.

[137] H. Bunjes, K. Westesen, M.H.J. Koch, Crystallization tendency and polymorphic transitions in triglyceride nanoparticles. Int. J. Pharm. 129(1-2) (1996) 159-173.

[138] V. Jenning, S. Gohla, Comparison of wax and glyceride solid lipid nanoparticles (SLN®). Int. J. Pharm. 196 (2000) 219-222.

[139] T. Helgason, T.S. Awad, K. Kristbergsson, D.J. McClements, J. Weiss, Effect of surfactant surface coverage on formation of solid lipid nanoparticles (SLN). J. Colloid Interface Sci. 334(1) (2009) 75-81.

[140] T. Helgason, T.S. Awad, K. Kristbergsson, D.J. McClements, J. Weiss, Influence of polymorphic transformations on gelation of tripalmitin solid lipid nanoparticle suspensions. J. Am. Oil Chem. Soc. 85(6) (2008) 501-511.

[141] C. Freitas, R.H. Müller, Correlation between long-term stability of solid lipid nanoparticles (SLN(TM)) and crystallinity of the lipid phase. Eur. J. Pharm. Biopharm. 47(2) (1999) 125-132.

[142] K. Westesen, B. Siekmann, Investigation of the gel formation of phospholipid-stabilized solid lipid nanoparticles. Int. J. Pharm. 151(1) (1997) 35-45.

[143] T.S. Awad, T. Helgason, J. Weiss, E.A. Decker, D.J. McClements, Effect of Omega-3 Fatty Acids on Crystallization, Polymorphic Transformation and Stability of Tripalmitin Solid Lipid Nanoparticle Suspensions. Crystal Growth & Design 9(8) (2009) 3405-3411.

[144] A.A. Attama, B.C. Schicke, C.C. Müller-Goymann, Further characterization of theobroma oil-beeswax admixtures as lipid matrices for improved drug delivery systems. Eur. J. Pharm. Biopharm. 64(3) (2006) 294-306.

[145] H. Bunjes, M.H.J. Koch, K. Westesen, Influence of emulsifiers on the crystallization of solid lipid nanoparticles. J. Pharm. Sci. 92(7) (2003) 1509-1520.

[146] H. Ohshima, A. Miyagishima, T. Kurita, Y. Makino, Y. Iwao, T. Sonobe, S. Itai, Freeze-dried nifedipine-lipid nanoparticles with long-term nano-dispersion stability after reconstitution. Int. J. Pharm. 377(1-2) (2009) 180-184.

[147] H.L. Wong, R. Bendayan, A.M. Rauth, Y. Li, X.Y. Wu, Chemotherapy with anticancer drugs encapsulated in solid lipid nanoparticles. Adv. Drug Deliv. Rev. 59(6) (2007) 491-504.

[148] P. Blasi, S. Giovagnoli, A. Schoubben, M. Ricci, C. Rossi, Solid lipid nanoparticles for targeted brain drug delivery. Adv. Drug Deliv. Rev. 59(6) (2007) 454-477.

[149] V. Venkateswarlu, K. Manjunath, Preparation, characterization and in vitro release kinetics of clozapine solid lipid nanoparticles. J. Controlled Release 95(3) (2004) 627-638.

[150] A. zur Mühlen, C. Schwarz, W. Mehnert, Solid lipid nanoparticles (SLN) for controlled drug delivery - Drug release and release mechanism. Eur. J. Pharm. Biopharm. 45(2) (1998) 149-155.

[151] C. Olbrich, R.H. Müller, Enzymatic degradation of SLN--effect of surfactant and surfactant mixtures. Int. J. Pharm. 180(1) (1999) 31-39.

[152] M. Oyewumi, R. Mumper, Gadolinium-Loaded Nanoparticles Engineered from Microemulsion Templates. Drug Dev. Ind. Pharm. 28(3) (2002) 317.

[153] L.B. Jensen, E. Magnussson, L. Gunnarsson, C. Vermehren, H.M. Nielsen, K. Petersson, Corticosteroid solubility and lipid polarity control release from solid lipid nanoparticles. Int. J. Pharm. 390(1) (2010) 53-60.

[154] J. Williams, R. Lansdown, R. Sweitzer, M. Romanowski, R. LaBell, R. Ramaswami, E. Unger, Nanoparticle drug delivery system for intravenous delivery of topoisomerase inhibitors. J. Controlled Release 91(1-2) (2003) 167-172.

[155] M.E. Carlotti, S. Sapino, E. Peira, M. Gallarate, E. Ugazio, On the Photodegradation of Dithranol in Different Topical Formulations: Use of SLN to Increase the Stability of the Drug. J. Dispers. Sci. Technol. 30(10) (2009) 1517 - 1524.

[156] B. Siekmann, K. Westesen, Thermoanalysis of the recrystallization process of melt-homogenized glyceride nanoparticles. Colloids Surf. B Biointerfaces 3(3) (1994) 159-175.

[157] M. Uner, S.A. Wissing, G. Yener, R.H. Muller, Influence of surfactants on the physical stability of solid lipid nanoparticle (SLN) formulations. Pharmazie 59(4) (2004) 331-332.

[158] D. Wang, P. Zhao, F. Cuia, X. Li, Preparation and characterization of solid lipid nanoparticles loaded with total flavones of Hippophae rhamnoides (TFH). PDA J. Pharm. Sci. Technol. 61(2) (2007) 110-120.

[159] M.K. Rawat, A. Jain, A. Mishra, M.S. Muthu, S. Singh, Development of repaglinide loaded solid lipid nanocarrier: selection of fabrication method. Curr. Drug Deliv. 7(1) (2010) 44-50.

[160] J.M. Koziara, T.R. Whisman, M.T. Tseng, R.J. Mumper, In-vivo efficacy of novel paclitaxel nanoparticles in paclitaxel-resistant human colorectal tumors. J. Controlled Release 112(3) (2006) 312-319.

[161] P. Ma, X. Dong, C.L. Swadley, A. Gupte, M. Leggas, H.C. Ledebur, R.J. Mumper, Development of idarubicin and doxorubicin solid lipid nanoparticles to overcome Pgp-mediated multiple drug resistance in leukemia. J. Biomed. Nanotechnol. 5(2) (2009) 151-161.

[162] X. Dong, C.A. Mattingly, M. Tseng, M. Cho, V.R. Adams, R.J. Mumper, Development of new lipid-based paclitaxel nanoparticles using sequential simplex optimization. Eur. J. Pharm. Biopharm. 72(1) (2009) 9-17.

[163] C.H. Hsu, Z. Cui, R.J. Mumper, M. Jay, Preparation and characterization of novel coenzyme Q10 nanoparticles engineered from microemulsion precursors. AAPS PharmSciTech 4(3) (2003) E32.

[164] W.S. Rasband, ImageJ. Vol. 2010, U.S. National Institutes of Health, Bethesda, Maryland, USA, 1997-2009.

[165] M. Garcia-Fuentes, D. Torres, M. Martin-Pastor, M.J. Alonso, Application of NMR spectroscopy to the characterization of PEG-stabilized lipid nanoparticles. Langmuir 20(20) (2004) 8839-8845.

[166] F.G. Gandolfo, A. Bot, E. Flöter, Phase diagram of mixtures of stearic acid and stearyl alcohol. Thermochimica Acta 404(1-2) (2003) 9-17.

[167] L. Ventola, M. Ramirez, T. Calvet, X. Solans, M.A. Cuevas-Diarte, P. Negrier, D. Mondieig, J.C. van Miltenburg, H.A.J. Oonk, Polymorphism of N-Alkanols: 1-Heptadecanol, 1-Octadecanol, 1-Nonadecanol, and 1-Eicosanol. Chemistry of Materials 14(2) (2002) 508-517.

[168] H. Chen, X. Chang, D. Du, W. Liu, J. Liu, T. Weng, Y. Yang, H. Xu, X. Yang, Podophyllotoxin-loaded solid lipid nanoparticles for epidermal targeting. J. Controlled Release 110(2) (2006) 296-306.

[169] R.R. Zhu, L.L. Qin, M. Wang, S.M. Wu, S.L. Wang, R. Zhang, Z.X. Liu, X.Y. Sun, S.D. Yao, Preparation, characterization, and anti-tumor property of podophyllotoxin-loaded solid lipid nanoparticles. Nanotechnology 20(5) (2009) 7.

[170] R. Cavalli, A. Bargoni, V. Podio, E. Muntoni, G.P. Zara, M.R. Gasco, Duodenal administration of solid lipid nanoparticles loaded with different percentages of tobramycin. J. Pharm. Sci. 92(5) (2003) 1085-1094.

[171] B. Coldren, R. vanZanten, M.J. Mackel, J.A. Zasadzinski, H.T. Jung, From Vesicle Size Distributions to Bilayer Elasticity via Cryo-Transmission and Freeze-Fracture Electron Microscopy. Langmuir 19(14) (2003) 5632-5639.

[172] M.A. Schubert, M. Harms, C.C. Müller-Goymann, Structural investigations on lipid nanoparticles containing high amounts of lecithin. Eur. J. Pharm. Sci. 27(2-3) (2006) 226-236.

[173] A.A. Attama, B.C. Schicke, T. Paepenmüller, C.C. Müller-Goymann, Solid lipid nanodispersions containing mixed lipid core and a polar heterolipid: Characterization. Eur. J. Pharm. Biopharm. 67(1) (2007) 48-57.

[174] H. Bunjes, F. Steiniger, W. Richter, Visualizing the Structure of Triglyceride Nanoparticles in Different Crystal Modifications. Langmuir 23(7) (2007) 4005-4011.

[175] J.A. Champion, Y.K. Katare, S. Mitragotri, Particle shape: a new design parameter for micro- and nanoscale drug delivery carriers. J. Controlled Release 121(1-2) (2007) 3-9.

[176] I. Friedrich, S. Reichl, C.C. Müller-Goymann, Drug release and permeation studies of nanosuspensions based on solidified reverse micellar solutions (SRMS). Int. J. Pharm. 305(1-2) (2005) 167-175.

[177] H. Bunjes, T. Unruh, Characterization of lipid nanoparticles by differential scanning calorimetry, X-ray and neutron scattering. Adv. Drug Deliv. Rev. 59(6) (2007) 379-402.

[178] T. Unruh, H. Bunjes, K. Westesen, M.H.J. Koch, Observation of Size-Dependent Melting in Lipid Nanoparticles. J. Phys. Chem. B 103(47) (1999) 10373-10377.

[179] M. Garcia-Fuentes, M.J. Alonso, D. Torres, Design and characterization of a new drug nanocarrier made from solid-liquid lipid mixtures. J. Colloid Interface Sci. 285(2) (2005) 590-598.

[180] V. Jenning, A.F. Thünemann, S.H. Gohla, Characterisation of a novel solid lipid nanoparticle carrier system based on binary mixtures of liquid and solid lipids. Int. J. Pharm. 199(2) (2000) 167-177.

[181] F.-Q. Hu, S.-P. Jiang, Y.-Z. Du, H. Yuan, Y.-Q. Ye, S. Zeng, Preparation and characterization of stearic acid nanostructured lipid carriers by solvent diffusion method in an aqueous system. Colloids Surf. B Biointerfaces 45(3-4) (2005) 167-173.

[182] F. Castelli, C. Puglia, M.G. Sarpietro, L. Rizza, F. Bonina, Characterization of indomethacin-loaded lipid nanoparticles by differential scanning calorimetry. Int. J. Pharm. 304(1-2) (2005) 231-238.

[183] A.J. Almeida, E. Souto, Solid lipid nanoparticles as a drug delivery system for peptides and proteins. Adv. Drug Deliv. Rev. 59(6) (2007) 478-490.

[184] Z. Cui, R.J. Mumper, Plasmid DNA-Entrapped Nanoparticles Engineered from Microemulsion Precursors: In Vitro and in Vivo Evaluation. Bioconjug. Chem. 13(6) (2002) 1319-1327.

[185] D. Zhu, X. Lu, P.A. Hardy, M. Leggas, M. Jay, Nanotemplate-engineered nanoparticles containing gadolinium for magnetic resonance imaging of tumors. Invest. Radiol. 43(2) (2008) 129-140.

[186] S. Morel, E. Terreno, E. Ugazio, S. Aime, M.R. Gasco, NMR relaxometric investigations of solid lipid nanoparticles (SLN) containing gadolinium(III) complexes. Eur. J. Pharm. Biopharm. 45(2) (1998) 157-163.

[187] R.H. Müller, S.A. Runge, V. Ravelli, A.F. Thünemann, W. Mehnert, E.B. Souto, Cyclosporine-loaded solid lipid nanoparticles (SLN®): Drug-lipid physicochemical interactions and characterization of drug incorporation. Eur. J. Pharm. Biopharm. 68(3) (2008) 535-544.

[188] S.A. Wissing, R.H. Muller, L. Manthei, C. Mayer, Structural characterization of Q10-loaded solid lipid nanoparticles by NMR spectroscopy. Pharm. Res. 21(3) (2004) 400-405.

[189] L.H. Reddy, R.S. Murthy, Etoposide-loaded nanoparticles made from glyceride lipids: formulation, characterization, in vitro drug release, and stability evaluation. AAPS PharmSciTech 6(2) (2005) E158-166.

[190] A. zur Muhlen, W. Mehnert, Drug release and release mechanism of prednisolone loaded solid lipid nanoparticles. Pharmazie 53(8) (1998) 552-555.

[191] P. Ahlin, J. Kristl, M. Sentjurc, J. Strancar, S. Pecar, Influence of spin probe structure on its distribution in SLN dispersions. Int. J. Pharm. 196(2) (2000) 241-244.

[192] R. Sivaramakrishnan, C. Nakamura, W. Mehnert, H.C. Korting, K.D. Kramer, M. Schäfer-Korting, Glucocorticoid entrapment into lipid carriers - characterisation by parelectric spectroscopy and influence on dermal uptake. J. Controlled Release 97(3) (2004) 493-502.

[193] A.H.S. Stancampiano, G. Puglisi, R. Pignatello, Effect of lipophilicity of dispersed drugs on the physicochemical and technological properties of solid lipid nanoparticles. Open Drug Delivery J. 2 (2008) 26-32.

[194] M. Doi, T. Ishida, S. Sugio, T. Imagawa, M. Inoue, Physicochemical properties of dexamethasone palmitate, a high fatty acid ester of an anti-inflammatory drug: polymorphism and crystal structure. J. Pharm. Sci. 78(5) (1989) 417-422.

[195] R.S. Mulik, J. Mönkkönen, R.O. Juvonen, K.R. Mahadik, A.R. Paradkar, Transferrin mediated solid lipid nanoparticles containing curcumin: Enhanced in vitro anticancer activity by induction of apoptosis. Int. J. Pharm. 398(1-2) (2010) 190-203.

[196] M. Uner, S.A. Wissing, G. Yener, R.H. Muller, Solid lipid nanoparticles (SLN) and nanostructured lipid carriers (NLC) for application of ascorbyl palmitate. Pharmazie 60(8) (2005) 577-582.

[197] J.-K. Kim, M.D. Howard, T.D. Dziubla, J.J. Rinehart, M. Jay, X. Lu, Uniformity of Drug Payload and Its Effect on Stability of Solid Lipid Nanoparticles Containing an Ester Prodrug. ACS Nano 5(1) (2010) 209-216.

[198] K. Abdulmajed, C.M. Heard, Topical delivery of retinyl ascorbate co-drug: 1. Synthesis, penetration into and permeation across human skin. Int. J. Pharm. 280(1-2) (2004) 113-124.

[199] D. Swern, Solubility and specific rotation of L-ascorbyl palmitate and L-ascorbyl laurate. J. Am. Chem. Soc. 71(9) (1949) 3256-3256.

[200] W. Cort, Antioxidant activity of tocopherols, ascorbyl palmitate, and ascorbic acid and their mode of action. Journal of the American Oil Chemists' Society 51(7) (1974) 321-325.

[201] S. Palma, P. Lo Nostro, R. Manzo, D. Allemandi, Evaluation of the surfactant properties of ascorbyl palmitate sodium salt. Eur. J. Pharm. Sci. 16(1-2) (2002) 37-43.

[202] S. Fujisawa, T. Atsumi, M. Ishihara, Y. Kadoma, Cytotoxicity, ROS-generation Activity and Radical-scavenging Activity of Curcumin and Related Compounds. Anticancer Res. 24(2B) (2004) 563-570.

[203] B.T. Kurien, A. Singh, H. Matsumoto, R.H. Scofield, Improving the solubility and pharmacological efficacy of curcumin by heat treatment. Assay Drug Dev. Technol. 5(4) (2007) 567-576.

[204] S. Lapenna, A.R. Bilia, G.A. Morris, M. Nilsson, Novel Artemisinin and Curcumin Micellar Formulations: Drug Solubility Studies by NMR Spectroscopy. J. Pharm. Sci. 98(10) (2009) 3666-3675.

[205] V.R. Yadav, S. Suresh, K. Devi, S. Yadav, Effect of Cyclodextrin Complexation of Curcumin on its Solubility and Antiangiogenic and Anti-inflammatory Activity in Rat Colitis Model. AAPS PharmSciTech 10(3) (2009) 752-762.

[206] P. Spiclin, M. Gasperlin, V. Kmetec, Stability of ascorbyl palmitate in topical microemulsions. Int. J. Pharm. 222(2) (2001) 271-279.

[207] M.D. Howard, X. Lu, J.J. Rinehart, M. Jay, T.D. Dziubla, Physicochemical Characterization of Nanotemplate Engineered Solid Lipid Nanoparticles. Langmuir 27(5) (2011) 1964-1971.

[208] B. Li, M. Sedlacek, I. Manoharan, R. Boopathy, E.G. Duysen, P. Masson, O. Lockridge, Butyrylcholinesterase, paraoxonase, and albumin esterase, but not carboxylesterase, are present in human plasma. Biochem. Pharmacol. 70(11) (2005) 1673-1684.

[209] G. Xu, W. Zhang, M.K. Ma, H.L. McLeod, Human Carboxylesterase 2 Is Commonly Expressed in Tumor Tissue and Is Correlated with Activation of Irinotecan. Clin. Cancer Res. 8(8) (2002) 2605-2611.

[210] S.P. Sanghani, S.K. Quinney, T.B. Fredenburg, Z. Sun, W.I. Davis, D.J. Murry, O.W. Cummings, D.E. Seitz, W.F. Bosron, Carboxylesterases Expressed in Human Colon Tumor Tissue and Their Role in CPT-11 Hydrolysis. Clin. Cancer Res. 9(13) (2003) 4983-4991.

[211] A. Kabalnov, Ostwald ripening and related phenomena. J. Dispers. Sci. Technol. 22(1) (2001) 1-12.

[212] S. Verma, S. Kumar, R. Gokhale, D.J. Burgess, Physical stability of nanosuspensions: Investigation of the role of stabilizers on Ostwald ripening. Int. J. Pharm. 406(1-2) (2011) 145-152.

[213] H. Cabane, D. Laporte, A. Provost, An experimental study of Ostwald ripening of olivine and plagioclase in silicate melts: implications for the growth and size of crystals in magmas. Contributions to Mineralogy and Petrology 150(1) (2005) 37-53.

[214] L. Ratke, D. Uffelmann, W. Bender, P.W. Voorhees, Theory of Ostwald ripening due to a second-order reaction. Scripta Metallurgica et Materialia 33(3) (1995) 363-367.

[215] M. Hamidi, A. Azadi, P. Rafiei, Pharmacokinetic Consequences of Pegylation. Drug Deliv. 13(6) (2006) 399-409.

[216] K.Y. Choi, K.H. Min, H.Y. Yoon, K. Kim, J.H. Park, I.C. Kwon, K. Choi, S.Y. Jeong, PEGylation of hyaluronic acid nanoparticles improves tumor targetability in vivo. Biomaterials 32(7) (2011) 1880-1889.

[217] T.-H. Chow, Y.-Y. Lin, J.-J. Hwang, H.-E. Wang, Y.-L. Tseng, V.F. Pang, R.-S. Liu, W.-J. Lin, C.-S. Yang, G. Ting, Therapeutic Efficacy Evaluation of 111In-Labeled PEGylated Liposomal Vinorelbine in Murine Colon Carcinoma with Multimodalities of Molecular Imaging. J. Nucl. Med. 50(12) (2009) 2073-2081.

[218] V. Zabaleta, M.A. Campanero, J.M. Irache, An HPLC with evaporative light scattering detection method for the quantification of PEGs and Gantrez in PEGylated nanoparticles. J. Pharm. Biomed. Anal. 44(5) (2007) 1072-1078.

[219] S.O. Auriola, K.M. Ronkko, A. Urtti, Determination of polyethylene glycols by high-performance liquid chromatography-thermospray mass spectrometry. J. Pharm. Biomed. Anal. 11(10) (1993) 1027-1032.

[220] M.J. Parr, S.M. Ansell, L.S. Choi, P.R. Cullis, Factors influencing the retention and chemical stability of poly(ethylene glycol)-lipid conjugates incorporated into large unilamellar vesicles. Biochim. Biophys. Acta - Biomembranes 1195(1) (1994) 21-30.

[221] B. Romberg, W.E. Hennink, G. Storm, Sheddable coatings for long-circulating nanoparticles. Pharm. Res. 25(1) (2008) 55-71.

[222] D.T. Auguste, S.P. Armes, K.R. Brzezinska, T.J. Deming, J. Kohn, R.K. Prud'homme, pH triggered release of protective poly(ethylene glycol)-b-polycation copolymers from liposomes. Biomaterials 27(12) (2006) 2599-2608.

[223] H. Sun, B. Guo, R. Cheng, F. Meng, H. Liu, Z. Zhong, Biodegradable micelles with sheddable poly(ethylene glycol) shells for triggered intracellular release of doxorubicin. Biomaterials 30(31) (2009) 6358-6366.

[224] D. Kirpotin, K. Hong, N. Mullah, D. Papahadjopoulos, S. Zalipsky, Liposomes with detachable polymer coating: destabilization and fusion of dioleoylphosphatidylethanolamine vesicles triggered by cleavage of surface-grafted poly(ethylene glycol). FEBS Lett. 388(2-3) (1996) 115-118.

[225] T.J. Harris, G. von Maltzahn, M.E. Lord, J.-H. Park, A. Agrawal, D.-H. Min, M.J. Sailor, S.N. Bhatia, Protease-Triggered Unveiling of Bioactive Nanoparticles. Small 4(9) (2008) 1307-1312.

[226] B.M. Liederer, R.T. Borchardt, Stability of oxymethyl-modified coumarinic acid cyclic prodrugs of diastereomeric opioid peptides in biological media from various animal species including human. J. Pharm. Sci. 94(10) (2005) 2198-2206.

[227] H. Pan, P. Kopečková, J. Liu, D. Wang, S. Miller, J. Kopeček, Stability in Plasmas of Various Species of HPMA Copolymer–PGE1 Conjugates. Pharm. Res. 24(12) (2007) 2270-2280.

[228] A. Gabizon, H. Shmeeda, Y. Barenholz, Pharmacokinetics of Pegylated Liposomal Doxorubicin: Review of Animal and Human Studies. Clin. Pharmacokinet. 42(5) (2003) 419-436.

[229] J. Kristl, B. Volk, M. Gasperlin, M. Sentjurc, P. Jurkovic, Effect of colloidal carriers on ascorbyl palmitate stability. Eur. J. Pharm. Sci. 19(4) (2003) 181-189.

[230] W. Abdelwahed, G. Degobert, S. Stainmesse, H. Fessi, Freeze-drying of nanoparticles: Formulation, process and storage considerations. Adv. Drug Deliv. Rev. 58(15) (2006) 1688-1713.

[231] M.K. Lee, M.Y. Kim, S. Kim, J. Lee, Cryoprotectants for freeze drying of drug nano-suspensions: effect of freezing rate. J. Pharm. Sci. 98(12) (2009) 4808-4817.

[232] J. Varshosaz, S. Ghaffari, M.R. Khoshayand, F. Atyabi, A. Jafarian Dehkordi, F. Kobarfard, Optimization of freeze-drying condition of amikacin solid lipid nanoparticles using D-optimal experimental design. Pharm. Dev. Technol. 0(0) (2010) 1-8.

[233] L. Greenspan, Humidity Fixed Points of Binary Saturated Aqueous Solutions. Journal of Research of the National Bureau of Standards-A. Physics and Chemistry 81A(1) (1977) 89-96.

[234] S. Kamiya, Y. Nozawa, A. Miyagishima, T. Kurita, Y. Sadzuka, T. Sonobe, Physical Characteristics of Freeze-Dried Griseofulvin-Lipids Nanoparticles. Chem. Pharm. Bull. (Tokyo). 54(2) (2006) 181-184.

[235] H. Heiati, R. Tawashi, N.C. Phillips, Drug retention and stability of solid lipid nanoparticles containing azidothymidine palmitate after autoclaving, storage and lyophilization. J. Microencapsul. 15(2) (1998) 173-184.

[236] S. Subramanian, P. Dandekar, R. Jain, U. Pandey, G. Samuel, P.A. Hassan, V. Patravale, M. Venkatesh, Technetium-99m-Labeled Poly(DL-lactide-co-glycolide) nanoparticles as an alternative for sentinel lymph node imaging. Cancer Biother. Radiopharm. 25(6) (2011) 637-644.

[237] Z. Cui, C.H. Hsu, R.J. Mumper, Physical characterization and macrophage cell uptake of mannan-coated nanoparticles. Drug Dev. Ind. Pharm. 29(6) (2003) 689-700.

[238] M. Sameti, G. Bohr, M.N.V. Ravi Kumar, C. Kneuer, U. Bakowsky, M. Nacken, H. Schmidt, C.M. Lehr, Stabilisation by freeze-drying of cationically modified silica nanoparticles for gene delivery. Int. J. Pharm. 266(1-2) (2003) 51-60.

[239] C. Schwarz, W. Mehnert, Freeze-drying of drug-free and drug-loaded solid lipid nanoparticles (SLN). Int. J. Pharm. 157(2) (1997) 171-179.

[240] O.D. Bochkova, et al., Silica nanoparticles with a substrate switchable luminescence. Journal of Physics: Conference Series 291(1) (2011) 012038.

[241] F.-L. Yen, T.-H. Wu, C.-W. Tzeng, L.-T. Lin, C.-C. Lin, Curcumin Nanoparticles Improve the Physicochemical Properties of Curcumin and Effectively Enhance Its Antioxidant and Antihepatoma Activities. J. Agric. Food Chem. 58(12) (2010) 7376-7382.

[242] F. De Jaeghere, E. Allemann, J. Feijen, T. Kissel, E. Doelker, R. Gurny, Freeze-drying and lyopreservation of diblock and triblock poly(lactic acid)-poly(ethylene oxide) (PLA-PEO) copolymer nanoparticles. Pharm. Dev. Technol. 5(4) (2000) 473-483.

[243] J. Lee, Y. Cheng, Critical freezing rate in freeze drying nanocrystal dispersions. J. Controlled Release 111(1-2) (2006) 185-192.

[244] K.M. Gura, Is There Still a Role for Peripheral Parenteral Nutrition? Nutr. Clin. Pract. 24(6) (2009) 709-717.

[245] S.-J. Lim, C.-K. Kim, Formulation parameters determining the physicochemical characteristics of solid lipid nanoparticles loaded with all-trans retinoic acid. Int. J. Pharm. 243 (2002) 135-146.

[246] N.A. Williams, G.P. Polli, The Lyophilization of Pharmaceuticals: A Literature Review. PDA J. Pharm. Sci. Technol. 38(2) (1984) 48-60.

[247] S. de Chasteigner, G. Cavé, H. Fessi, J.-P. Devissaguet, F. Puisieux, Freeze-drying of itraconazole-loaded nanosphere suspensions: a feasibility study. Drug Development Research 38(2) (1996) 116-124.

[248] M. Nango, H. Yamamoto, K. Joukou, M. Ueda, A. Katayama, N. Kuroki, Solubility of aromatic hydrocarbons in water and aqueous solutions of sugars. Journal of the Chemical Society, Chemical Communications(3) (1980) 104-105.

[249] P.A. Webb, A Primer on Particle Sizing by Static Laser Light Scattering, Micromeritics Instrument Corp., 2000.

[250] Dynamic Light Scattering: An Introduction in 30 Minutes, Malvern Instruments.

[251] Delsa Nano Submicron Particle Size and Zeta Potential Particle Analyzer, Beckman Coulter, 2007.

[252] Laser Diffraction Particle Sizing. Malvern Instruments Ltd. , 2011.
[253] S. Bradbury, D.C. Joy, B.J. Ford, Transmission electron microscope (TEM). Encyclopedia Brittanica, 2011.
[254] L.G. Wade, Organic Chemistry, Pearson Education, Inc., Upper Saddle River, NJ, 2003.
[255] S. Clare, Functional MRI: Methods and Applications. Physics, Vol. Ph.D., University of Nottingham, Nottingham, England, 1997.
[256] Q.s. University, Advanced NMR Course. 1999.
[257] G.W.H. Hohne, W.F. Hemminger, H.-J. Flammersheim, Differential scanning calorimetry, Springer-Verlag Berlin Heidleberg, 2003.
[258] S. Speakman, Basics of X-ray Diffraction, Massachusetts Institute of Technology.
[259] D.C. Harris, Quantitative Chemical Analysis, W.H.Freeman and Company, New York, NY, 2003.
[260] D.C. Harris, Quantitative Chemical Analysis, W.H.Freeman and Company, New York, NY, 2003.
[261] C. Aurand, Moisture Determination by Karl Fischer Titration: Background of the Chemistry and Recent Developments, Sigma-Aldrich, 2010.
[262] A. Nakajima, Solvent effect on vibrational structures of fluorescence and absorption-spectra of pyrene. Bull. Chem. Soc. Jpn. 44(12) (1971) 3272-3277.
[263] K. Kalyanasundaram, J.K. Thomas, Environmental effects on vibronic band intensities in pyrene monomer fluorescence and their application in studies of micellar systems. J. Am. Chem. Soc. 99(7) (1977) 2039-2044.
[264] J. Aguiar, P. Carpena, J.A. Molina-Bolívar, C. Carnero Ruiz, On the determination of the critical micelle concentration by the pyrene 1:3 ratio method. J. Colloid Interface Sci. 258(1) (2003) 116-122.
[265] J. Karllson, Kollicoat IR/Brij 78: A stable couple? - Storage stability of aqueous pharmaceutical coatings. Department of Chemical and Biological Engineering, Vol. Masters of Science, Chalmers University of Technology, Goteborg, Sweden, 2010, p. 40.
[266] S.K. Hait, S.P. Moulik, Determination of Critical Micelle Concentration (CMC) of nonionic surfactants by donor-acceptor interaction with iodine and correlation of CMC with Hydrophile-Lipophile Balance and Other Parameters of the Surfactants. Journal of Surfactants and Detergents 4(3) (2001) 303-309.
[267] V.P. Torchilin, Structure and design of polymeric surfactant-based drug delivery systems. J. Controlled Release 73(2-3) (2001) 137-172.
[268] Y. Matsumura, K. Kataoka, Preclinical and clinical studies of anticancer agent-incorporating polymer micelles. Cancer Science 100(4) (2009) 572-579.
[269] T.L. Andresen, D.H. Thompson, T. Kaasgaard, Enzyme-triggered nanomedicine: Drug release strategies in cancer therapy (Invited Review). Mol. Membr. Biol. 27(7) (2010) 353-363.
[270] E.S. Lee, Z. Gao, Y.H. Bae, Recent progress in tumor pH targeting nanotechnology. J. Controlled Release 132(3) (2008) 164-170.
[271] D. Oosterhoff, H.M. Pinedo, I.H. van der Meulen, M. de Graaf, T. Sone, F.A. Kruyt, V.W. van Beusechem, H.J. Haisma, W.R. Gerritsen, Secreted and tumour targeted human carboxylesterase for activation of irinotecan. Br. J. Cancer 87(6) (2002) 659-664.

[272] M.G.V. Heiden, L.C. Cantley, C.B. Thompson, Understanding the Warburg Effect: The Metabolic Requirements of Cell Proliferation. Science 324(5930) (2009) 1029-1033.

[273] Y. Bae, S. Fukushima, A. Harada, K. Kataoka, Design of Environment-Sensitive Supramolecular Assemblies for Intracellular Drug Delivery: Polymeric Micelles that are Responsive to Intracellular pH Change. Angew. Chem. Int. Ed. 42(38) (2003) 4640-4643.

[274] A. Ponta, Y. Bae, PEG-poly(amino acid) Block Copolymer Micelles for Tunable Drug Release. Pharm. Res. 27(11) (2010) 2330-2342.

[275] Y. Bae, K. Kataoka, Intelligent polymeric micelles from functional poly(ethylene glycol)-poly(amino acid) block copolymers. Adv. Drug Deliv. Rev. 61(10) (2009) 768-784.

[276] K. Kataoka, A. Harada, Y. Nagasaki, Block copolymer micelles for drug delivery: design, characterization and biological significance. Adv. Drug Deliv. Rev. 47(1) (2001) 113-131.

[277] M.S. Kim, C.J. CotÃ©, C. Cristoloveanu, A.G. Roth, P. Vornov, M.A. Jennings, J.P. Maddalozzo, C. Sullivan, There Is No Dose-Escalation Response to Dexamethasone (0.0625â€“1.0 mg/kg) in Pediatric Tonsillectomy or Adenotonsillectomy Patients for Preventing Vomiting, Reducing Pain, Shortening Time to First Liquid Intake, or the Incidence of Voice Change. Anesth. Analg. 104(5) (2007) 1052-1058.

[278] S.R. Croy, G.S. Kwon, Polymeric Micelles for Drug Delivery. Curr. Pharm. Des. 12(36) (2006) 4669-4684.

[279] C.G.M. Jordan, How an increase in the carbon chain length of the ester moiety affects the stability of a homologous series of oxprenolol esters in the presence of biological enzymes. J. Pharm. Sci. 87(7) (1998) 880-885.

[280] Y. Bae, N. Nishiyama, S. Fukushima, H. Koyama, M. Yasuhiro, K. Kataoka, Preparation and Biological Characterization of Polymeric Micelle Drug Carriers with Intracellular pH-Triggered Drug Release Property: Tumor Permeability, Controlled Subcellular Drug Distribution, and Enhanced in Vivo Antitumor Efficacy. Bioconjug. Chem. 16(1) (2005) 122-130.

VITA

Melissa Howard was born on November 17, 1985 in Louisville, Kentucky, USA. She received a Bachelor of Arts degree in biochemistry from Asbury College (Wilmore, Kentucky, USA) in May 2007 and joined the Department of Pharmaceutical Sciences Graduate Program at the University of Kentucky that fall. She has been awarded numerous fellowships, including a National Science Foundation Integrative Graduate Education and Traineeship (IGERT) Award (2008-2010), a Philanthropic Educational Organization Scholar Award (2010-2011), an American Foundation for Pharmaceutical Education Pre-Doctoral Fellowship (2010-2011, declined), as well as Dissertation Year (2010-2011) and Reedy Quality Achievement (2007-2010) Fellowships from the University of Kentucky. Other notable accomplishments include winning first place at the 2008 University of Kentucky Graduate Student Interdisciplinary Conference poster competition, being chosen as one of the two representatives from the University of Kentucky to attend the 2008 Globalization of Pharmaceutics Education Network Conference, and receiving the Award for Communications Excellence at the National Science Foundation IGERT 2010 Project Meeting poster competition. She is the author or co-author of six publications, including a review article on PEGylation of nanoparticles, and has three additional manuscripts submitted for review.

Publications:

1. **Howard MD**, Ponta A, Eckman A, Jay M, and Bae Y. Polymer Micelles with Hydrazone-Ester Dual Linkers for Tunable Release of Dexamethasone. Pharmaceutical Research. 2011; DOI 10.1007/s11095-011-0470-1.

2. **Howard MD**, Lu X, Rinehart JJ, Jay M, and Dziubla TD. Physicochemicial Characterization of Nanotemplate Engineered Solid Lipid Nanoparticles. Langmuir. 2011; 27(5): 1964-1971.
3. Kim J, **Howard MD**, Dziubla TD, Rinehart JJ, Jay M, and Lu X. Uniformity of Drug Payload and its Effect on Stability of Solid Lipid Nanoparticles Containing an Ester Prodrug. ACS Nano. 2010; 5(1): 209-216.
4. Lu X, **Howard MD**, Talbert DR, Rinehart JJ, Potter PM, Jay M and Leggas M. Nanoparticles Containing Anti-inflammatory Agents as Chemotherapy Adjuvants II: Role of Plasma Esterases in Drug Release. AAPS J. 2009; 11(1):120-122.
5. **Howard MD**, Jay M, Dziubla TD and Lu X. PEGylation of Nanocarrier Drug Delivery Systems: State of the Art. Journal of Biomedical Nanotechnology. 2008; 4:133-148.
6. Lu X, **Howard MD**, Mazik M, Eldridge J, Rinehart JJ, Jay M and Leggas M. Nanoparticles Containing Anti-inflammatory Agents as Chemotherapy Adjuvants: Optimization and *In Vitro* Characterization. AAPS J. 2008; 10:133-140.

Melissa Howard
Author

July 19, 2011
Date